GEOPHYSICAL INVESTIGATION INTO THE INTERNAL DYNAMICS OF MOVING LAHARS

MASSEY UNIVERSITY

A thesis presented in partial fulfillment of the requirements for the degree of

Doctor of Philosophy

in

Earth Science

at Massey University, Palmerston North, New Zealand

Susan Elizabeth Cole

Department of Soil and Earth Sciences

2011

Frontispiece. *Aerial view downstream overlooking the Tangiwai rail (foreground) and road (backgound) bridges during the Crater Lake-breakout lahar from Mt. Ruapehu, New Zealand, on 18th March 2007. The inundated memorial to the 151 people who died in the 1953 Tangiwai Disaster, caused by a similar style lahar, is located between the two bridges. (Photograph courtesy of H.J.R. Keys.)*

Abstract

Lahars and other mass flows are highly hazardous phenomena that can pose great risk to areas in their path. Due to their often unpredictable onsets, scientific observations are limited. In addition, the erosive capabilities of a lahar mean that the most commonly used monitoring and sampling methods, such as load cells and bedload traps, are often damaged early in the flow. The cost of repair and maintenance of these instrumentation prohibits comprehensive coverage of each channel that might be at risk from lahars. The development of seismic sensors as an alternative monitoring method could prove effective as they do not require contact with a flow and are therefore less at risk from damage. The complex behaviour of a lahar can be witnessed in the geophysical record of its passage which, in combination with more traditional monitoring methods, can be used to record the detailed evolution of a flow. The three-dimensional analysis of seismometer recordings can provide an approximation of the frontal velocity that may differ from maximum velocity estimates made using super-elevation calculations. Comparisons of the seismic records of different mass flow types illustrate that it is possible to differentiate between them. Frequency analysis allows for the distinction of the flow mechanisms, particle interactions, and dominant rheology of a lahar. Low frequencies are more indicative of bedload frictional motion, while higher frequencies reflect the collisional impacts of particles, either between themselves or with the substrate. Detailed records of a flow at a single site provide a comprehensive understanding of the temporal variations that occur within the duration of a lahar, while comparative analyses of numerous sites along a channel highlight its downstream evolution. While initial onset signals can be recorded at local-to-source sites, they are attenuated too quickly to be observed further downstream. The records at proximal sites can, however, reflect the stages, or packets, involved during the main bulk of lahar initiation. At more distal sites, observations show that a lahar transitions to a [minimal] 4-phase behaviour. This consists of a frontal bow wave of ambient streamwater that increases

in volume with distance from source, and immediately precedes the lahar proper. The following phases are defined by variations in sediment concentration, velocity, stage, and, in the case of Crater Lake-originating lahars, water chemistry. The understanding of the variable behaviour possible during a lahar, as well as the identification of the specific flow type recorded, is fundamental to modelling approximations of flow volumes, sediment concentrations, likely inundation areas, and probable damage by the flow. It is essential for the development of future warning systems that the variations that can occur within a single lahar are better understood, as lahars represent a serious threat to the slopes of many volcanoes worldwide.

Acknowledgements

This research would not have been possible without the assistance of my chief supervisor, Prof. Shane Cronin. He has provided invaluable assistance in the collection of the data which form the basis of this study. I would like to thank him for the support to attend national and international conferences and field studies. I would also like to thank him for helpful discussions throughout my study and for his thorough reviews of my thesis, papers, and conference abstracts.

I would also like to thank my co-supervisors, Prof. Vince E. Neall (Massey University) and Dr. Steve Sherburn (GNS Science), for their helpful discussions over the course of my study. I would especially like to thank Vince for providing many of the more obscure and hard-to-find references that have been useful in this research, and for his comprehensive review of the bulk of my thesis. I would like to thank Steve for providing (through GeoNet) one of the seismic sensors used within this study and some of the programs used to analyse the data collected.

The breadth of data available for study in this work would not have been possible without the contributions and help of everyone who collected samples and/or surveyed the deposits of the lahars examined herein. For this, I gratefully acknowledge the following people:

In Indonesia: Prof. Shane Cronin, Ms. Céline Dumaisnil, Dr. Vern Manville, Dr. Jon Procter, Prof. Jean-Claude Thouret, Mrs. Lilianne Thouret, and also Bruno and the villagers by the Semeru site who helped install and look after our equipment.

At Ruapehu: the rest of the Crater Lake lahar research team: Mr. Ian Chapman, Prof. Shane Cronin, Dr. Kat Holt, Mr. Matthew Irwin, Mr. Phil Kellman, Dr. Jerome Lecointre, Dr. Gert Lube, Dr. Vern Manville, Ms. Kim Martelli, Dr. Hilary McMillan, Prof. Vince Neall, Ms. Anja Möbis, Dr. Karoly Nemeth, Dr. Jon Procter, Ms. Claire Robertson, Dr. Robert B. Stewart, Prof. Jean-Claude Thouret, Mrs. Lilianne Thouret, Dr. Michael Turner, and Dr. Anke Zernack.

I would also like to thank Dr. Harry Keys and the Department of Conservation for providing the data collected by Ruapehu's ERLAWS sensors, and the NZ Army for allowing access through their land to sections of the Whangaehu Channel for data collection.

I gratefully acknowledge and thank Dr. Emma Doyle for providing the volumes calculated for Mt. Semeru lahars (Chapter 3.2) and the wetted perimeter profiles at the OnTrack Flood Gauge (Chapter 6.2.4). Also deserving of thanks is Dr. Hilary McMillan for her help in better understanding the Kinematic wave and Manning formula theories and providing much of the data contained within Chapter 3.3. Their contributions to and discussions of parts of this thesis were invaluable. Additionally I would also like to thank Dr. Kat Holt, Ms. Emma Phillips, and Dr. Gert Lube for the many hours spent calculating stage heights and flow velocities from the video footage of the lahars.

Special thanks are needed for Dr. Kate Arentsen and Mrs. Moira Hubbard for their invaluable help in dealing with all the administrative issues that arose throughout this study. I would also like to extend my thanks to Mr. Matthew Irwin and Mr. Mike Bretherton for their assistance whenever I had major computer problems.

I would like to thank the Commonwealth Scholarship Scheme and the NZ Vice Chancellors Committee for the funding to support my research. In addition, I gratefully acknowledge the Marsden Fund (MAUX0512 "Capturing the secrets of a life-sized lahar") for providing the funding for the instrumentation used in this study and the financial support for our field seasons in Indonesia. I would also like to thank the New Zealand Earthquake Commission (EQC) for the funding to attend the Cities on Volcanoes 5 conference in Shimabara, Japan.

I wish to thank all of my fellow post-graduate students and the other members of the Volcanic Risk Solutions Group for the many shared experiences of my life in New Zealand. Their friendships have been invaluable over the past four years. I would especially like to thank Dr. Emma Doyle and my office mates, Dr. Michael Turner and Ms. Anja Möbis, for joining me in tea and biscuits whenever we needed a break, and to Dr. Kat Holt for listening and letting me Buddy-sit.

Additionally, I would like to thank the many friends I have made in my time in New Zealand from all over the world. Special mention should be made to all of the flatmates

that I have lived with in the past few years. There have been so many experiences that we have shared that I am thankful for. I would like to especially thank Mr. Hamish White, Ms. Sarah McGray, and Ruby for all of their support, understanding, and patience during the final phase of this study and the writing of this thesis.

Finally, I would like to thank my family for all of their support and encouragement throughout my studies, even when I moved to the other side of the world. My greatest thanks go to my parents, Sarah and Steve, whose unwavering love and support has continually inspired me to persevere during the hard years of MESci and PhD study.

Addendum: I would also like to extend my grateful thanks to my examiners Prof. Jim Jones (Massey University), Prof. Martha Savage (Victoria University of Wellington), and Dr. John Latter (Consultant, Australia) for comments and advice that have enhanced this manuscript.

Author's Declaration

I declare that the work in this thesis was carried out in accordance with the Regulations of Massey University. The work is original except where indicated by special reference in the text and no part of the dissertation has been submitted for any other degree. Any views expressed in the thesis are those of the author and do not necessarily represent those of Massey University. The thesis has not been presented to any other university for examination either in New Zealand or overseas.

Susan Elizabeth Cole

Date:

Viva Examination: 24th August 2011

For my Mum and Daddy.

Contents

List of Tables

List of Figures

Chapter 1

Introduction

Chapter 1 explains the inception and motivation for this study and describes the known properties of lahars and the various field sites and core studies utilised within it.

1.1 Introduction

Due to their rapid emplacement and highly destructive potential, volcanic debris flows, or lahars, represent a great hazard to the infrastructure and populations of towns and cities around volcanoes. Between 1950 and 2001, lahars occurred at 31 volcanoes, claimed more than 28,000 lives, and cost governments many millions of dollars in damages (*Major et al.* (2005); *Witham* (2005)). With detailed knowledge of the travel times, nature, and depositional processes of such flows, we can now more accurately model their flow paths, volumes, and destructive potential. This will allow for the improvement of public safety and emergency planning for such hazards.

Lahars are flowing mixtures of sediment and water that, irrespective of their triggering mechanisms, originate from a volcano (*Smith and Fritz* (1989)). Volcanic debris flows can vary widely in both size and extent; as such, the hazard posed by them also varies considerably. Flows that originate from snow-covered volcanoes are generally larger than those from non-glaciated edifices, especially when triggered by eruptions (*Major et al.* (2005)). A catastrophic example occurred on 13$^{\text{th}}$ November 1985 with the

eruption of Nevado del Ruiz, Columbia, where small volume pyroclastic flows eroded and entrained snow and ice to bulk up and descend into stream valleys. These flows continued down the valleys and buried the town of Armero, situated on a fan c. 74 km downstream, killing more than 23,000 people, destroying more than 5,000 homes, and causing damage valued at millions of dollars (US) (e.g., *Janda et al.* (1986); *Lowe et al.* (1986)).

Difficulties arise in understanding and accurately modelling the physics, motion, and impacts of lahars, primarily due to the presence of sediment within the flows. Within the flow, sediment may be variably incorporated and deposited as a lahar travels down a channel under a range of slope, geology, and confinement conditions (e.g., *Pierson and Scott* (1985); *Cronin et al.* (1997); *Procter et al.* (2009)). By understanding the nature of sediment entrainment and deposition, it will be possible to more accurately describe and model the transport and physical properties of moving lahars, including velocity, frictional contact, basal interaction, erosion, sedimentation etc. Current models developed (e.g., *Pierson* (1995); *Iverson* (1997); *Pierson* (1998); *O'Brien* (1999); *Doyle et al.* (2009)) that attempt to describe the basic properties of a debris flow struggle to replicate the fine-scale process within the flow, and do not take into account any variations in rheology that may occur along the flow in space and time. Continuous observations and measurements of debris flows in motion are necessary if our fundamental understanding of lahars is to grow. Development of new instrumentation and further analysis of results from current instrumentation will help to more realistically define and model debris flows.

The physics of the processes of sediment transport, erosion, and deposition of lahars is very poorly understood (e.g., *O'Brien* (1999); *Doyle et al.* (2009)). More empirical information is needed about the way in which lahars carry sediment, both spatially and temporally. Models of inundation are increasingly realistic due to better constrained topographic descriptions and improved computational hardware and software engineering. However, these are still limited by a lack of basic understanding of the effects of topography, primary driving forces, and other variable factors, such as channel width, depth, and sediment content on lahar dynamics (e.g., *Iverson and Denlinger* (2001); *Fagents and Baloga* (2006); *Carrivick et al.* (2008)). It is important to use observations and geophysical measurements of debris flows to further qualify, as well as quantify,

numerical models to predict possible future lahars.

Much of the current research on the internal properties, flow, and emplacement mechanisms of lahars has been the result of artificial experiments (e.g., *Major and Iverson* (1999)) or from observations of repeated seasonal rain-triggered mass-flows (e.g., *Lavigne and Thouret* (2002)). Limited real-world scientific observations have been possible (e.g., *Cronin et al.* (1997); *Cronin et al.* (2000b); *Cronin et al.* (2000a)), due to the unpredictable onsets of such flows.

Even in situations when conventional scientific observation methods have been possible, it remains very difficult to see 'into' and monitor the changing properties of moving lahars. Due to their high sediment concentrations, particularly in fines (mud), visual observations are limited to the surface of the flow. Velocity estimates are also typically limited to surface measurements. Direct sampling of flows is generally carried out by tossing sampling containers into the channel from steep-edged banks or bridges; hence they also cannot be taken as a complete representation of the entire flow depth (e.g., *Cronin et al.* (1999)). None of these measurements, therefore, have produced any convincing account of vertical stratification in the velocity and sediment profiles of moving lahars.

Despite these difficulties, a number of instrumental techniques to record a lahar have been developed and possible vertical stratifications have been tested. These include load cells, to measure the weight and, with independent measurements of flow depth, the concentration of the flow above (e.g., *Genevois et al.* (2000)), scour chains buried below the channel floor to measure the depths to which bedload transport reaches (e.g., *Berger et al.* (2010)), and bedload traps to capture samples of the sediment concentrations of the lower parts of the flow (e.g., *Sear et al.* (2000)). Problems arise, however, due to the violence and scale of lahars, where instruments are buried, scoured out completely, or destroyed. Bedload traps are able to capture parts of the passing lahar; unfortunately, once they are filled they cannot collect any more samples, because they are unable to be excavated until after the flow has passed completely. The samples are also collected over an unknown length of time, which means that they are representative of a period within the flow, rather than a true measurement of a particular moment.

Geophysical monitoring of lahars, however, can allow for a more complete view of

the internal properties of flows with less potential for damage, because it does not rely on actual contact with them. Non-contact methods ensure the equipment will survive the passing of a flow, while also being able to record its entire passage. Instruments such as seismometers and acoustic flow monitors can be installed in a variety of places near to the channel to record the flow; others, including stage gauges, can be installed on bridges or other structures above the flow path (e.g., *Marcial et al.* (1996); *Cole et al.* (2009)). New forms of load cells and pore pressure transducers that have internal memory capability and do not, therefore, require connection to a separate datalogger can be used where erosion at banks and channel sides are high. By bolting these instruments into a hard rock bed, they resist erosion by the flow (e.g., *Doyle et al.* (2009)).

This study aims to progress research about lahar flow by (1) developing geophysical methods for empirical and field-based flow observations in order to (2) test current hypotheses of lahar horizontal and vertical structure and flow transformation that have been derived from past studies (e.g., *Hodgson and Manville* (1999); *Cronin et al.* (2000a)) and (3) to provide new lahar warning and monitoring methods. Primarily data recorded by seismometers and acoustic flow monitors will be used, as they show promise for the most robust non-invasive measurement technique that provides a rich depth of multicomponent data. Additional techniques such as pore pressure transducers, load cells, stage gauges, direct flow sampling, and visual observations made during lahar flows will be used to develop and interpret the seismic-based tools.

1.2 Objectives and strategy of the study

The aim of this study is to investigate the internal properties of lahars. To this end, observational and instrumental monitoring data will be utilised from many different flows: 1) the Crater Lake-breakout lahar that occurred on 18$^{\text{th}}$ March 2007 at Mt. Ruapehu, New Zealand; 2) three snow-slurry lahars generated by the 25$^{\text{th}}$ September 2007 eruption of Mt. Ruapehu; 3) a single largely-granular rain-triggered lahar from Mt. Merapi, Central Java, Indonesia, recorded in January 2007; and 4) repeated rain-triggered lahars of variable volumes recorded at Mt. Semeru, Eastern Java, Indonesia, during field seasons in February 2006, February 2007, and February-March 2008.

Each of the many records chosen in this study were used to concentrate on the major sub-aims of this thesis work:

1. understanding of the complexity of lahars and how this is related to the water-sediment ratio and rheology of the flows,

2. interpreting the changing signals recorded of a flow both over time at a specific site and with distance from source,

3. developing models of vertical concentration profiles and particle motions within a flow, and their implications regarding the basal and channel-side friction and collisional interactions of particles.

Primarily this study will concentrate on using the data recorded by broadband seismometers and acoustic flow monitors to find new ways to understand the internal dynamics and flow characteristics of lahars. Additional instrumental and observational data will also be used to facilitate understanding of the seismic signals. Methods will be developed to test the application of seismic data as a proxy for sediment concentration, as well as further understanding and identifying the degrees and nature of turbulence within the flow. Analysis of the onset signals may lead to identification of the triggering mechanism of an individual lahar.

The results of the lahar studies will be compared with data from both block-and-ash flows and snow avalanches to see the differences and similarities in signal between the various types of mass flows. This may lead to a means of remote identification of each type of flow from a seismic recording, eliminating (at least, to a degree) the necessity for visual confirmation of what type of flow was recorded. Many volcanoes have seismic stations scattered around and on their flanks; the methodology presented here will, hopefully, allow scientists to identify, locate, and quantify the types of flow recorded by the instruments without having to enter potentially highly hazardous areas.

1.3 Thesis outline

The remainder of this chapter provides a background to volcanic debris flows and also gives details of the field sites selected for instrumentation to monitor lahars in flow. This thesis then comprises a further 6 chapters. Chapter 2 provides a review of the

tools utilised in the study of mass flows, as well as the decisions made in order to select those instruments used in the study. Chapter 3 describes the methodology behind investigation of the frequency distributions within the seismic record of a lahar. This includes details of the theory behind using the seismic record as a proxy for sediment concentration. Chapter 4 provides details of the seismic excitation of flows within 3-dimensions. This allows for increased understanding of the velocity of flow, with respect to the area local to the recording site, as well as giving a possible means to 'see' the flow upstream before it arrives. This in turn could allow for increased warning systems for areas downstream within flow inundation catchments. This chapter has been partially published within Geophysical Research Letters under the title "Seismic signals of snow-slurry lahars in motion: 25 September 2007, Mt Ruapehu, New Zealand", by: Susan E. Cole, Shane J. Cronin, Steven Sherburn, and Vern Manville (Vol. 36; L09405; doi: 10.1029/2009GL038030). Chapter 5 illustrates the character of a lahar wave, as revealed in the signals recorded by broadband seismometers. The record of a lahar past a site changes with regards to time depending on the erosional and depositional abilities of the flow at a single moment within its path length. By utilising a variety of different monitoring styles, it is possible to capture the changing details of a flow at a certain site over time. With a series of sites along a channel, the same methodology can be applied to each site to give a record of a flow over distance. This is the subject of Chapter 6. In conclusion, Chapter 7 summarises the attainment of the study objectives and how they can be utilised as a method for monitoring lahars. Recommendations are also made for future research. The Appendices document the original datasets and programs written or adapted to help analyse the data, as well as provide background information about some of the more complex seismological theories utilised within this study.

1.4 Background on lahars

Lahar definitions vary within the literature but they can be generally described as a flowing mixture of water and debris from a volcano that has a fraction of solids greater than a normal streamflow (*Smith and Fritz* (1989)). These flows can be broken down into groups defined by their sediment concentration and bulk flow appearance or

behaviour as: (1) hyperconcentrated flows; and (2) debris flows.

Hyperconcentrated flows are a specific type of water and sediment combination that flows like a liquid and has measureable yield strength, as defined by *Pierson and Costa* (1987). Sediment concentration is typically 20-60 vol.% (*Beverage and Culbertson* (1964)); *Smith* (1986) interprets sediment support by bouyancy, turbulence, and dispersive grain forces, while deposition of the massive, horizontally-bedded, poorly-sorted flows is explained by the settling of grains at the base and margins of the flow.

Debris flows can be defined as highly concentrated viscous sediment and water mixtures with high yield stress (*Coussot and Meunier* (1996)). Sediment is supported by the matrix strength and dispersive pressure between the grains (*Smith* (1986)), while grain-grain collisions and forces of inertia influence the motion of the flow (*Iverson* (1997)). Debris flows occur commonly as a series of surges, which tend to run over previous deposits (*Major* (1997)). *Coussot and Meunier* (1996) define two extreme types of debris flow, muddy and granular, while *Scott et al.* (1995) define them as cohesive and noncohesive flows. Cohesive flows contain >5% matrix clay, which remains highly concentrated over the full distance of the flow, and are generally formed by the collapse of hydrothermally altered parts of a volcanic edifice (*Scott et al.* (1995)). Flows that contain <5% matrix clay are defined as noncohesive debris flows, and are diluted by entrainment of water along their path, causing a transformation to streamflow via an intermediate stage of hyperconcentrated flow (*Scott et al.* (1995)). Streamflow surges or floods often form noncohesive debris flows by erosion and entrainment of sediment, such as during a lake-breakout flood (*Cronin et al.* (2000a)) or jokulhlaup (*Rodolfo* (2000)).

1.4.1 Triggering mechanisms

Lahars can be triggered by a variety of different mechanisms, both eruptive and non-eruptive. The former type include eruptions through crater lakes, melting of snow and ice, admixing of water with pyroclastic flows, and phreatic explosions. Non-eruptive mechanisms include the sudden release of large amounts of water from crater lakes or subglacial lakes due to edifice collapse and heavy rainfall on volcanic slopes. Examples of each of these mechanisms is given below as evidence of the widespread variety and effects of such flows.

1.4.1.1 Eruptions through crater lakes

A prime example of lahars generated by eruptions through a crater lake have occurred at the Indonesian volcano of Gunung Kelut in Java. Over the last 1000 years, 29 lahars of this type have been responsible for the loss of more than 15,400 lives. The dangers posed by these flows are exacerbated by the natural levees in the river that force inundation of the lowlands adjacent to the channels (e.g., *Alzwar* (1985)).

Mt. Kelut has the capacity for a very large crater lake. Prior to the eruption of 1901, the most reliable estimate of lake volume was 78×10^6 m^3; post-eruption, the volume dropped to around 40×10^6 m^3 (*Alzwar* (1985); *Neall* (1996)). The following eruption occurred in 1919, and emptied the lake of all water, forming lahars with depths of up to 58 m, travelling up to 38 km from source, inundating a total of 131 km^2, and killing 5,160 people (*Alzwar* (1985); *Neumann van Padang* (1951)). After this, the government instigated plans to protect against future disasters of this magnitude by draining the lake of the bulk of its content. The eruption of 1923 illustrated that a step-wise drainage of the lake would be better, after 5 workers were killed; finally, the lake was drained to a volume of less than 2×10^6 m^3 (*Neall* (1996)). The next eruption in 1951 evaporated the waters, and no sizable lahars occurred. The tunnels, however, were blocked, the crater deepened, and the risk of future flows increased. The tunnel drainage system was re-established in 1954 and further tunnels built to drain the deeper crater (*Zen and Hadikusumo* (1965)). These systems were again damaged after the 1966 eruption that triggered the expulsion of c. 20×10^6 m^3 of water from the lake and killed more than 200 people (*Neall* (1996)). Another eruption in 1990 ejected only small volumes of water that produced limited lahars, killing 32 people (*Verstoppen* (1992)). Subsequent extrusion of a lava dome in 2007-2008 displaced nearly the entire lake volume without eruption or major lahar flows (*Smithsonian Institute* (2008)). Despite this, history has shown that once the dome is removed, the lake will return and highly destructive lahars may still eventuate.

1.4.1.2 Melting of snow and ice, and the admixing of pyroclastic flows

As mentioned previously in this Chapter, the eruption of Nevado del Ruiz, Columbia, on 13$^{\text{th}}$ November 1985 produced a series of lahars that caused the deaths of more than

23,000 people. The eruption involved pyroclastic surges and flows and a small Plinian tephra; the total volume erupted was estimated at 1.9×10^7 m^3 (*Calvache* (1990)). *Pierson et al.* (1990) found evidence that the majority of snow and ice melt was caused by two pyroclastic flows, which scoured channels in the ice c. 100 m wide and 2-4 m deep. The material removed was entrained by the flows and melted, generating dilute slurries of water and debris. These lahars were also enlarged by the entrainment of avalanches predominantly comprised of snow, ice, and rock debris. Peak discharge of these cumulative flows was estimated at c. 48,000 m^3/s at 9.6 km from source, decreasing to c. 27,000 m^3/s above Armero, at c. 74 km from source, where over 21,500 people were buried in the deposits (*Pierson et al.* (1990)). The worst part of this disaster was that the great loss of life could have been prevented. The hazards posed by an eruption were forecasted by scientists, but their recommendations for evacuation were not initiated by the government.

1.4.1.3 Phreatic explosions

Phreatic explosions that involve no magma include the 1888 eruption of Bandai-san Volcano in Honshu, Japan. This event comprised 15-20 explosions directed to the north that followed 15-30 minutes of violent seismicity. The first explosion occurred on the flanks of the volcano, with later explosions concentrated around the base and accompanied by a lateral blast (*Williams and McBirney* (1979)). The northern flank of the cone collapsed and produced a debris avalanche with a volume of 1.5 km^3 that, in turn, initiated lahars along major stream channels, covered 34 km^3, and buried 7 villages (*Glicken and Nakamura* (1988)). *Blong* (1984) stated that the events of, and subsequent to, the collapse killed a total of 461 people and injured a further 70.

1.4.1.4 Collapse of crater lakes

Collapses of crater lakes have been documented at several volcanoes, including Mt. Kelut in Indonesia in 1875, Agua in Guatemala in 1541, and Mt. Ruapehu in New Zealand in 1953. It is the event at Mt. Ruapehu on the evening of 24th December 1953 that is the most well documented, and occurred when part of the barrier of ice and ash at the lowest rim of the lake, emplaced during eruptions in 1945, collapsed suddenly. Around 340,000 m^3 of water was released, and formed a lahar in the Whangaehu River

with a depth of about 7 m. The flow was predominantly constrained to the river channel, but was responsible for the destruction of the Tangiwai railway bridge (*Healy* (1954)). Unfortunately, the collapse of the railway bridge coincided with the passage of the night express train from Wellington to Auckland. The train was unable to stop, and plunged into the river, killing 151 people. The flow itself carried a train carriage 2.4 km downstream (*Neall* (1996)), two 5-ton blocks from the bridge 60 yards downstream, and the 126-ton base of a pier 70 yards downstream (*Stilwell et al.* (1954)). As a response to the Tangiwai Disaster, a lahar warning system was installed upstream of the reconstructed bridge and is still in operation today. This disaster highlights the unpredictable nature of this type of event, and the necessity for adequate warning systems.

1.4.1.5 Heavy rainfall

After most eruptions, the slopes of volcanoes are covered with easily erodible, loose pyroclasts and ash. These deposits are vulnerable to remobilisation by rainfall, particularly in tropical climates where heavy rainfall occurs seasonally. The heavy rain, combined with easily available and entrainable material, can lead to significant and sizable lahar hazards. Mt. Pinatubo in the Philippines, for example, produced many large lahars in the aftermath of its 1991 eruption (e.g., *Marcial et al.* (1996)). Typhoons released large volumes of water over the Philippines, and were the initial cause of the more than 200 lahars that occurred between 12$^{\text{th}}$ June and 10$^{\text{th}}$ September and killed a total of 83 people (*US Department of Commerce* (1992)).

There are many other examples of heavy rainfall causing lahars found around the world. In 1963, renewed activity at Irazù Volcano in Costa Rica produced large volumes of ash, which covered a wide area around the volcano. Several lahars triggered by heavy rainfall occurred after this, including the December 1963 flow in the Reventado River that killed 20 persons and destroyed over 300 houses (e.g., *Waldron* (1967)). In 1902, a few hours prior to the eruption of Mt Pelée that killed 28,000 people in Saint-Pierre, a lahar swept down the slopes and killed 400 people in the town of Le Prêcheur (*Tanguy* (1994)). Yet other examples occur yearly at such places as Mt. Merapi and Mt. Semeru in Indonesia, where seasonal rainfall occurs and causes almost daily lahar flows following numerous ash eruptions (e.g., *Lavigne et al.* (2000a); *Lavigne et al.* (2000b);

Thouret et al. (2007)).

1.4.2 Observations of flow dynamics

1.4.2.1 Real-world examples

Numerous studies have been made which examine and model the internal stratifications and depositional nature of lahars. *Pierson and Scott* (1985) observed a 4×10^6 m^3 lahar that travelled down the slopes of Mt. St. Helens after the eruption on 19^{th} March 1982 as a result of snow and ice melt. The flow eroded large volumes of sediment and material left by the 1980 eruption on the flanks of the volcano before depositing material along the Toutle River channel. Total sediment concentration decreased as the flow moved more than 27 km from source, transforming it from a debris flow into a hyperconcentrated flow. *Pierson and Scott* (1985) hypothesised that this transformation was the result of a combination of dilution by overtaking and incorporating existing streamflow, erosion of saturated streambed, and the progressive deposition of the coarsest clasts within the flow.

Mt Ruapehu, New Zealand, provided an opportunity for scientific observations when multiple lahars were formed due to the eruptive sequence of September 1995. The lahars were originally generated by expulsion of Crater Lake waters during the early phreatic and phreatomagmatic eruptions. Later, after the lake waters had emptied, lahars were formed by rainfall-triggered remobilisation of snowpack and erupted tephra. *Cronin et al.* (1997) identified four types of flow within the sequence: (1) initial snow-slurry lahars; (2) large dilute lahars; (3) concentrated lahars; and (4) remobilised tephra lahars. Type 1 lahars composed of Crater Lake waters and entrained granular snow and ice that formed deposits containing 2.5-20% sediment volume. Type 2 lahars were hyperconcentrated flows dominately comprised of lake water and snow. Deposits were left along channel margins over distances that extended up to 84 km from source. The lahars of type 3 were smaller, with high sediment concentrations (46-52%) maintained over the length of the flows by the entrainment of sediment from earlier flow deposits. The largest tephra eruptions in the sequence preceded the remobilised tephra lahars (type 4), generated by heavy rainfall on the snowpack and tephra deposits. Fall deposits on the Mangatoetoenui Glacier, for example, failed on 28^{th} October 1995, due to heavy

rain, which generated a lahar down the Mangatoetoenui Stream (*Hodgson and Manville* (1999); Figure 1.1). Evidence of multiple units of this hyperconcentrated-flow deposit suggests that the lahar flowed as a series of surges or waves, which were caused by episodic releases of debris within a channel or inputs from a divergent flow.

Cronin et al. (2000a) examined the closely spaced sequence of lahars that occurred on Ruapehu on 25th September 1995. Observations of the flows and the deposits allowed them to infer that the transformation of the lahars from debris flows to hyperconcentrated streamflows was caused by the selective deposition of coarse clasts, rather than by dilution by overrunning of incorporated water as was previously thought. *Cronin et al.* (2000a) presented the model that the deposition of the near-channel deposits included the emplacement of sediment wedges of a coarse, basal, sediment-concentrated channel flow. Preservation of the lahar is suggested to only include lateral-flow deposits by the observed rapid erosion of the channel-flow deposits. The study of the transit and emplacement of lahars is, therefore, vital to the full interpretation of a debris flow.

The nature of a lahar past a site was investigated by *Cronin et al.* (1999). The observations and analysis of samples of several flows during September and October 1995 led to the formation of a four-phase model of a non-cohesive wave. This model comprised of an initial phase of ambient streamwater pushed ahead of the actual lahar wave by hydrostatic pressure, followed by a mixing zone that incorporated streamwater into the front of the lahar wave. At this point, peak discharge occurs. The third phase of the flow is the least diluted part of the flow, containing the highest sediment concentrations and is the remnant of the original lahar. As the flow passes downstream, this phase becomes progressively shorter and more diluted. The final phase of flow is the tailing end of the lahar.

1.4.2.2 Experimental flows

Experimental flows can provide more information about the transition between the different flow regimes. *Parsons et al.* (2001) used a semi-circular flume to investigate the number of different slurry mixes that are formed by the varying fractions of silt, clay, and sand used. The different compositions produced markedly different flow front concentrations and behaviour. In muddy slurries, where the silt and clay fractions were high, a blunt nose forms at the front of a flow and moves forward by constant

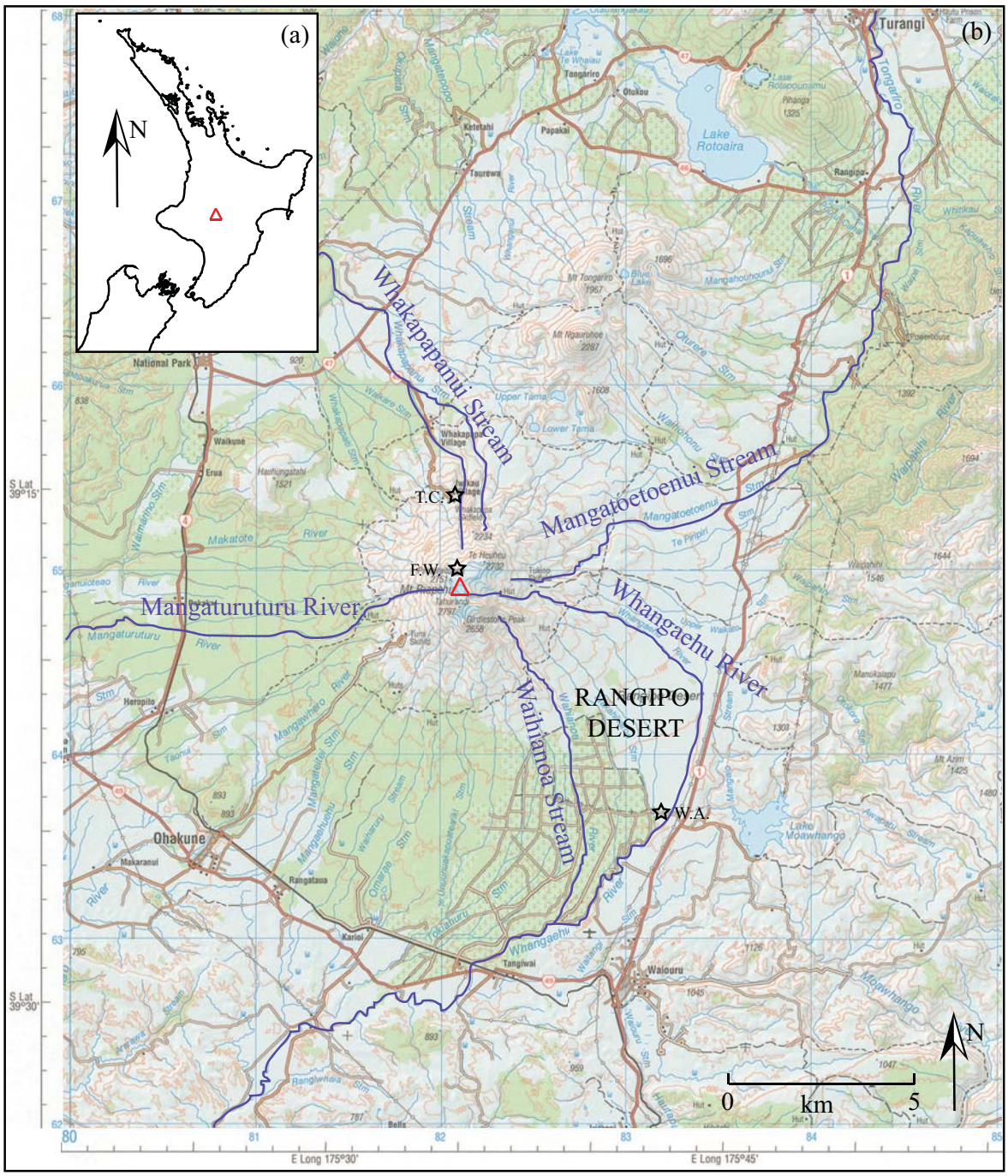

Figure 1.1: *Locations of historical lahar-affected channels on Mt. Ruapehu. (a) Location of Mt. Ruapehu (red triangle) within the North Island of New Zealand. (b) River channels affected by lahars from the Crater Lake, Ruapehu (red triangle). Also shown are locations (black stars) of GeoNet monitoring stations Far West (F.W.), Tongariro Chateau (T.C.), and Waihianoa Aqueduct (W.A.). Topographic map sourced from NZTopo250-9 Taumarunui; scale 1:50,000. Crown Copyright Reserved.*

overrunning of the frontal part. In contrast, coarser-grained flows form a drier, granular nose that gradually incorporates more material that, when of significant size, slows down the flow body (*Parsons et al.* (2001)).

Many experiments have also been made using the large USGS flume, e.g., *Major and Pierson* (1992); *Iverson* (1997); *Major* (1997); *Denlinger and Iverson* (2001). This flume allows fairly sizable volumes of slurries, generally c. 10 m^3, to be released down a 95 m-long slope with a 31° angle. The runout zone at the base of the flow is unconfined, planar, and nearly horizontal. At several places along the flume the depth and the base normal stress and pressure of each flow were measured. Each of the studies observed the formation of an abrupt flow front, a gradually tapering body, and a watery tail. The main body of the flow elongated with distance down the flume, while the frontal thickness remained relatively constant. Deposition of debris flows are also given new insight by *Major and Iverson* (1999) using the measurements of pore-fluid pressure and total bed-normal stress. Debris flow interiors continue near-liquefaction pore-fluid pressures during flow deceleration and deposition; dissipation only occurs significantly during consolidation of post-depositional sediment. There is, in contrast, no pore-fluid pressure visible within the leading edges of the debris flows. *Iverson* (1997) also illustrated the liquefaction of material within the body as basal pore pressures were measured similar to the total normal stress, giving values of shear strength as close to zero. *Major and Iverson* (1999) conclude that the deposition results from grain-contact friction and flow margin concentrated bed friction. This model contradicts others which model deposition due to a uniform viscoplastic yield strength, decay of excess pore-fluid pressure, or pervasive grain-collision stresses. Deposition thickness is also unable to infer the strength of a debris flow (*Major and Iverson* (1999)).

Flix and Thomas (2004) investigated the relation between the deposits and the rheology of the flow that formed them. They observed distinct regions within the deposits that are formed by segregation and reorganisation of material. The outer boundaries of the flow comprise the more coarser-grained particles, while the core of the deposits contain the muddy, finer-grained part of the flow. The granular boundaries form lateral levees to the deposit; *Flix and Thomas* (2004) do not, however, ascribe this to the segregation of particles as the phenomenon is also seen in dry granular flows.

The above experiments have shown the co-existence of two zones that characterise

poorly-sorted flows. *Ancey* (2007) describes the fluid mechanics of the behaviours of each zone. The coarser-grained outer boundary zone moves with Coulomb frictional behaviour, while the behaviour of the finer-grained core of material is more viscoplastic. As evidenced by the different flows at the flume and within its runout zone, the formation of levees limit the amount of lateral spreading (e.g., *Iverson* (1997)). This phenomenon is a direct result of the organisation of material within the flow by the different rheological behaviours (*Ancey* (2007)).

1.4.3 Flow models and simulations

It is very important for hazard assessment and mitigation in lahar-prone areas to accurately calculate travel times and flow depths in order to determine the destructive potential of a lahar. In the past, models have been hampered by unrealistically simple topographic descriptions, which meant the transit times and flow paths were not as accurate as would be desired. With the increased availability of digital elevation data, however, natural topographic descriptions are better resolved, and can be used to calculate transit models with greater accuracy, e.g., *Fagents and Baloga* (2005). Kinematic and volumetric characteristics are used to determine a model of transport dynamics in order to define a flow (*Pierson* (1995)). *Pierson* (1995) combined volumetric flow rate data from historical lahars to determine and define the upper ranges of magnitude of possible future debris flows. Local gradients of a slope influence the flow velocities of a debris flow; the overall flow depths and rates are the result of these cumulative effects (*Pierson* (1995), *Fagents and Baloga* (2005)).

Fagents and Baloga (2005) were able to adapt a continuum model based on conservation of lahar volume over the advancing length of the flow, and use a time-dependent boundary condition at the source to solve the problem of digital topography for the propagation of the lahar. The slope model used is divided into a sequence of inclined planes with the conservation of volume and flow rate imposed on the interface between each adjacent plane. By keeping careful account of the changing boundary conditions between each interface, *Fagents and Baloga* (2005) are able to find the transit times and flow profiles (velocity and depth) at any given point along the flow path. The model is sensitive to the number of inclined planes within the sequence; the greater the number of planes, the greater the resolution of the digital topography. The model

is, however, flawed; it calculates only a crude estimate of the transit time, as faster travel times over steep slopes do not offset the slower rates on shallow slopes with the same drop in elevation. Transit times over real topography are likely to differ from those calculated by the model, although by how much is uncertain. The model also breaks down when presented with certain combinations of parameters of the lahar over topography; the model only works when gravity is the primary driving force behind flow movement.

Pierson (1998) uses a least-squares best-fit model to determine four broad classes of flow from plots of travel time at the front of the flow as a function of distance from the source. These flow classes can be described as moderate (100-1000 m^3/s), large (1000-10,000 m^3/s), very large (10,000-1,000,000 m^3/s) and extremely large (>1,000,000 m^3/s). It is suggested that near-source flow rates can be estimated from the strong non-linear correlation between the 'instantaneous' flow rates generated and initial flow volume, while little effect is displayed by the factors controlling geomorphology on the correlations between the travel time and distance from source. *Pierson* (1998) allows for a difference of an order in magnitude from the calculated and real travel times at a given distance from the source depending on the rate of flow; the effects of differences in flow type were not evaluated.

Stevens et al. (2003) investigated the effect that innate errors in digital elevation models would have on a model designed to determine areas at risk from a lahar. The source data was gathered from two models: (1) digitised topographic maps, and (2) airborne C-band synthetic aperture radar (SAR) interferometry. Predicted flow paths by both models are in general agreement on steep slopes ($\geq 4^\circ$) with deeply incised drainage channels, while problems occur for shallower slopes in both models due to interpolation errors. Contour-derived digital elevation models need refining to reduce the error given in predicted flow paths. Space-borne instruments measuring topography at high resolutions will probably be invaluable in the future (*Stevens et al.* (2003)).

Savage and Hutter (1989) first suggested the use of depth-averaged granular continua to define a debris flow, originally in only one dimension. This was later generalised by the same authors to two dimensions using a curvilinear coordinate system. This model was not suitable over a general terrain, however, as the equations were not frame invariant. *Iverson and Denlinger* (2001) used these depth-averaged granular

flows, governed by Coulomb-type interactions with or without a pore fluid, to define equations that are frame-invariant for three-dimensional terrain. The equations allow for the effect of interstitial fluid and create a system of hyperbolic conservation laws. Basic numerical solutions to the equations can be found using a first-order Godunov method and an approximate Riemann solver (*Denlinger and Iverson* (2001)).

Patra et al. (2005) base their simulation on the work of *Iverson and Denlinger* (2001), and use as a starting point their equations in the dry limit. *Patra et al.* (2005) solve the model equations using a numerical algorithm of an adaptive grid second-order Godunov solver (*Toro* (1997)) and a finite volume scheme. Flow features were reliably resolved by local mesh adaptivity, which also dealt with the necessary shock capture. Topographic data was obtained as needed from direct connections to geographic information system (GIS) databases. The software for this is publicly available and versions have been developed to run on both supercomputers and personal desktop computers, though the more accurate the calculation required, the greater the memory needed to run the program (*Patra et al.* (2005)).

1.5 Selection of field sites

1.5.1 Ruapehu, New Zealand

1.5.1.1 *Setting*

Ruapehu is a 110 km^3 mostly andesitic composite stratovolcano rising to 2797 m, and surrounded by a ring plain of similar volume (*Hackett and Houghton* (1989)). It is situated within the central North Island, and is part of the Tongariro Volcanic Centre (Figure 1.2a). The summit supports six glaciers, surrounding a 9×10^6 m^3 Crater Lake at the active vent, 2540 m above sea level (Figure 1.2b; *Hackett and Houghton* (1989); *Christenson and Wood* (1993)). The overflow of the Crater Lake lies next to the Whangaehu Glacier, out of which the flow travels along the Whangaehu River (Figure 1.2c). These glaciers descend to an altitude of around 2000 m; below 1800 m, the slopes of the volcano are covered with alpine vegetation and are cut through by deep valleys. Forest covers much of the lower slopes of the mountain and the ring plain, with tussock cover in the Rangipo Desert (*Manville et al.* (2000); Figure 1.1, page 13).

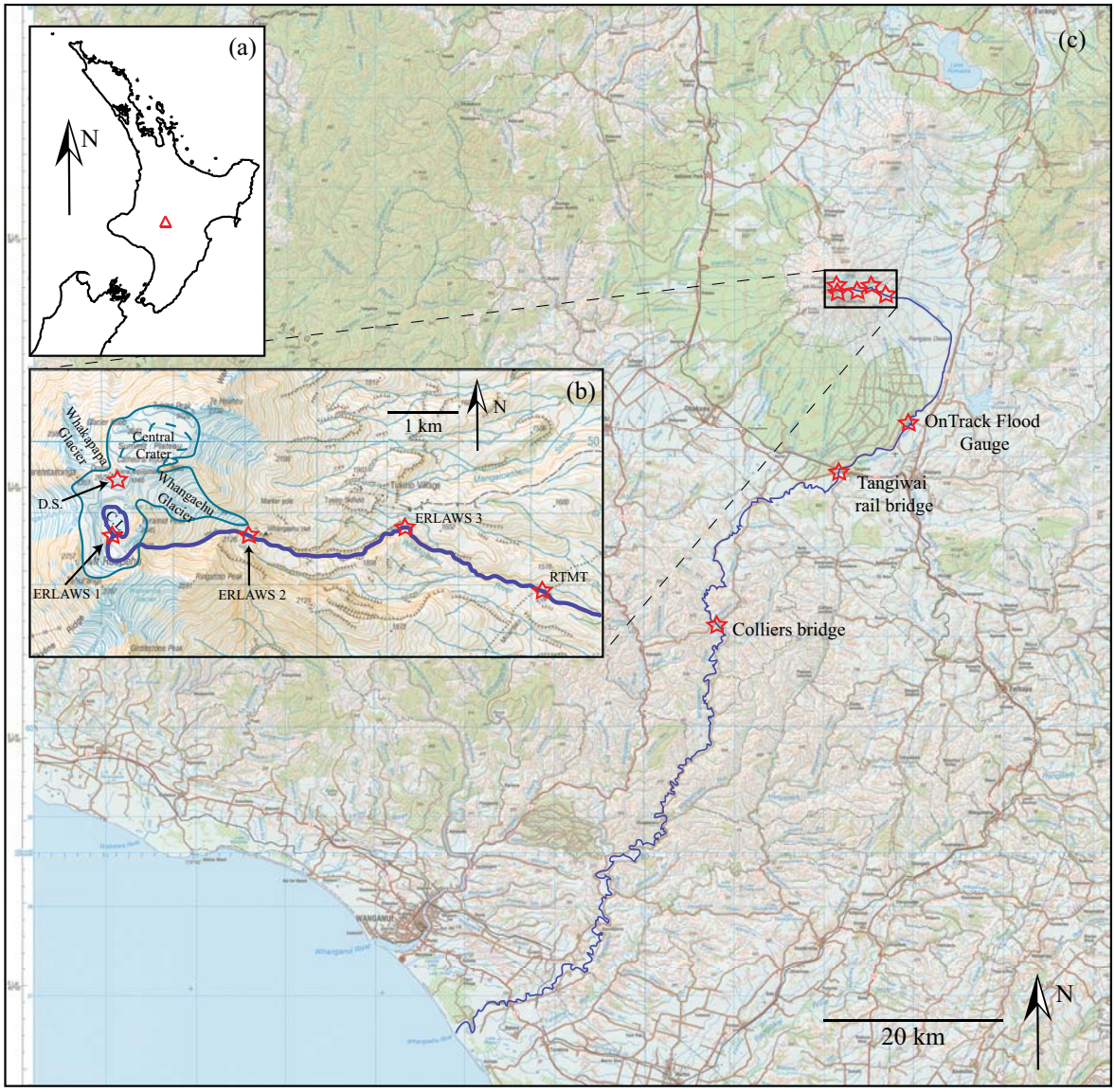

Figure 1.2: *Locations of monitoring sites along the Whangaehu River catchment used within this study. Details of the instrumentation installed at each site can be found in Table 1.1 (23). (a) Location of Mt. Ruapehu (red triangle) within the North Island of New Zealand. (b) Enlargement of upper catchment sites seen within black rectangle in (c), highlighting Crater Lake (C.L.), the GNS Science/GeoNet volcano monitoring site at Dome Shelter (D.S.), the Department of Conservation lahar warning sites (ERLAWS 1, 2, and 3), and the Massey University/GNS Science monitoring site at the Round-the-Mountain-Track (RTMT). Topographic map sourced from NZTopo50-BJ34 Mount Ruapehu; scale 1:50,000. Crown Copyright Reserved. (c) Installation sites (red stars) along Whangaehu River (dark blue line), superimposed upon topographic maps of the region. Topographic maps sourced from NZTopo250-9 Taumarunui and NZTopo250-14 Palmerston North. Map scales are 1:250,000. Crown Copyright Reserved.*

The climate of the area around the mountain is temperate, with an average yearly rainfall of 1051-2851 mm, measured at 9 stations between 629 m and 1100 m elevation (*Thompson* (1984)). This rainfall, coupled with glacial ice breaking into the lake, causes increases in the lake level.

Lahars have previously occurred along several channels at Mt Ruapehu, most notably along the Whangaehu, Mangaturuturu, Whakapapa, Waihianoa, and Mangatoetoenui catchments (*Cronin et al.* (1999); Figure 1.1, page 13). The most commonly affected of these channels is the Whangaehu (*Donoghue* (1991); *Hodgson* (1993)). Lahars have occurred along this channel in 1860, 1889, 1895, 1903, 1925, 1966, 1968, 1969, 1971, 1975, 1977, 1988, 1995, and 1996 as a result of phreatic or phreatomagmatic eruptions (*Nairn et al.* (1979); *Hodgson* (1993); *Cronin et al.* (1996); *Cronin et al.* (1997)). Breakout lahars have also occurred; the last such flow to happen was on Christmas Eve in 1953. It damaged infrastructure, most notably destroying the Tangiwai rail bridge and causing the Tangiwai railway disaster, in which 151 people died (Figure 1.3; *O'Shea* (1954)).

1.5.1.2 *Situation with Crater Lake*

The 1995-1996 eruptions form one of the largest eruption episodes of historical times (*Donoghue et al.* (1997)). During this period, the earlier eruptions in September 1995 ejected water from the lake, almost emptying it. Later eruptions from October 1995 onwards were, as a result, more sustained and contained less water, allowing ash to be deposited as far as 250 km from the volcano (*Johnston et al.* (2000)). A tephra dam, formed from erupted material, built up on the hard rock rim of the Crater Lake, at its overflow to the Whangaehu River. This dam allowed for an increase in the volume capacity of the lake by around 1×10^6 m^3. As time went by the lake refilled and increased to occupy this new additional volume capacity. The higher the water level against the dam, the greater the likelihood of collapse and risk to infrastructure and life.

In response to the threat posed by the dam collapse and resultant lahar, several alternatives were proposed to best deal with the situation (*Hancox et al.* (1997)). These included the possibility of removing the dam using explosives and/or drainage before lake levels rose too high so as to minimise the effect from, and damage caused by, any

Figure 1.3: *The aftermath of the 1953 Tangiwai Disaster: (a) front page of the New Zealand Herald, 26th December 1953; (b) Restoration of the railway bridge began on 26th December, 2 days after it was destroyed by an breakout lahar as the Wellington-Auckland express train passed across. Remains of the locomotive's driving controls visible in left foreground, draped in debris; (c) Damage to the road bridge, looking upstream. Far abutment remained firm as it was founded on sandstone, while near abutment was undermined by scour; (d) View downstream from railway embankment, showing resting places of several railway carriages, the engine cab, and one of the bridge piers across the channel. Two carriages were swept across the road in the background during the peak of lahar flow. All photographs taken on 26th December 1953, and included courtesy of the New Zealand Herald.*

lahar. It was, however, the decision of the relevant authorities (including the regional councils (Horizons and Environment Waikato), the Department of Conservation, and GNS Science) to leave the dam alone and to allow the natural breakout lahar to occur (*Hancox et al.* (1997); *Keys and Green* (2008); *Keys* (2009)). As most lahars are either triggered by eruptions or rainfall, data collection and scientific observations of flows are rare due to the unpredictability of their occurrence. By allowing the tephra dam at Ruapehu to remain, there was a high probability of a lahar; the only unknown factors about it happening were when and how large. As any predicted lahar would travel within the Whangaehu channel, monitoring equipment could be installed along its length to capture the flow as it passed. The scientific rewards from such a decision would lead to the largest and best collection of data of any lahar in the world.

1.5.1.3 *Breakout lahar, 18th March 2007*

In order to capitalise on the probable lahar expected to result from the collapse of the tephra dam at Ruapehu, numerous sites along the Whangaehu River channel were selected for instrumentation. Table 1.1 summarises many of the main sites at which data were collected, either by instrumentation alone or in conjunction with in-situ observations and sampling. While there were several other sites at which data were also recorded, namely stage and sediment concentration profiles, this study is focused on determining information of a lahar flow from primarily geophysical instrumentation. As such, only those sites that have provided such data as utilised within this study have been listed.

Prior to the emplacement of the tephra dam, the barrier at the lake outlet constrained its level to c. 2529.3 m a.s.l. (*Keys* (2003)). Over subsequent years, the lake level rose irregularly, and areas of localised erosion and seepage began to appear by December 2006-January 2007. On 18$^{\text{th}}$ March 2007, the long-awaited breach of the unconsolidated tephra barrier occurred following a long period of wet weather. Records from the lake-level sensors indicated a rise in lake level of 0.3 m from c. 2535.4 m a.s.l. between 13$^{\text{th}}$ and 15$^{\text{th}}$ March. On the morning of 18$^{\text{th}}$ March, the lake level again increased by a further 0.1 m due to a concentrated rainstorm, triggering the failure of the dam (*Massey et al.* (2009)). This failure released a flood of c. 1.3×10^6 m^3 of water over several hours, resulting in a decrease of the lake level by c. 6 m (e.g., *Manville and*

Cronin (2007); *Graettinger et al.* (2010); *Procter et al.* (2010)). The outflow entrained snow and other debris material from the upper Whangaehu valley, transforming into a non-cohesive debris flow. The lahar continued along the narrow, steep course of the upper valley, before spreading across the 6 km-long and up to 4.5 km-wide laharic and fluvial Whangaehu fan beyond the cone (*Palmer et al.* (1993)). The flow was then confined into a shallow channel until c. 42 km from source, which then deepened for the majority of the remainder of its c. 160-km pathway to the coast (*Cronin et al.* (1999)).

1.5.1.4 *Eruption, 25th September 2007*

On 25$^{\text{th}}$ September 2007, a small eruption occurred without warning at Ruapehu at c. 20:26 NZST (c. 08:26 UT). This eruption was accompanied by an ultrasonic shock-wave, recorded at the GeoNet microbarograph stations at Far West and the Tongariro Chateau (Figure 1.1, page 13). The explosion ejected c. 5700 m^3 of water and debris across both the Whakapapa and Whangaehu Glaciers (Figure 1.2b). This then entrained material from the former producing a lahar on the upper slopes of the Whakapapa Skifield. Direct fallout onto the latter travelled immediately down the glacier, followed a very short time later (within 1-2 minutes) by additional material that had briefly ponded within the central crater. These two lahars travelled down the glacier, and into the Whangaehu, collecting debris, snow, and ice as they passed. Each of the flows reached the Round-the-Mountain-Track site (RTMT; Figure 1.2b), though deposits show they stopped within 500-800 m downstream. A later lahar, consisting primarily of water rather than snow and ice, was recorded at the site more than an hour after the other flows had passed, with a duration of c. 1.5 hours. It is believed this flow was generated by streamflow from the Crater Lake that eroded and reworked some of the deposits of the previous two flows. It carried material at least as far down the channel as the Aqueduct (Figure 1.1, page 13), where ice was seen rafting upon streamwater (S.J. Cronin, pers. comm. 2007).

While the pore pressure transducer and the load cell had been removed after the Crater Lake dam-breakout lahar in March 2007, the broadband seismometer, one of the AFMs, and the radar stage gauge were still installed at the RTMT site. They were, therefore, able to record the passage of each of the flows past the site. The

Table 1.1: *Details of instrumentation at lahar monitoring sites along the Whangaehu Valley catchment, Ruapehu, New Zealand. Each site is listed in order of distance from source, and corresponds to those shown in Figure 1.2. Abbreviations of institutions operating each site are provided for clear reference of data ownership. These institutions are as follows: Massey University (MU), GNS Science (GNS), Department of Conservation (DOC), and Horizons Regional Council (HRC).*

Station name	Operated by:	Chainage (km)	visual obs. & photos	stills camera	video camera	trip wire	broadband seismometer	AFM/ geophone	stage gauge	pore pressure	load cell	gas bubbler	sample team	super-elevation
Dome Shelter	GNS	0					✓							
Crater Lake	DOC/GNS	0		✓								✓		
ERLAWS 1	DOC	0.019				✓		✓×3						
ERLAWS 2	DOC	c. 2.2						✓						
ERLAWS 3 (Tukino)	DOC	c. 4.6	✓*		✓*			✓						
RTMT	MU/GNS	c. 7.4					✓	✓×2	✓	✓	✓			✓
OnTrack flood gauge	MU/GNS/HRC	c. 28		✓			✓	✓	✓			✓		✓
Tangiwai rail bridge	MU/GNS	c. 42			✓**			✓	✓					✓
Colliers bridge	MU	c. 83	✓		✓		✓						✓	✓

* Photographs and video clips kindly provided by witnesses at the Tukino skilodge

** Aerial video taken by DOC from helicopter of the lahar arrival and front of flow

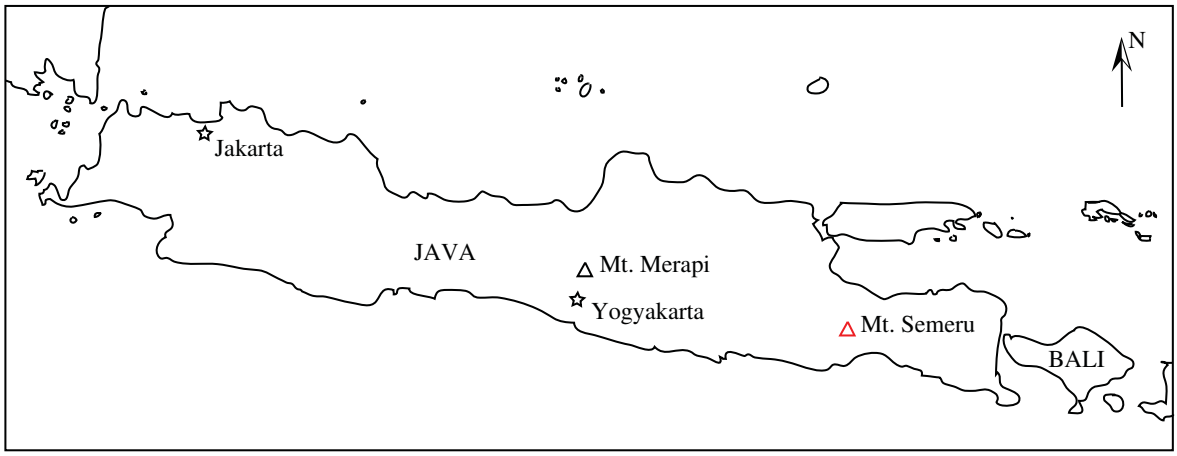

Figure 1.4: *Map showing location of Mt. Semeru, Indonesia*

second glacial lahar arrived within 1-2 minutes of the first, so unfortunately the two signals recorded by the seismic sensors interfere with each other, and cannot easily be resolved. The snow lahars show a marked difference in the seismic signal they generate compared with the more watery lahar produced later, or even the March dam-break lahar.

1.5.2 Semeru, Indonesia

1.5.2.1 *Setting*

Mt Semeru (3676 m) in Eastern Java is the largest of Indonesia's volcanoes as well as one of its most active (Figure 1.4); it has been in a constant state of eruption since 1967. The daily eruptions mostly consist of vulcanian explosions that last anywhere between 10 minutes and an hour in length, generating ash plumes that rise above the active crater as much as 300-1000 m (*Lavigne* (2004)). Less common are the more destructive pyroclastic flows that occur as a result of either dome-collapse or column-collapse and can reach distances as far as 11.5 km from the vent along valleys primarily on the south and southeast flanks. These flows occur on average every 1-7 years, the latest flows being in 1994, 1995, and 2002 (*Lavigne* (2004)). Other activity includes lava flows, although these are uncommon, occurring on average twice every century, both from the active crater and from parasite cones, such as in 1941-42 (*Lavigne and Suwa* (2004); *Lavigne* (2004)).

1.5.2.2 *Installation Site*

Figure 1.5: *Photographs of lahar deposits and erosion at Mt. Semeru, Indonesia. (a) High sediment delivery rates fill sabo dams within weeks of construction, while the erosive nature of flows also causes additional damage to the dams; (b) lahar sediment volumes are dramatically increased by the downcutting and lateral bank erosion of previously emplaced material; (c) retaining wall used to minimise bank erosion, as seen during 2006 and 2007 field tests; (d) by the field campaign of 2008, the retaining wall had been completely eroded away. (Photographs (c-d) courtesy of S.J. Cronin.)*

Field tests were carried out during several rainy seasons: January 2006, February 2007, and February-March 2008. On each of these occasions, monitoring of lahars was undertaken along the Curah Lengkong River channel, c. 9.5 km away from the summit, on the south-western flank of Mt Semeru (as shown in Figure 3.1). Sediment delivery rates at this volcano are so high that newly constructed or excavated sabo dams are filled within a matter of a few days or weeks (Figure 1.5a). *Lavigne* (2004) calculates the average annual erosion rate of sediment at our monitoring site to be c. 740 m^3/m/yr. This erosion can be attributed to several sources: (1) the sheetwashing of daily ashfall deposits; the annual volume of ejected tephra is estimated as c. 4×10^4

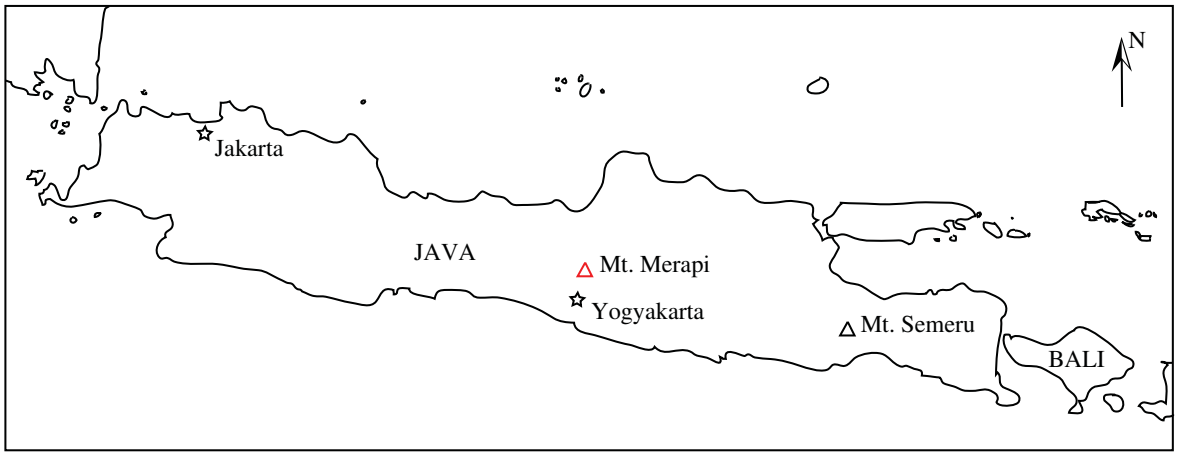

Figure 1.6: *Map showing location of Mt. Merapi, Indonesia*

m^3/yr (*Siswowidjojo et al.* (1994)); (2) erosion of rockfall and small-scale pyroclastic-flow deposits that persistently form part of the supply of lahar sediment volume, as evidenced by the deposits (*Lavigne* (2004)); and (3) lateral bank erosion of old and young volcaniclastic deposits. It is this last that appears to provide the majority of the sediment volume within the lahars (Figure 1.5b-d).

1.5.3 Merapi, Indonesia

1.5.3.1 *Setting*

Mt Merapi (2965 m) is situated in the densely populated area of central Java, c. 30 km north of Yogyakarta (Figure 1.6). There have been 67 historical eruptions since the mid-1500s; at least 24 of these eruptions have produced debris that acted as source material for lahars (*Lavigne et al.* (2000b) plus the 2006 eruption). Pyroclastic flows are the main danger, occurring on average every two to four years, due to the collapse of parts of lava domes; examples of this occurred during the November 1994 (*Lavigne* (2004)) and June 2006 eruptions. The main dangers from Merapi are as a result of pyroclastic flows, surges, and lahars; out of the more than 1.1 million people who live on the volcano's flanks, over 440,000 are at risk from these phenomena (*Thouret et al.* (2000)).

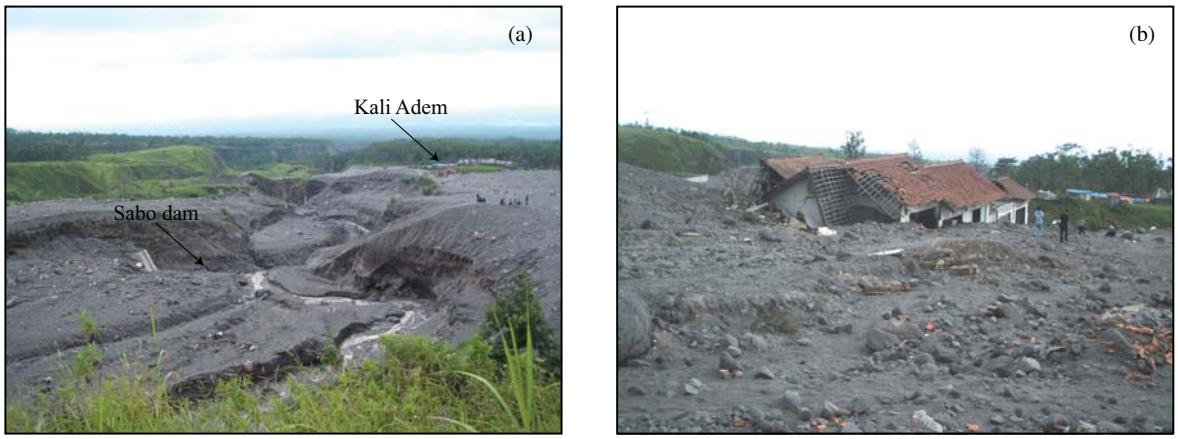

Figure 1.7: *Photographs of the destruction of the village of Kali Adem on the southern flanks of Mt. Merapi due to pyroclastic flows from the eruption of June 2006. (a) Previously deposited material within the unexcavated sabo dam near to the village of Kali Adem led to (b) the inundation and burial of Kali Adem village due to overbank flow.*

1.5.3.2 *Installation Site*

The Gendol valley, on the southern slopes of Mt Merapi, was inundated by block-and-ash flows resulting from the 14th June 2006 lava-dome collapses. While relatively confined within the channel in the uppermost 3.5 km, below this point the flows were restricted by canyon-like steep-sided channels which, when their capacity was overcome, forced overbank flow in many areas not regarded as direct hazard zones (*Lube and Cronin* (2008)). A series of sabo dams had been constructed at various points along the valley; the village of Kali Adem, evacuated before the collapses, was situated near one of these sites (Figure 1.7a). Unfortunately, these dams were filled by previous flows, and contributed to the overbank flow that swept through and buried Kali Adem, causing the deaths of 2 people (Figure 1.7b).

Seasonal rainfall within the channel has induced considerable erosion of the pyroclastic deposits, leading to a succession of hot lahars. During fieldwork carried out in Indonesia in February 2007, we were able to install a 3-component broadband seismometer alongside the channel slightly to the north of Kali Adem (<1 km), within the block-and-ash-flow deposits, in order to capture a record of some of these hot lahars. Video records and detailed notes were also taken to correlate with and describe the lahars. While rainfall did occur on several days, we were only able to record one significant lahar, on the 31st January. This flow was quite large and highly granular, containing many large boulders ($\geq$ 1-2 m in diameter), and eroded great amounts of

Figure 1.8: *Comparison photographs of the different laharic flow types examined within this study: (a) highly granular flow recorded at Mt. Merapi on 31st January 2007; (b) typical hyperconcentrated streamflow recorded at Mt. Semeru on 6th February 2007; (c) near-peak sediment concentration of the Mt. Ruapehu Crater Lake-breakout lahar recorded at Colliers bridge on 18th March 2007. (Photograph courtesy of A.V. Zernack); (d) frozen-in-place snow-slurry deposit, with underlying ice layer visible, generated by the eruption of Mt. Ruapehu on 25th September 2007 (photographed and sampled on 26th September).*

block-and-ash-flow deposits. It is, therefore, very different from other flows recorded at Semeru and Ruapehu (Figure 1.8), giving additional scope to the laharic dataset.

Chapter 2

Geophysical investigation of mass flows

Chapter 2 outlines the state of knowledge in geophysical monitoring techniques for lahars and provides information about those utilised in this study, with particular emphasis on seismic tools.

2.1 Introduction

The use of geophysical tools in the monitoring of mass flows provides a number of advantages over direct sampling methods. Techniques, such as bedload traps and bucket sampling, suffer from the disadvantage of being unable to sample the entire flow depth and length, and also are often damaged or destroyed by the flow itself (e.g., *Manville* (2006); *Arattano and Marchi* (2008)). Geophysical sampling, however, does not involve direct contact with the flow, and hence the risk of damage to, or loss of, the equipment is greatly reduced. As such, maintenance trips, commonly frequently required for the use of direct sampling methods, are needed less often for geophysical monitoring equipment. This chapter details the most common monitoring techniques, both direct and indirect, used in this study, and provides greater analysis on the use of seismic monitoring.

2.2 Direct sampling tools

2.2.1 Bedload traps

The bedload traps utilised at Semeru consist of three containers, c. 1 m^3 in size, made of concrete and placed adjacent to one another near the margins of the channel (Figure 2.1). The lids of the traps were made of concrete, balanced against the Sabo dam. They were connected to a wooden slab via a thick chain. When a sizable force, such as a large boulder with momentum, strikes the wooden slab, the force is transferred along the chain and pulls the concrete lid of the trap down and closed, sealing the sample of flow inside. This method allows for the collection of both bedload and suspended sediment, which can then be analysed later for content. There are, however, several problems with this sampling method. Due to the nature of the flow, it is impossible to see the base of the channel, and it is therefore not possible to tell exactly when the bedload traps are closed. As it is often observed that large stones and boulders accumulate at the front of a flow, it is perhaps likely that these boulders are what closes the trap (*Lavigne* (2004)). As such, the sample collected may not be an accurate representation of the entire flow, as, dependent upon when the lid was closed, the trap may have only been open for a short time. The trap must then be excavated and the wooden slab and chain rebuilt as it is often destroyed or damaged beyond repair before the trap can be reused for another flow (Figure 2.1b). Owing to the almost daily occurrence of lahars at Semeru, it is perhaps unsurprising that the traps are not always excavated before the next flow occurs. This causes an additional problem; some traps, such as those on the outskirts of a channel, collect samples of a flow, but do not shut and seal them in (Figure 2.1c). Consequently, if the sample is not removed after a flow, any subsequent flow would add to this, giving a misleading representation of a single lahar as it will be a collection of material from several events.

2.2.2 Dip / bucket samples

Dip samples of the flow will not necessarily be able to give a full sediment concentration profile or illustrate vertical stratification, because the largest rocks and boulders may, predominantly, be carried along the base of a channel and therefore will not be

Figure 2.1: *Photographs of bedload traps in use at Semeru Volcano, Indonesia. (a) Construction of the traps alongside the downstream side of a sabo dam. (Photograph courtesy of S.J. Cronin); (b) Damage common to these sampling traps caused by the passing flows; (c) During the waning period of lahar flow. Two of the traps have successfully closed, trapping material, while the trap farthest from the channel centre remains open.*

sampled (e.g., *Pierson* (2005) and other references therein). They do, however, give a relatively accurate profile of the surface sediment concentration, which can be inferred approximately as the suspended sediment profile of the flow. The water samples are also analysed for a variety of chemical components that can, in the event of a lahar involving Crater Lake water, show the addition and concentrations of such (e.g., *Cronin et al.* (1996)).

In this study, dip samples were collected at regular intervals during the March 2007 Ruapehu lahar and several flows at Mt Semeru in Indonesia. While the Indonesian samples were simply made using buckets, the Ruapehu lahar was sampled using 5 L plastic containers with 100 × 30 mm holes cut into the top. These were thrown into the flow thalweg[1] from a bridge or steep channel bank, and allowed to float within the

[1] A thalweg is defined as the line which joins the lowest (deepest) points along the entire length of

Figure 2.2: *Sampling a lahar at Colliers bridge, Ruapehu, New Zealand. (a) Sample container is thrown into the flow thalweg from channel bank. (Photograph courtesy of A.V. Zernack); (b) Transfer of sample to sealable container for transport to laboratory. (Photograph courtesy of S.J. Cronin)*

lahar until full (Figure 2.2a). This method meant that, while not a representation of the entire of the flow depth, the sample gives a fairly accurate sampling of the top 0.5-1 m. The samples were transferred from the collection buckets into sealed bottles for later analysis (Figure 2.2b).

Snow-slurry lahars, such as those seen at Ruapehu in September 2007, are sampled differently than those of more water-rich flows. The flows were not observed and sampled in passing; instead, they were sampled after the deposits were emplaced (Figure 2.3). Snow-slurry lahars contain not only large contents of ice and snow but also have pockets and pores of air held within the matrix of the deposit. 2 L containers were used, the sample cut away from the bulk of the solidly-frozen deposit using the container as a guide. As snow-slurry lahars move and freeze as [near] solid plugs, the sample is then an accurate portrayal of a 2 L volumetric section of the flow. The ice and snow will melt, but by using this method the percentage of the sample that were air holes will be preserved.

2.2.3 Visual observations, recordings, and analysis

Visual observations and descriptions recorded by witnesses of lahars can give much additional data about the state of the lahar as it passes that can then be inferred in

a streambed or valley in its downward slope. The thalweg is almost always the line of fastest flow in any river.

Figure 2.3: *Sampling sequence of a snow-slurry lahar, Ruapehu, New Zealand. (a) Deposit is cut away around area to be sampled using a 2 L sealable container as a guide; (b) Container is then pushed down into deposit and sample excavated from beneath; (c) Excess material is scraped from top of sample; (d) Sample is then accurate representation of 2 L section of flow.*

the geophysical record. Photographs, that are accurately timed, can provide snapshots of the state of a flow at a particular point in its duration.

Where possible, video records were taken of all lahars used in this study. These are invaluable for several reasons; not only do they show the changing behaviour of the flow, but they can also be used to calculate the surface velocity and stage height profiles of the lahar over time (e.g., *Lavigne et al.* (2003); *Doyle et al.* (2010)). Ideally, the camera must be set at an angle to the channel, with a view across the entire width. By showing the full width of the channel we can see the lateral stratification and changes in flow behaviour over time, as well as cross-flow velocity profiles, due to velocity and stage height differences.

Surface velocity and stage height profiles can be calculated from the video footage using the Particle Image Velocimetry method (PIV; *Dalziel* (2005)). The concept of PIV analysis is to use successive images at known time intervals to calculate veloc-

ity vectors of the flow field. These vectors are calculated by following known tracer particles between two successive images. The images are then divided into small sub-areas, known as "interrogation areas", from which local displacement vectors are then calculated using auto- and cross-correlation techniques. It is then assumed that all particles within each of the interrogation areas move homogeneously between the two images. By taking into account the time delay between the two images and the image magnification, the projection of each vector is resolved and a velocity calculated (e.g., *Raffel et al.* (1998); *Raffel et al.* (2007); *Kim et al.* (2008)).

The video cameras used within this study were set up alongside the river channel at each site to have fixed focus points within the centre of the channel whilst still allowing for the full width of channel to be seen within the image frame. The images were taken at a rate of 30 frames-per-second, and a resolution of 640 × 480 pixels. Analysis of the recorded video was made using the freely-available software program "DigiFlow", which uses the PIV method to calculate time-dependent velocity profiles by quantifying vectors between identified tracer particles in successive images within a movie sequence (e.g., *Dalziel* (2005)).

2.2.4 Super-elevation and tide-lines

Lahars leave residual tide-lines along the sides of their flow path channels; by mapping these tide-lines with GPS equipment after an event, maximum stage[2] heights can be gained along straight stretches of the channel. Around bends in the channel, the tide-lines will give super-elevation[3] measurements that can be used to estimate local maximum flow velocities with the application of Newton's second law of motion to the centrifugal action around the bend (e.g., *Chow* (1959); *Pierson and Scott* (1985)). The equation needed to calculate this is as follows:

$$v = \left(\frac{g \cdot \Delta h \cdot r_c}{b} \right)^{1/2} \tag{2.1}$$

[2]The stage can be defined as the height of the water surface above an established zero level at a given location. While this zero level can be arbitrary, for this study it was defined as the bottom of the stream or river during pre-lahar conditions.

[3]Superelevation is defined as the vertical distance by which the height of the outer edge of a curve exceeds the height of the inner edge. In terms of this study, it relates to the difference in height of the tide-lines on either side of a channel bend.

where v is the mean flow velocity (m/s), Δh is the height difference between the tidelines on the inner and outer bends (m), r_c is the radius of the curvature of the bend, and b is the width of the channel (m).

2.3 Geophysical tools

2.3.1 Stage gauge

Stage height records can be collected using acoustic, gas-pressure, or radar stage gauges. These instruments are non-intrusive and do not require contact with the lahar surface. As a result, they are less likely to be destroyed by the flow. Ideally, they should be bolted onto the side of a bridge in the middle of the channel, looking directly down at the surface of the passing lahar (*VEGA Grieshaber KG* (2009)). In situations where this is not possible, such as at the Round-the-Mountain-Track (RTMT) on Ruapehu, then they can be bolted into rock walls alongside the channel, pointing straight down. In this case, the instrument used was a VEGAPULS sensor gauge. The gauge records the travel time for a radar beam to reach the surface of a flow and be reflected back to the instrument. From this, it can then calculate the height of the surface flow below the sensor. Due to the highly irregular nature of the surface of lahars, reflection angles greater than the optimal recordable angles of the instrument can occur and either deflect the returning beam away from the sensor or, should they be received, can produce anomalous readings. The optimal reflection angles are dependent upon the type of sensor deployed and are determined by the emitted beam angle, itself dependent upon the diameter of the transmitting horn (*VEGA Grieshaber KG* (2009)). Additionally, the changing stage height can occur too rapidly for the sensor to record the data; stage heights that change at a rate of more than 1 m/min cannot be accurately measured by the instrument. Anomalous readings result; the sensor simply records the value of the past reading until it recovers, giving flat line readings. As the stage height tends to only change faster than the maximum recordable rate at the onset arrival of the flow, data recorded after this can be considered relatively reliable. Reconstructed stage heights can be made using correlation with other data and instrumentation readings, giving an approximate onset stage height.

2.3.2 Pore pressure

The pore pressure transducers used in this study are HOBO U20 Water Level Logger (*Onset Computer Corporation* (2006)) and Solinst Levelogger Gold (*Solinst Canada Ltd* (2006)) sensors. In order to prevent the removal of the sensor by the lahar, it is installed in holes drilled into the hard rock channel base. In pure-water conditions, the pore pressure should produce identical results as the stage record (*Onset Computer Corporation* (2006); *Gray and Gartner* (2009)). The differing conditions inherent in a lahar mean that the records may no longer match, illustrating the changing conditions of the flow. It is hypothesised that the density of fluid may be increased due to the inclusion and entrainment of sediment within the flow, increasing the pore pressure. Turbulence at the base of the flow may also cause an increase in the pore pressure, due to fluid motion sustained in an upwards or downwards direction. Pore pressure may be decreased due to fluid dilation caused by collisions of particles in a highly concentrated flow. Neither of these phenomena, however, were observed in tests of the instruments in lahars at Mt. Semeru, Indonesia (*Doyle et al.* (2009)).

2.3.3 Load cell

Load cells are used to measure the weight, and hence height, of a flowing body of water. In a pure-water condition, the load cell should record the same height as the stage gauge. With the changing densities and weight of a lahar, the records of a load cell will differ from the stage gauge. Increasing weight of flow due to sediment incorporation will show in the record as higher stage readings. Between the two sensors, information about the sediment concentration of the flow can then be extracted. Just as with the pore pressure, the load cells need to be bolted into the hard rock channel to prevent erosion by the lahar. The current load cells used in this study have in-built dataloggers to avoid the necessity of cabling that can be easily eroded or sheared by the nature of the lahar, as was the result during our first field tests in Indonesia in 2006 (*Manville* (2006)).

2.4 Seismic tools

2.4.1 Geophones / Acoustic Flow Monitors (AFMs)

The Acoustic Flow Monitor (AFM) was designed by the Cascades Volcano Observatory of the U.S. Geological Survey (*Hadley and LaHusen* (1995); *LaHusen* (2005)). It was initially designed for the detection and monitoring purposes of debris flows originating from a volcano; additionally, it has been successful in monitoring non-volcanic flows as well. The AFM system has been an effective tool in real-time warning systems at active channels across the world (e.g., *Marcial et al.* (1996); *Lavigne et al.* (2000b)).

The AFM consists of an inexpensive geophone, that senses ground vibrations, and a microprocessor, that analyses the signals recorded. The signals are compared against any previously defined 'threshold' signals of amplitude and duration. If the signal is below this threshold, the recording will not change and the unit will send reports at standard time intervals, usually every ten minutes. Should the signal recorded be greater in amplitude and duration than the threshold, then the AFM will switch to 'alert mode' and will send recorded data reports at one minute intervals. Once the signal drops below the threshold, the recording and reports will be returned to normal operating modes (*LaHusen* (2005)). As the system is almost completely enclosed, needing only a separate power supply, it is able to work well under challenging environmental conditions, such as snow and ash fall.

The geophones used in this study at Mt Semeru and at several sites at Ruapehu are 10 Hz vertical geophones, and can sense ground vibrations with frequencies ranging from 1 Hz to 100 Hz. The ERLAWS warning system (Eastern Ruapehu Lahar Warning System; *Keys* (2009)) consisted of AFM systems positioned along the channel at three sites (see Chapter 1.5.1). These latter systems were able to transmit data to the base station via a telemetered system and give adequate warning for the response and disaster prevention teams downstream (*Leonard et al.* (2008)).

2.4.2 Broadband seismometer

During the course of this study, we have used seismometer sensors designed and built by Guralp Systems, Reading, U.K. (www.guralp.co.uk). The first of the sensors used

was an analogue CMG-6T in combination with a Reftek datalogger (Model 130-01; www.reftek.com); the second was a digital CMG-6TD sensor, similar to the CMG-6T but with the addition of an internal digitiser memory. The sensors themselves are ultra-lightweight, rugged, and waterproof; in addition, they require no levelling as long as the base is $\pm 3^{\circ}$ from the horizontal, as an aid to installation.

The sensors will automatically start measuring and recording once attached to a 10-28 V power supply. Information regarding the time can be accurately gained from a GPS unit, connected either to the Reftek datalogger for the 6T or through a breakout box to the 6TD. The sensors constantly monitor the GPS status and record it to a plain text status stream file. The internal temperature of each unit is monitored using an electrical thermometer; the results of which are also recorded into the status stream file.

Each unit consists of three sensors within a sealed case, that can simultaneously measure the ground motion in the east / west, north / south, and vertical component directions. They are sensitive to a range of frequencies within the ground vibrations, usually 0.033-50 Hz as standard. The 6TD also contains an in-built 24-bit digitiser that allows for the conversion of the recorded ground motion to digital data at source.

2.4.3 Seismic records of mass flows

There have been numerous studies that have utilised seismic recordings to recognise, locate, and/or monitor mass flows (e.g., *Tungol and Regalado* (1996); *Arattano* (1999); *Jolly et al.* (2002); *Caplan-Auerbach et al.* (2004)). The aims of these studies, with regards to their seismic component, varies. Often, they have merely been used to either inform of the passage of a flow and send alert warnings (e.g., *Bessason et al.* (2007)), or as a trigger to increase the sampling record of other geophysical instrumentation (e.g., *Lavigne et al.* (2000b)). There have, however, been a number of studies where seismic monitoring has been used to derive information about a flow itself (e.g., *Surinach et al.* (2005)).

2.4.3.1 Warning systems

Monitoring and warning of mass flows using seismic studies include work developed in the European Alps (e.g., *Leprettre et al.* (1996)), Norway, and Iceland (e.g., *Bessason*

et al. (2007)). The system provided in Norway to alert traffic on roads is based upon the use of geophones, located above the roads in the paths of avalanches. Minimum thresholds were given, above which avalanches would produce signals, and the traffic alerted. The system did not always work well; the threshold level had to be set high enough to avoid false triggers but low enough to not miss events. Despite the application of these threshold levels, false alarms were triggered and events were missed (*Bessason et al.* (2007)).

In 1992, *Leprettre et al.* (1996) investigated a method of real-time seismic detection of avalanches in the Alps. Approximately 300 events were recorded over a 3-year period, with additional information providing confirmation of avalanche trigger mechanism for c. 15% of the events. The rest were triggered by a combination of earthquakes, animals, storms, and traffic. The study highlighted the need for more than just instrumentation at a site; *Leprettre et al.* (1996) introduced new methods for automatic recognition of an avalanche based upon signal analysis.

More recently, *Bessason et al.* (2007) have developed a more complex monitoring system that automatically detects and analyses flows in the West Fjords Peninsula, Iceland. This system, initially installed in 1996 (*Bessason et al.* (1999, 2000)), is based on comparison of known events to detect and identify new events. Ten characteristic parameters of the signals are evaluated: peak value, power, power duration, total duration, impact factor, characteristic frequencies, half-power bandwidth, lower spectral limit, minimum and maximum amplitudes, and the frequency of the maximum in the power density spectrum. The results of these analyses are not as satisfactory as could be hoped; many events are incorrectly classified, although it is suggested that the process will become more reliable as more events are detected (*Bessason et al.* (2007)).

Monitoring on volcanoes is generally less specific to channels than the above avalanche monitoring. Primarily, the systems are used to monitor the changing nature of the volcano itself; lahar or other mass flow monitoring is both incidental and additional to the other recordings made. *Jolly et al.* (2002) took advantage of the 8-station network of seismometers deployed by the Montserrat Volcano Observatory to monitor the growing dome and subsequent collapses. The study uses a best-fit model to find the location of a pyroclastic flow as source, similarly to earthquake location methods (e.g., *Lahr* (1989)). Similar analyses have been carried out at other volcanoes to locate rockfalls

(e.g., at Piton de la Fournaise; *Aki and Ferrazzini* (2000)) and pyroclastic flows (e.g., at Unzen Volcano, Japan; *Yamasoto* (1997)).

Warning systems that are more specifically designed to monitor the passage of lahars and debris flows are also found. *Lavigne et al.* (2000b) details the system in place for the monitoring of channels at Mt. Merapi, Indonesia, where alerts are sent to the Volcanological Survey of Indonesia. The systems emplaced to monitor the flows of Mt. Pinatubo in the Philippines also alerts to passing flows once minimum amplitude thresholds are exceeded (e.g., *Tungol and Regalado* (1996)). A similar system has also been established at Mt. Ruapehu, New Zealand. This latter system, the Eastern Ruapehu Lahar Warning System (ERLAWS), comprises geophones at three stations along the Whangaehu channel. It was installed to specifically monitor the threat from crater lake collapse, but remains installed as a result of its effectiveness during the March 2007 lahar (*Leonard et al.* (2008)). In combination with the Eruption Detection System (EDS) also installed at Ruapehu, early warnings for both eruption-triggered and other lahars can be provided (*Keys* (2007)).

2.4.3.2 Velocity of flow

Seismic data have, in the past, been used to estimate the frontal velocity of mass flows. This requires the use of a series of sensors deployed along a channel at known distances. *Suwa et al.* (2000) showed that, while flow-induced ground vibrations did occur prior to the arrival at a site, the peaks coincided with the peaks in the hydrograph records. As such, it is a simple matter to pick the arrival of a flow at a site using seismic records. Correlation between sites will give an average frontal velocity. Many studies have utilised this method (e.g., *Galgaro et al.* (2005); *Lavigne et al.* (2000b); *Tungol and Regalado* (1996)). In some cases, however, there is not always an unique, well-defined flow front that easily heralds the arrival of a flow. *Arattano and Marchi* (2005) present a cross-correlation method that can be employed in such cases between data to define the mean velocity of the flow.

2.4.3.3 Flow discharge and size

A number of studies have attempted to use recordings of the seismic amplitude of lahars and other mass flows to estimate their size and discharge. The maximum signal

amplitude recorded at Unzen Volcano, Japan, during pyroclastic flows shows a good correlation with the volume of rocks within the flow (*Uhira et al.* (1994)). This relationship, however, is not a simple one (*Calder et al.* (2002)). The best-fit of flow size and discharge will vary considerably with sensor distance from the channel and type of flow (*Tungol and Regalado* (1996)). It is, however, not surprising that the longer the seismic record of an event, the larger the volume of material within a flow (*Zobin et al.* (2005)).

Suwa et al. (2000) proposed that the peak vibrational energy recorded by a seismometer is proportional to the peak discharge of a flow, while volume estimations could be made by integrating the acceleration amplitude. *Galgaro et al.* (2005) calculated the discharge of a flow in the Acquabona catchment, Italy, using mean frontal velocity and flow section area. They also used a regression line to estimate the total volume of the flow from the integral of ground vibrations. AFM data was used at Mt. Pinatubo to define a pseudohydrograph, the strength of which was used as a proxy for relative discharge. Absolute discharge could then be calculated by calibration with actual discharge measurements at the site (*Tungol and Regalado* (1996); *Marcial et al.* (1996)).

2.4.3.4 Signal characteristics

As illustrated above, previous studies have been made to investigate the ground vibrations generated by different types of flows. For example, the dynamics of the more than 50 lahars on Mt Merapi that followed the *nuees ardentes* of 22$^{\text{nd}}$ November 1994 were monitored using acoustic flow monitoring (AFM) systems, real-time seismic amplitude measurements (RSAM), and seismic spectral amplitude measurements (SSAM) (*Lavigne et al.* (2000b)). The lahar durations on average ranged from between 30 and 90 minutes, the majority of which occurred in the afternoon. Instrumental thresholds were proposed following observations of mean velocities and peak discharges in order to improve the warning systems. Large lahars were identified by >1500 mV AFM value on the low-gain, broad-band setting, >400 RSAM units, or >80 SSAM units on the highest frequency band (*Lavigne et al.* (2000b)).

Studies have also been made with regards to the individual frequencies excited by a flow. *Chen et al.* (1991) observed the passage of 18 debris flows at Jiangjia Gully

in China; the frequencies generated by the flows are mainly between 25-85 Hz, with a peak frequency of c. 50 Hz. Others have concluded energy from hyperconcentrated and debris flows are concentrated in the 10-100 Hz range (*Marcial et al.* (1996); *Lavigne et al.* (2000b)).

Experimental flows made by *Huang et al.* (2003, 2004) investigated the sources of the ground vibrations generated by debris flows. The signals recorded are due to both the collisions of large boulders and particles within the flow and the frictional interaction of the flow with bedload. *Huang et al.* (2003, 2004) measured bed-friction generated signals with frequencies in the range 10-300 Hz, although predominantly between 20 Hz and 80 Hz. The frequencies of collisional motion produced signals between 10-500 Hz. These studies were followed by *Huang et al.* (2007), in which ground vibrations were measured during field experiments in Taiwan. These showed that individual rocks produced frequencies of 10-150 Hz, with larger rocks generating signals at the lower end of the spectrum. The observation was also made that the signals of a debris flow front produces ground vibrations of lower frequencies (< 50 Hz) than those of the body and tail of the flow (50-100 Hz). The reason for this is ascribed to the accumulation of larger stones [sic] at the front of the flow (*Huang et al.* (2007)).

The above studies were made with sensors installed next to the channels and/or the flumes used in the experiments. Distinguishing different frequencies made by a flow using the records of sensors deployed for volcano monitoring is much harder. This is because the higher amplitudes will not be observed due to the anelastic attenuation of higher frequency propagating waves with distance (*Aki* (1980)). *Surinach et al.* (2005) illustrate that snow avalanche signals can be resolved as different from earthquakes and explosions due to the increase in the high frequency component as a flow approaches the sensor. Similar behaviour could be expected with signals from lahars. For sensors installed away from channels, however, the attenuation of higher frequencies will make this much harder to see. *Zobin et al.* (2009), for example, show peak frequencies for lahars recorded at Volcán de Colima, Mexico, as in the range of 6-8 Hz. The sensors, however, are at least 2 km from the source of the ground vibrations and this will have a distinct effect on the maximum frequencies recorded. Comparisons made between the records of lahars and pyroclastic flows, however, made by the same instrument indicate that, despite this, the two flow types can be resolved as the latter produce

peak frequencies of 3-4 Hz (*Zobin et al.* (2009)).

2.5 Analysis of collected seismic data

The seismic data collected during this study were analysed in a variety of ways in order to obtain as much information about each lahar as possible. While the signals recorded by each geophone sensor could merely be plotted against other recorded parameters, such as sediment concentration or velocity profiles, the broadband records allowed for more detailed dissection of the signals associated with each lahar. To this end, a number of programs were utilised and are discusses below; of these, many are freely and / or widely available within existing software, such as Seismic Analysis Code (SAC) and MATLAB, while others were written during this study and can be found in Appendix A.

As has been previously described in Section 2.4.2, the broadband records were collected using Guralp sensors, and recorded onto either internal dataloggers or attached Reftek dataloggers. In the instances where internal dataloggers were available, the data recorded could be, and were, extracted in a number of formats; that is, gcf, sac, and mseed. This allowed for the easy application of different software to each dataset where file-type compatibility issues could arise. The data recorded onto the Reftek dataloggers, however, was only available for extract in mseed format. These files were then converted to sac format using the program ms2sac provided by my supervisor, Dr. Steve Sherburn.

Each of the seismic records was analysed using the same methodology. To allow for correlation of analysis results, it was first necessary to ensure that each signal had the same basis; that is, each respective component was aligned in the same way at each site, the same sampling rate was used for each record, etc. In some cases, it was necessary to use the 'rotate' command within SAC to rotate the E and N component data to align with channel-perpendicular and channel-parallel directions, respectively, while others required the use of the 'upfirdn.m' program within MATLAB's seismic analysis software to downsample (reduce) the sampling rate of a signal. For those files where the start time of the file was not 00:00:00 UT, the program 'seis_true_time.m' (Appendix A) was written to set up the correct start time of the file. As the seismic

data was recorded in units of bits, each signal needed to be converted in m/s to obtain the velocity amplitude of the trace. To this end, the program 'trace_yaxis' was written, encorporating the digitiser and seismometer conversion factors to do so (Appendix A).

For analyses that required the extraction of seismic velocity amplitude and seismic energy data, three programs were written during this study: 'signal_analysis_suzy_0902.m', 'signal_analysis_suzy_0903.m', and 'energy_extract_data.m' (Appendix A). The first two of these are used to create an answer matrix containing an amplitude and energy spectra for each seismic file. As these files are often made up of long signals, 'signal_analysis_suzy_0903.m' is used to break the long signal into a series of short signals before it calls the program 'signal_analysis_suzy_0902.m' to calculate the amplitude, energy, and frequency distributions for each short signal. The programs then write the data to the aforementioned answer matrix. The 'energy_extract_data.m' program can then be run to extract seismic energy data from the answer matrix for each lahar and/or any "packets" contained within. Chapter 3.2.2 contains a more detailed description of the calculations for seismic amplitude and energy, and how they are used within the context of this study.

Many of the other analyses of the seismic data within this study were made using standard components of the Seismic Analysis Code (SAC) and MATLAB software, specifically 'lowpass', 'highpass', and 'bandpass' filters used to filter certain frequencies from the data, 'fft' and 'pds' used to create power density spectra for each file or time-slice of file, and 'spectrogram' used to create and plot spectragrams of the data, using 256-sample windows and 50% overlap. RSAM profiles were produced using a program provided by S. Sherburn called 'sac2rsam_10s', which calculates each RMS point over a 10-second interval along the length of a time trace. After many of the above analyses were made, some answer files remained in .sac format. In such cases, the program 'sac_sp2gmt', also provided by S. Sherburn, was used to convert them into ascii files for greater ease of data extraction.

2.6 Background noise and flow analysis methods

Any seismic recording is a combination of data made up of "signal" and "noise" components. Noise data can be defined as everything not of interest within a record. This

noise is made up of both coherent and incoherent noise. The former is caused by, for example, ground roll, refracted reflections, and air wave-generated signals. Incoherent noise is more commonly referred to as random or background noise. Random noise is, by definition, unpredictable and cannot be correlated between traces. As a result, it is not possible to accurately gauge the amplitude produced by any given mechanism generating such a signal.

Seismic noise has been shown to affect signals across a wide range of frequencies, from 0.0001 Hz to 100 Hz (e.g., *Burtin et al.* (2008)). Previous studies have highlighted certain frequency bands that are affected by known sources. At frequencies less than 0.1 Hz, for example, local weather conditions (i.e., variations in temperature or atmospheric pressure) can produce substantial levels of noise in a seismic record (e.g., *Beauduin et al.* (1996)). Oceanic-sourced noise, recorded everywhere on Earth, generates signals in the "micro-seism" band between 0.05 Hz and 0.2 Hz, with peak amplitudes at 0.2 Hz (e.g., *Peterson* (1993), *Stutzmann et al.* (2000)). Above 1 Hz, seismic noise can be mainly attributed to cultural sources, such as traffic (e.g., *McNamara and Buland* (2004)), or other natural sources, such as high winds (e.g., *Bahavar and North* (2002)) or volcanic tremor (e.g., *Hurst and Sherburn* (1993)).

For the purposes of this study, the "noise" signal contained within the seismic record can be defined as the general background signals attributed to normal streamflow within the channel at each site. In addition to this, added signals from phenomena such as ash eruptions at Mt Semeru, Indonesia, can also be classed as noise. These phenomena are illustrated in Figure 2.4.

For those lahars where the flow is of such considerable size and sediment concentration that any normal streamflow can be regarded as relatively min, its associated noise profile is likely to be of little consequence. Some flows, however, are very small, or of such nature as to be relatively seismically quiet, that the noise fraction may be of significant enough a level as to be considered not so easily dismissable. In such cases, in order to better view the signals as produced by a lahar alone, the noise fraction needs to be either removed or, at least, minimised. Due to the nature of a flow, any strictly noise-generated component within the signal will be hard to identify. Average background noise from normal streamflow and atmospheric conditions will be somewhat easier to remove. The close proximity of the source to the receiver in much of

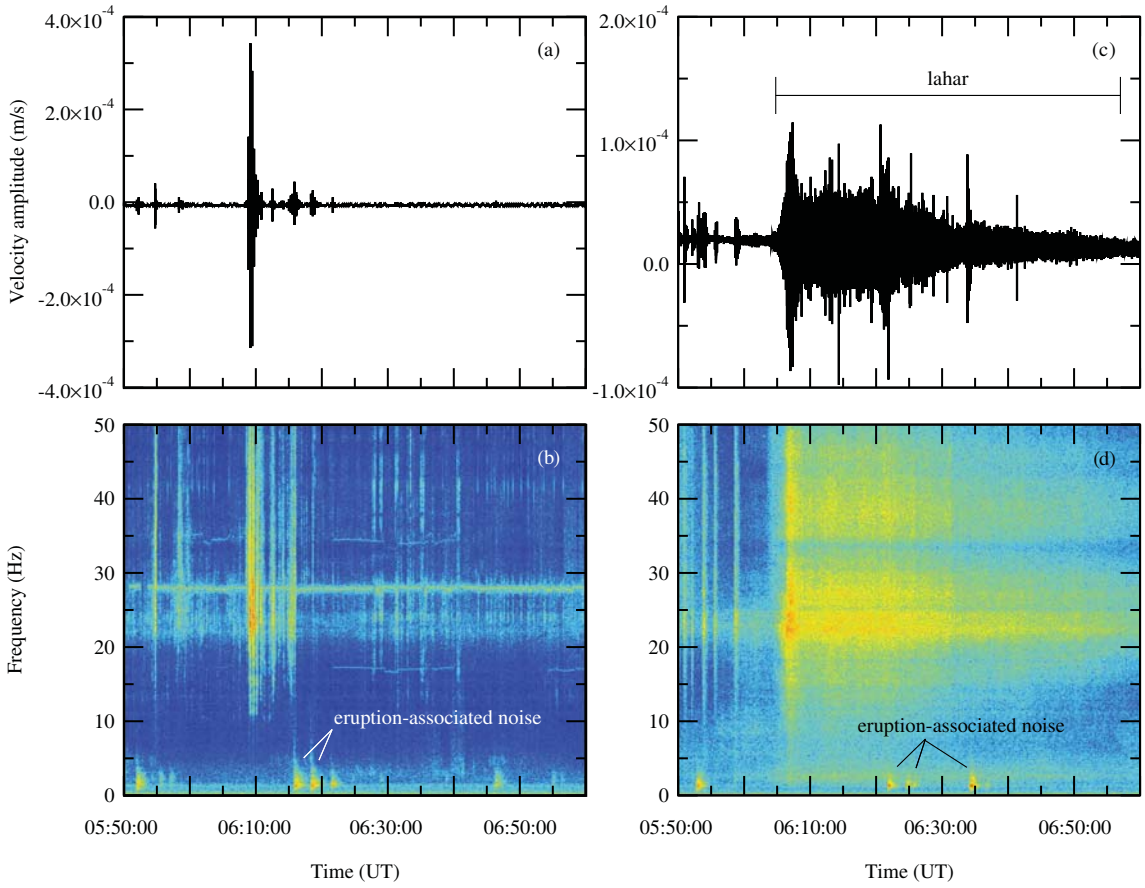

Figure 2.4: *Vertical component signals (100 sps) of background noise and lahar-generated signals recorded at Semeru Volcano, Indonesia. Top: seismograms; bottom: spectrograms, with 256-sample windows and 50% overlap. (a-b) Background noise; (c-d) Lahar signals. Note very low frequency (<5 Hz) eruption-associated signals concurrent with passage of lahar.*

this study means that any source-to-receiver pathway influences upon the signal should be at a minimum. The remainder of this chapter outlines a few noise removal / minimisation methodologies that may be useful in order to better characterise the seismic signal of a lahar.

2.6.1 Calculating background noise

Before the noise component of a signal can be removed from the record, it must first be calculated. In order to get the best possible match to noise as would be present during the lahar, only records from the days close to, but prior to, the flow are used. This is because any change to the geometry or properties of the channel would have an effect on the signal produced from normal streamflow. By averaging over several days worth of streamflow-generated signals, any anomalous peaks on a single record can be

minimised. Similarly, by using the same time window for the noise traces as for the lahar trace, both in length and time of day, any signals localised to the site and that time can also be accounted for.

The removal of any noise profile from a seismic record necessitates the transfer of the data from the time domain into the frequency domain. For this purpose, the Fast Fourier Transform (FFT; *Cooley and Tukey* (1965)) was used to identify the frequency-domain content of the signal. The MATLAB scripts 'signal_analysis_suzy_0902.m' and 'signal_analysis_suzy_0903.m' (Appendix A) were created to calculate the spectra of a signal.

While the above method works well for most of the flows used within this study, there are several for which it is not viable. The noise signal generated at Colliers bridge on 18th March 2007, for example, cannot be calculated from data recorded over days prior to the flow for the simple reason that such data do not exist: the seismometer was, on that occasion, installed a mere twenty minutes before the arrival of the flow. To use the data from this small time frame would, unfortunately, be misleading; prior to the arrival of the flow, many additional noise signals were generated from the installation of the sensor and the movement of people preparing for the flow's arrival. In this case, it is therefore necessary to use the seismic record from after the lahar. As the seismometer was removed less than 24 hours after the end of the lahar, averaging the signal over a period of days is not possible. As such, the average background signal is calculated as an average of three time slices of the same length as the lahar signal. While not ideal as lahars can cause extensive remodelling of a channel by erosion and/or deposition, thereby altering site characteristics that may affect normal "background noise" signals, this will at least give some indication of the signal produced by normal streamflow.

In the case of the snow-slurry lahars recorded at the Round-the-Mountain-Track on 25th September 2007, another problem emerges. A noise profile for the first of the three flows can easily be calculated by the above method of averaging a time window over several days prior to the flow. For the other two flows, however, it is more complicated. The arrival and subsequent deposition of the first snow-slurry flow, E1, means that the channel geometry was significantly changed as much of the channel base was filled with the poorly compacted snow and ice deposit. Exactly how much this affected the seismic record of the following flows is undetermined. It can, however, be averred that such

an effect would cause a dampening of the signal record. Additional deposition from the second snow-slurry lahar, E2, would compound this problem for the third flow, E3. Any calculation of noise from similar time periods in days prior to the events would, therefore, overestimate the amount of background noise present during these flows. It would, as a result, be preferable to calculate the noise profile from periods between each of the flows.

The arrival of the second snow-slurry flow, E2, occurred approximately 3 minutes after the passing of the tail of the first flow, E1. Calculating an accurate average of background noise during the time between these flows is unrealistic. This is because, despite cutting the trace for the most accurate start and end times for each flow, they are still limited by human error that may mean possible contamination of the record by either flow. As such, it would be better to use another time period for calculating the background noise. The lapse period of more than an hour between the passing of E2 and the arrival of E3 provides a long enough time period to calculate an average of several similar-to-E2-length time windows. Due to the additional dampening of the signal as a result of the deposition of the E2 flow, however, it can be argued that this would underestimate the amount of noise present. Hence, for this flow, an average noise profile from days prior to, and the time windows after, the flow are used.

The time lapse period between E2 and E3 can also be used to calculate an average background noise profile for E3. The time between the passing of E2 and the arrival of E3 is less than the length of the third snow-slurry signal. The dampening effects of the previous flows, however, would mean that any calculations from days prior to the event may give a vastly misleading profile of the noise. For this reason, the time period between E2 and E3 is considered to be the most appropriate to use, despite its limitations. To calculate the best possible noise profile from this time, almost the entire length of the period was used. The average background noise profile was then taken from the average of the many fft windows used. A similar method was applied to the calculations of the noise profiles for many of the flows at Mt Semeru in Indonesia. In these cases, such was necessary as often other noise-generating factors complicated large parts of the signals only when no flow passed the monitoring site, e.g. the use of a generator and a rock corer.

2.6.2 Removal of background noise

The following provides a detailed critique of a number of ways in which to either remove or minimise the noise profile from that of the signal that is of interest. Figure 2.5 illustrates the different results produced by each of the methods. No single method is capable of removing all outside factors and possible noise contaminations of a signal. There are both advantages and disadvantages to each of the methods, which are examined in turn. As such, it should be noted that, unless otherwise stated, the signals investigated in subsequent chapters are those of the raw data, comprising both lahar signal and any noise present during the flow.

2.6.2.1 Signal minus Noise

The most basic of all noise removal methods must be a simple subtraction of certain affected frequencies from the raw data (e.g., *Baher* (2004)). This filtering of specific frequencies can easily be applied to those signals where ocean-sourced or eruption-associated noise is concurrent with lahar passage, such as the low frequency (<5 Hz) signals seen at Mt. Semeru (Figure 2.4). Normal streamflow, however, can produce signals that affect all frequencies in a lahar profile. If it is assumed that there are no other factors (e.g., earthquakes or air waves) that might contribute to the noise profile, the average background noise, as calculated above, can then be subtracted from the seismic record of a lahar (Figure 2.5e). This method has the advantage of not only removing the noise from a signal, but also leaving the remaining lahar signal intact. That is, no part of the signal that could reasonably be attributed to the flow is removed.

There is, however, one disadvantage to this. As a lahar passes a site, it is often highly energetic and turbulent. As such, ground vibration can be extensive. The background noise calculations above take into account the signals from normal streamflow in a channel at a specific site and any effects of the source-to-receiver pathway. The behaviour of a lahar, however, will have the effect of increasing the amplitude of any signal that is due to this source-to-receiver path. This method, therefore, will be able to remove normal streamflow "noise" but only minimise the noise due to the increased resonance along, and excitation of, the site-specific characteristic source-to-receiver path. The resultant signal will, as a result, not be free of all noise; instead, the noise

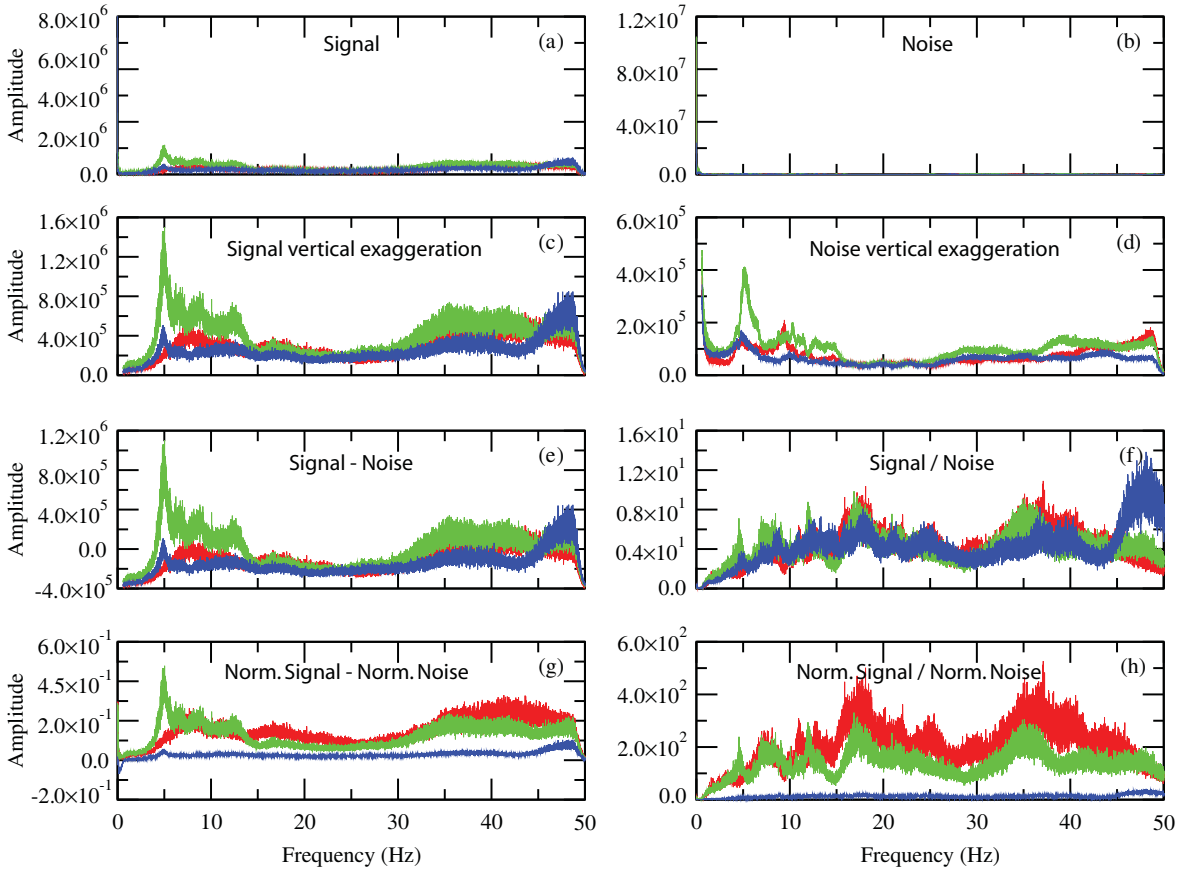

Figure 2.5: *Results of the effects of various noise removal methodologies on the total spectra as applied to signals recorded at the Round-the-Mountain-Track monitoring site of the Crater Lake-breakout lahar at Mt. Ruapehu, New Zealand, on 18th March 2007. Blue lines are vertical motion; Red lines are cross-channel motion; Green lines are channel-parallel motion. All lines are 20-point running average total spectra profiles. (a) Raw signal, illustrating the high amplitudes at very low frequencies (<1 Hz); (b) Raw noise profile; (c) Raw signal spectra with exaggerated vertical axis to show higher-than-peak frequency detail (peak signal at <2 Hz); (d) Raw noise spectra with exaggerated vertical axis to show higher-than-peak frequency detail (peak signal at <2 Hz); (e) Signal minus noise; (f) Signal divided by noise; (g) Normalised-to-peak-amplitude signal minus normalised noise; (h) Normalised-to-peak-amplitude signal divided by normalised noise.*

component will only be minimised.

2.6.2.2 Signal-to-Noise ratio

The traditional signal-to-noise ratio is a measure of the "size" of a signal in comparison to the "size" of the noise in which it is embedded. For a seismic record as collected by a series of geophones, the signal-to-noise ratio can be described as:

$$\frac{S}{N} \approx \frac{\overline{x}}{\sigma} = -\frac{\overline{x}}{\sqrt{\frac{1}{n}\sum N_i^2}} \tag{2.2}$$

where $\overline{x}$ is the average of a measurement and the best estimate of the original signal S, σ is the standard deviation, N_i is the random noise, and n is the number of geophones used in the measurement of the record (*Hatton et al.* (1986)). This, however, is just one approximation of the signal-to-noise ratio; there is no unique definition as the concept has been applied to many different records in numerous sciences. The uncertainties, or variances, inherent in windows of short, finite lengths containing signals of interest mean that their signal-to-noise ratios may be statistically misleading due to insufficient sampling within those windows. It is, therefore, better to calculate estimators for the signal-to-noise ratio, rather than exact quantitative measurements. *Hatton et al.* (1986) give several possible candidates for the estimators, such as:

$$\frac{peak\ to\ peak\ signal}{peak\ to\ peak\ noise} \tag{2.3}$$

and:

$$\frac{RMS\ of\ signal}{RMS\ of\ noise} \tag{2.4}$$

The ratio of signal-to-noise is, in effect, a power ratio that measures the relative effectiveness or reliability of a seismic record. The higher the value of the ratio, the better the record and the more clear the signal in relation to the noise.

While the variety of ways of calculating a signal-to-noise ratio provides a versatile measure of this estimator, the changes in the distribution and spectrum of the noise will result in markedly different values depending on the method used. It is, therefore, necessary to be very clear about which method is used for each calculation. The reason for these differences can be attributed to the inclusion of noise within the signal of interest. The signal-to-noise ratio is actually the ratio of signal plus noise over noise (Figure 2.5f).

2.6.2.3 Normalisation of Signal and Noise

By normalising the noise profiles, the data is reduced to a relative distribution over the recorded frequencies. The normalisation can be made to either the peak amplitude of each trace or to the amplitude of a specific frequency. The choice of frequency should be made from the distributions seen in the noise profiles so as to be uninfluenced by any lahar-specific ground-vibrational energy. When a lahar signal that was recorded at the same site is normalised to the same frequency as that chosen for the noise profiles,

the results can then be directly compared using one of the methods above to better highlight those parts of the signal more affected by the lahar (Figure 2.5g and h).

While this method can produce interesting results, care must be taken over which frequencies are chosen to normalise to, especially when a comparison of the results between different sites is required. Not only will frequency distributions of a signal be affected by differences in site characteristics, each of the noise profiles calculated at a different site in this study show peak amplitude at vastly different frequencies. At the Round-the-Mountain-Track (RTMT) on Mt. Ruapehu, for example, the peak amplitudes occurred at very low frequencies (< 1 Hz; Figure 2.5a and b). The source of these amplitudes is likely to be the result of oceanic-sourced "micro-seism" noise (e.g., *Peterson* (1993)) as it is predominantly confined below 0.2 Hz, with possible additional noise sourced from background volcanic tremor (*Hurst and Sherburn* (1993)). At Colliers bridge, however, the peak amplitudes occur at approximately 30-32 Hz. The different peak amplitudes in these noise profiles may be attributed to the variation in site characteristics, differences in the source-to-receiver pathway effects, and volume of normal streamflow in the channel (normal streamflow is much less at RTMT than at Colliers bridge). Also, while ocean-sourced noise will be felt at both sites, the degree of volcanic tremor will be much lessened at Colliers bridge due to attenuation with distance from source.

2.7 Conclusions

There are many different ways to monitor and sample a lahar flow. Direct sampling methods have the advantage of capturing detailed records of either a part, or the whole, of a flow. They are also, however, generally subject to damage and/or destruction by that flow. As such, they are not the most reliable or often the most long-term cost-effective monitoring methods because of the continual need of repair between events. In contrast, geophysical methods are a more robust method of capturing a lahar as they can detect and monitor an event without the need of direct contact with the flow. While these methods can provide insight into a passing flow, and have the advantage of less maintenance issues, they do have their own inherent problems. Of all the potential geophysical monitoring instrumentation currently available, seismic sensors appear to

be the most promising.

Seismic sensors have been used to monitor the status of volcanoes for decades. These instrumentation have also proven useful in the past as a tool for monitoring mass flows, though predominantly this usage has been as a trigger mechanism for warning systems and/or in conjunction with more elaborate recording arrays. Development of seismic sensors for use as the sole monitoring instrument in a lahar-prone catchment may prove to be highly beneficial, especially for catchments that are often inundated by mass flows and are hence regarded as highly dangerous regions. Investigation into the signals recorded from a variety of different flows may provide the basis for the development of an identification system to isolate and sort different mass flow events from one another using possible flow-specific excitation frequencies. The incorporation of new seismic instruments into or utilisation of those already within existing volcano-monitoring arrays for lahar and other mass flow monitoring purposes could be invaluable at many volcanoes throughout the world.

The main disadvantage to seismic sensors is the incorporation of noise-related signals within the lahar profiles. In order to fully evaluate the signals related solely to any lahar, all background and site-related amplified noise must be removed from the recorded data. To this end, a number of different noise minimisation methods have been explored, such as signal minus noise, signal-to-noise ratios, and normalisation-related analyses. Each of the different methods, however, have both advantages and disadvantages to their usage. Further understanding of the dynamics of, and particle motions within, a lahar, as well as any effects on a signal related to site characteristics, is necessary for the effective removal of all noise-related signal as it is these motions which appear to dictate the frequencies and amplitudes of signal recorded. Until such time as a noise-removal method is developed that removes all noise and preserves all lahar-related signal, it is likely that the use of the above mentioned noise minimisation methodologies would produce misleading results. It is because of this current inability to completely separate lahar-related and noise-related signals that has led to the general inclusion of all data recorded at the time of a flow during the analyses of lahars within this study, except where otherwise indicated.

Chapter 3

Seismic signals as proxy for flow characteristics

Chapter 3 examines the use of seismic records as a measure for flow discharge between multiple flows at a single site. Variability in the frequency distributions for this type of record are also used to explore its use as a sediment concentration proxy for the same flow at multiple sites.

3.1 Introduction

Lahars can range from small, seasonal rain-triggered flows to much larger and higher discharge eruption-triggered or crater lake-breakout events (Chapter 1.4.1). Mitigation of the risks resulting from any such event is dependent upon several factors. The most significant of these are the accurate characterisation of the event itself, including a determination of its discharge and sediment concentration, and, by extension, its predicted inundation and impact areas. For crater lake breakouts, it can be possible to estimate prior to the event an approximate volume of water likely to be released. From this, initial estimates of the hazard posed by a lahar, and its zones of impact, can be readily deduced in the uppermost reaches of a catchment (*Procter* (2009); *Procter et al.* (2009)). It is common, however, for non-cohesive lahar flows to undergo considerable bulking and transformation as they travel from source (e.g., *Pierson and Scott* (1985);

Cronin et al. (2000a); *Procter et al.* (2010)). For events such as repeated seasonal rain-triggered lahars, these issues are compounded by the unpredictable volumes of runoff water at flow initiation (e.g., *Lavigne and Thouret* (2000); *Lavigne et al.* (2000a)). For these, quantification of the likely discharge of a flow becomes more complicated.

While there are a number of simulations and models that can provide pre-event estimates for factors such as discharge, entrainment, and deposition (e.g., *O'Brien* (1999); *Pitman et al.* (2003); *Carrivick et al.* (2008)), they are limited by simplified assumptions of the complex flow behaviours often witnessed in real-world events (e.g., *Doyle et al.* (2009)). As such, the results from these simulations require validation from syn-event observations and/or measurements, as well as post-event depositional surveys. Due to the unpredictable onset of lahars, however, scientific observations are limited (e.g., *Cronin et al.* (1999); *Lavigne and Thouret* (2002)). In addition, when such observations are possible, data collection can often be hindered by the flow itself (e.g., *Arattano and Marchi* (2008)). As detailed in Chapter 2, many direct sampling methods are in regular need of maintenance and/or replacement, making them cost-prohibitive in nearly all but the most commonly-affected channels. The non-contact nature of seismic monitoring, however, may provide an acceptable alternative, as it is commonly already used for detection of mass movements (e.g., *Tungol and Regalado* (1996); *Bessason et al.* (2007); *Leonard et al.* (2008)). This chapter provides a validation of the use of such methods to calculate approximate volumes of multiple flows at a single site, and investigates their use in determining changing sediment concentrations of a single flow between multiple recording sites.

3.2 Determination of flow volume proxy

As has been previously stated in Chapter 2.4.3.3, there have been several studies that have utilised the seismic records of mass flows in an attempt to estimate their size and discharge. Comparison of the seismic records of an event and its recorded discharge and volume can lead to good correlations between measured ground vibrations and flow size (e.g., *Tungol and Regalado* (1996); *Brodscholl et al.* (2000); *Suwa et al.* (2000)). These relationships can then be tested using the coefficient of determination, as defined

by:

$$R \equiv \sqrt{1 - \frac{SS_{err}}{SS_{tot}}} \tag{3.1}$$

where SS_{err} is the sum of the squared errors and SS_{tot} is the total sum of squares. The R coefficient gives the proportion of variability in a dataset that is accounted for by the statistical model. As such, it provides a measure of the predictability of the likelihood of future outcomes by the model.

In the case of lahars, for example, *Tungol and Regalado* (1996) analysed data from acoustic flow monitor (AFM) records of debris flows at Mt. Pinatubo, Philippines. From their results, they were able to determine a positive correlation between the mean discharge of a debris flow and its corresponding mean ground-vibration-velocity amplitude. They were also able to calculate a positive correlation between the flow volume and the integration of mean velocity-amplitude over time. The coefficients of determination of these correlations, however, were low, R=0.61 and R=0.56, respectively. Hence, the resolution of volumes predicted from this correlation would not be very high. It is likely that this inaccuracy is due, at least in part, to the relative location of the sensor from the affected channel. In their case, the sensor was located 2-2.5 km from the source of the ground vibrations. Due to the attenuation of frequencies with distance (*Aki* (1980)), it can be reasonably assumed that a large proportion of the ground-velocity amplitude was therefore not recorded by the instrument.

Another example of positive correlation between seismic amplitude and debris-flow discharge was calculated by *Suwa et al.* (2000). Their installation of the recording instrument was located 15 m from the true right bank of the channel, buried at a depth of 1 m. This meant that signal attenuation was minimised, and a much better correlation coefficient was found between peak ground-vibrational acceleration and peak discharge (R=0.90), and between the time integral of ground-vibration-acceleration amplitude and flow volume (R=0.98). From this, *Suwa et al.* (2000) were able to conclude that estimates of the peak discharge of a flow can be readily made from the peak acceleration of ground vibrations, while the volume of the flow can be estimated precisely from the integral of the amplitude of this acceleration.

High correlations between ground-vibrational amplitudes and flow volumes and discharge are not unique to debris flows. There have been a number of studies that have found similar results for other mass flows, such as rockfalls (e.g., *Norris* (1994))

and pyroclastic flows (e.g., *Brodscholl et al.* (2000)). *Norris* (1994) analysed the seismic records associated with 14 rockfall events at Mt. St. Helens, Mt. Adams, and Mt. Rainier in the Cascade Range, USA. From these, an extremely high correlation between the signal amplitudes recorded of these events and their estimated source volumes was found (R=0.99), despite being recorded at a distance from source of c. 70 km. As with the signals recorded by *Tungol and Regalado* (1996), attenuation of signal with distance would have occurred. The higher correlation of the data presented in *Norris* (1994) may have been influenced by the error of 50% involved in the estimation of source volume for each event. In addition, rockfalls generate seismic responses that are fundamentally different from those of debris flows. When rockfalls impact the ground, they produce sharp signals that simultaneously affect a wide-range of frequencies (e.g., *Vilajosana et al.* (2008)). In constrast, debris flows produce a gradual increase in spectral amplitudes with time. Typically, the front produces signals of <50 Hz, which increase to 50-100 Hz in the body and tail of the flow (e.g., *Okuda et al.* (1979); *Huang et al.* (2007)). The proportions of water and clay within a debris flow will also effect the signal amplitudes by affecting saltation, friction, and cohesion, as well as dampening of the signal through the different media (*Huang et al.* (2007)).

Each of the above studies have been concerned with mass flows with primarily collisional motions of particles. The high sediment concentrations of typical debris flows (>60 vol.% sediment; *Coussot and Meunier* (1996)) mean that the predominant influences over particle motion are grain-grain collisions and forces of inertia (*Iverson* (1997)). Flows that have lower sediment concentrations, such as hyperconcentrated flows (20-60 vol.%; *Beverage and Culbertson* (1964)), have fewer particle-particle collisions due to greater freedom of movement within suspension. It is not unsurprising, therefore, that observations of the two flow types show greater amplitudes of ground vibration result from debris flows than hyperconcentrated flows. The question then arises as to what effect this would have upon the proportional relationship between ground-vibrational amplitudes and flow volume, as observed in the studies detailed above. To this end, analyses were made of a series of hyperconcentrated flows recorded at Mt. Semeru, Indonesia, in 2008.

3.2.1 Geological setting and instrumentation details

A lahar monitoring site on the southern flanks of Mt. Semeru was located beside the Curah Lengkong river channel, at c. 9.5 km from the summit. The channel is a c. 30 m-wide box-shaped valley, with an underlying base of boulders, gravel, and lava bedrock. This site was occupied in February-March 2006, 2007, and 2008 (Figure 3.1; Chapter 1.5.2). Instrumentation in each of these years has included a 3-component broadband seismometer (Guralp CMG-6TD), pore pressure transducers, load cells, and video cameras (*Manville* (2006); *Doyle et al.* (2009); *Doyle et al.* (2010)). For the analyses presented here, however, only the seismometer and video records were used. Figure 3.1 shows the relative locations of the seismometer for each year. In 2006 and 2007, ground vibrations were recorded at 100 sps, while in 2008 they were recorded at 200 sps (February) and 125 sps (March). Particle Image Velocimetry (PIV; *Dalziel* (2005)) analyses were made on the video records in order to estimate surface-flow velocity (see Chapter 2.2.3 for details). Flow volumes (Q(t)) were calculated using the monitored cross-sectional area and the average body velocity, calculated by multiplying the surface velocity of these turbulent river flows by 0.75 ± 0.1 in order to take into account differences in velocities across the channel surface (*Doyle et al.* (2009)).

3.2.2 Proxy analysis and results

The seismic signals of the lahars recorded during the 2006, 2007, and 2008 field campaigns were analysed to find both the ground-vibrational amplitudes and the vibrational energies of each flow, using the programs as described in Appendix A. The higher sampling rates used for the 2008 flows were downsampled[1] to allow for correlation between the cumulative amplitudes of all flows. To this end, the MATLAB function 'upfirdn.m' was used. In addition to this, all of the studied data were filtered above 5 Hz in order to remove any unwanted low-frequency effects that would influence the results, such as ocean-sourced noise and signals demonstrably due to the repeated ash eruptions commonly occuring at Semeru (Chapter 2.6).

The 2008 lahars at Semeru had a rapid onset, followed by a surging and unsteady flow. *Doyle et al.* (2009) were able to trace a series of "pulses" between two instru-

[1]Downsampling is the signal processing technique used to reduce the sampling rate of a signal.

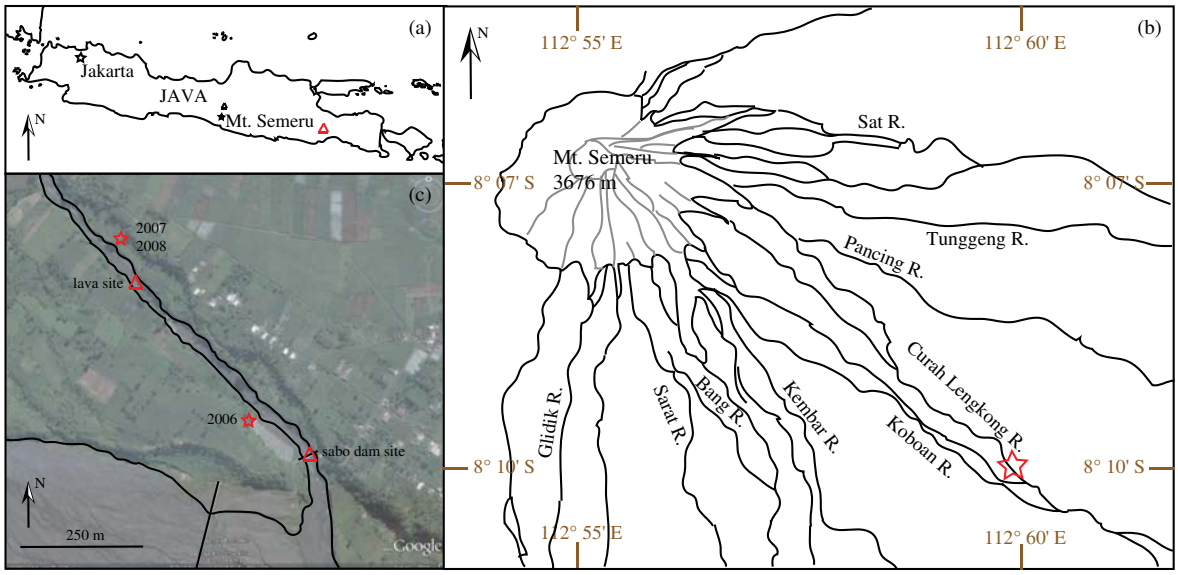

Figure 3.1: *Location of the monitoring sites along the Curah Lengkong channel, Mt Semeru, with details of the instrumentation and observational locations. (a) Map shows location of Mt. Semeru in Java, Indonesia; (b) Map of main tributaries and drainage channels of Mt. Semeru, highlighting the general location of the monitoring sites on the Curah Lengkong river (red star); (c) exact locations of the monitoring sites at the lava site and sabo dam site (red triangles) at which pore pressure transducers and video cameras were installed. Bucket samples were also taken at these sites. Red stars indicate installation locations of the broad-band seismometer in each year. Details superimposed upon aerial photograph sourced from GoogleEarth^{TM}, Cnes/Spot Image, Image ©2010 DigitalGlobe ©2010 TeleAtlas, Imagery Date 15th June 2004.*

mentation sites 500 m apart, and described them as "packets" within the flow. Similar behaviour had been previously observed at Semeru (e.g., *Lavigne and Suwa* (2004)), as well as at many other locations (e.g., *Marchi et al.* (2002); *Zanuttigh and Lamberti* (2007)). These "pulses" have been ascribed to a variety of causes, including ponding, damming, or surging of the flow, along with the coalescence of material from a number of upstream tributary inputs. The seismic records of each flow where this occurred record this phenomenon in short periods of relative amplitude maxima. From this observation, it is seen that a single amplitude maximum for the entire flow is of little relevance. As a result, analyses of the relationship between flow volume and peak ground-vibrational amplitude have not been undertaken here. Instead, the study has focused on the cumulative values of these parameters to better evaluate bulk flow volume.

In order to evaluate the relationship between the volume of each recorded flow and its cumulative ground-vibrational amplitude and seismic energy, the cumulative volume

Table 3.1: *Summary of 2008 data used to calculate the regression lines of Equations 3.5 and 3.6.*

Date (dd/mm/yyyy)	Packet No.	Sampled conc. (%)	Cum. Volume (m^3)	range (+/-)	Cum. Seismic Energy (> 5 Hz; m^2/s^2)	range (-)	range (+)	Cum. Amplitude (m/s)	range (-)	range (+)
26/03/2006	total		unavailable	unavailable	5.08×10^{-9}	1.32×10^{-11}	6.55×10^{-11}	2.01×10^{-2}	1.22×10^{-4}	2.05×10^{-4}
28/03/2006	total		unavailable	unavailable	1.42×10^{-7}	0	0	6.03×10^{-2}	-6.34×10^{-2}	6.38×10^{-2}
06/02/2007	total		unavailable	unavailable	3.04×10^{-8}	1.00×10^{-10}	0	3.15×10^{-2}	2.12×10^{-4}	1.95×10^{-4}
26/02/2008	p1	10	678	90	3.85×10^{-10}	3.38×10^{-11}	3.46×10^{-11}	1.55×10^{-3}	1.54×10^{-3}	1.49×10^{-4}
	p2	13	4439	592	3.33×10^{-9}	4.71×10^{-11}	3.13×10^{-11}	8.48×10^{-3}	1.69×10^{-4}	1.39×10^{-4}
	p3*	18	unavailable	unavailable	2.56×10^{-9}	4.53×10^{-11}	5.17×10^{-11}	8.03×10^{-3}	1.67×10^{-4}	1.77×10^{-4}
	total[a]		5116	682	3.71×10^{-9}	4.40×10^{-11}	2.96×10^{-11}	1.00×10^{-2}	1.61×10^{-4}	1.35×10^{-4}
28/02/2008	p1	19	4496	599	2.86×10^{-9}	1.50×10^{-10}	1.16×10^{-10}	6.18×10^{-3}	2.24×10^{-4}	1.94×10^{-4}
	p2	9	1001	133	4.05×10^{-9}	2.25×10^{-10}	2.31×10^{-10}	6.57×10^{-3}	3.82×10^{-4}	3.77×10^{-4}
	total		5497	733	6.90×10^{-9}	1.10×10^{-10}	7.77×10^{-11}	1.27×10^{-2}	2.11×10^{-4}	1.72×10^{-4}
04/03/2008	p1		8315	1109	1.64×10^{-2}	1.00×10^{-10}	1.00×10^{-10}	1.14	3.23×10^{-4}	3.34×10^{-4}
	p2		13601	1813	1.55×10^{-8}	2.15×10^{-10}	1.85×10^{-10}	2.41×10^{-2}	4.60×10^{-4}	4.15×10^{-4}
	total		21915	2922	1.64×10^{-2}	2.00×10^{-10}	1.00×10^{-10}	1.16	3.44×10^{-4}	3.09×10^{-4}
05/03/2008	p1	26	3362	448	8.35×10^{-11}	8.25×10^{-12}	2.12×10^{-11}	8.92×10^{-4}	7.44×10^{-5}	1.11×10^{-4}
	p2	48	5157	688	3.75×10^{-9}	1.01×10^{-10}	7.37×10^{-11}	6.23×10^{-3}	2.78×10^{-4}	2.31×10^{-4}
	p3	60	4565	609	6.80×10^{-9}	7.31×10^{-10}	6.66×10^{-10}	7.31×10^{-3}	6.90×10^{-4}	6.86×10^{-4}
	p4	40	6149	820	2.21×10^{-8}	6.79×10^{-10}	7.33×10^{-10}	2.67×10^{-2}	7.01×10^{-4}	6.96×10^{-4}
	total		15870	2564	3.26×10^{-8}	8.79×10^{-11}	8.17×10^{-11}	4.11×10^{-2}	2.22×10^{-4}	2.10×10^{-4}
07/03/2008	p1		7696	1026	1.41×10^{-8}	1.59×10^{-10}	1.48×10^{-10}	1.66×10^{-2}	2.83×10^{-4}	2.97×10^{-4}
	p2		5514	735	4.64×10^{-9}	3.91×10^{-10}	3.13×10^{-10}	8.34×10^{-3}	5.69×10^{-4}	5.22×10^{-4}
	p3*		unavailable	unavailable	4.10×10^{-8}	2.61×10^{-10}	3.25×10^{-10}	3.75×10^{-2}	4.79×10^{-4}	5.14×10^{-4}
	p4**	14	unavailable	unavailable	7.49×10^{-9}	2.41×10^{-10}	2.02×10^{-10}	1.63×10^{-2}	4.75×10^{-4}	4.32×10^{-4}
	total[b]		13210	1761	1.87×10^{-8}	2.45×10^{-10}	1.67×10^{-10}	2.50×10^{-2}	3.46×10^{-4}	3.17×10^{-4}
12/03/2008	total		18237	2432	5.07×10^{-8}	2.45×10^{-10}	2.16×10^{-10}	4.12×10^{-2}	3.34×10^{-4}	3.37×10^{-4}

* End time derived from video footage only and therefore is approximate

** Start and end times derived from video footage only and therefore are approximate

[a] Total not including packet 3

[b] Total not including packets 3 and 4

of a flow was calculated from its discharge Q (m^3/s) over the time integral of the flow duration, such that:

$$Cumulative\ Volume = I_Q = \int_{t_1}^{t_2} Q(t)dt \tag{3.2}$$

where t_1 is the arrival time of the flow front and t_2 is the time at which the end of the tail passes the sensor. Similarly to this, the ground-vibrational parameters can also be determined for the same time interval:

$$Cumulative\ Seismic\ Amplitude = I_A = \int_{t_1}^{t_2} |A(t)|dt \tag{3.3}$$

$$Cumulative\ Seismic\ Energy = I_{S.E.} = \int_{t_1}^{t_2} S.E.(t)dt \tag{3.4}$$

where *A(t)* is the velocity amplitude envelope of ground vibration and *S.E.(t)* is the seismic energy, at a time *t*. The seismic energy is calculated as a proxy for power, and is assumed to be equivalent to the velocity amplitude (*A(t)*) squared. The results of the above integrals for the 2008 data can be found in Table 3.1. Ranges for each of the parameters (I_Q, I_A, and $I_{S.E.}$) were calculated using an error of ± 30 seconds for t_1 and t_2 of each time integral due to the difficulty in picking exact flow arrival and cessation times. The results show a very strong positive correlation between volumes of each of the recorded flows and their associated seismic records. The data recorded on 4th March 2008 were not included in the regression calculations due to repeated sharp spikes that swamped the record across all frequencies. Figure 3.2 illustrates that there also appears to be a linear relationship between flow volume and cumulative seismic amplitude, similar to those seen in other mass flow analyses (e.g., *Norris* (1994); *Suwa et al.* (2000)), such that:

$$I_Q = 1433.9 + (3.9047e^{+05} \times I_A) \tag{3.5}$$
$$(R = 0.97)$$

where I_Q is the cumulative volume and I_A is the cumulative seismic amplitude as defined above in Equations 3.2 and 3.3 respectively, and R is the coefficient of determination. This very high correlation coefficient indicates that calculations of volumes

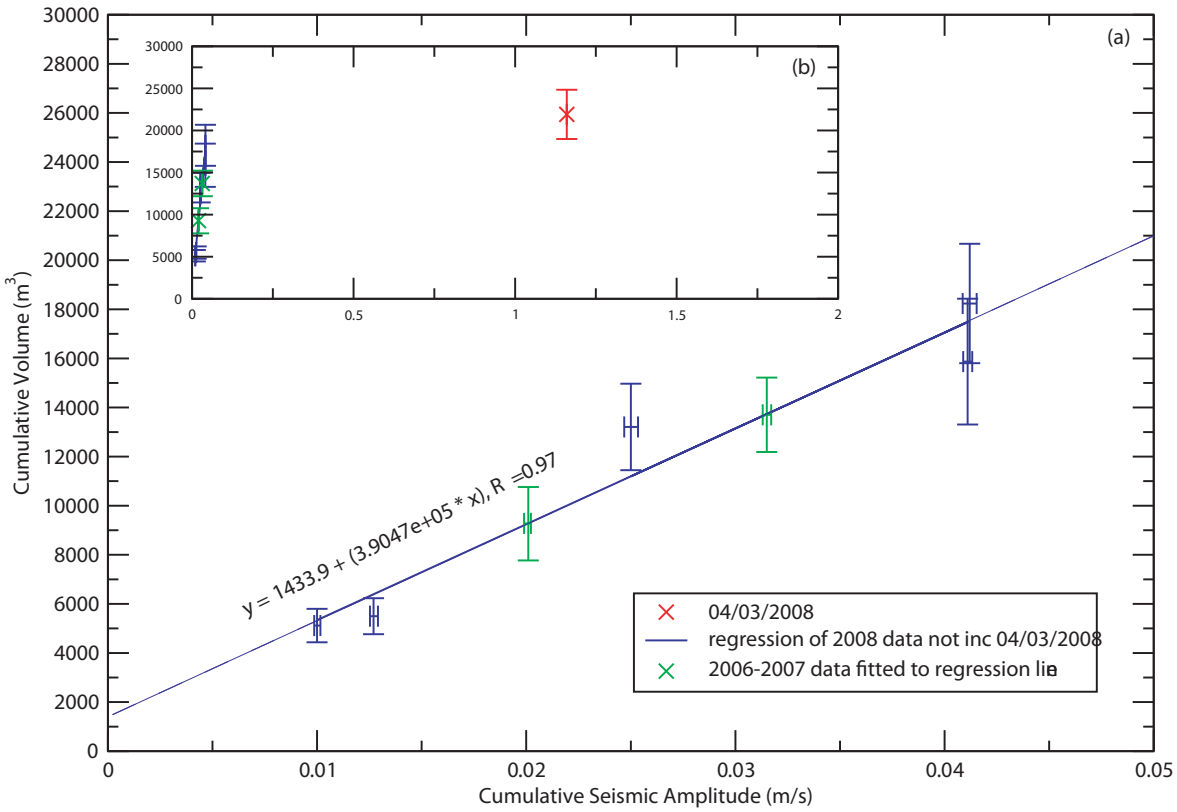

Figure 3.2: *Total cumulative volume vs total cumulative seismic amplitude for flows recorded at Mt. Semeru, Indonesia. (a) All data recorded, not including 4^{th} March 2008 data; (b) all data, including 4^{th} March 2008 data. Blue line: regression fit for 2008 data, not including 4^{th} March 2008 data; Red cross: data from 4^{th} March 2008; Green cross: 2006-2007 data, as fitted to regression line.*

based upon the cumulative seismic amplitudes using the regression line will result in predicted values that have only small deviations, or errors, from recorded (real) values (Table 3.2).

Similarly to the above, the comparisons of cumulative volumes versus cumulative seismic energy of a flow also show a very high correlation (Figure 3.3). The regression line that follows from this is:

$$I_Q = 1.8317e^{+08} \times I_{S.E.}^{0.54429} \qquad (3.6)$$

$$(R = 0.98)$$

where $I_{S.E.}$ is the cumulative seismic energy as defined above in Equation 3.4. The results of calculations of estimated cumulative volumes from this regression are presented in Table 3.2. The [slightly] higher correlation coefficient for these factors suggest the volumes calculated from this regression are likely to be more accurate than those

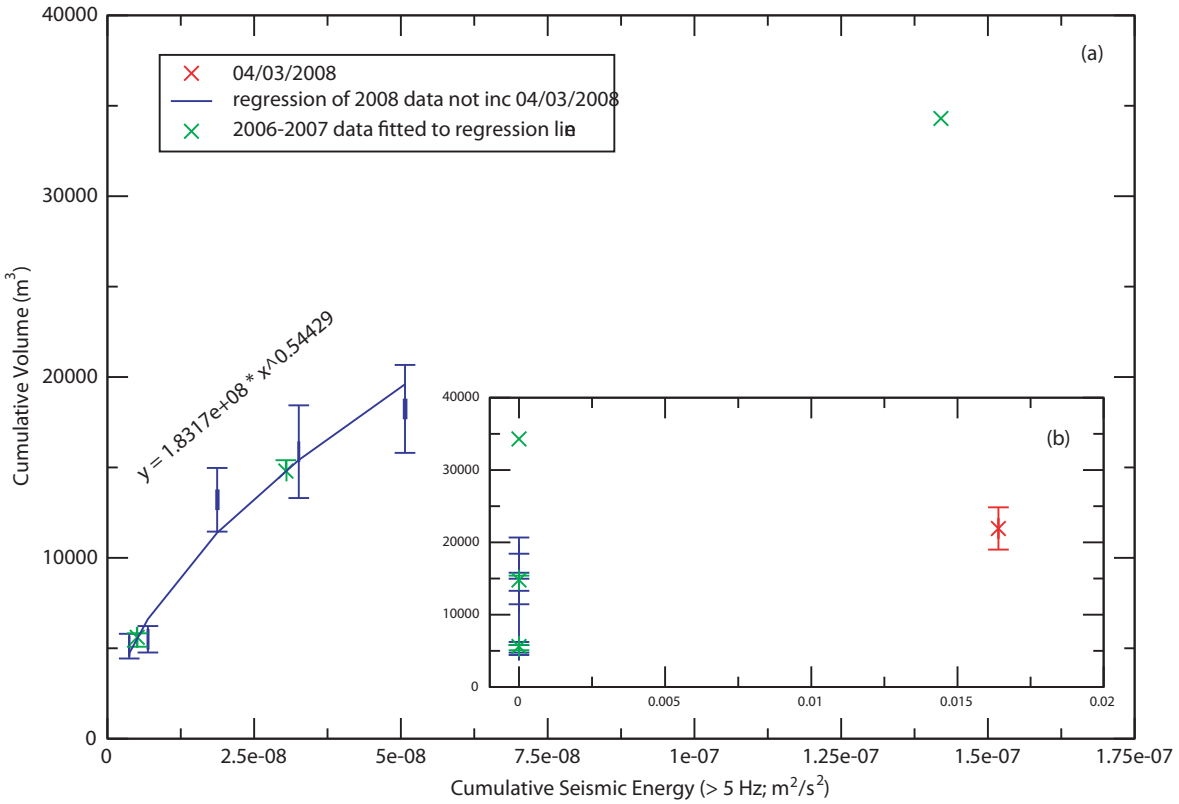

Figure 3.3: *Total cumulative volume vs total cumulative seismic energy (>5 Hz) for flows recorded at Mt. Semeru, Indonesia. (a) All data recorded, not including 4^{th} March 2008 data; (b) all data, including 4^{th} March 2008 data. Blue line: regression fit for 2008 data, not including 4^{th} March 2008 data; Red cross: data from 4^{th} March 2008; Green cross: 2006-2007 data, as fitted to regression line.*

calculated from Equation 3.5.

In analysing the variations in seismic data relating to pyroclastic flow signals recorded at Mt. Merapi, Indonesia, in 1994, *Brodscholl et al.* (2000) assumed an equivalence between total source volume and cumulative seismic amplitude envelope area. From this, volumes of discrete collapse events within the total were calculated using a similar method to that investigated above. Assuming this reasoning holds true for lahars, it follows that the relative volumes of individual "pulses" or "packets" within a flow can be calculated from the cumulative seismic amplitude, or energy, over the time integral of each pulse. It would then be reasonable to assume that the relationships of known volume and known cumulative seismic amplitude, or energy, within each of the packets observed during the 2008 lahars at Semeru would conform to those in Equations 3.5 and 3.6. Figure 3.4 illustrates that this holds true for most of the packets observed. There are a few notable exceptions. Packets with very low total vol-

Using regression line: $I_Q = 1433.9 + (3.9047e^5 \times I_A)$

Date (dd/mm/yyyy)	Cum. Amplitude (m/s)	range (-)	range (+)	Cum. Volume (m^3)	range (-)	range (+)
26/03/2006	2.01×10^{-2}	1.22×10^{-4}	2.05×10^{-4}	9280	1480	1510
28/03/2006	6.03×10^{-2}	-6.34×10^{-2}	6.38×10^{-2}	25000	-23300	26300
06/02/2007	3.15×10^{-2}	2.12×10^{-4}	1.95×10^{-4}	13700	1520	1510

Using regression line: $I_Q = 1.8317e^8 \times I_{S.E.}^{0.54429}$

Date (dd/mm/yyyy)	Cum. Seismic Energy (> 5 Hz; m^2/s^2)	range (-)	range (+)	Cum. Volume (m^3)	range (-)	range (+)
26/03/2006	5.08×10^{-9}	1.32×10^{-11}	6.55×10^{-11}	5610	219	525
28/03/2006	1.42×10^{-7}	0	0	34300	0	0
06/02/2007	3.04×10^{-8}	1.00×10^{-10}	0	14800	601	0

Table 3.2: *Summary of 2006 and 2007 data used by, and calculated from, the regression lines in Equations 3.5 and 3.6.*

umes (<1500 m^3) appear to have relatively high cumulative seismic amplitudes. Also, the fourth packet recorded on 5th March exhibits a much higher cumulative seismic amplitude than expected from its total volume.

Studies have shown that the distribution of sediment held in suspension within a turbulent hyperconcentrated flow is relatively uniform, depending upon the degree of turbulence (e.g., *McCutcheon and Bradley* (1984); *Rickenmann* (1991); *Pierson* (2005)). Despite this, at depths near to the channel bed, there will be a noticeable increase in sediment concentration due to the area of exchange between suspended sediment and bedload material. *Wilson* (1985) noted four distinct changes that occur in the suspended-sediment concentration as flow velocity decreases: (1) particles settle out of suspension, (2) the average suspended-sediment particle size becomes finer, (3) suspended sediment becomes progressively more concentrated in near-bed regions, and (4) vertical column stratification increases. Observations of the 2008 lahars at Semeru indicate that the packets exhibiting anomalously high cumulative seismic amplitudes, while having very low total volumes and suspended-sediment loads, travel at lower velocities than other packets within the same flow (E.E. Doyle, pers. comm. 2009). This may be attributed to increased particle collisions near, and saltation along, the channel base, resulting when sediment settles out of suspension and near-bed concentrations increase. The fourth packet observed during the flow on 5th March also appears to

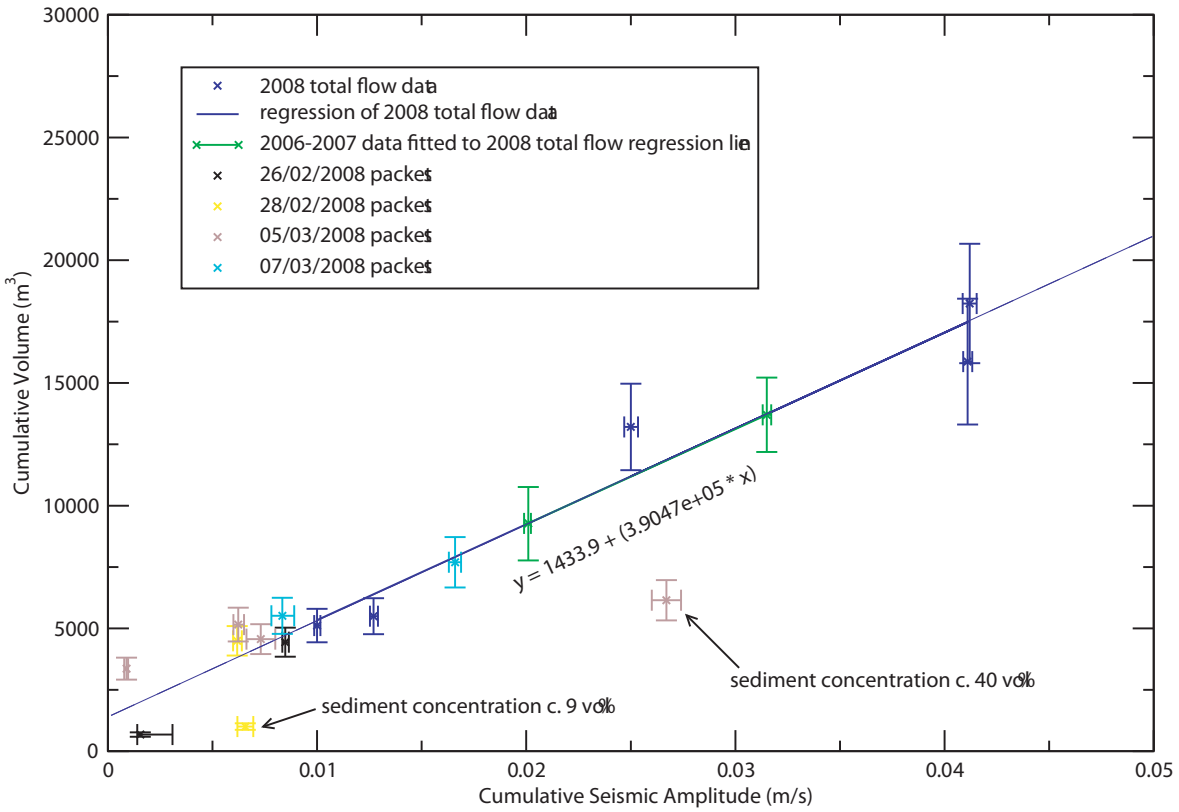

Figure 3.4: *Total and packet cumulative volume vs total and packet cumulative seismic amplitude for flows recorded at Mt. Semeru, Indonesia. Plot includes total flow data: 2008, except that recorded on 4th March (dark blue); Regression fit for 2008 data, not including 4th March (dark blue line); 2006-2007 data, as fitted to regression line (green). 2008 packet data plotted by flow: 26th February (black); 28th February (yellow); 5th March (brown); 7th March (pale blue).*

display this. Velocities associated with this packet were much lower than those of the one previous to it (1.8±0.1 vs 4.0±0.3 m/s; *Doyle et al.* (2010)) and sampled suspended sediment concentration was lower (Table 3.1). Observations of the bulking capabilities of the packets between the upper "lava" site and the downstream "sabo" site indicate an overall debulking occurs between the sites within packet 4, further suggesting the occurrence of sedimentation. The higher total volume of this packet can likely be attributed to a combination of higher discharge at its onset and longer duration until cessation of flow, as compared with the other recorded examples.

3.3 Volume proxy between multiple sites

The above study has illustrated that seismic records can act as a proxy for flow volume at a single site. This applies to repeated flows, initiated by the same mechanisms, with

similar source material, and similar descent paths in the same channel. Such events are common at locations where the predominant lahar-trigger is seasonal rainfall, such as at Semeru (e.g., *Lavigne and Thouret* (2002); *Lavigne and Suwa* (2004)), but many other areas are not subject to such conditions. Lahars can be triggered by a variety of contrasting mechanisms, which may hinder application of a uniform proxy relationship (e.g., Chapter 1.4.1; *Neall* (1996)). In cases such as these, determination of a volume proxy must be made using a different method.

Numerical models of lahar waves have been attempted in the past, with varying degrees of complexity. One-dimensional models have ranged from simple empirically-derived relationships between flow volume and inundation area (e.g., *Iverson et al.* (1998)), or velocity and discharge (e.g., *Pierson* (1998)), to hydraulic models based upon the application of the Saint-Venant Equations to explore dynamic (e.g., *Caruso and Pareschi* (1993)) or kinematic (e.g., *Vignaux and Weir* (1990); *Fagents and Baloga* (2005)) wave theory. The Saint-Venant Equations have also been applied in two-dimensional models with a depth-average dependence solved via the shallow water assumption (e.g., *Carrivick et al.* (2008)) or modified shear stress terms that include corrections for viscous and yield slopes (*O'Brien* (1999)). Complications and complexities involved in each of these models arise from the effects of changing sediment concentration and flow volume on the rheology of the lahar in question. While standard hydrodynamic models can be used to adequately simulate dilute Newtonian flows, assumptions regarding flow rheology must be included to simulate flows that lie within the debris flow regime (e.g., *Chen* (1988); *O'Brien* (1999))). While these assumptions are generally encorporated into a lumped resistance term (e.g., *Macedonio and Pareschi* (1992)), some studies have concluded that they are more appropriately modelled using governing equations drawn from single- (e.g., *Savage and Hutter* (1989); *Patra et al.* (2005)) or two-phase (e.g., *Denlinger and Iverson* (2001); *Iverson and Denlinger* (2001); *Williams et al.* (2008)) Coulomb mixture theory. These latter models, however, are temporally and computationally demanding, and, despite their greater sophistication, are arguably no better at determining the likely bulk behaviour of a lahar than their simpler one-dimensional counterparts that neglect internal flow dynamics. To this end, the following is an evaluation of current understanding of kinematic wave theory[2]

[2]Special acknowledgement must be given to Dr. H.K. McMillan for help involving the understand-

as it pertains to a lahar.

3.3.1 Kinematic theory

Kinematic wave theory is commonly used to evaluate the hazards associated with hydrological events, such as floods (e.g., *Mukhopadhyay et al.* (2003)). The application of this theory to the multiple site record of the March 2007 Crater Lake-breakout lahar may allow for a possible method of calculating flow volume and discharge between sites. In-situ observations of the lahar made at multiple sites show that it maintained a steep frontal arrival wave. This type of behaviour is predictable by the kinematic theory (e.g., *Chow* (1988)), suggesting that the use of the kinematic approximations of the Saint-Venant Equations would be appropriate (e.g., *Mascarenhas et al.* (2005)).

The Saint-Venant Equations are derived from the principles of continuity, or conservation of mass, and momentum to describe unsteady flow in an open channel, and in differential form are written as:

$$Continuity : \frac{\partial Q}{\partial x} + \frac{\partial A}{\partial t} - q = 0 \tag{3.7}$$

$$Momentum : \left(\frac{1}{A}\right)\frac{\partial Q}{\partial t} + \left(\frac{1}{A}\right)\frac{\partial \left(Q^2/A\right)}{\partial x} + g\frac{\partial y}{\partial x} - g(S_0 - S_f) = 0 \tag{3.8}$$

where Q is the discharge (m^3), A is the cross-sectional area (m^2), q is the lateral flow per unit length of the channel ($m^3/s/m$), x is the distance along the channel (m), y is the depth of flow (m), g is the gravitational acceleration (m^2/s), S_0 is the bed slope of the channel, and S_f is the friction slope (e.g., *Chow* (1988); *Rangaraju* (1993)). In the momentum equation (Equation 3.8), term 1 describes the change in momentum due to change in velocity over time, term 2 describes the change in momentum due to change in velocity along the channel, and term 3 describes a pressure force proportional to the change in in water depth along the flow. Term 4 combines a gravity force term and a friction force term; that is, forces proportional to the bed slope and the friction slope, respectively. Based upon the inclusion and/or elimination of any of the four terms to approximate a flood wave, it can be described as a dynamic wave, diffusion wave, or

ing of the Kinematic Theory and Manning Formula methodology and for providing much of the data contained within. It should also be noted that the work involving comparisons of Colliers bridge and Round-the-Mountain-Track data to provide a sediment concentration proxy is the result of a collaboration between Dr. McMillan and myself.

kinematic wave as follows (e.g., *Chow* (1988); *Rangaraju* (1993)):

$$Dynamic: \left(\frac{1}{A}\right)\frac{\partial Q}{\partial t} + \left(\frac{1}{A}\right)\frac{\partial\left(Q^2/A\right)}{\partial x} + g\frac{\partial y}{\partial x} - g(S_0 - S_f) = 0 \tag{3.9}$$

$$Diffusion: g\frac{\partial y}{\partial x} - g(S_0 - S_f) = 0 \tag{3.10}$$

$$Kinematic: g(S_0 - S_f) = 0 \tag{3.11}$$

As can be seen above, the kinematic approximations assume gravitational and frictional forces balance, and acceleration and pressure terms can be ignored (e.g., *Chow* (1959); *Chow* (1988); *Mascarenhas et al.* (2005)). They do, however, assume that a channel is generally free from obstructions or flood storage areas, and backwater effects are insignificant. The recording sites of the Round-the-Mountain-Track and Colliers bridge (Chapter 1.5.1) meet these requirements and are therefore considered ideal candidates for the application of these parameters.

3.3.1.1 The Friction Slope

The friction slope term (e.g., *Chow* (1988)) in its traditional form is described by:

$$S_f = \frac{n^2}{R^{4/3}} \cdot v^2 \tag{3.12}$$

where S_f is the friction slope, n is the Manning's n parameter, R is hydraulic radius (m) that is equal to the cross-sectional area divided by the wetted perimeter[3], and v is velocity (m/s). The discharge Q can be obtained from the product of the cross-sectional area A and the velocity v. The friction slope term considers only the shear stress components that are turbulent and dispersive. These components are typically combined in a Manning's n value (e.g., *Chow* (1988)). The Manning's n parameter is an empirically-derived coefficient dependent on a number of factors, including surface roughness and sinuosity of the channel, and amalgamates bed and flow resistance terms.

[3]In open channel flow, the wetted perimeter is defined as the surface of the channel sides and bottom that is in direct contact with the aqueous body. Mathematically, it can be written as:

$$\int_{i=0}^{\infty} l_i$$

where l_i is the length of each surface in contact with the aqueous body.

While the Manning's equation, normally expressed as a reconfiguration of the friction slope term above (where

$$v = \frac{R^{3/2} S^{1/2}}{n} \tag{3.13}$$

), can and is used to describe open-channel fully-turbulent Newtonian streamflows, lahar flows have rheologies that are markedly different. A number of studies have proposed modifications of the friction slope term (Equation 3.12) to account for these differences. *Macedonio and Pareschi* (1992) assume a relationship between the shear rate (dv/dz) and the shear stress (τ) : $\tau = \tau_0 + \mu_1 (dv/dz)^\eta$, where τ_0 is the yield stress, μ_1 is a proportionality coefficient, and η is the flow behaviour index. They contend that for flows where η=1, μ_1 is viscosity, and the model is a viscous one, whereas for flows where η=2, dilatent flow behaviour is expected. Applying these expectations in relation to the mean horizontal flow velocity

$$v = \frac{\eta}{\eta + 1} \left[\frac{\rho_{mo} g sin\theta}{\mu_1} \right]^{\frac{1}{\eta}} \left[\frac{z_0}{h} \right]^{\frac{\eta+1}{\eta}} \left[1 - \frac{\eta}{2\eta + 1} \frac{z_0}{h} \right] h^{\frac{\eta+1}{\eta}} \tag{3.14}$$

where z_0 is the vertical coordinate from the bed where shear stress is equal to yield stress and ρ_{mo} is a "modified" mass density of the mixture as defined by *Chen* (1988), and assuming that, in a fully dynamic state, $h = z_0$ and ρ_{mo} is equal to the mixture density ρ, they were able to deduce the friction slope terms relating to both viscous and dilatant flows:

$$Viscous\ Flows : S_f = 3 \cdot \frac{\mu_1}{\rho g} \cdot \frac{v}{h^2} \tag{3.15}$$

$$Dilatant\ Flows : S_f = \frac{24}{4} \cdot \frac{\mu_1}{\rho g} \cdot \frac{v^2}{h^3} \tag{3.16}$$

where μ_1 is the flow viscosity, ρ is the bulk density (kg/m^3), and h is the stage (m). *Takahashi* (1991), however, proposed that the friction slope can be calculated as:

$$S_f = \frac{v^2}{ghp^2} \tag{3.17}$$

where:

$$p = \frac{1}{\kappa} \left[ln \left(\frac{1 + \sqrt{1 + \chi}}{H + \sqrt{H^2 + \chi}} \right) - \sqrt{1 + \chi} + \sqrt{\chi} \right] \tag{3.18}$$

and:

$$\chi = \lambda^2 \cdot \frac{0.02}{\kappa^2} \cdot \frac{\sigma}{\rho} \cdot \left(\frac{d}{h} \right)^2 \tag{3.19}$$

where κ is the Karman constant[4], $H = k/30h$ for a rough bed, λ is the linear concentration of sediment, and d is the median particle diameter (m). The linear concentration, λ, can be described by $[c\star/c)^{1/3} - 1]^{-1}$, where $c\star$ is the maximum packed sediment concentration and c is the sediment concentration by volume.

O'Brien (1999) also proposed modifications to the friction slope term, but used a different approach where the term is described as the sum of three slopes; that is, the turbulent dispersive, viscous, and yield slopes:

$$S_f = \frac{n_{td}^2 v^2}{h^{4/3}} + \frac{K\eta v}{8\rho h^2} + \frac{\tau_y}{\rho h} \tag{3.20}$$

where n_{td} and K are resistance parameters, η is the viscosity, and the other parameters are defined as above. The sum of the turbulent and dispersive shear stresses define the inertial flow regime for a mud flow, while the sum of the viscous and yield stresses define the total shear stress of a cohesive mudflow within a viscous flow regime. The equation is solved as a quadratic to find the velocity, v, based on parameter values either estimated or empirically-derived. With any given flow event, however, it may be very hard to estimate these values with any degree of accuracy.

3.3.1.2 Velocity-stage relationships

The above friction slope terms can be used in conjunction with the kinematic momentum equation to provide a relation between velocity and stage that is dependent upon which term is used. When a Manning- or Chezy-type formula is chosen, the form of this law can be described as:

$$v = \alpha(x) \cdot R^k \tag{3.21}$$

[4]The Karman constant is a dimensionless constant that describes the logarithmic velocity profile of a turbulent fluid flow near a boundary with a no-slip condition. Mathematically, it is defined as:

$$\kappa = \frac{u_\star}{u} \cdot ln\left(\frac{z}{z_0}\right)$$

where u is the mean flow velocity at a height z above the boundary, while roughness height z_0 is the height at which u appears to go to zero. $u_\star$ is the friction velocity and is dependant upon the shear stress τ_w at the boundary of the flow and the fluid density ρ of the flow itself by:

$$u_\star = \sqrt{\frac{\tau_w}{\rho}}$$

The Karman constant has a typical value of 0.40 ± 0.01 (e.g., *Zargola and Smits* (1998); *Österlund et al.* (2000)).

where $\alpha(x)$ incorporates factors that integrate channel slope, shape, and roughness, and k is a constant (e.g., *Chow* (1988)). The Chezy- or Manning's n coefficient used to describe $\alpha(x)$ (in the form of $\alpha(x) = Slope^{1/2}/n$) have values either empirically-derived for the particular channel in question, or are obtained at a time during flow where v and h are known. *Chow* (1988) gives typical values of Manning's n that lie within the range of 0.03 - 0.1 for natural open-channel flows that, respectively, range from channels of clean, straight streams through to channels with heavy brush and timber. In theory, the coefficient will change with changing water level due to the effects of bed roughness at low water levels and channel-side vegetation interactions at high water levels. In practice, however, the coefficient is assumed to be constant at any given site. In regard to lahar waves, the value of the coefficient can radically change as it is a proxy for the dissipation of energy by sediment entrainment and boulder movements.

The constant k used in Equation 3.21 is representative of the relationship between the flow and its hydraulic radius, and therefore the stage. This relationship is likely to be highly dependent on the volume and type of sediment that is entrained. As with the Manning's n coefficient, the value of the exponent k is considered to be constant for each lahar and, as such, is independent upon the location of flow within a channel. The experimental data derived by *Chow* (1959) provided a Manning value of 2/3. It should be noted that this value was derived from the study of water floods and not from those of lahars; however, with no alternative data provided from studies of these latter flow types, this value has been adopted by many using Manning's n despite the differing conditions between them (e.g., *Caruso and Pareschi* (1993)). Other values have been used in some studies, but are based on similar arguments, such as the value of 0.5 used by *Fagents and Baloga* (2005). The assumption that standard values can be used may not, in many cases, be reasonable, because flow behaviour and conditions greatly differ in high sediment concentrated lahar flows from those of water floods. The studies of *Vignaux and Weir* (1990) utilise the results of kinematic theory combined with data from observations of lahars at Mt Ruapehu in 1969, 1971, 1975, and 1977, in order to determine a value of exponent k. The results of this study suggest k values of 0.23 - 0.47. These values, however, were determined using stage records that were used to calculate discharges via a formulaic or empirical method; as such, it is perhaps uncertain as to actually how much new information was gained (H.K. McMillan, pers.

comm. 2007)

For flows where higher sediment concentration exist, the particle-particle contacts are very important, and a more complex form of the velocity-stage relationship is needed to model the flows. The relationships suggested by *Macedonio and Pareschi* (1992), as described in Equations 3.15 and 3.16, may provide a possible answer. Quantification of the degree of viscosity or dilatency of a hyperconcentrated flow, however, is notoriously difficult, and direct measurement *a priori* is often not possible. A modification of Manning's n coefficient is suggested by *O'Brien* (1999) as an alternative, and incorporates a dependency upon the concentration of sediment within the flow:

$$n_{td} = nbe^{mC_v} \tag{3.22}$$

where b and m are coefficients with suggested values of 0.0538 and 6.0896, respectively, and C_v is the sediment concentration.

3.3.1.3 Forms of velocity law

The above assumptions made of the kinematic wave theory allow for a simplification of the lahar wave recorded at Mt Ruapehu in March 2007. The decision was made to retain the use of, and the form of, the $\alpha(x)$ term as described in Equation 3.12 due to the wide use and understanding of the Manning Formula, and its related coefficients. The equation does assume prior knowledge of the channel characteristics, roughness, and hydraulic radius, and, as such, variable cross-sections of the channel are allowed for. The following relation, therefore, is both the simplest and the one to be tested here:

$$v = \frac{S^{1/2}}{n} \cdot R^k \tag{3.23}$$

where v is the velocity (m/s), S is the channel slope, and R is the hydraulic radius (m) (e.g., *Chow* (1988)). Calibration is required for two parameters: the Manning coefficient, n, ($\mathrm{m}^{-1/3}$ s), and the exponent k. These parameters can be found using a least-squares regression technique using the equation below, and tested according to the interpretation of the physical characteristics and its predictive ability.

$$log(v) = log\left(\frac{S^{1/2}}{n}\right) + k \cdot log(R) = k_n + k_1 \cdot log(R) \tag{3.24}$$

where k_n and k_1 are exponents. It is, however, probably necessary to include a dependency upon the sediment concentration, without which Equation 3.23 would be

unlikely to satisfactorily describe the relationship between stage height and velocity of flow. To incorporate this, two further relationships will be tested, based on the works of *Macedonio and Pareschi* (1992) and *O'Brien* (1999). The first relationship is based on the formers' work and can be described as follows:

$$v = \frac{S^{1/2}}{n} \cdot C_v^{k_1} R^{k_2} \tag{3.25}$$

where the dependence on the volume of sediment concentration (C_v) is expressed in a more generic form. This, therefore, leads to the linear relationship:

$$log(v) = k_n + k_2 \cdot log(C_v) + k_1 \cdot log(R) \tag{3.26}$$

where k_n, k_2, and k_1 are exponents. The second relationship tested is based the work of *O'Brien* (1999) and utilises the sediment concentration dependency described in Equation 3.22. Yield slope and viscosity slope terms are ignored as typical concentrations of Mt Ruapehu lahars would mean their values have both a relatively negligible effect and would be directly unobtainable. The velocity law can therefore be defined as:

$$v = \frac{S^{1/2}}{n \cdot e^{\alpha C_v}} \cdot R^k \tag{3.27}$$

which, in turn, provides the relationship:

$$log(v) = k_n + k_2 \cdot C_v + k_1 \cdot log(R) \tag{3.28}$$

3.3.2 Application to the Mt Ruapehu breakout lahar of 18$^{\text{th}}$ March 2007

3.3.2.1 Observations of the Colliers bridge field site

The three forms of the stage-velocity relationship as described above are tested at the Colliers bridge site (as shown in Figure 1.2) where the most comprehensive dataset of the 18$^{\text{th}}$ March breakout lahar was recorded. This site included observations and video footage (as described in Table 1.1) made throughout the lahar passage that allowed for greater constraints of stage, velocity, and discharge measurements.

The peak discharge at Colliers bridge was calculated at 673 m^3/s using the video-measured velocity from PIV analyses, a multiplication factor of 0.75 ± 0.1 to obtain an average body velocity, and cross-sectional area surveys of the channel (Section 3.2.1).

By comparison, at a site c. 2 km downstream, it was calculated at 738 m^3/s using the super-elevation method, which is in good correlation considering the field constraints. The arrival time of the lahar frontal wave produced an average velocity of 4.87 m/s. The observed peak velocity, however, was calculated from PIV analyses as 6.76 m/s. It should be noted, however, that these velocities are not directly comparable.

3.3.2.2 Method 1: Manning Formula

The stage-velocity law as described in Equation 3.24 is based on the Manning Formula; if this is used, we must assume a simple relationship between stage and velocity. To test the validity of this assumption, the variables can be simply plotted against each other. The records were gained through analysis of video footage taken at two nearby but distinct locations. In each location, the video camera was set up to focus on fixed points in the centre of the flow, while allowing for the full channel width to still be in frame. This ensured that not only could PIV analyses be made to obtain flow velocity but also flow height (stage) could be approximated against the channel sides. Since it is not possible to directly compare the stage values between sites, these approximations were used in conjunction with post-lahar GPS site surveys to provide flow cross-sectional area measurements for points throughout the flow. The results of this comparison are plotted in Figure 3.5, and clearly illustrate a more complex relationship. The velocity of the flow initially increases with cross-sectional area, but then is significantly depressed during the falling limb of flow while cross-sectional area still remains relatively high. Using an average relationship would lead to under-estimations of velocity on the rising limb of the flow and over-estimations on the waning limb. The velocity must, therefore, incorporate a dependency upon another factor of the flow, such as sediment concentration.

3.3.2.3 Method 2: Power Law Formula using hydraulic radius and sediment concentration

As is well illustrated in the recordings of the video footage and observations, the surface turbulence of the lahar was increasingly dampened with rising levels of sediment concentration. The greater the degree of damping of the turbulence, the smoother the surface of the flow becomes, and the more the velocity drops. It is, therefore, logical to

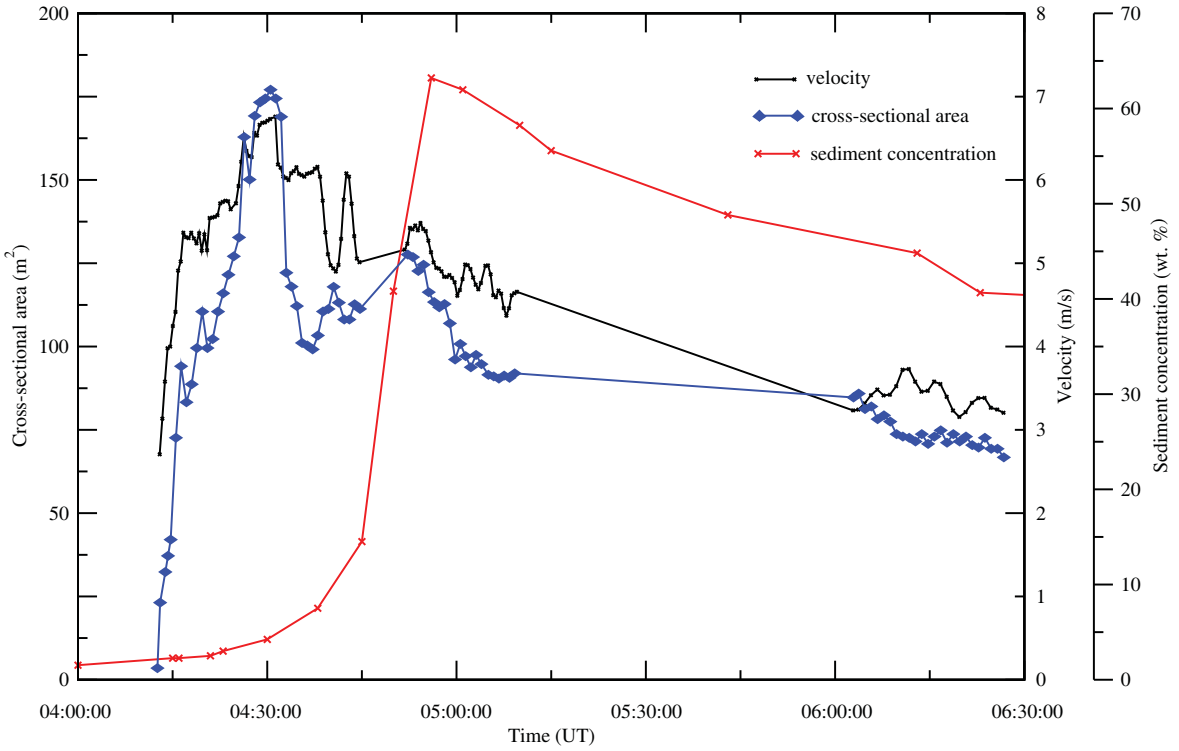

Figure 3.5: *Cross-sectional area, velocity, and sediment concentration profiles recorded at the Colliers bridge monitoring site.*

assume a link between the velocity, stage, and sediment concentration. A model that reflects this is required. Using the regression of Equation 3.26 (page 73), the coefficients of k_1, k_2, and k_3 can be obtained (Table 3.3; H.K. McMillan, pers. comm. 2007).

k_1	k_2	k_3
0.55	-0.18	1.10

Table 3.3: *Regression coefficients for Method 2 Power Law Relationship.*

The power law relationship has an R correlation coefficient value of 0.96, indicating a good correlation between recorded (real) and predicted values of velocity (Figure 3.6). It should be noted, however, that the use of the power law relationship methodology (Equation 3.25) is not valid when zero sediment is contained within a flow. Additionally, very low amounts of sediment produce anomalously highly negative values for the term. In order to avoid this problem, the term was set to zero when sediment concentrations were low (that is, less than 1%).

Using the power law relationship of Equation 3.25, we then find that:

$$v = \frac{0.0178^{1/2}}{0.12} \cdot C_v^{-0.18} R^{0.55} \tag{3.29}$$

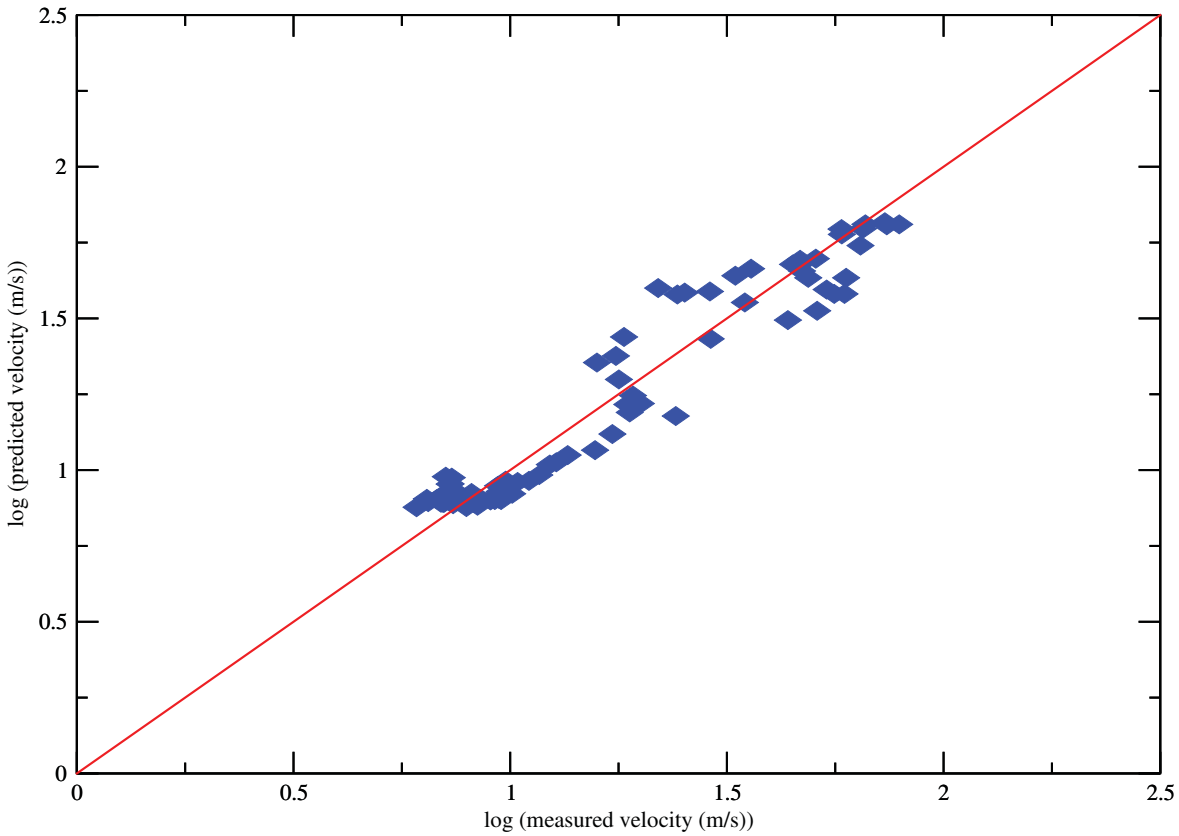

Figure 3.6: *Predicted velocity estimates made using measurements of the hydraulic radius and sediment concentration combined within a power law formula. Best-fit line is also shown. Courtesy of H.K. McMillan.*

where 0.0178 is the average water surface slope at Colliers bridge and 0.12 is the calculated Manning's n value (Equation 3.13). Ordinarily, when applied to the standard Manning's equation for pure water flow, a value of n this high would only result from channels where trees, brush, or debris line and obstruct the banks or floodplains. In the case of Colliers bridge, the high n value is likely to be a response to the different rheologies inherent in a lahar and a weaker force from the hydraulic radius (exponent of 0.55 as opposed to 0.67).

3.3.2.4 Method 3: Combined power law and exponential formula using hydraulic radius and sediment concentration

This method requires the use of Equation 3.27 (page 73). The coefficients of k_1, k_2, and k_3 are obtained by the regression using the formula in Equation 3.28 and are presented in Table 3.4 (H.K. McMillan, pers. comm. 2007).

Similarly to method 2, the regression coefficients are used to predict flow velocities

k_1	k_2	k_3
0.71	-0.017	0.90

Table 3.4: *Regression coefficients for Method 3 Power Law and Exponential Relationship.*

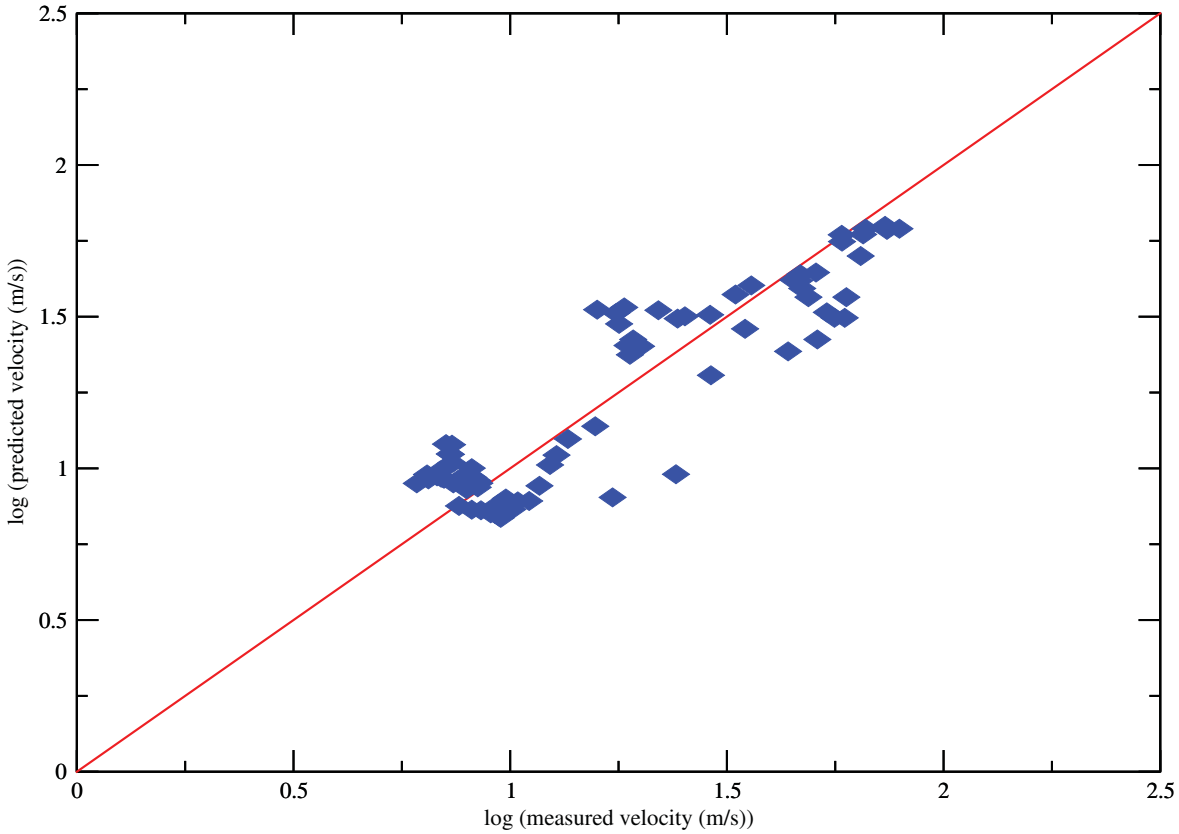

Figure 3.7: *Predicted velocity estimates made using measurements of the hydraulic radius and sediment concentration used within a combined exponential and power law formula. Best-fit line is also shown. Courtesy of H.K. McMillan.*

with the use of Equation 3.27 that are then tested with the R coefficient of determination. This determination produces a reduced value of R of 0.91 (compared with 0.96 for method 2), illustrating the combined power law and exponential formula using hydraulic radius and sediment concentration is a less accurate method for the prediction of velocities (Figure 3.7).

3.3.3 Determination of sediment concentration proxy

The results detailed above suggest that information about the changes in sediment concentration throughout the lahar is necessary for good predictions of the velocity of flow. This may be difficult in real-world situations. An alternative method for

gathering approximate sediment concentrations is needed. Data collected during this study allow for an investigation into the use of seismic recordings as a proxy for sediment concentration.

As detailed in Section 3.2, the comparison of the seismic records of an event and its recorded discharge and volume can lead to good correlations between measured ground vibrations and flow size. They are, however, dependent upon the similarity of source areas, materials, and descent paths. The comparison of a flow recorded at different sites along a channel is more complicated because of both the evolution of the flow, due to entrainment, deposition, and mixing of material, and the effects of localised site-specific characteristics. The seismic signals associated with the Ruapehu 2007 lahar recorded at Colliers bridge show distinct variations in ground-vibrational amplitudes that broadly correlate with a series of phases within the bulk flow associated with variations in stage, velocity, and sediment concentration. These variations will be examined in greater detail in Chapter 5. It is not necessary to evaluate every fluctuation in a signal record. Instead, it is more useful to quantify the relative change in signal intensity with time as a flow passes a sensor. To this end, the Real-time Seismic Amplitude Measurement method was used (RSAM; *Endo and Murray* (1991)).

The Real-time Seismic Amplitude Measurement (RSAM) method was initially developed by the USGS in order to characterise the seismic activity during periods of heightened volcanic activity (e.g., *Endo and Murray* (1991)). During these periods, it is often difficult to differentiate individual seismic events. By using the RSAM method, known locations and magnitudes of earthquakes and tremor are not required. The measurements are calculated in real-time using the average seismic signal amplitudes. As the amplitude, rate of occurrence, or size of the events increases, so too do the values of the RSAM. Traditionally, the RSAM is calculated over a consecutive 10-minute average interval and provides a simplified measure of seismic activity proportional to the absolute voltage output, representing amplitude and ground velocity. Adaptations were made to this existing methodology for use in this study. The RSAMs herein are calculated over consecutive 10-second intervals.

From the RSAM profiles of the signal recorded at Colliers bridge, it can be seen that the relative change in signal intensity over time drops dramatically during the waning limb of the lahar. In contrast, stage, velocity, and hence discharge levels remain

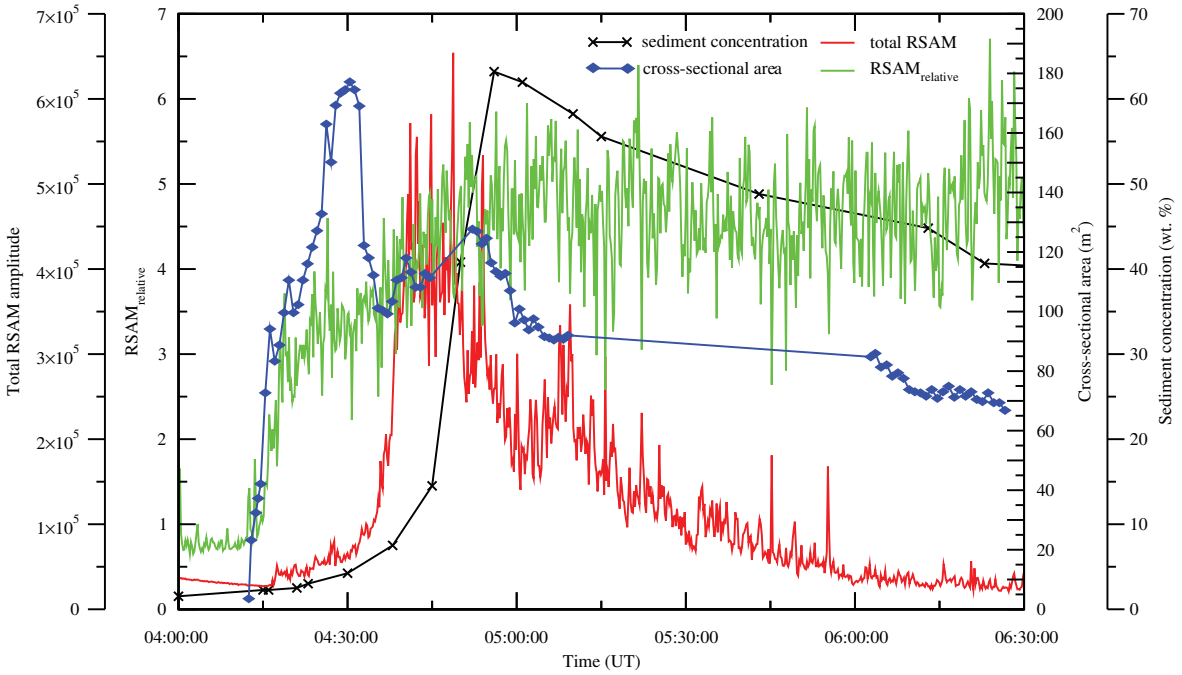

Figure 3.8: *Comparison of cross-sectional area and sediment concentration of the March 2007 Ruapehu breakout lahar recorded at Colliers bridge with RSAM profiles used to determine the relative change in signal intensity over time. Total RSAM profile calculated as RSAM over all frequency ranges, while $RSAM_{relative}$ is calculated as the ratio of RSAMs of the 40-49.5 Hz and 2.5-10 Hz bands (as defined in Equation 3.30).*

elevated for several hours (Figure 3.8). It is suggested that the decrease in the RSAM profile results from the increased dampening of turbulence associated with increased sediment concentration within the flow. Comparisons between RSAMs calculated over different frequency bands, however, indicate that only some of the frequencies recorded are affected in such a way. Many instead show a localised increase with the rising sediment concentration (Figure 3.9). From this, it is proposed that, as suspended-sediment concentration increases within a flow, there is a corresponding increase in the higher frequency fraction that is absent in the lower frequency ranges. This is supported by observations made by other studies where high frequency signals appear associated with particle collisions such as *Huang et al.* (2007) and *Okuda et al.* (1979). A simple descriptor is hence defined to relate the suspended-sediment concentration with relative change in seismic energy based upon bands of highest and lowest frequencies as recorded by the sensor and displayed in Figure 3.9. It is defined as follows:

$$RSAM_{relative} = \frac{RSAM(40 - 49\ Hz\ band)}{RSAM(2.5 - 10\ Hz\ band)} \tag{3.30}$$

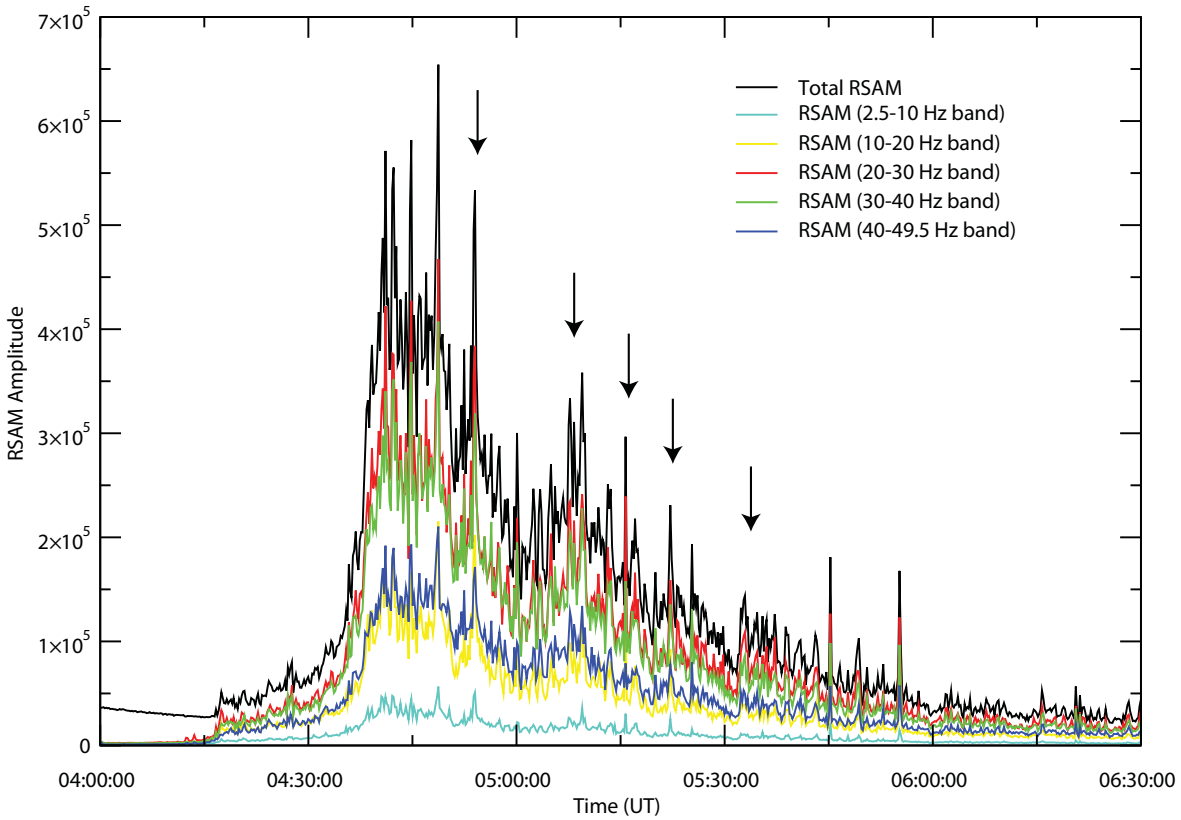

Figure 3.9: *Comparison of RSAM profiles calculated from different frequency bands of the seismic record from the March 2007 Ruapehu breakout lahar recorded at Colliers bridge. Arrows denote times of localised increase on RSAM profiles associated with rising sediment concentration within the flow.*

As before, both power law and combined power law / exponential relationships, as defined in Equations 3.26 and 3.28, were considered. The higher correlation coefficient of determination resulting from the use of the combined relationship defined in Equation 3.31 illustrated that this was a better predictor for flow velocity (R=0.94 vs R=0.84).

$$log(v) = k_3 + k_2 \cdot RSAM_{relative} + k_1 \cdot log(R) \tag{3.31}$$

The regression coefficients for this relationship are defined in Table 3.5:

k_1	k_2	k_3
0.53	-0.24	1.82

Table 3.5: *Regression coefficients for seismic method power law and exponential relationship.*

When sediment concentration is used, the predictive capability of this relationship decreases (Figure 3.10). It is, however, still considered an adequate method and it

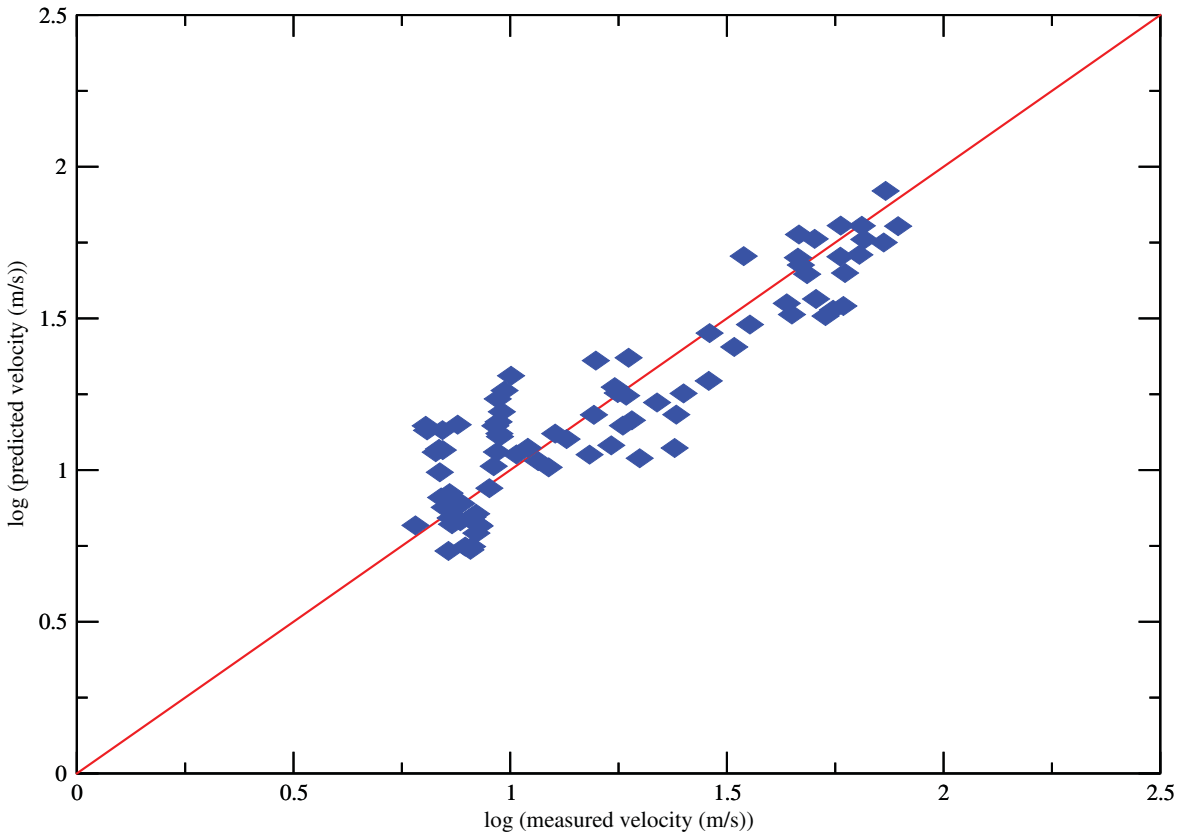

Figure 3.10: *Velocity prediction from hydraulic radius and $RSAM_{relative}$, using the combined exponential and power law formula as defined in Equation 3.31.*

suggests that it may be possible to use the relative change in seismic energy during a flow as a proxy for sediment concentration when applied to velocity predictions.

3.3.4 Trial use of sediment concentration proxy at an unmanned site

The sediment-concentration-proxy method was applied to estimate the sediment concentration at the Round-the-Mountain-Track (RTMT) using the seismic signals of the March 2007 lahar recorded there. During this flow, this site was inaccessible. No record of the sediment concentration or flow velocity profiles exist. By using the initial arrival times of the flow recorded on geophones at Tukino Skifield, c. 2.2 km upstream of the RTMT site, and on the seismometer at the RTMT, an average frontal velocity of the lahar is calculated as 9.25 m/s. This is important for calibrating the "Manning's n" parameter, and providing a scaling for the estimated velocity record.

As is stated in Chapter 1.5.1, this site had detailed stage and seismic records of the

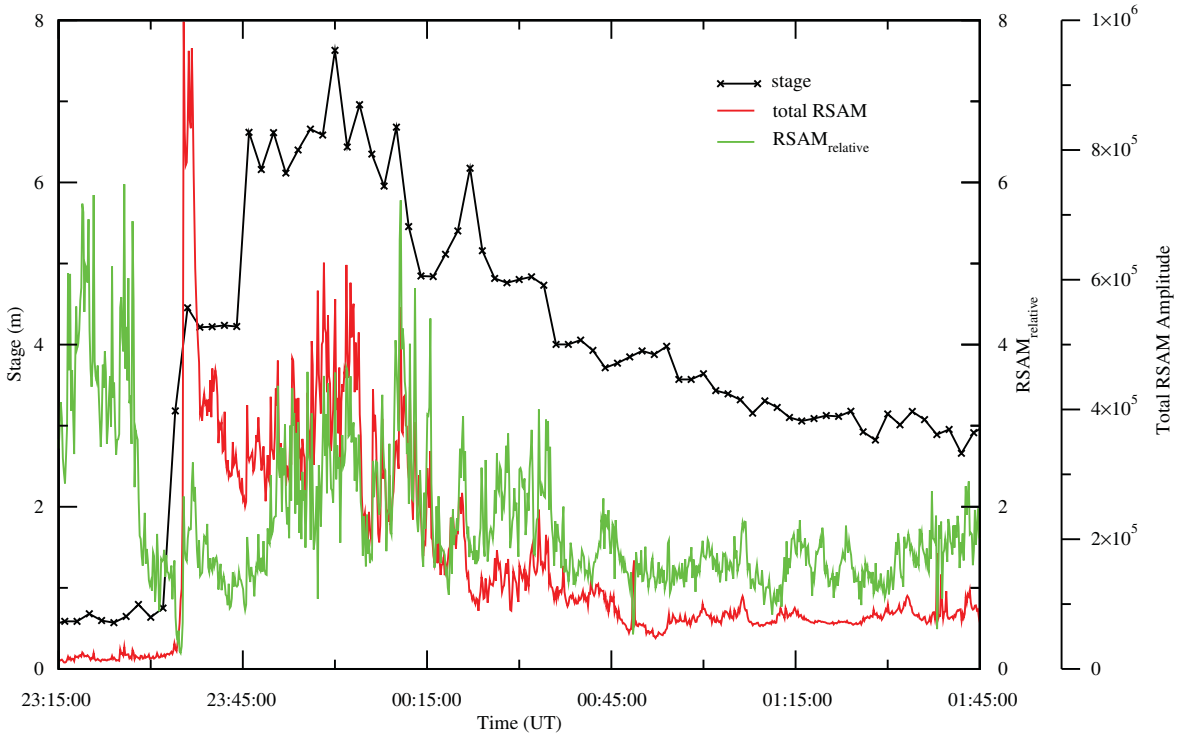

Figure 3.11: *Recorded data streams at the RTMT site for the March 2007 Crater Lake-breakout lahar.*

event (Figure 3.11). Issues regarding rapid changes in stage height not being recorded by the stage gauge sensor (see Chapter 2.3.1) meant that a more complete and reliable record of the stage profile was made using a pore pressure sensor at the same site. Figure 3.11 also shows the $RSAM_{relative}$ profile as defined by the ratio of frequency bands in Equation 3.30 used as the proxy for sediment concentration. The small peak in this variable observed at the time of the frontal arrival at the site may indicate a weak bouldery-front to the lahar. The main peak of the $RSAM_{relative}$ profile lags the flow front by c. 40 minutes, suggesting a relatively dilute frontal phase while sediment concentration is confined to the later portion of the flow. As observations were not possible at this site, a comprehensive explanation for this phenomenon is not known. It is possible that it can be explained by the incorporation of snow and ice melt within the frontal phase of the lahar as it flowed over the glacier- and snowfall-covered upper reaches of the channel, before exposure of the underlying sediment made it available for entrainment.

The stage and $RSAM_{relative}$ profiles recorded at the RTMT site were substituted into the respective parameters defined in Equation 3.31. The resulting velocity profile

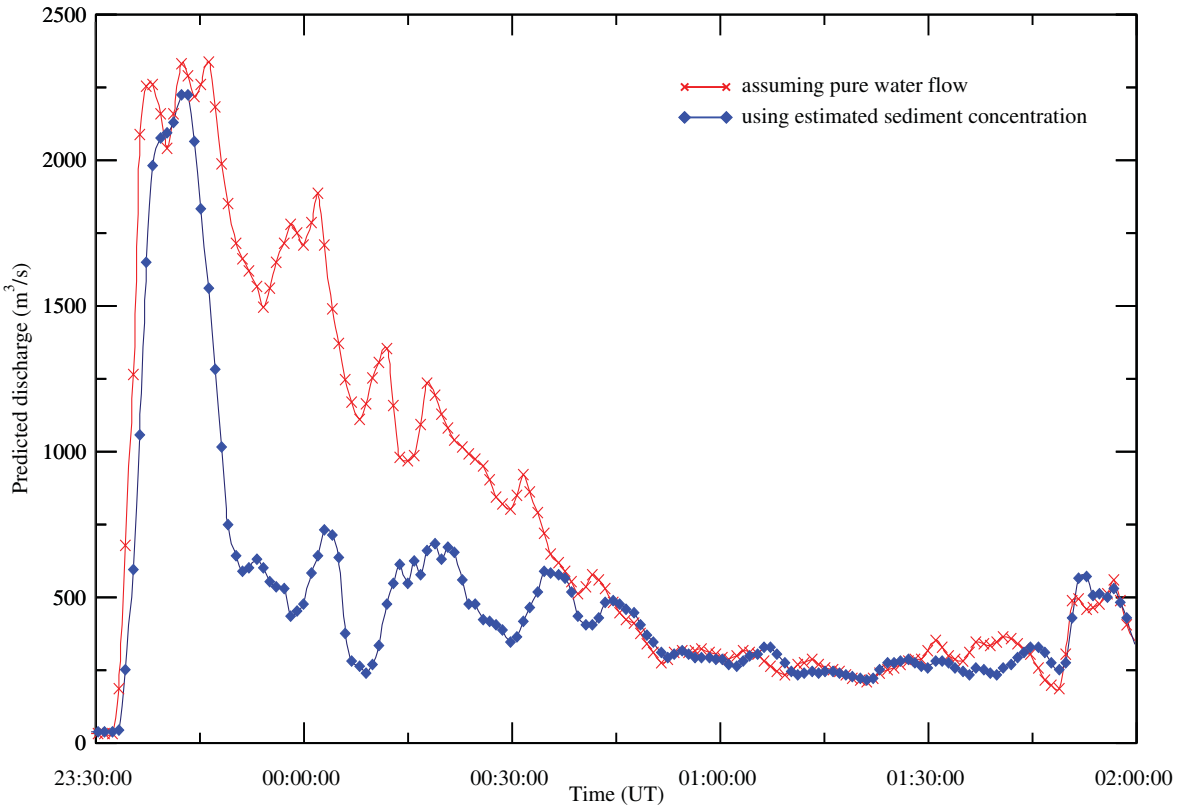

Figure 3.12: *Predicted discharge profiles at the RTMT site for the March 2007 Crater Lake-breakout lahar. Courtesy of H.K. McMillan.*

was then scaled using the average frontal velocity of the flow defined above in order to compensate for differing channel properties, such as shape and roughness. As this velocity profile is assumed to relate to the average channel cross-sectional area in the channel reach, it is then adjusted by the ratio of this area to that of the instrumentation site (H.K. McMillan, pers. comm. 2007). The discharge profile can then be calculated and is shown in Figure 3.12.

The discharge profile shown in Figure 3.12 shows a steep frontal phase, sustained for a short while (c. 10 minutes), and followed by a long drawn-out body and tail of much lower discharge, typical of a sudden release and more-extended draining of water from a dam. To check the validity of the profile values, however, it is necessary to calculate the approximate volume that would be resultant from such discharge values. This results in a volume of c. 3.28×10^6 m^3. As the volume of water originally lost from the Crater Lake was calculated to be c. 1.3×10^6 m^3, the volume calculated at the RTMT would suggest a bulking factor of 2.5. In comparison, the discharge profile formed from analyses using the standard Manning's formula (also presented in Figure

3.12; H.K. McMillan, pers. comm. 2007) gives a total volume for the bulk of flow at the RTMT site of c. 5.91×10^6 m^3. This would represent a bulking factor of 4.5, suggesting a sediment concentration of $\geq 70\%$. From the records at the site, the likely-erodable material available for bulking (mainly snow and ice, with some underlying sediment), and post-event surveys, this is not considered a realistic value. Comparative analysis of pre- and post-event aerial LiDAR surveys suggest entrainment of up to 3×10^6 m^3 of boulder-rich, gravelly sand, giving a bulking factor of 3.3 (*Procter et al.* (2010)). From this, it can be concluded that, while standard Manning's-formula analyses overestimate lahar volumes, the sediment-concentration-proxy method using seismic records is likely to slightly underestimate the total volume of a flow.

3.4 Conclusion

It is widely acknowledged that lahars and other mass flows can pose a serious threat to the infrastructure and populations which reside near river catchments on a volcano. As many communities live alongside lahar-prone channels at volcanoes all over the world, mitigation of the risks of such phenomena is necessary. Such mitigation requires not only a knowledge of any approaching danger, but also a quantifiable sense of the size and extent of the threat it poses. Lahars range in size from very small rain-triggered flows that occur seasonally, through to much larger, and more destructive, eruption- or breakout-triggered events. Simulations and models do exist to provide estimates of the likely volumes and inundation areas that might be affected. They are, however, limited by relatively simple assumptions of flow dynamics, sediment interactions and associated effects, and the availability of both fluid and sediment for incorporation into a flow. In addition, validation of a model requires syn-event observations, measurements, and post-depositional surveys. Often this is unrealistic; most lahars are not scientifically observed and, when they are, direct measurements are often hindered by the destructive nature of the flow itself. It would therefore be preferable to find a method of determining the volume and sediment content of a lahar without the necessity of direct contact with, or observation of, the flow. Many lahar warning systems are based upon the use of seismic sensors that do not require direct contact with a flow. Investigation into seismic records of both multiple lahars at a

single site and a single lahar at multiple sites have shown that these type of sensors have the potential to be of use as a proxy for characteristics of a flow.

The seismic records of multiple lahars recorded at a single site at Mt. Semeru, Indonesia, were analysed in combination with video records and sediment concentration samples. This allowed for a comparative study of the volume of the lahars with their associated seismic energies and ground-vibrational amplitudes. From this, a strong correlation between the seismic record and volume of a flow was determined. Analyses of this relationship provided a proxy for calculating a reasonable volume for several lahars recorded seismically, but not sampled, in previous years. The correlation between the volume of a flow and its resulting ground vibrations was further explored with regards to the often-seen pulses, or packets, that can occur during the passage of a flow following the assumption that the same relationship between total volume and cumulative seismic amplitude, or energy, applies to each packet. The analysis proved that this proxy method, while limited to similar flows recorded at the same site, can provide reasonable estimates for a lahar volume.

Models that predict the discharge and volumes of phenomena such as floods at multiple sites along a channel use traditional volume proxies based upon kinematic wave theory. Due to their complex interactions with sediment particles, however, lahar flows have markedly different rheologies than Newtonian streamflows. As such, the kinematic wave equations must be modified to take this into account. In order to best calculate the volume of a lahar at a site using only its seismic record and a comparative record of the same flow at a different site, it is necessary to quantify the relative changes in signal intensity as the flow passes each site. To this end, the Real-time Seismic Amplitude Measurement (RSAM) method was utilised as an indication of the changing concentrations of sediment within the flow. Analyses of different frequencies excited by a lahar suggest that higher frequencies increase in intensity corresponding to increases in suspended-sediment concentrations. By using a simple ratio descriptor between high and low frequency ranges as a proxy for the relative concentrations of suspended sediment in combination with modified kinematic wave equations and adjustments made to account for differing channel properties between sites, a discharge profile can then be calculated. Comparisons between the volumes calculated via this methodology with pre- and post-LiDAR data suggest that it is likely to underestimate the total

volume of a lahar. While this method does show great potential, it is dependent upon highly simplified assumptions regarding the frequencies excited by suspended sediment loads and their particle interactions. In addition, the reliability of the $\text{RSAM}_{relative}$ proxy using highest and lowest frequency bands is subject to variation due to changes within the seismic frequency distribution of a lahar, both within a flow and between sites, and may not therefore be the best representation for a flow volume proxy. In order to further develop a more robust sediment concentration proxy based on the seismic record of a lahar, greater understanding of the role of sediment particle interactions within a flow are necessary to quantify the complex relationship between discharge, concentration, and the ground vibrational response to its passage.

Chapter 4

Differential 3-dimensional seismic excitation of lahars

Chapter 4 investigates the 3-dimensional excitation of three types of lahar: snow-slurry flow, hyperconcentrated streamflow, and granular debris flow. From this, estimations can be made of the frontal velocity, internal dynamics, and channel interactions of a flow.

4.1 Introduction

As discussed in previous chapters, the seismic records of lahars can be instrumental not only in the detection of such flows, but also in the estimation of their frontal velocities, internal property variations, and channel interactions. Analyses of the variable intensities of the 3-dimensional excitations produced by a lahar should reflect differences in the fundamental characteristics of that flow. Water content, sediment concentration, and particle-particle and particle-substrate interactions all influence the resultant ground vibrations. Correct interpretation of these phenomena will provide invaluable information that can be used to increase the effectiveness of warning systems.

The first part of this chapter consists of the manuscript "Seismic signals of snow-slurry lahars in motion: 25 September 2007, Mt Ruapehu, New Zealand", by: Susan E. Cole, Shane J. Cronin, Steven Sherburn, and Vern Manville, published within Geophysical Research Letters (Vol. 36; L09405; doi: 10.1029/2009GL038030). This manuscript presents an analysis of three snow-slurry lahars recorded during the September 2007 eruption of Mt Ruapehu, New Zealand, and compares them to the record of the water-

dominated, Crater Lake-breakout flow of March 2007 at the same site. Comparisons are made between both the sizes of flow and the signal strength of each seismic record. The results illustrate the importance of distinguishing the type of lahar recorded before simple interpolations of size are concluded from direct examination of signal strength. By using the 3-dimensional seismic excitation record, the dominant rheology and gross physical composition of a flow can be distinguished, providing a more complete assessment of the nature and degree of hazard posed.

The contributions of each author to the study were as follows:
Susan E. Cole: Principal Investigator: Carried out:

- Data collection
- Analysis of seismic data
- Seismological interpretation
- Manuscript preparation and writing

Shane J. Cronin: Chief Advisor: Aided the study by:

- Assistance in data collection
- Discussion of data and interpretation
- Editing and discussion of manuscript

Steven Sherburn: Co-advisor: Aided the study by:

- Discussion of data and interpretation
- Editing and discussion of manuscript

Vern Manville: Aided the study by:

- Editing and discussion of manuscript

The rest of this chapter consists of more detailed investigation into the usefulness and variability in the results of analyses of 3-dimensional seismic records of lahars. In Section 4.3, the necessity for multiple recording sites to calculate frontal velocities of a flow is challenged. By using a series of closely-spaced bends, it is possible to estimate

a [relatively] accurate velocity for the front of a mass flow. The final section of this chapter (Section 4.4) provides a comparison of the 3-dimensional seismic signals of a hyperconcentrated streamflow and a granular debris flow, as recorded at the Indonesian volcanoes of Mt. Semeru and Mt. Merapi, respectively. The internal dynamics and particle interactions within the two flow regimes produce distinctly different results in the seismic records.

4.2 Seismic signals of snow-slurry lahars in motion: 25 September 2007, Mt Ruapehu, New Zealand

Susan E. Cole[1], Shane J. Cronin[1], Steven Sherburn[2], Vern Manville[2]

[1]Volcanic Risk Solutions, Institute of Natural Resources, Massey University, Private Bag 11-222, Palmerston North, New Zealand

[2]GNS Science, Wairakei Research Centre, Private Bag 2000, Taupo, New Zealand

4.2.1 Abstract

Detection of ground shaking forms the basis of many lahar-warning systems. Seismic records of two lahar types at Ruapehu, New Zealand, in 2007 are used to examine their nature and internal dynamics. Upstream detection of a flow depends upon flow type and coupling with the ground. 3-D characteristics of seismic signals can be used to distinguish the dominant rheology and gross physical composition. Water-rich hyperconcentrated flows are turbulent; common inter-particle and particle-substrate collisions engender higher energy in cross-channel vibrations relative to channel-parallel. Plug-like snow-slurry lahars show greater energy in channel-parallel signals, due to lateral deposition insulating channel margins, and low turbulence. Direct comparison of flow size must account for flow rheology; a water-rich lahar will generate signals of greater amplitude than a similar-sized snow-slurry flow.

4.2.2 Introduction

Seismic or acoustic monitoring in catchments surrounding active volcanoes is used as the basis of lahar warning systems (e.g. Pinatubo, *Marcial et al.* (1996); Indonesia,

Lavigne et al. (2000b); Ruapehu, *Leonard et al.* (2008)) and for mass flow monitoring in other alpine areas (*Hurlimann et al.* (2003)). Geophones or seismometers are particularly useful because they can be placed outside the path of highly destructive/erosive flows, and can operate during multiple events (e.g. *Itakura et al.* (2005)). Acoustic Flow Monitor (AFM) systems are cheap, produce low data rates, and have low power needs. Broad-band seismometers are more expensive and have higher data rates, but enable better resolution of flow magnitude and understanding of internal flow properties.

Analyzing a wide range of seismic frequencies over several sites enables estimation of mass-flow frontal velocity, variations in internal flow properties, and interactions with the channel. Variations in signal intensity across 3-D should reflect fundamental differences in the water content as well as particle-particle and particle-substrate interactions between flows. In order to use this information effectively in warning systems, these features need to be interpreted.

Presented here is an analysis of seismic signals from snow-dominated flows that descended the slopes of Ruapehu Volcano, New Zealand, on 25 September 2007. These were generated by a small phreatic eruption that ejected water from Crater Lake (*Lube et al.* (2009)). Instrumentation installed along the Whangaehu River captured the eruption and passage of two snow-dominated lahars and a later water-rich hyperconcentrated flow. These data provide valuable insights into the physical and dynamic properties of snow-slurry lahars in relation to snow avalanches and other larger-scale lahars at this site (*Manville and Cronin* (2007)).

4.2.3 Geological setting and instrumentation details

Mt. Ruapehu (2797 m) is an andesitic stratovolcano in the central North Island of New Zealand (Figure 4.1). The acidic Crater Lake (9-10 $\times$ 10^6 m^3) typically covers an active vent at c. 2540 m a.s.l. (e.g. *Cronin et al.* (1996)). Crater Lake is surrounded by several glaciers, which have fed snow and ice into lahars generated by: eruptions through the lake in 1969, 1971, 1975, and 1995 (*Cronin et al.* (1996)), or by collapse of ice/tephra dams such as in 1953 and March 2007 (*Manville and Cronin* (2007)). The majority of these lahars occurred in the Whangaehu River catchment (Figure 4.1).

We installed a monitoring station alongside the Whangaehu River in 2006, c. 7.4 km downstream from the Crater Lake at the Round-the-Mountain-Track (RTMT; Figure

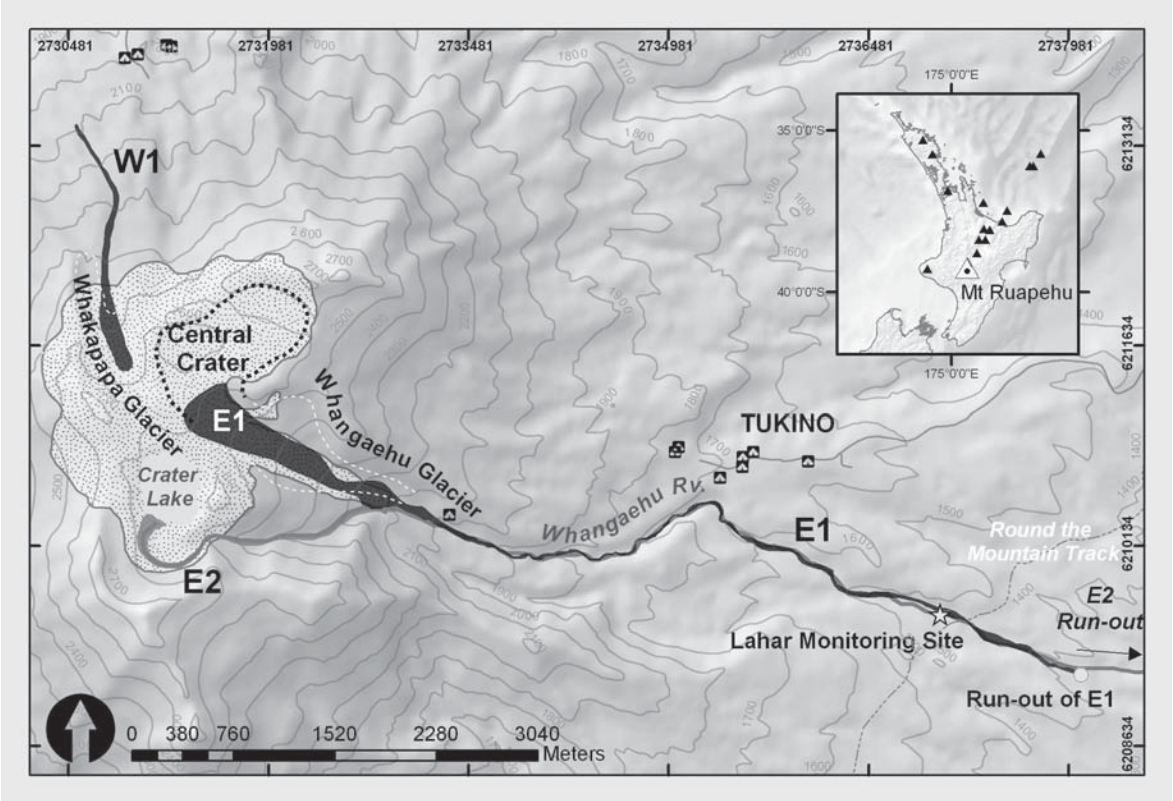

Figure 4.1: *Location of the monitoring site Round-the-Mountain-Track (RTMT) on Mt Ruapehu, showing Crater Lake, and the deposits of the snow-slurry lahars of 25th September 2007. Insert shows location of Mt. Ruapehu in the Central North Island, New Zealand, and locations of other Holocene volcanoes in the area (solid black triangles). Courtesy of J.N. Proctor.*

4.1). It consists of a 3-component broadband seismometer (Guralp-6TD), an AFM, and a radar water-level gauge (VEGAPULS), installed along the south bank of the channel on a lava bluff. The seismometer is buried 1 m into soil directly overlying coherent lava that extends beneath most of the main channel. This sensor is located c. 4 m from the channel edge and c. 20 m above the river bed. The broadband recorded data with a sample rate of 100 Hz. Other instruments recorded observations at 5 s intervals. The AFM and broadband seismograph successfully recorded the lahars, but the radar stage gauge reacted too slowly to the sudden change in flow level caused by the onset of the lahar fronts, and/or could not process reliable reflections from the highly irregular and "solid" surfaces of the snow-slurry lahars.

4.2.4 Eruption seismicity

The seismometer at the RTMT station recorded initial tremors associated with the eruption starting at 08:16 (UT). A single explosion which expelled jets of water, lake sediment, and rock debris was recorded at 08:26 (UT) by two microbarograph stations on the western slopes of the volcano (GeoNet, New Zealand). At the RTMT, the eruption explosion and jetting event is represented as a brief spike across all frequencies (Figure 4.2). At least four other low-frequency spikes were recorded, but none generated an associated air wave. It is unlikely that additional material was ejected from Crater Lake, as evidenced in the deposits (*Lube et al.* (2009)).

4.2.5 Lahar seismicity

Three lahars were generated from the single explosion at 08:26, two in the eastern Whangaehu catchment, and one in the north-western Whakapapa ski field area (Figure 4.1; *Lube et al.* (2009)). We consider only those lahars that traveled down the Whangaehu Channel past the RTMT. The first snow lahar (E1) was caused by run-off of explosively ejected Crater Lake water and c. 200,000-400,000 m^3 of entrained snow and ice from the Central Crater and Whangaehu Glacier, while the second (E2) was due to displacement of water over the lake outlet (*Lube et al.* (2009)). A third watery flood (E3) was recorded c. 1 hour after the eruption with no associated anomalous seismicity and thought to be related to further collapse and drainage from the upper-catchment ice-slurry deposits.

4.2.6 Flow velocity and range of detection

Analyses of seismic signal from the three lahars along the Whangaehu valley were made using total spectra and spectrogram profiles on all components (Figure 4.3). Time-series data clearly shows the approach and passage of the flows, but spectrogram profiles allow for easier detection of flow arrival at the site. Due to the unique frequency content of the signal, increases in frequencies and amplitudes can be seen earlier in the spectrogram than in the time series trace.

The spectral plots of the September lahars show a distinct triangular shape resulting from an increase in high frequency signal with time, as is also observed in seismic signals

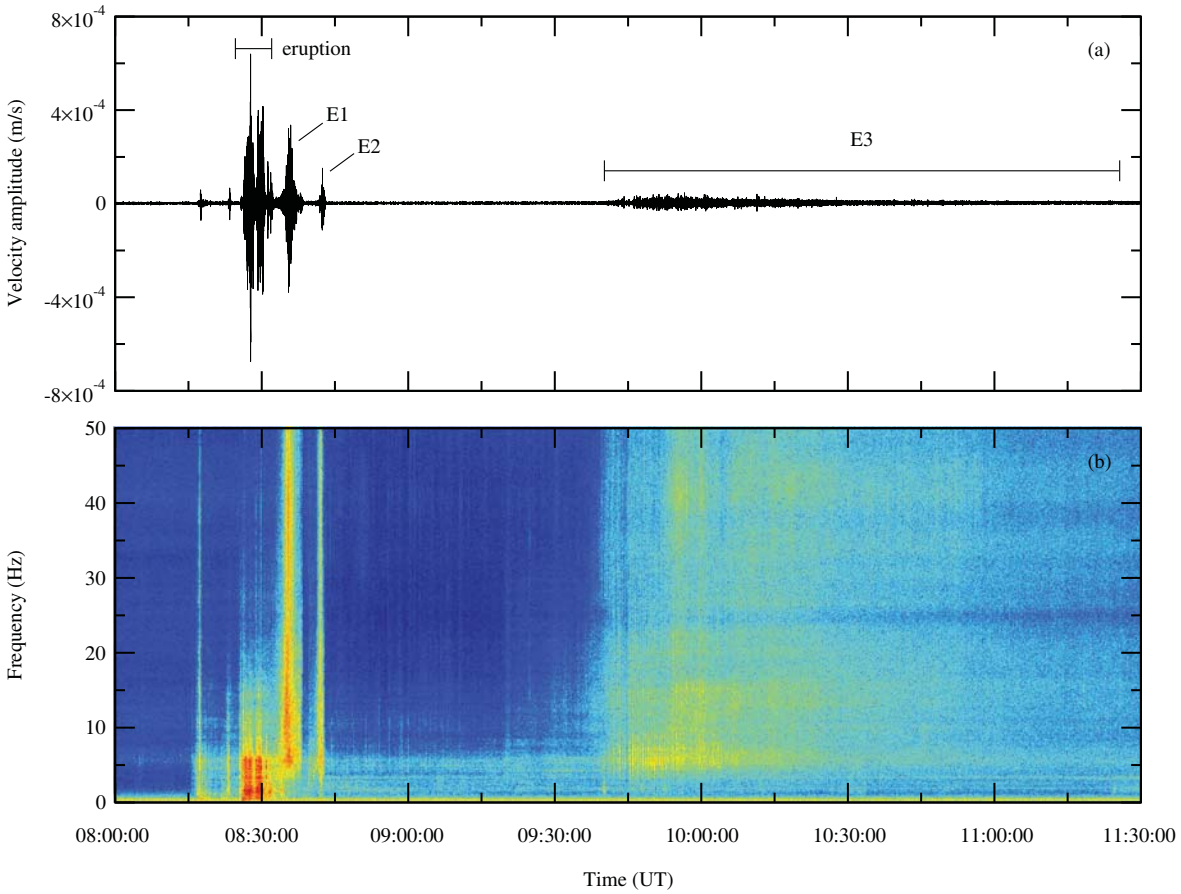

Figure 4.2: *(a) Seismogram (100 sps) showing recorded energy along the vertical component due to the eruption of 25th September 2007, related seismicity, and the subsequent 3 lahars that passed the monitoring site, RTMT. (b) Spectrogram with a 256-sample window and 50% overlap. Note absence of triangular shape of increasing high frequencies at start of eruption signal contrasting with those of the lahars.*

from snow avalanches (*Surinach et al.* (2005)). This shape contrasts with earthquake signals (e.g. *Surinach et al.* (2005)) and volcanic eruptions (e.g. Figure 4.2). We attribute the shape to either: a) anelastic attenuation of the propagation waves with distance, due to the more rapid attenuation of high frequencies compared to low (*Aki* (1980)), or b) increase in energy, due to the entrainment of sediment causing a rise in the signal amplitude (*Surinach et al.* (2005)). Since the E1 and E2 lahars had primarily entrained material in the upper reaches of their travel path, and deposit analyses indicate that they were not erosive in or near the instrumented reaches (*Lube et al.* (2009)), we conclude that the latter explanation has, at best, a minimal effect on the amplitude of the signal. The triangular shape most likely reflects the decreasing attenuation of the signal as the flow approaches the sensor. Conversely, an inverted

triangular shape seen in the spectrogram after a period of full frequency signal is attributed to the attenuation of signal as the flow-tail passed beyond the sensor. We therefore conclude that amplitude profiles are at their greatest when the flow directly passes the sensor (e.g. *Caplan-Auerbach et al.* (2004)). Accordingly, the arrival times of E1 and E2 at RTMT are estimated at 08:35:35 and 08:42:20 UT, respectively. Their true travel paths to this point were 6870 m for E1 and 7470 m for E2 (Figure 4.1). Using onset and cessation of the eruption as boundaries for flow start time, average velocities to the RTMT are 12.1-13.6 m/s for E1 and 7.7-8.2 m/s for E2. For comparison, local velocity estimates of c. 5 m/s were calculated for both flows from super-elevation measurements (*Lube et al.* (2009)).

The seismic spectrogram of E1 (Figure 4.3b) shows an unusually brief and sharply terminating tail, which either indicates movement of the bulk of the flow a critical distance away from the instrument where detection suddenly ceases, or a sudden waning of flow size and energy. As it contrasts with the long tails more typically recorded in water-rich lahars at this site (such as E3), the sharp cessation is interpreted to represent the sudden halt of the E1 ice slurry. Mapped deposits constrain the final runout of E1 to 830 m downstream of the site, with a sharp front to the deposit implying a sudden halt (*Lube et al.* (2009)). This suggests that the front traveled from the RTMT to the final runout point at an average velocity of 4.5 m/s, corresponding well with the super-elevation estimates. Projecting estimates of local velocity, the first vibrations relating to the detection of E1 were seen when it was c. 600-670 m upstream of the sensor.

4.2.7 Flow-substrate interaction, flow dynamics and rheology

4.2.7.1 Vibrational energy and frequency spectra

Suwa et al. (2000) proposed that the peak vibrational energy recorded by a seismometer is proportional to the peak discharge of a passing lahar, while volume estimations could be made by integrating the acceleration amplitude. Direct comparisons of vibrational energies between similar flows recorded at the same site should, therefore, provide a means for calculating their relative size and peak discharge (or mass flux). The peak discharge of E1 was independently calculated as 1700 m^3/s, with a sharp-fronted peak

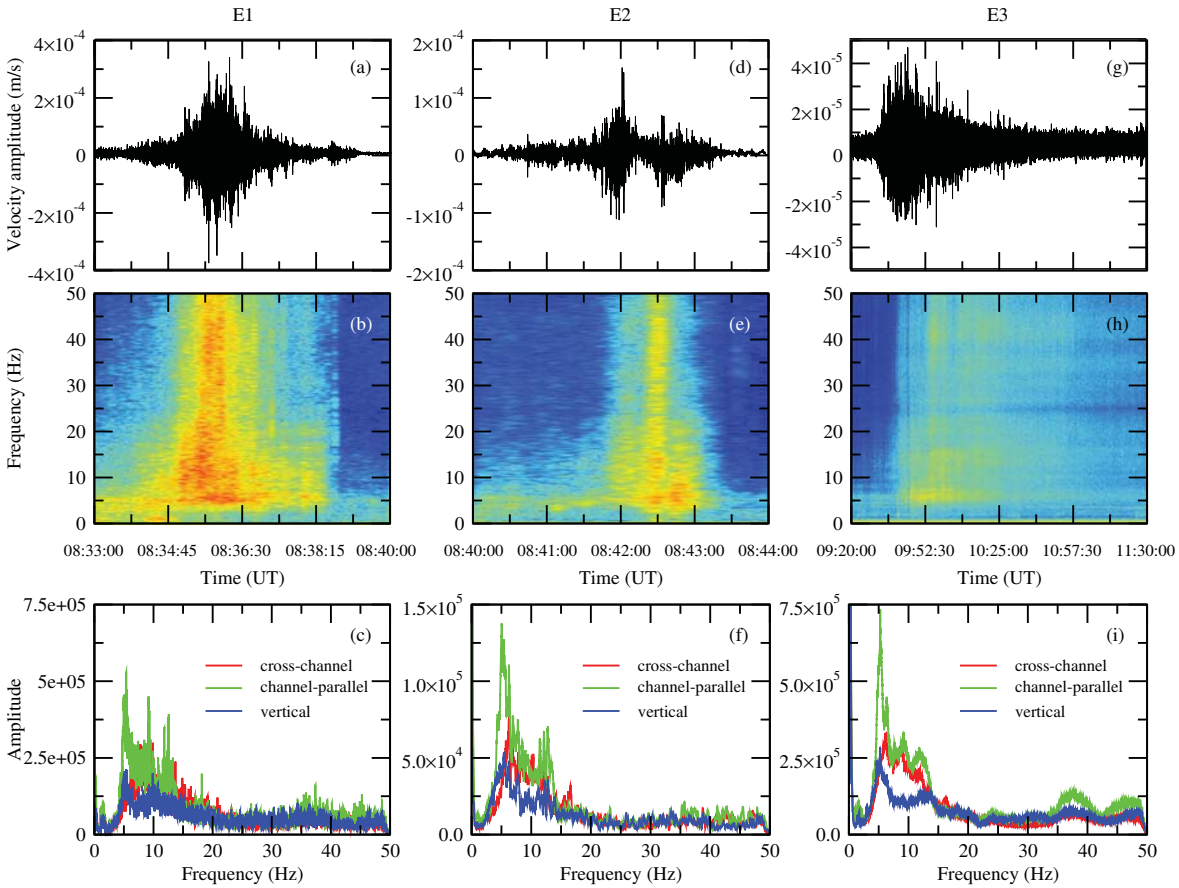

Figure 4.3: *Lahars E1, E2 and E3 vertical component signals (100 sps) recorded at the monitoring site RTMT. Top: seismograms; middle: spectrograms, with 256-sample windows and 50% overlap, using same colour palette as Figure 4.2; bottom: 20-point running average total spectra. Blue lines are vertical motion; Red lines are cross-channel motion; Green lines are channel-parallel motion. (a-c) E1; (d-f) E2; (g-i) E3.*

wave of 6.2 m in height (*Lube et al.* (2009)). In comparison, the break-out lahar of 18th March 2007, at the same site, had an estimated peak discharge of 2000-2200 m^3/s and a maximum stage height of 8 m. The peak wetted perimeter of the E1 snow-slurry lahar was c. 70% of the March event, but it only produced 10-12% of the peak vibrational energy of the 18 March sediment-laden flow. It is less easy to compare these flows with E2 and E3, as the relative amplitudes of the signals are likely to have been dampened by the loosely-compacted deposits of E1 that would decrease the efficiency of wave propagation through the unit. The discrepancy between flow volume and seismic amplitude for the different flow types is an important observation, as it implies seismic amplitudes alone cannot be used to determine flow volume. We infer the differences are a result of the freedom movement of large particles within the flow, especially their ability to saltate/collide with the substrate and flow-substrate frictional interaction.

Previous seismic studies of hyperconcentrated and debris flows suggest that particle collisions transferred to the channel bed or sides generate signals of higher frequency than does motion of frictional-sliding bedload. *Huang et al.* (2004) measured bed-friction generated signals with frequencies in the range 10-300 Hz, though predominantly between 20-80 Hz. Collisional motion produced signals between 10-500 Hz. Other studies have concluded energy from hyperconcentrated and debris flows are concentrated in the 10-100 Hz range (*Marcial et al.* (1996); *Lavigne et al.* (2000b)).

Depositional indicators of flow-parallel lateral shear structures in the September flows show that the ice-slurries moved by frictional sliding as a plug-like Bingham material (e.g. *Ancey* (2007)), with little free motion of particles within the flow, above a basal zone of high pore water pressures (*Lube et al.* (2009)). As such, we interpret the seismic signal to show little component relating to particle collisions; instead, we infer that the dominant 5-20 Hz spectral peaks of the E1 signal (Figure 4.3b) are representative of the frictional interaction of the moving snow-rich material over the channel substrate. In comparison, visual observations of the 18 March 2007 lahar imply it was a sediment-rich hyperconcentrated streamflow, producing high levels of bedload saltation and particle collisions. Correspondingly, higher seismic frequency ranges were recorded (Figure 4.4c). From this, we infer that the water content of E1 was very low (consistent with physical estimates from deposits (*Lube et al.* (2009))). If it were higher, saturation of air-filled porosity would be expected, along with vertical drainage, generation of a watery underflow, and a seismic profile more typical of a hyperconcentrated flow.

Lahar E2 produced signals that were generally less energetic than those of E1 (Figure 4.3d), with a less-pronounced increase in frequency and amplitude as the flow front passed the sensor and a more rapid tail drop-off, despite traveling c. 2 km farther (Figure 4.3e). The stratigraphy of the deposit shows that E2 traveled on top of the already-frozen E1 deposits. We infer that the reduced seismic amplitudes result from insulation/attenuation of seismic energy by the E1 deposits, reducing coupling between E2 and the channel base. The tail of E2 showed an increase in amplitude in the higher frequency range as it passed the sensor (Figure 4.3e), which may reflect a more watery and turbulent tail.

The third flow (E3; Figure 4.3g) occurred c. 1 hour after the eruption event, and

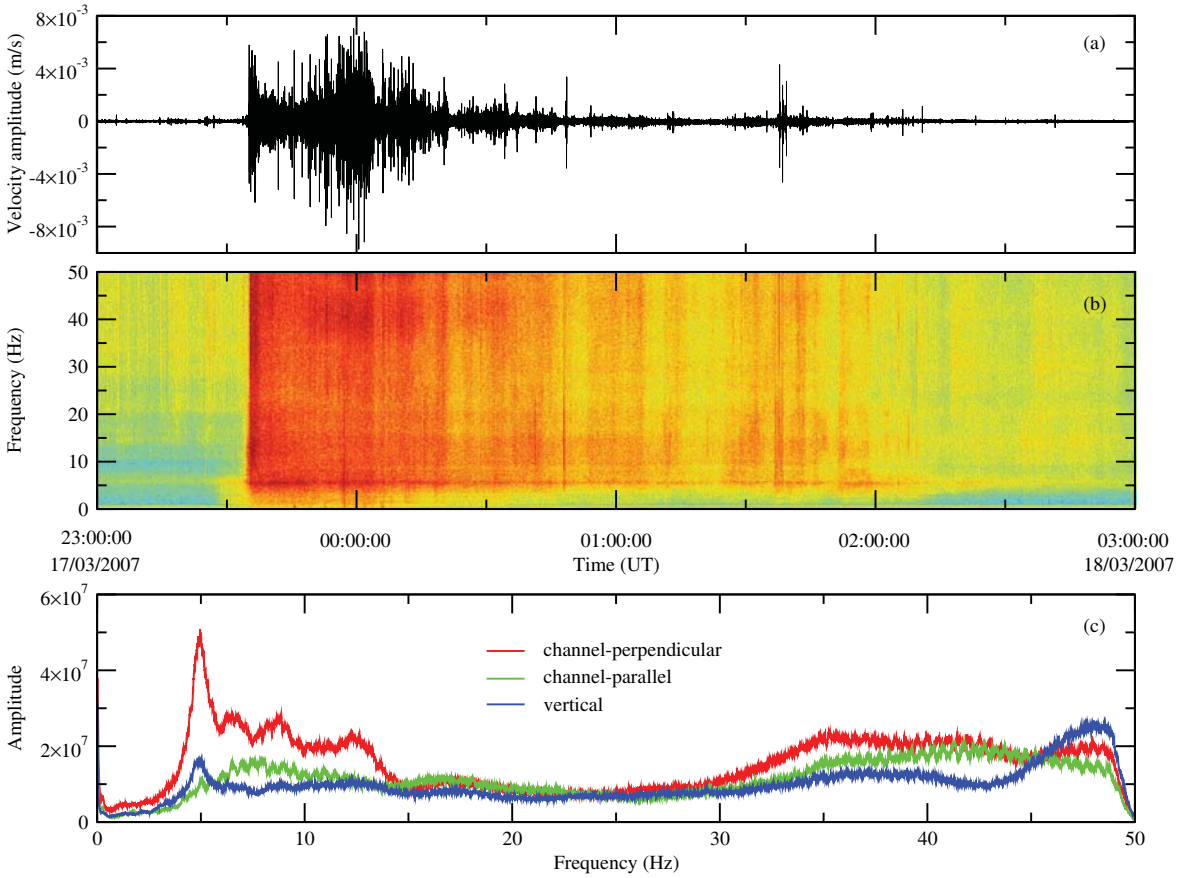

Figure 4.4: *(a) Vertical component seismogram (100 sps) of 18th March 2007 breakout lahar recorded at the monitoring site RTMT. (b) Spectrogram with a 256-sample window and 50% overlap, using same colour palette as Figure 4.2. (c) 20-point running average total spectra. Blue line is vertical motion; Red line is cross-channel motion; Green line is channel-parallel motion.*

lasted over 90 minutes. The arrival of E3 generated a similar spectrogram profile to E1 and E2, but with lower energy amplitudes (Figure 4.3i). An abrupt energy increase across the entire frequency range occurred only in the vertical component c. 15 minutes after E3's arrival (Figure 4.3h). This is interpreted to represent the moment when E3 eroded through the deposits of E1 and E2 to directly contact the channel base. A site survey showed that E3 had cut a c. 10 m-wide slot through the earlier frozen deposits. A corresponding increase in the horizontal components is absent, probably due to the attenuation of signals through the porous frozen deposits that filled the c. 80 m-wide channel. The frequency distribution after c. 09:55 (UT; Figure 4.3h) shows a similar, though less energetic, profile to the March 2007 lahar (Figure 4.4c). This suggests that E3 was dynamically similar, being turbulent and water-dominated. E3 left only a few cm of mantling deposit at the monitoring site, consistent with low

sediment concentration.

4.2.7.2 Signal directionality

Comparisons of the channel-perpendicular and channel-parallel vibrational energies of the March and September 2007 lahars show significant differences in the excited frequencies and amplitudes. We hypothesize that this can provide further information on flow dynamics and rheology. The water-rich, turbulent March lahar had flow-perpendicular amplitudes up to 3 times higher than those in flow-parallel directions (Figure 4.4c). By contrast, the ice slurry flows E1 and E2 produced more flow-parallel energy (Figures 4.3c and 4.3f). Depositional evidence of the E1 and E2 flows indicate a plug-like behavior, with little internal motion, minimizing collisions within the flow. Water-rich hyperconcentrated flows, however, allow for greater freedom of particle motion, leading to random collisions within the flow and against channel margins. We suggest that it is this behavior that produces the significant lateral, channel-dispersive and collisional forces responsible for the observed higher amplitudes in cross-channel directions in the March flow compared to the September flows. Deposition inward from the margins is implied for the ice slurry flows (*Lube et al.* (2009)), as exhibited by lateral-shear structures in the deposits; this would likely increase damping of seismic energy within the cross-channel orientation.

The directionality signals generated by the E3 flow should be similar to the March 2007 lahar, with higher cross-channel amplitudes. However, they were more like those of E1 and E2 with proportionally lower cross-channel energy (Figure 4.3i). We infer this pattern to be due to attenuation as the signal passed through the channel-lining E1 and E2 deposits, damping the likely higher frequency content signal induced by E3.

4.2.8 Discussions and Conclusions[1]

We find that water- and snow-dominated lahars show distinctly different seismic signatures. Strong seismic signals and broad frequency responses relate to water-rich flows and high turbulence as they cause both bedload movement and frequent randomly-oriented particle-particle and particle-bed collisions. The multiple trajectories, along

[1]**Acknowledgments:** SEC thanks the Commonwealth Scholarship Scheme and Massey University Graduate Research School. SJC and VM acknowledge support from the Marsden Fund (MAUX0512) and SJC from the NZ Foundation for Research, Science and Technology (MAUX0401).

with collisional contact with channel margins, produce more energetic cross-channel vibrations than flow-parallel. By contrast, snow-slurry flows have very low seismic energy compared to watery lahars of similar size as they involve little-to-no collisional interaction. They also generate stronger flow-parallel signals due to insulation of channel margins by lateral deposition and low incidence of channel-side collisions.

Distinguishing different lahar types by these features will provide a more complete assessment of the nature and degree of hazard posed. This step must be made before simple interpolations of size are concluded from direct examination of signal strength. For snow-slurry lahars, signal strength estimates using thresholds developed for more dilute flows will strongly underestimate flow size (discharge/volume). This implies that typical AFM warning systems, with minimum recording thresholds designed to avoid trigger by background volcanic seismicity, may not be triggered by the seismically quieter snow-rich lahars. This was notably the case at Ruapehu in September 2007, where despite successful recording at RTMT, the lahar-warning system using AFMs was not triggered (H. Keys, pers. comm. 2007). This is of concern, as ice-slurry lahars are highly efficient at transporting large volumes of ice and snow from volcanoes to generate significant downstream lahar hazards (*Pierson et al.* (1990)).

4.3 Using seismic signals for flow velocity calculations at the OnTrack Flood Gauge

One of the recording sites for the March 2007 lahar at Ruapehu was that of the OnTrack Flood Gauge (OT), installed after the 1953 Tangiwai Disaster to warn of future floods or lahars that could affect the Tangiwai rail bridge (see Figure 4.5; e.g., *Manville* (2004)). Horizons Regional Council installed a stage gauge and camera at the flood gauge itself, while Massey University and GNS Science contributed a seismometer and an acoustic flow monitor (AFM), placed approximately 250 m upstream (Chapter 1.5.1). This site is unique amongst the areas in this study as it consists of a series of sharp bends that ensured the flow passed near the instruments from several directions (Figure 4.5).

The distinct triangular shape seen in other seismic records of lahars, as detailed above, is also clearly visible within the record of the OT seismometer (Figure 4.6). In this case, however, it can be argued that the assumption that peak amplitude occurs

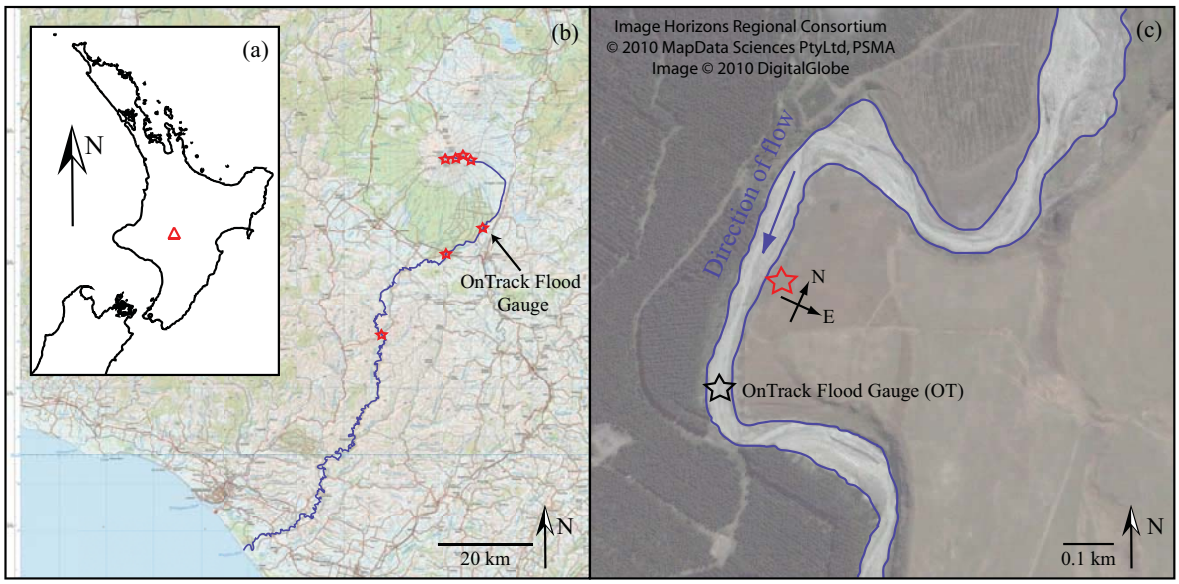

Figure 4.5: *Location of the OnTrack Flood Gauge (OT) monitoring site and associated sensors. Table 1.1 (page 23) details all monitoring methods used within this study. (a) Location of Mt. Ruapehu (red triangle) within the North Island of New Zealand; (b) location of the OnTrack Flood Gauge (OT) monitoring site relative to Mt. Ruapehu, the Whangaehu River catchment (blue line), and the sites used in this study (red stars), superimposed upon topographic maps of the region. Topographic maps sourced from NZTopo250-9 Taumarunui and NZTopo250-14 Palmerston North. Map scales are 1:250,000. Crown Copyright Reserved. (c) Location of the monitoring sensors along the river channel at this site (blue lines mark inundation area of the 18th March 2007 lahar): Massey University / GNS Science seismometer (red star); OnTrack tower warning system and Horizons Regional Council bubbler (black star); an Horizons Regional Council webcam was situated c. 200 m south east of the tower gauge. Details superimposed upon aerial photograph sourced from GoogleEarth^{TM}, Image Horizons Regional Consortium, ©2010 MapData Sciences PtyLtd, PSMA, Image ©2010 DigitalGlobe, Imagery Date 22nd March 2007.*

when a flow directly passes the sensor may be misleading. Owing to the geometry of the channel, the lahar passes the sensor relatively closely (within c. 300 m) on three sides. If seismically-quiet snow-slurry lahars can be detected 600-670 m upstream of a site (Section 4.2.6), then it is reasonable to assume that the seismic record of the turbulent water-rich March lahar will be affected by the flow on each of these segments of the channel. In addition, photographic images from the site suggest a delay in the arrival of sediment with relation to the front of the flow (*Manville and Cronin* (2007)). As such, the amplitude of the signal may have risen with the increase of particles within the flow.

By utilising the RSAM method as described in Chapter 3.3.3, it may be possible to more clearly define the times at which the lahar passes each of the bends in the channel,

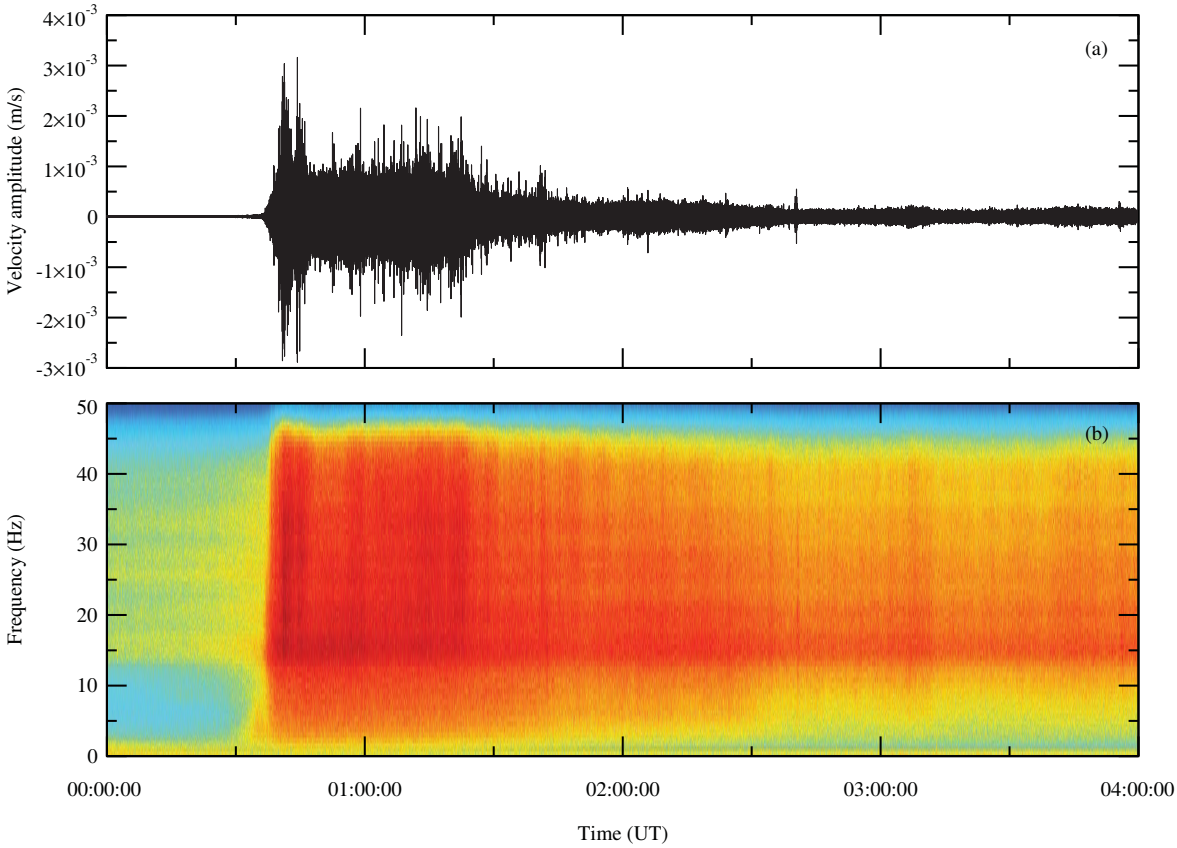

Figure 4.6: *(a) Seismogram (100 sps) showing recorded energy along the vertical component due to the Crater Lake breakout lahar of 18th March 2007 that passed the OT monitoring site. (b-d) Spectrograms of the channel-perpendicular, channel-parallel, and vertical components, respectively, calculated with 256-sample windows and 50% overlap.*

and therefore calculate an approximate velocity for the front of the flow. As the three segments of the channel in question are aligned either parallel or perpendicular to the horizontal components of the instrument (Figure 4.5), there should be a clearly defined change in the ratio of these components coinciding with the passage of the flow. Figure 4.7 demonstrates that the clarity of this change is dependent upon the frequencies of the signal used. The variation between the components is much more visible in the higher frequency (40-50 Hz) range than in the lower ones. This can be attributed to a combination of the inter-particle collisions and particle-channel collisions inherent in water-rich flows, and the lack of any coherent bed-frictional motion in the dilute head of the flow.

Ideally, the ratio of parallel and perpendicular RSAM traces will change coincidentally with the passage of the lahar along each of the different segments. As the flow had a water-rich, turbulent front, we can infer that the predominant motion on any

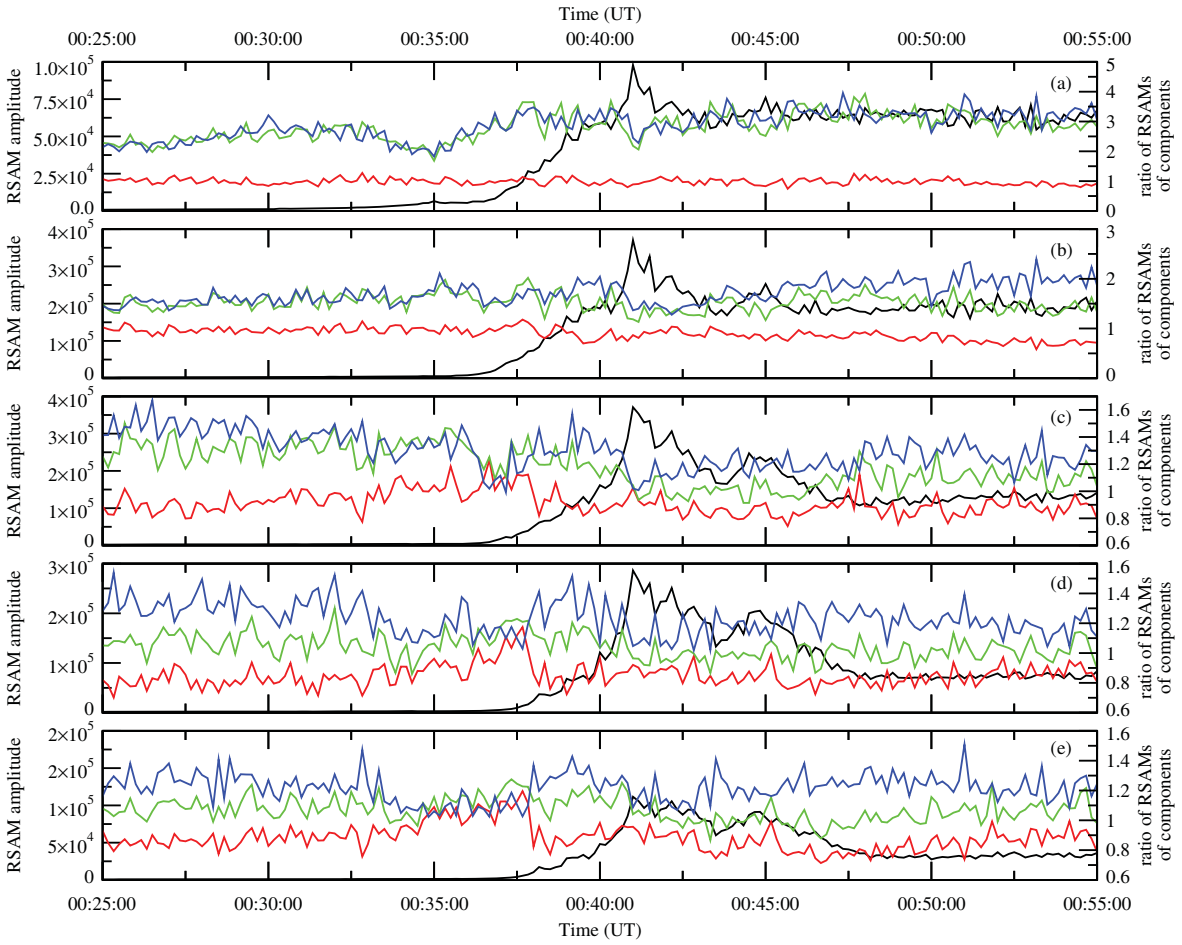

Figure 4.7: *Comparison between the ratios of channel-parallel, -perpendicular and vertical components of RSAM records of different frequency bands from the seismometer at the On-Track Flood Gauge (OT) monitoring site on Mt Ruapehu, 18th March 2007. Red lines are East-component over North-component; Green lines are East-component over vertical; Blue lines are North-component over vertical; and Black lines are the vertical RSAM trace for each of the respective frequency bands. (a) 2.5-10 Hz; (b) 10-20 Hz; (c) 20-30 Hz; (d) 30-40 Hz; (e) 40-50 Hz.*

of the segments would be in the channel-perpendicular direction (see Section 4.2.7.2). For this site, we define the parallel and perpendicular directions as aligned along the North and East components, respectively, coinciding with the second and longest segment of the bend (Figure 4.5). As such, the records of the flow between the first and second bends, as well as the third and fourth bends, should show an increase in the vibrations of signal on the North component. The signal from between the second and third bends will show the opposite; that is, an increase in the East-component signals with respect to those recorded on the North-component. Examination of the respective RSAM ratios over each of the frequency distribution bands, however, do not

individually distinguish variations due to each change in direction of the flow. This can be attributed to a combination of the long length of the lahar and its increasing stage and discharge, which continued to have an effect on each segment of the overall bend after the front had past by. Instead, there appears to be an overall increase in the localised East-component signals over North-component during a nearly 3-minute-long period prior to, and during, the arrival of flow at the flood gauge at c. 00:36 (UT). This indicates the period over which the flow front is passing through all four of the bends, after which the signals return to pre-flow ratios as all segments are still affected by the flow. Assuming therefore that the time window over which the change in RSAM ratios corresponds to this period, we can calculate an average "total bend" velocity of 3.73-4.21 m/s. This correlates well with the average arrival time of 4.07 m/s between the closest upstream recording site at the Aqueduct and the OT (Table 1.1).

4.4 Hyperconcentrated streamflow vs debris flow: Mt Semeru and Mt Merapi, Indonesia

The seismic data recorded during field seasons in Indonesia are demonstrative of different types of laharic flow (Figure 4.8). Those recorded at Mt. Semeru are primarily small (<1 m), hyperconcentrated streamflows. Despite this, they do have the potential to incorporate relatively high concentrations of sediment (50-60 wt.% sediment; Chapter 1.5.2; *Doyle et al.* (2009)). Of the flows recorded within this study, the vast majority were not able to reach these concentrations; peak concentrations were generally not more than c. 40 wt.% sediment. The hyperconcentrated streamflow considered here is a typical example of those recorded at Semeru, and was recorded on 6th February 2007. The flow was small, with a peak depth of c. 0.5 m, and covered approximately half of the c. 15-20 m-wide channel (Figure 4.8a).

In contrast, the single flow recorded at Mt. Merapi was a highly granular debris flow, with relatively high sediment content (Chapter 1.5.3). The flow was confined to a narrow channel previously carved through block-and-ash-flow deposits by other lahars. As a result, the width of the lahar was restricted to a few metres as it passed the monitoring site. While average flow depth was only c. 1 m, it was still capable of eroding large volumes of pyroclastic-flow deposits from the 2006 eruption that comprised the

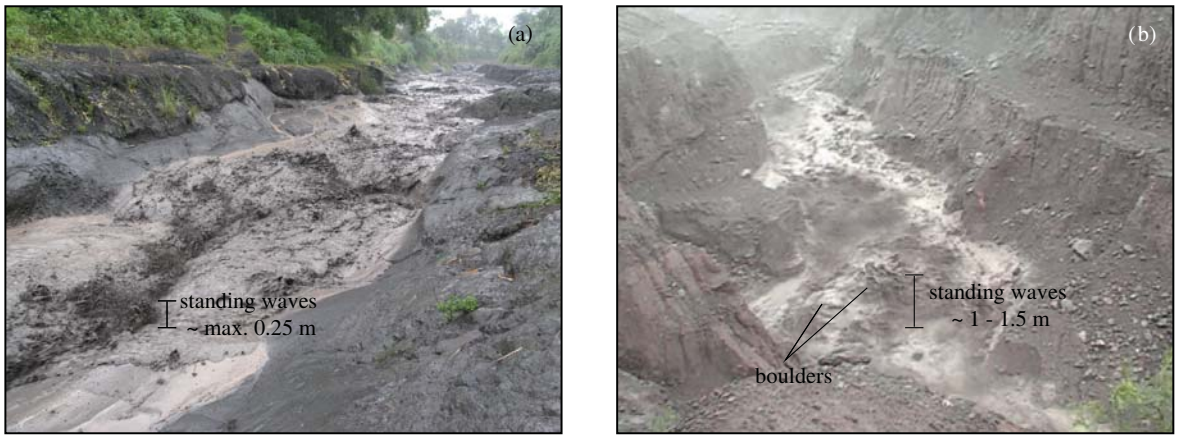

Figure 4.8: *Photographs illustrating different laharic flow types that were recorded during the 2007 field season in Indonesia: (a) Hyperconcentrated streamflow at Mt. Semeru, recorded on 6th February 2007; (b) Granular debris flow at Mt. Merapi, recorded on 31st January 2007.*

channel walls. The sudden quenching of this still-hot material produced steam that rose over the lahar (Figure 4.8b). Ground vibrations were strong throughout the passage of the flow, indicative of the observed large-boulder movements. This was markedly different from the relatively similar-sized, but seismically-quieter hyperconcentrated streamflow at Semeru (Figures 4.9a and 4.9g).

The time-series vertical component signals from the hyperconcentrated streamflow at Semeru (Figure 4.9a) clearly show the passage of the flow. By looking at the vertical-component spectrogram profile (Figure 4.9d), however, it can be seen that the majority of the ground vibrations are focused above 20 Hz. Indeed, between 5 and 15 Hz, there is only a small increase in the amplitude of the signals above background noise. As such, the distinct triangular shape that results from an increase in high frequency signal with time as a flow approaches a sensor (Section 4.2.6) is not easily seen here. By contrast, the spectrogram profiles from the two horizontal components show the expected triangular shape, as well as increased signal amplitudes in the frequency range 5-15 Hz. This latter is shown in Figures 4.9b and c and higlighted in the summed power density spectra for each component seen in Figure 4.9f.

The vertical RSAM profile from Semeru shows little change throughout the lahar time period, although the flow is clearly visible on the two horizontal components (Figure 4.9e). There are three spikes that are seen on all components and are easily distinguishable from the rest of the profile. The first of these is slightly broader than the other two and coincides with the start of the flow. It is, therefore, reasonable

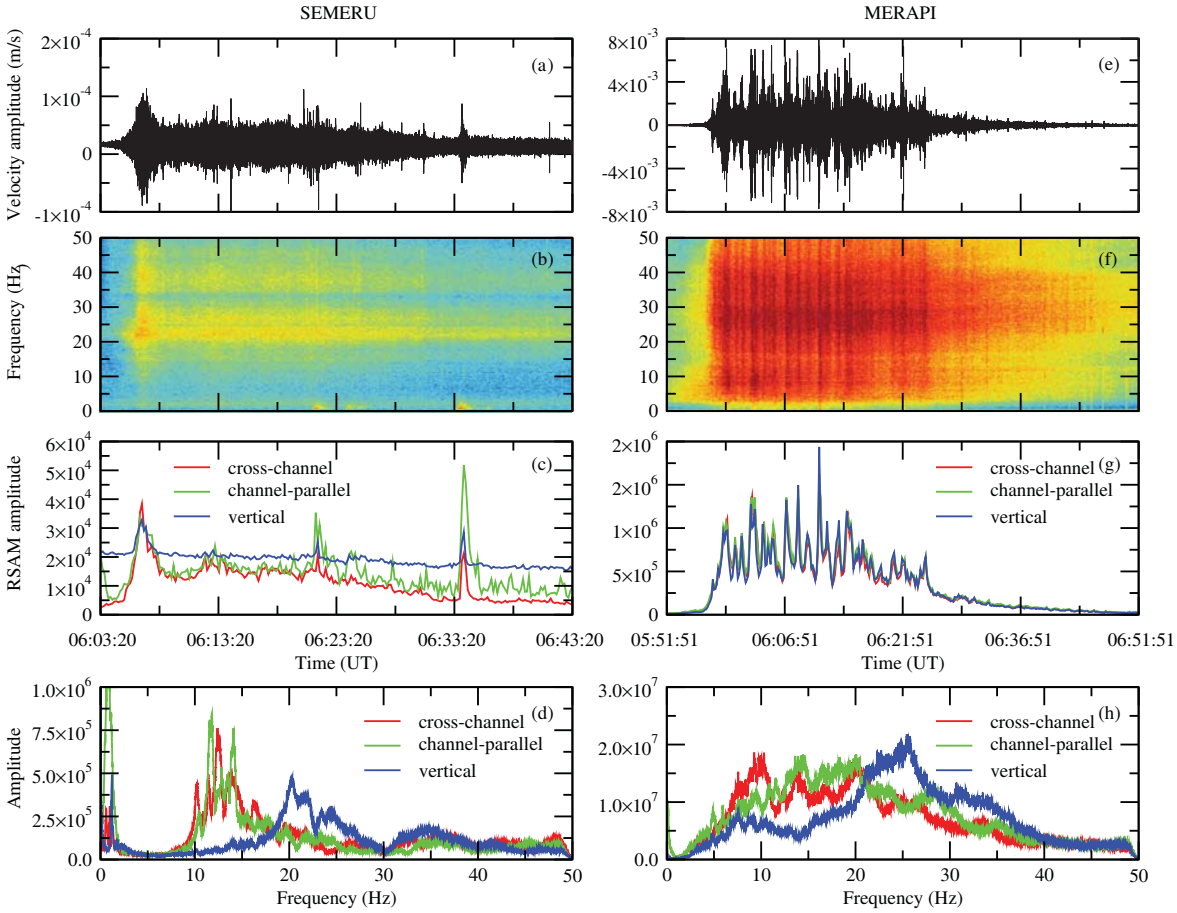

Figure 4.9: *Vertical component signals (100 sps) of lahars recorded in Indonesia in 2007. Top row: seismograms; 2nd, 3rd, and 4th rows: Spectrograms of the channel-perpendicular, channel-parallel, and vertical components, respectively, calculated with 256-sample windows and 50% overlap, using same colour palette as Figure 4.2; 5th row: RSAM amplitude for each component. Blue lines are vertical motion; Red lines are cross-channel motion; Green lines are channel-parallel motion; bottom (6th) row: 20-point running average total spectra. Blue lines are vertical motion; Red lines are cross-channel motion; Green lines are channel-parallel motion. (a-d) Hyperconcentrated streamflow at Mt. Semeru, recorded on 6th February 2007; (e-h) Granular debris flow at Mt. Merapi, recorded on 31st January 2007.*

to conclude that this represents when the flow passes the sensor. The second and third spikes are shorter in duration, and have greater amplitude in the channel-parallel component relative to the others. Video analysis and in-situ observations show no distinct changes in the behaviour of the lahar at these times. The spikes do, however, coincide exactly with two very low frequency spikes in the spectrogram profile. These, and hence the RSAM spikes, are attributed to small ash eruptions at the volcano summit. As the channel-parallel component is aligned to the summit, it is expected that this component would show the greatest increase in signal resulting from seismic events at this source. A third low frequency spike occurs at c. 06:24 (UT). This

spike is, however, much smaller in intensity and is not clearly distinguishable in the RSAM profiles (except perhaps on the channel-parallel component). These results have important implications for hazard systems that are based upon the use of single-component RSAM profiles. If only the vertical component is considered, it should be stated that without the incorporation of the time-series and spectrogram profiles in the analysis of the data, it would be hard to distinguish a lahar like the one recorded here from an eruption. While this flow was small at this site, it has the capability of bulking quite considerably and, under the right conditions, pose a serious threat to downstream infrastructure.

The time-series and spectral profiles for the granular flow at Merapi are considerably different from those at Semeru. As has been previously stated, ground vibration velocities are much higher than for the hyperconcentrated flow. The spectrogram profiles also clearly show the distinct triangular shape indicative of the approach of the flow to the sensor (Figure 4.9h-j). In contrast to the hyperconcentrated streamflow, the debris flow is easily distinguishable on the RSAM profiles of all three components. Interestingly, these profiles show approximately the same intensity of relative changes in the seismic signal on all components. As the flow contained many large boulders of c. 1 m in diameter, as well as smaller boulders and cobbles and a high concentration of sand and silt particles, it can reasonably be assumed that the volume of particle-particle and particle-substrate collisions was high. Video analysis and in-situ observations confirm this assumption. The random nature of these collisions would produce a noisy RSAM profile in any channel orientation. This behaviour is, therefore, attributed to the profiles produced, as seen in Figure 4.9k. Some of the peaks may be the result of both this action and the calving of pyroclastic deposit by the flow, as observed at the time. These two processes are, however, impossible to accurately distinguish in the record.

Previous studies have suggested that the motions of suspended particles within a turbulent flow can be considered to be either higher in concentration in near-bed regions (e.g., *Wilson* (1985)) or relatively uniform with distance from the bed (e.g., *Pierson* (2005)). Bedload-regional material, however, has been illustrated to consist of two zones: a lower frictional zone, in which particles move slowly and remain in contact with each other, and an upper collisional zone, through which continual exchange

between bedload and suspended load occurs due to the rolling, saltating, and sliding of individual grains (e.g., *Wilson* (1985); *Sohn* (1997); *Pierson* (2005)). It has previously been inferred that the low frequency (<20 Hz) signals can be attributed to frictional bedload movement (see 4.2.7), while high frequency (>30 Hz) signals result from the collisional motion between particles and the substrate, indicating the relative water content within a flow. Collisional motion has also been suggested to result in higher amplitudes in cross-channel directions than channel-parallel for water-rich flows (Section 4.2.7.2). As the Semeru and Merapi flows both contained water and were observed to have collisional components, their spectral profiles should show high amplitudes in the high frequency range, as well as greater intensity on the channel-perpendicular component compared to the channel-parallel. These explanations, however, do not take into account the changes increasing sediment content can have on flow rheology. Observed variations in velocity profiles across a channel have been attributed to the presence of regions of shear along sidewall margins with a rigid, non-deforming plug flow in the central part of the channel (e.g., *Genevois et al.* (2000); *Parsons et al.* (2001)). In addition, increasing sediment content, especially in fines ($< 63\ \mu$m), alters the properties of the interstitial fluid by increasing the volume of slurry within a flow, which in turn decreases the void ratio of the material, making the gravel bed more acoustically compact. While this would improve the transmission of seismic waves within the base of a flow, the higher viscosity of the flow itself preferentially dissipates higher frequencies from the main bulk of the lahar (e.g., *Huang et al.* (2004)). It can, therefore, be reasonably inferred that the frictional- and collisional-induced signals from within the near-bed region are likely to be well-recorded while particle collision-induced signals from the bulk of suspended load are not. In addition, both the hyperconcentrated streamflow and the granular debris-flow recorded at Semeru and Merapi, respectively, were small and shallow in depth, which prevented much of the flow from contact with the sides of the channel. It is likely that this is why the intensities of channel-parallel and channel-perpendicular motion are similar, and the highest frequencies (>40 Hz) are relatively low in amplitude (Figures 4.9f and l).

Low frequency peaks (<20 Hz) in the power density spectra occur during both the Semeru and Merapi flows. Interestingly though, they are predominantly confined to the channel-parallel and channel-perpendicular components (Figures 4.9f and l). It

is inferred, therefore, that frictional bedload motion is primarily associated with the channel-side contacts. The vertical seismic components of both flows show predominant excitation within the mid-frequency range (20-30 Hz). If frictional motion is represented by frequencies below 20 Hz and collisional motion is represented by frequencies above 30 Hz, it is reasonable to assume that the frequencies between these ranges are indicative of some phenomena that combines these two motions. Video analysis and observations at Merapi show clearly that the many large boulders within the flow were not held in suspension and were not subject to collisions with the substrate. Instead, they appear to roll and saltate along the channel. Observations at Semeru also show similar behaviour by the larger boulders within that flow. It is therefore inferred that the mid-frequency-range peaks seen in both power density spectra occur as a result of this rolling and saltating motion of large boulders within shallow flows.

4.5 Conclusions

Fundamental to the understanding of the hazard posed by a lahar is the accurate modelling of its dynamics. Different concentrations of water and sediment within a lahar, as well as particle-particle and particle-substrate interactions, can affect the behaviour of a flow. The variations in flow characteristics as a lahar passes a site produce ground vibrations that resonate in three dimensions across a wide range of frequencies. Comparisons of the 3-dimensional seismic excitation resulting from a lahar can reveal fundamental characteristics of the flow without the necessity for in situ monitoring or sampling by a wide range of instruments.

It is very important to hazard warning systems and models to accurately predict not only when a lahar will arrive at a site, but also the approximate velocity at which it is travelling. Such knowledge is necessary for the accurate predictions of zones of potential inundation and the likely damage that will result. It is often not possible to scientifically witness a lahar passing and measure directly its velocity, either because of their frequently unpredictable onsets or because the inundation area is in an area that is hard to reach or dangerous to remain in. By using the comparison of the 3-dimensional seismic excitation that result from the ground vibration of a passing flow, it is possible to calculate an approximate frontal velocity of a lahar.

Comparisons of water-dominated and snow-slurry lahars illustrate how the recorded frequency content of the ground vibrations from a lahar can be used to identify the dominant motions of particles within a flow. Snow-slurry lahars, whose motion is dominated by frictional sliding along channel margins, resonate at low (<20 Hz) frequencies. In contrast, water-rich flows produce signals with much higher (>30 Hz) frequencies due to particle-particle and particle-substrate collisions. This is because the particles have a much greater freedom of motion than in the plug-like snow-slurry flows. Examination of hyperconcentrated streamflow and debris flows recorded at Mt. Semeru and Mt. Merapi in Indonesia, respectively, further illustrate this. In addition, mid-range (20-30 Hz) frequencies were associated with the rolling and saltating motions observed in these latter flows.

It is necessary to distinguish the type of lahar recorded before any interpretation of flow size is made from the seismic record. Signal strength estimates developed for water-dominated lahars will greatly underestimate flow size if used for snow-slurry lahars. In contrast, using the same estimates to calculate the size of a debris flow will greatly overestimate its size. This has important repercussions for typical lahar warning systems. In the case of snow-slurry lahars, the relatively seismically quiet flows may not trigger the minimum recording thresholds of most warning systems, as occurred at Ruapehu in September 2007. In contrast, alerts about an approaching large flow that is in fact very small could undermine public confidence in the reliability of the warning system.

Chapter 5

Temporal variations in a moving lahar at a single site

Chapter 5 describes visual and instrumental observations at a single site during the 18th March 2007 Mt. Ruapehu Crater Lake-breakout lahar. From these, interpretations are made of the temporally-varying internal dynamics and composition of the flow as it passed.

5.1 Introduction

As has been demonstrated in the previous chapter, the overall seismic record of a lahar can provide information on its dynamics and bulk composition. These interpretations, however, have only focused on the gross physical characteristics of the flows. Previous studies have shown that short-term variations in instrumental records during a flow passage are significant and may provide insight into the localised motions and dynamics of a lahar (e.g., *Pierson and Scott* (1985); *Cronin et al.* (2000a); *Doyle et al.* (2009)). By combining the seismic record at a single site with detailed visual observations, the Crater Lake-breakout lahar at Mt. Ruapehu, New Zealand, on 18$^{\text{th}}$ March 2007 was examined. Colliers bridge, c. 83 km from source, was the location where the most detailed visual and video observations were made of the lahar, with its entire passage occurring during daylight hours. At this site, a broadband seismometer was installed approximately 25 minutes before the lahar front arrived. This chapter presents the analysis and interpretation of these records and provides a model of the internal time-

varying properties of a lahar wave as it interacts with stream water in its path.

5.2 Geological setting and instrumentation details

5.2.1 Colliers bridge

At approximately 11:22 local time (23:22 UT, 17th March 2007), a tephra dam constraining the Crater Lake at the summit of Mt. Ruapehu collapsed. Over the subsequent two hours, an estimated 1.3×10^6 m^3 of water flowed out of the breach, and into the Whangaehu Valley. The flow path followed the narrow, steep course of the river, through a number of gorges, before spreading out and crossing the 6 km-long and up to 4.5 km-wide laharic and fluvial Whangaehu fan beyond the cone (*Palmer et al.* (1993)). Below the fan, the flow was confined to a shallow channel until c. 42 km from source, where upon it was confined within a deep channel for most of the rest of the c. 160 km to the coast (*Cronin et al.* (1999)).

Colliers bridge is situated c. 83 km from source along the path of the river (Figure 5.1), where the flow was fully observed from start to finish. Its initial onset began with a steeply rising water level, which passed the bridge at c. 16:12, local time (04:12 UT). The lahar lasted approximately 3.5-4 hours before the river level (but not water quality) returned to normal. By the time the lahar had arrived at Colliers bridge, its overall volume was c. 3×10^6 m^3, similar to that measured at sites at c. 28 km and c. 42 km from source (*Procter et al.* (2010)). A digital 3-component broadband seismograph and a video camera were installed c. 25 minutes before the lahar arrived and observers were on site to take samples, photos, and descriptions of flow phenomena throughout its passage (Chapter 1.5.1.3; Figure 5.1). Estimates were made of the lahar stage and velocity in the field. In addition, more accurate measurements of stage, velocity, wetted area, and wetted perimeter were calculated from the video footage and still photographs.

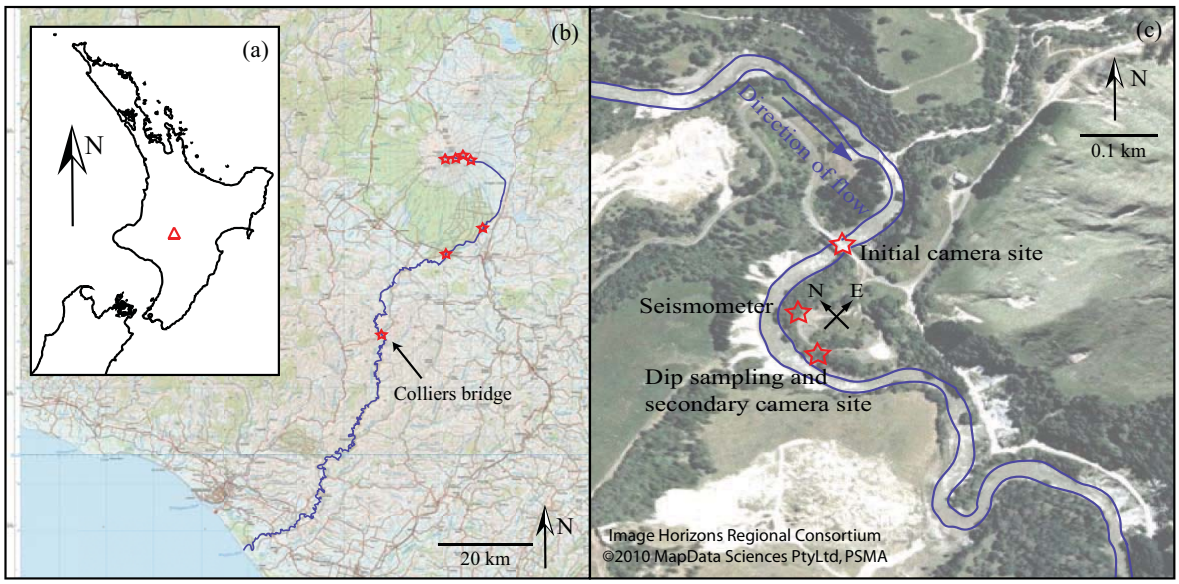

Figure 5.1: *Location of the Colliers bridge (CB) monitoring site and associated sensors. Table 1.1 (page 23) details all monitoring methods used within this study. (a) Location of Mt. Ruapehu (red triangle) within the North Island of New Zealand; (b) location of the Colliers bridge (CB) monitoring site relative to Mt. Ruapehu, the Whangaehu River catchment (blue line), and the sites used in this study (red stars), superimposed upon topographic maps of the region. Topographic maps sourced from NZTopo250-9 Taumarunui and NZTopo250-14 Palmerston North. Map scales are 1:250,000. Crown Copyright Reserved. (c) Location of the monitoring sensors along the river channel at this site (blue lines mark normal river bank outline pre-lahar). Details superimposed upon aerial photograph sourced from GoogleEarth^{TM}, Image Horizons Regional Consortium, ©2010 MapData Sciences PtyLtd, PSMA, Imagery Date 31st January 2005.*

5.2.2 Data collection

5.2.2.1 Observations: visual observations and video footage

Observations and notes were made throughout the duration of the lahar; these contained measurements of stage, velocity, and other characteristics, such as observed sediment concentration, presence and height of surface waves, surface debris, estimates of largest particle-sizes in motion, sounds and vibrations associated with periodically higher bedload motion, as well as viscosity, flow behaviour, and appearance. Stage measurements were approximated by the height of flow on the central support pylon of the bridge, and calibrated later by more accurate measurements to markings on the column and from scaled photographs. Velocity measurements were estimated using a surface float timed over a set distance at regular intervals during the flow.

A video camera was set up on the bridge, facing upstream to catch the onset of the

lahar. After c. 32 minutes, the camera was moved to overlook the flow dip-sampling site (c. 60 m downstream of the bridge), because large boulders hitting the central pylon of the bridge meant that it was deemed unsafe. After a c. 7.5 minute hiatus while the camera was moved, a further 18 minutes were filmed at the sample location before battery failure. A second camera was placed at the site c. 54 minutes later to collect an additional c. 30 minutes of footage.

5.2.2.2 Water samples

Water samples were collected prior to the lahar onset, and were then sampled every 10-15 minutes after its arrival. Further flow samples were also taken after the lahar to track the sediment concentration and water chemistry return to ambient levels. The sampling site had no interferences with tributary (clear) flows that would have affected the results. All samples were taken using a 5 L heavy-duty plastic fuel container, with 100 x 300 mm holes cut into its top and attached to the end of a rope (similar to those as described in previous lahar studies in this area, e.g. *Cronin et al.* (1999)). The sampler was then thrown upstream into the thalweg of the flow from the steep channel bank. It was allowed to float, fill, and sink into the flow for about 20 m of travel, before being carefully pulled out to avoid forcing of solids into the container. The dip samples were then transferred to completely-full sealable containers, and later analysed in the laboratory.

5.2.2.3 Seismic record

A Guralp CMG-6TD seismometer was installed on the true left bank of the channel at Colliers bridge. It was buried c. 0.5 m deep in sandy soil, c. 20 m downstream of the bridge, and c. 40 m upstream of the sampling site. The seismograph was placed in this location to minimise interference from movement of people near it, and c. 10 m from the channel margin, to maximize the signal from the flow.

5.3 Seismic implications for bulk flow behaviour

Analyses of the seismic signals recorded at Colliers bridge were initially made using the total spectra and spectrogram profiles on all components (Figure 5.2b-e). The

time-series signals and spectrogram profiles clearly show the passage of the flow. The time-series data show a long frontal period of relatively low ground-motion velocity that increases abruptly c. 20 minutes after the first signal arrival at the sensor. After this, the trace shows an overall decrease in amplitude. Some localised small increases in amplitude are seen, and are likely to be associated with wave "packets" or instabilities in flow, such as are seen in flows recorded at Mt. Semeru, Indonesia (*Doyle et al.* (2009)). While, as is the case at Mt. Semeru, it may be expected that these wave "packets", or instabilities, can be seen in the video records of a flow, the images available from Colliers bridge show negligible changes in flow height (stage) during these periods, preventing visual confirmation of their occurrence. It is possible, however, that the "packets" consisted primarily of fluctuations in sediment concentration and/or particle size rather than changes of bulk volume, which would not necessarily create discernable differences in stage height.

Spectral records of this flow from monitoring sites closer to source showed a distinct triangular shape that is a precursor to the arrival of a lahar (*Cole et al.* (2009); Chapter 4.2 and 4.3), similar to those seen in records of avalanches and other mass movements (*Surinach et al.* (2005)). At Colliers bridge, an easily-distinguishable triangular shape is visible in the spectrogram that corresponds with an initial lower-amplitude signal in the time-series data (Figure 5.2), although increases in lower frequencies do occur near the end of this period, possible indicating the inclusion of more bed-frictional-motion material (Chapter 4). The c. 20-minute duration of this increase in amplitude, however, would indicate that it could not be related to the approach of the flow to the sensor. If this had been the case, the flow would have first been detected when it was nearly 5 km upstream, based on an average arrival velocity of c. 4 m/s between sites. Comparison with other lahar records show this to be an unrealistic distance for such flows to affect the wide frequency spectrum seen here, due to the attenuation of frequencies with distance from source (e.g., *Cole et al.* (2009); *Zobin et al.* (2009)). A more realistic first-detection distance would be c. 1 km, based on the estimates of other flow records and accounting for the sinuosity of local channel reaches (Figure 5.1; c.f. Chapter 4.3). Assuming this, the c. 20-minute-long amplitude increase would necessitate an average frontal velocity of c. 0.8 m/s. In-situ observations and video records, however, show that the flow velocity was around c. 3 m/s as it reached the

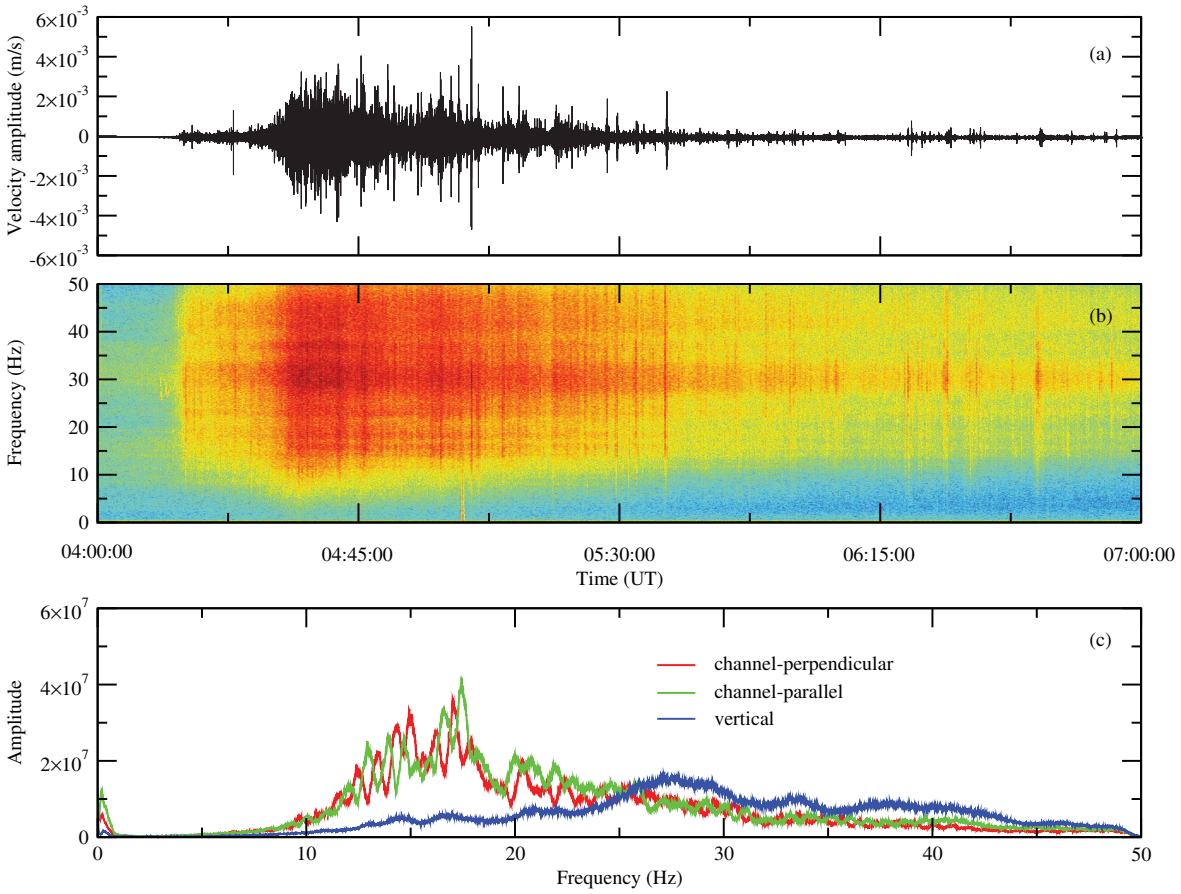

Figure 5.2: *(a) Vertical component seismogram (100 sps) of 18th March 2007 breakout lahar recorded at the monitoring site Colliers bridge. (b-d) Spectrograms of the channel-perpendicular, channel-parallel, and vertical components, respectively, calculated with 256-sample windows and 50% overlap. (e) 20-point running average total spectra. Blue line is vertical motion; Red line is cross-channel motion; Green line is channel-parallel motion.*

monitoring site, after which it rapidly accelerated (see Section 5.5; Figure 5.3). It is therefore concluded that, similarly to what is seen at the OnTrack Flood Gauge (Chapter 4.3), the peak amplitude does not necessarily occur when a flow first passes the sensor (c.f. *Caplan-Auerbach et al.* (2004)). Observations, as well as re-analysis of the video footage, indicate that this triangular shape actually corresponds to the arrival at c. 04:13 (UT) and subsequent gradual increase in stage of the flow as it passed the sensor. There is an indistinct increase in the higher frequencies prior to the actual arrival of the flow, although its precise onset is not clearly defined. This holds true for all three components of the record, although the precursor signal is slightly more distinguishable in the horizontal components (Figure 5.2b-d).

Studies of seismic records of lahars (e.g., *Huang et al.* (2004); *Cole et al.* (2009))

have suggested that the amplitude and distribution of affected frequencies is determined by: (1) type of particle motion; (2) particle size and distribution; (3) properties of the interstitial fluid; and (4) properties of the localised channel reach. Past observations have related frequency ranges to specific phases of a flow, e.g., *Okuda et al.* (1979) who recorded signals of 10-30 Hz at the surge front and 60-80 Hz at the flow tail, while *Huang et al.* (2004) recorded signals of <50 Hz during the frontal phase and 50-100 Hz in the body and tail phases. *Cole et al.* (2009) were able to further relate specific frequency ranges to flow rheology and motions by the comparison of markedly different flow types. This study showed that plug-like snow-slurry flows have produced signals that are predominantly confined to the 5-20 Hz range, while water-rich hyperconcentrated flows produced signals both in this range and also the 30-50 Hz range. This study has the advantage over others in that all of the records were made at the same site, where channel morphology remained relatively constant between the two events, minimising any variation in signals relating to localised channel properties. As such, correlations of motion could be made, resulting in the inference that bedload-frictional motion produces signals in lower frequency ranges than those of particle-collisional motion. Additional study of flows recorded in Indonesia have supported this inference and further suggested that signals seen in mid-frequency ranges are likely to relate to the saltation of particles along channel contacts (Chapter 4.4).

The frequency distribution of the signal seen in the flow recorded at Colliers bridge (Figure 5.2e) indicates a different predominant motion between the horizontal and vertical components. The horizontal components are dominated by primary peaks at low frequencies (<20 Hz), with smaller peaks at mid-range frequencies (20-30 Hz). There is little energy associated with higher frequencies (>30 Hz). In contrast, the vertical frequency profile shows greater energy in the mid- and high-frequency ranges (>25 Hz). These ranges are representative of the bulk flow behaviour as it relates to each component. As such, it assumes a temporally-homogeneous motion and distribution of particles. The recorded frequency distribution can, therefore, only give an indication of the predominant flow behaviour, irrespective of any variations in rheology, sediment concentration, or particle motion.

The lahar at Colliers bridge had a sampled peak sediment concentration of 63 wt.%. This falls well within the boundaries (40-80 wt.%) for hyperconcentrated flow

as defined by *Beverage and Culbertson* (1964). To consider bulk flow, therefore, a typical cross-section of a hyperconcentrated flow can be applied over the whole lahar. That is, the sediment content of the flow can be divided into regions of suspended load and bedload material. In turbulent flow, suspended sediment load consists of both fines and coarser pebbles, and has been considered relatively uniform with distance from the bed (e.g., *Pierson* (2005)), and alternatively considered to show a likely increase in concentration in near-bed regions (e.g., *Wilson* (1985)). In gradational or segregated flows, bedload-regional material consists of an upper collisional zone, in which rolling, sliding, and saltating of particles occur with a continual exchange between bedload and suspended load, and a lower frictional zone, in which grains move slowly and remain in frictional contact with each other (e.g., *Wilson* (1985); *Sohn* (1997); *Cronin et al.* (2000a); *Pierson* (2005)). From this, it could be expected that the frequency distributions of the recorded signals may reflect predominantly collisional motion in the horizontal components, and frictional and saltating motion in the vertical. This would be illustrated by the domination of higher frequencies for the horizontal and low-to-mid-range frequencies in the vertical, if the relationships between seismic frequency distribution and particle motion inferred from *Cole et al.* (2009) hold true. These explanations, however, do not take into account the effect of flow rheology that may change the properties of the interstitial fluid from normal streamwater to slurry behaviour with increasing sediment content, especially fines ($<$ 63 μm). Observations of flows have seen horizontal variations in velocity that are indicative of a rigid, non-deforming plug flow in the central part of the channel, with regions of shear at the sidewall margins (e.g., *Genevois et al.* (2000); *Parsons et al.* (2001)). In addition, increasing the volume of slurry within a flow makes a gravel bed more acoustically compact by decreasing the void ratio of the material, which hence improves the transmission of seismic waves in the channel base. Conversely, however, the higher viscosities of flow that result from increasing slurry content preferentially dissipate higher frequencies of signal (*Huang et al.* (2004)). It is inferred, therefore, that saltation- and collisional-induced signals in the bedload and near-bed regions are likely to be well-recorded, while signals from particle collisions within the main bulk of suspended load are not. Hence, it is suggested that the relationship between frequency distribution and motion of flow of *Cole et al.* (2009) can still be considered

applicable. The horizontal components preferentially record the motions associated with frictional shearing in sidewall margins, while the vertical component is indicative of particles saltating along the channel base. The bulk of signal due to particle collisions within the flow is dissipated due to the viscosity of the aqueous interparticle fill of the flow, producing the lower-than-expected higher-frequency content in the total spectra profiles.

5.4 Temporal variations in bulk flow characteristics

Changing profiles of seismic data in comparison with information of flow depth, velocity, and concentration of sediment can be used to provide further insights into the internal dynamics of a lahar. Figure 5.3 illustrates the variations in a range of flow properties over time at Colliers bridge. As previously stated, the seismic trace exhibits a general decrease in amplitude after the lahar peak in stage height has passed and sediment concentration begins to increase. The small, localised peaks in amplitude that occur after this may correlate with "packets" or waves of material within the lahar, or represent temporary changes in local bedload motion or entrainment. Distinct variations in flow stage and velocity occur either at the start, or just before, the first two of these localised pulses at c. 04:30 and c. 04:45 (UT), indicating probable variations in flow characteristics and/or behaviour. Absence of video records for the majority of the remainder of flow, specifically coinciding with the onset and duration of additional localised peaks, prevents further direct correlation with velocity and stage estimates. Unsteady flow has been observed in lahars at many other locations (e.g., *Arattano and Moia* (1999); *Marchi et al.* (2002); *Lavigne and Suwa* (2004); *Doyle et al.* (2009)). For this record, phases are defined as consecutive distinct changes in one or more characteristics of flow, such as stage or sediment concentration, and are used to decipher time-variable dynamics of the lahar.

The relatively low-amplitude signals seen in the seismic trace associated with the initial arrival of the flow at the sensor clearly correlate with the sharp rise in both stage and velocity (Figure 5.3). This is herein defined as the onset of phase 1. This initial portion of the flow consisted of nearly normal stream water, with only a small rise in concentration of sediment (<5 wt.%). Phase 1 is therefore described by rising stage

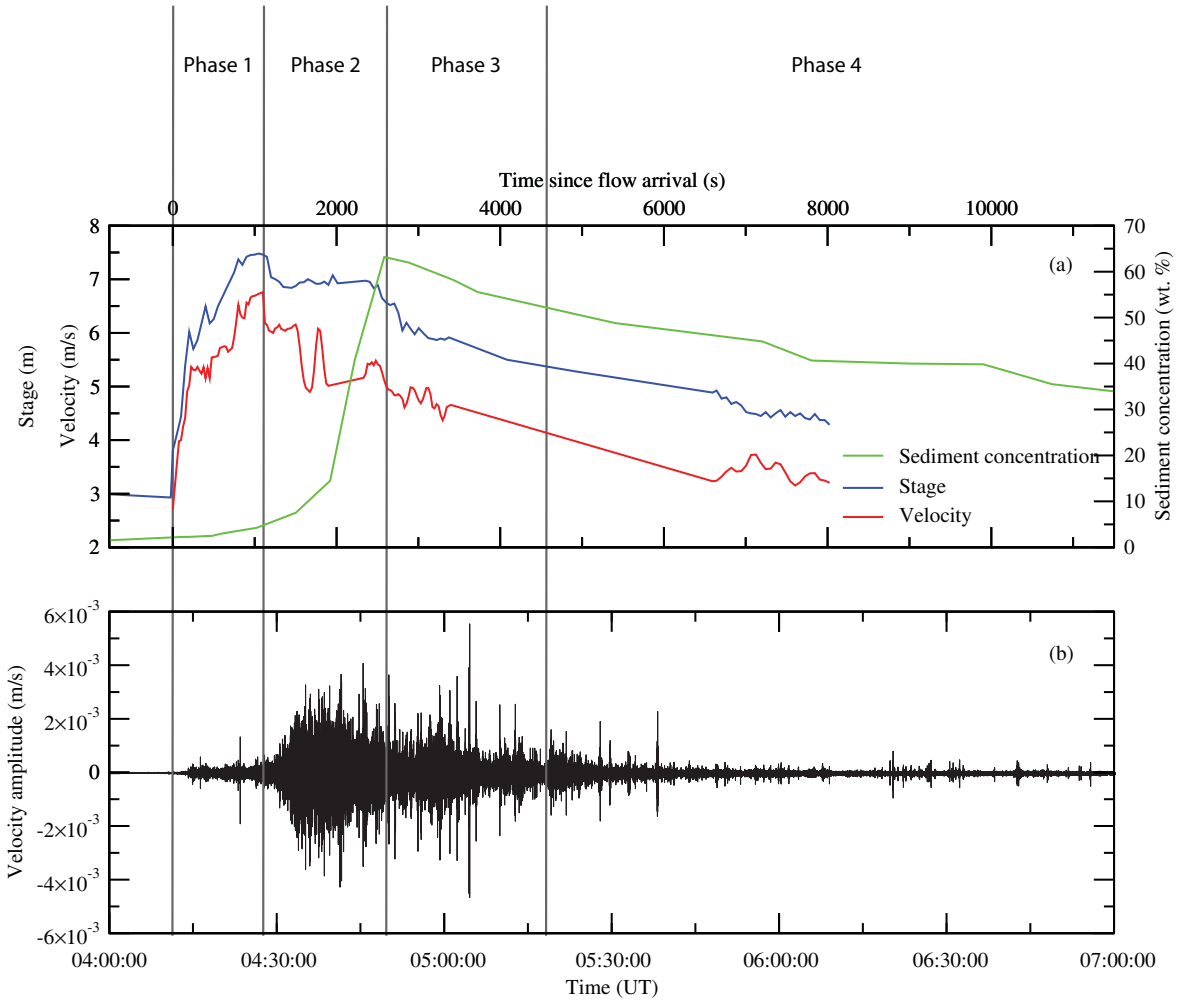

Figure 5.3: *Comparison of bulk flow characteristics: (a) variations in stage, velocity, and sediment concentration profiles. Blue line is stage; Red line is velocity; Green line is sediment concentration. (b) Vertical component time-series trace (100 sps) of lahar. Phases marked correspond to variations in flow behaviour, similar to that witnessed in Cronin et al. (1999).*

and flow velocity, low sediment content, and low seismic amplitude.

From Chapter 4.3 it was rationalised that peak amplitude may not necessarily occur when a flow passes a sensor if there is a delay in bulk sediment arrival. Increases in sediment concentration are likely to increase ground vibrations compared with normal streamflow due to higher rates of particle collisions, both between particles and with channel-side and -basal contacts. It would not therefore be unreasonable to assume that the peak vibrational amplitudes correspond to peak sediment concentration in the flow. Comparison between all variables, however, show that the peak vibrational amplitudes correspond to a relatively small rise in sediment concentration, but occur directly after peaks in both stage and velocity of the flow (Figure 5.3). Peak sediment

concentration did not occur until c. 20 minutes later. Phase 2 is therefore defined as that of peak vibrational amplitude, which directly follows peak stage and peak velocity, contains rising sediment concentration, and occurs between c. 04:28 and c. 04:50 (UT).

Observations by *Cronin et al.* (1999) of a dilute initial part of a flow followed by a sediment-rich flow of lower discharge support the segregation of the frontal part of the flow into two phases. Their study showed an almost pure stream water wave that, when sampled, showed sediment concentration remained below 5 vol.%, while water chemistry had little-to-no change from normal streamflow levels. Following this, the sediment concentration rose to its maximum, stage level started to drop, and water chemistry indicated the arrival of Crater Lake-derived water. From this, *Cronin et al.* (1999) determined that the fraction of flow that was near-pure streamwater (phase 1) was due to miscible displacement of normal streamflow in front of the lahar proper. Subsequent phases were then associated with the changing nature of the lahar.

The peak sediment concentration of the lahar coincided with a small, localised peak in ground velocity amplitude at c. 04:55 (UT), and marks the start of phase 3. By this point in the flow, both the stage and velocity had fallen below peak, though they still remained high. Peak sediment concentration was not sustained for long. Within minutes, the concentration dropped, along with flow depth. Subsequently, additional small, localised peaks in vibrational amplitudes occurred. As there was no video record between c. 05:09 and c. 06:02 (UT) and the record of sediment concentration is restricted to samples taken approximately every 10-15 minutes, it is unclear whether these correspond to other phases that may have occurred in the latter part of the flow. *Cronin et al.* (1999) observed only 4 phases in the lahars they witnessed. As with the lahar described herein, they determined the third-phase onset boundary as following the arrival of peak sediment concentration. In addition, they also sampled rising concentrations of Crater Lake-originating water chemistry. The boundary between phase 3 and the final, recessional phase of the lahar was designated as following the peak in Crater Lake-associated water concentration. As there is no clearly distinguishable boundary between the end of phase 3 and any possible other phases in the flow record from Colliers bridge, the 4-phase model of *Cronin et al.* (1999) is here applied. The tail of the flow is hence designated as phase 4, and extends over a long period. It is unclear from the seismic record when the river channel returned to

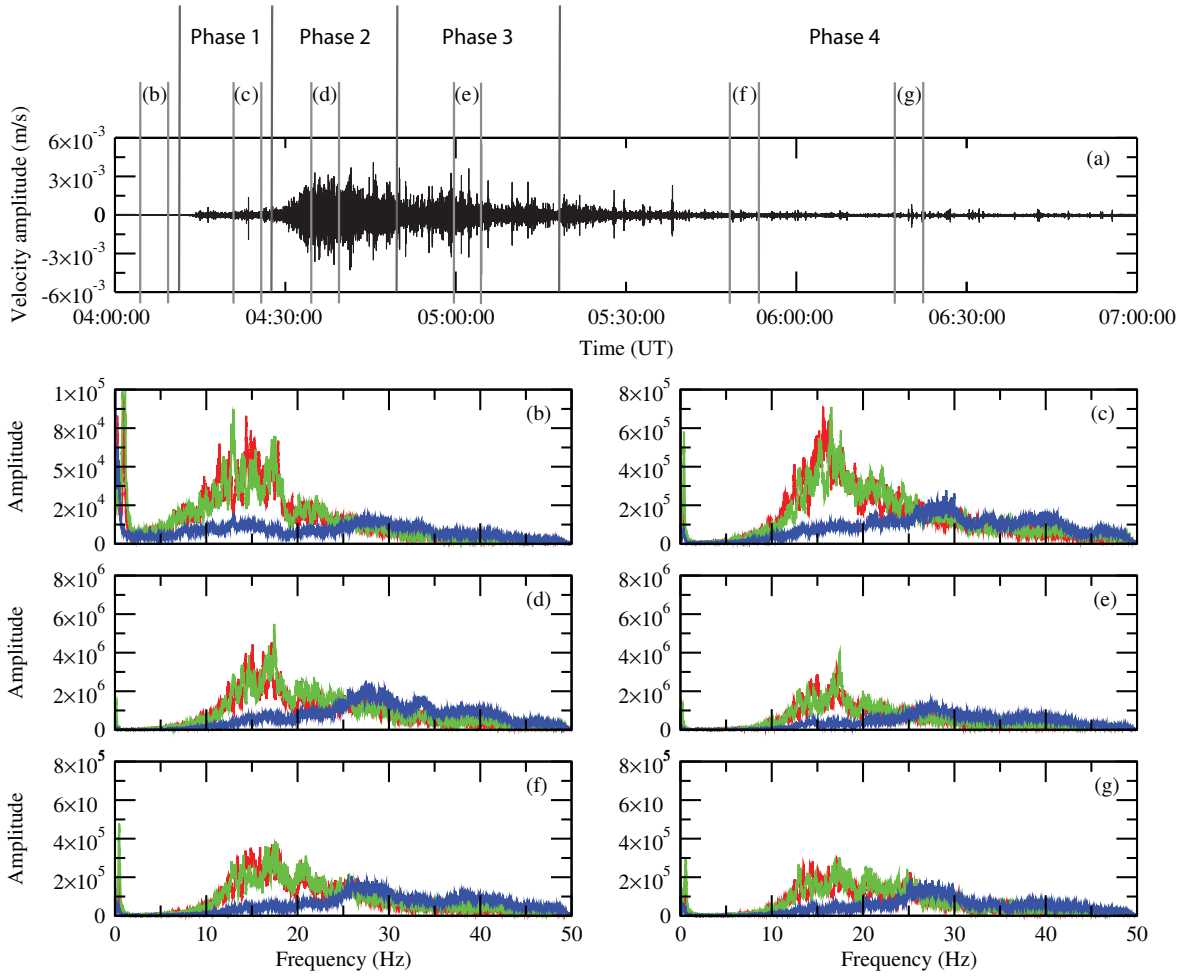

Figure 5.4: *Changing spectra associated with different phases in bulk flow characteristics: (a) Vertical component time-series trace (100 sps) of lahar. (b)-(g) 20-point running average total spectra calculated over 5-minute segments. Note different y-axis scales. Blue lines are vertical motion; Red lines are channel-perpendicular motion; Green lines are channel-parallel motion. Phases marked correspond to variations in flow behaviour, similar to that witnessed in Cronin et al. (1999).*

fully "normal" streamflow. Suspended sediment concentrations remained higher than normal for many hours after the flow had passed, despite a return to pre-lahar stage levels.

As with the spectrogram profile in Figure 5.2, the plots of Figure 5.4b-g illustrate the changing spectral density that occurs throughout the duration of the flow. The amplitude and distribution profiles for the two horizontal-component frequency ranges remain relatively self-consistent. Phase 1 is characterised by increased amplitude across the seismic frequency distribution, with greatest increases for frequencies above 10 Hz (Figure 5.4b and c). The amplitudes across the entire frequency spectrum continued to

rise during phase 2. Relative changes between frequencies were minor, though relative intensities between the horizontal and vertical components changed. That is, there was a greater increase in vertical intensity than in that recorded in the horizontal directions (Figure 5.4d). Figure 5.4e illustrates a dampening of the amplitudes of frequencies within phase 3. The change between phases 2 and 3 also corresponds to variations in the frequency distribution recorded on each component. Small peaks seen in the vertical component at high frequencies in phase 2 are not apparent in phase 3. Also, relative amplitudes of low- (<20 Hz) and mid- (20-30 Hz) range frequencies in the horizontal components become less distinct. Phase 4 is characterised by increasingly higher amplitudes in mid-range frequencies on all components relative to both the rest of the frequency distribution and normal streamflow values (Figure 5.4f and g vs b).

5.5 Correlation with other data

From the water samples taken of the flow at Colliers bridge, the sediment fraction was analysed (Figure 5.5b). The small (<5 wt.%) rise in sediment concentration associated with phase 1 almost completely consisted of fines (<63 μm), with only a very minor amount of very fine sand (Figure 5.5). In-situ visual records of this phase showed no discernable increase in sediment concentration, though broken logs and other debris were observed floating along the surface (Figure 5.6b). The <63 μm weight-fraction of sediment increased dramatically with the arrival of the more turbulent phase 2. There was a less conspicuous increase in the >63 μm fraction. Eye-witness observations during phase 2 indicate that boulders were also moving along the base of the flow, coupled with a visible increasing sediment concentration in the water samples (Figure 5.6c). As the flow progressed, the >63 μm fraction decreased with falling stage levels, although the <63 μm fraction remained relatively constant throughout the flow. The still-high sediment concentration of phase 3, combined with its decreasing stage and velocity profiles, led to the formation of a highly laminar-like rheology in which the flow surface exhibited subdued surface splashing only in its margins while the bulk of flow had a smooth, oily texture (Figure 5.6d). The elongated tail phase (4) of the flow continued to decrease the >63 μm fraction of sediment, resulting in a slow return to normal streamflow characteristics. During this phase, the flow became increasingly

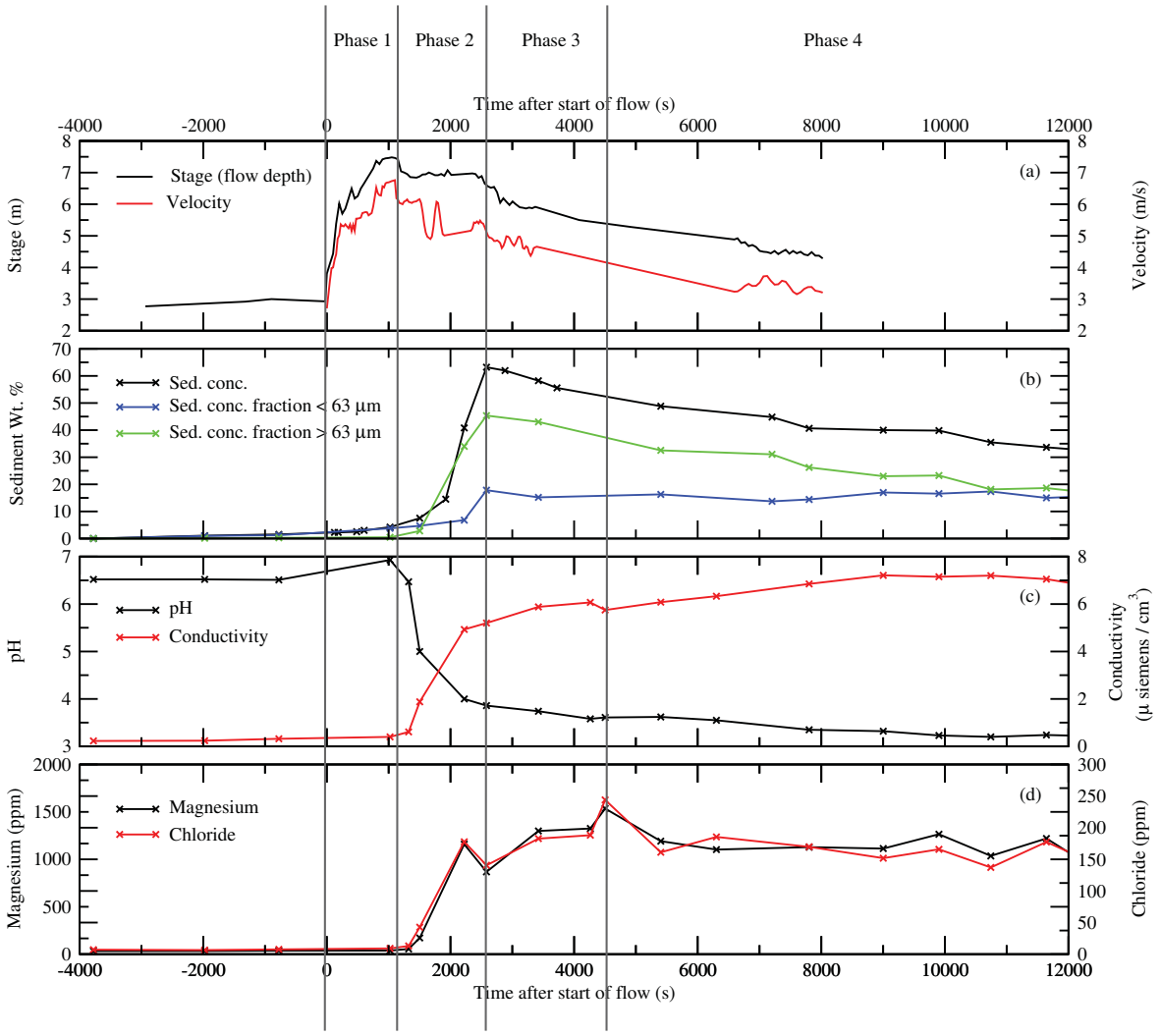

Figure 5.5: *Comparison of collected lahar bucket samples. (a) stage and velocity profiles. Black line is stage; Red line is velocity. (b) Sediment concentration fraction. Black line is total sediment concentration; Green line is sediment concentration fraction <63 µm; Blue line is sediment concentration fraction >63 µm. (c) pH and conductivity profiles. Black line is pH; Red line is conductivity. (d) Concentration profiles of magnesium (Mg^{2+}) and chloride (Cl^{-}). Black line is magnesium; Red line is chloride.*

water-dominated and standing waves developed in the outer margins of bends (Figure 5.6e and f).

The liquid fraction of the flow samples was analyzed for pH, conductivity, and for the concentrations of sulphate (SO_4^{2-}), magnesium (Mg^{2+}), and chloride (Cl^{-}). Since the levels of these ions are much higher in Crater Lake waters than the local streamflow, they can be used to evaluate the level of mixing of the lahar with normal stream water (*Christenson et al.* (1992); *Cronin et al.* (1996); *Cronin et al.* (1999)). As can be seen in Figure 5.5, the initial rise in stage is accompanied by little change

Figure 5.6: *Photographs illustrating the evolving nature of the lahar at Colliers bridge, approximately corresponding to times of spectra typical of different phases displayed in Figure 5.4. (a) pre-lahar normal streamflow (Photograph courtesy of A.V. Zernack); (b) onset of flow (phase 1) with broken logs and other debris floating on surface; (c) turbulent behaviour of phase 2 due to increasing sediment, with standing waves formed in mid-channel and outer bends; (d) smooth and oily surface typical of the more laminar-like behaviour of phase 3; (e) decreasing sediment concentration and increasing turbulence of early phase 4 (Photograph courtesy of A.V. Zernack); (f) latter phase 4 with decreasing stage and sediment concentration (Photograph courtesy of A. Möbis.*

in the chemistry of the flow. It is not until after the stage has peaked that the pH rapidly drops and the conductivity rises steeply (Figure 5.5c). These are explained by the changing volumes of salts and ions such as magnesium and chloride, which also rise steeply after peak stage (Figure 5.5d). Thus, it is inferred that the arrival of the Crater Lake water occurs first in phase 2, while the initial rise in stage (phase 1) is made up of ambient stream water. The pH, conductivity, and concentrations of Mg^{2+} and Cl^{-} continue to rise during phase 3. As with the model of *Cronin et al.* (1999), the peak of these concentrations are used to define the onset of phase 4. This phase represents the tail of the flow in which it gradually recedes back to normal streamflow values. The concentrations of the sampled ions initially becomes more uniform, before becoming more dilute by the latter part of the phase. It is probable that this is due to a combination of a more uniform mixing, incorporation of additional stream water, and decreased volume of original Crater Lake water within the flow.

5.6 Discussion

Seismic records of a lahar can be used to indicate changing characteristics and behaviour of a flow with time. As was previously stated in Section 5.3, the amplitude and distribution of frequencies affected by a lahar are determined by: (1) type of particle motion; (2) particle size and distribution; (3) properties of the interstitial fluid; and (4) properties of the localised channel reach (e.g., *Huang et al.* (2004); *Cole et al.* (2009)). As the study herein is a comparison of the temporal variations within a single-site record, the properties of the localised channel reach can be considered constant. As such, any variations in the seismic record are likely to be associated almost exclusively with the inclusion of sediment particles, their relative motion, and the effect they have on the properties of the interstitial fluid of the lahar itself.

Debris flows are mixtures of highly concentrated sediment and water that are driven by gravity and have a very high yield strength (*Pierson and Costa* (1987)). *Iverson* (1997) described the motion of these flows to be driven by inertial forces such as grain friction, grain collisions, and viscous fluid flow. Particle-size distribution is highly significant in correlating debris flow behaviour, especially the clay fraction. Debris flows can be classified as either cohesive (>3-5% clay) or non-cohesive (<3-5% clay).

Cohesive debris flows tend to remain as debris flows throughout their course, having usually formed by landslides or collapse of part of a volcanic edifice. Non-cohesive flows typically form from the erosion and entrainment of sediment by surges in dilute streamflows, which then undergo periods of downstream transition to hyperconcentrated flow followed by sediment-laden streamflow (e.g., *Pierson and Scott* (1985); *Scott et al.* (1995)).

The concentration of fines within a hyperconcentrated lahar plays a highly significant and complex role. As previously mentioned in Section 5.3, a hyperconcentrated flow consists of both bedload and suspended sediment load. In turn, this suspended sediment is made up of both fines and coarser particles. The fine material ($<$63 μm, clay and silt) is held in stable suspension for the duration of flow, and is independent of flow concentration, velocity, or discharge (e.g., *Xu* (1999)). The coarser material ($>$63 μm, sand and gravel), however, is generally only intermittently suspended within the flow. Particle size is relative to the length of time this material may be held in suspension. Sand grains may be transported in suspension for long periods, only rarely in contact with the bed, while larger cobbles may be in suspension only briefly, preferentially moving via saltation along the channel base (e.g., *Pierson* (2005)). It has long been observed in both field and experimental evidence that a minimum amount of fines must be held in suspension before large quantities of sand can be transported by a flow (e.g., *Beverage and Culbertson* (1964); *Rickenmann* (1991); *Pierson* (2005)). In addition, the higher the concentration of fines within a flow, the larger the average particle size of sand that can be transported (e.g., *Xu* (1999)). High concentrations of suspended fines also increase both the apparent viscosity and the density of the interstitial fluid, thereby also increasing the buoyancy of particles within it. This increase in the apparent dynamic viscosity leads to a decrease in the fall velocity of particles, reducing the rate of settling (e.g., *Beverage and Culbertson* (1964); *Xu* (1999)).

Entrainment of material into suspension occurs in the near-bed region of flow. These particles move into suspension via dynamic forces, such as drag and lift, exerted on them by the overlying flow. Once in suspension, the particles are held there by a combination of upward-directed fluid flow and collisional transfer of momentum between grains (*Pierson* (2005)). Upward-directed turbulence in the flow fluid has been observed in natural flows (e.g., *Pierson and Scott* (1985)). *Bridge* (2003) sug-

gested dynamic processes include increased drag produced by turbulent eddies in the overlying flow and collisional-induced upward dispersive stress. The numerical simulations of *Schmeeckle and Nelson* (2003) support the first of these processes as their study showed increased bed-load concentrations and transport rates resulted from the increase in amplitude of turbulent fluctuations across three dimensions. Correlations have been made between horizontal forces acting on a particle with the downstream velocity of a flow (*Schmeeckle et al.* (2007)), while observations have linked deposition of particles with decreased streamwise velocities and erosion with rising velocities (*Bottacin-Busolin et al.* (2008)). Particle settling has also had observed effect on the upward-directed fluid flow via the displacement of irregular cylindrical or planar zones of fluid by the downward motion of larger, denser particles (*Major* (2003)). This displacement by settling material can cause the elutriation[1] of fines held in suspension, forcing them to the surface (*Cronin et al.* (1999)).

By analysing the surface velocities of distinct particles across a channel centreline to its edge, *Genevois et al.* (2000) found that constant velocity zones existed in the central part of the channel, while shear zones existed along the margins. Flow velocity is a function of several factors, such as: (1) channel slope; (2) channel-bed roughness; (3) flow depth; and (4) sediment concentration. As the records examined in this study are restricted to a single site, channel slope and bed roughness can be considered roughly constant; temporal variations may exist in the events of scouring and deposition, but are unlikely to result in any largely appreciable difference. The variations in sediment concentration that occur because of the incorporation or loss of material from erosion or deposition respectively have a greater impact on the behaviour of the flow. *Parsons et al.* (2001) observed a similar central non-deforming plug with shear margins. Their study showed addition of sand or small amounts of clay led to a more Bingham-like[2] behaviour in the main body of the flow. Despite high concentrations of sand (>50 vol.%) within the flow, it was determined that flow resistance in the body was predominantly regulated by yield-stress and shear-thinning

[1] Elutriation is the process by which lighter particles are separated by heavier ones using a vertically-driven stream of gas or liquid. The lighter particles rise within the fluid as they have terminal velocities lower than the velocity of the rising liquid.

[2] A Bingham fluid is a viscoplastic fluid that behaves as a rigid solid if the stress applied to it is below a critical value (usually termed the yield stress), and as a fluid at stresses exceeding this threshold. The term "Bingham-like" is used to indicate flows that exhibit these characteristics but are not necessarily attributable as ideal Bingham fluids.

properties, with no boundary slip discernable. These yield-stress and shear-thinning properties were associated with the fluid-mud behaviour predominantly exhibited by slurry rheology. *Major and Pierson* (1992) found that, in flows of sufficiently high sand concentrations, densely-packed grain clusters could form in areas of shear, producing areas of anisotropy in the distribution of particles. These in turn would create further frictional grain contact opportunities due to the altered grain-size distribution and hence increase the probability of more particle clusters.

The relative motion of sediment particles within a lahar generate pressures that can be recorded by seismic sensors monitoring that flow as a function of ground motion or vibrations. These vibrations are either in direct response to the impact of particles along channel boundaries or result from the transmission of particle-particle interactions via pressure pulses through the interstitial fluid. In such cases, stresses and pressures can be transmitted through "force chains" over distances of many particles (e.g., *Liu et al.* (1995)). The concentration of sediment within a flow greatly influences the magnitude of the measured pressures from any particle interactions. *Zenit et al.* (1997) analysed the pressures recorded as a result of particle collisions within experimental flows that comprised a variety of different sediment concentrations and were repeated for variable particle sizes. These experiments indicated an optimum concentration of 30-40 vol.% of solids for maximum measured particle pressure. In dilute systems, particles have a greater freedom of motion and will encounter other particles less often, leading to fewer collisions. For more concentrated mixtures, the greater proportion of particles in the flow serve to increase the frequency of collisions but can also, at high concentrations, limit the movement of individual grains because of the geometric constraints of the packed state. In this same way, the particles can also limit the velocities at which they can move and therefore the impact pressures from collisions will be lower than those produced by particles that can reach terminal velocity in less packed states. The observations of *Zenit et al.* (1997) conclude that the magnitude of the measured particle pressure appears to scale with $\mu_p u_t^2$, where μ_p is the particle density and u_t its terminal velocity. Similar effects of optimal sediment concentrations for maximum pressure generation have been witnessed in a variety of real-world examples (e.g., *Scott et al.* (1995); *Pierson* (2005); *Cole et al.* (2009)). These flows, however, are further complicated by the effects of the variable grain-size distribu-

tion of sediment concentration particles on the hydrodynamics of the interstitial fluid that might account for added mass or drag on each grain (e.g., *Nott and Brady* (1994); *Bulthuis et al.* (1995)).

The concentration of particles, especially fines, has great influence on the behaviour of the flow itself, not just in its ability to entrain and deposit material but also by the effect such has on the interstitial fluid in which it travels. The viscosity of a flow is determined by concentration of sediment and the relative size distribution of particles. *Major and Pierson* (1992) illustrated that those slurries comprised of low concentrations of sediment have significantly lower effective viscosities than those with higher concentrations of particles. The concentration of fine-grained material is particularly important to the sensitivity of viscosity, especially at high sediment concentrations and high ratios of silt and clay to sand. Increases in the proportion of sand at a given total concentration will cause a corresponding decrease in the strength of the slurry and hence its viscosity. In contrast, increases in the concentration of fine material (clay and silt particles) increases the proportion of slurry, or at least slurry-like behaviour, within the flow. This has a significant effect on the transmission of collisional impact pressures between particles and through the interstitial medium. Due to the increase in finer material that can occupy interparticle space between larger grains in a more packed state, the addition of slurry improves the transmission of sound (or ground vibrations) by making the channel boundaries more acoustically compact. This is, however, offset to a degree by the dissipation of higher frequency signals from suspended sediment collisions that results from higher viscosity of the slurry medium (*Huang et al.* (2004)).

The initial phase of the lahar recorded at Colliers bridge was associated with a rapid rise in near-pure streamwater. The corresponding rise in velocity would have exerted increasing horizontal forces on particles in the downstream direction of flow, enabling the onset of erosion of material. Initial movement of particles along the channel bed prior to the advent of mixing into suspension would be frictional motion. Small amounts of fine material were incorporated into suspension, while more coarser material was confined to the frictional and saltational motion along the near-bed regions. Steadily increasing ground vibrational energy recorded on the seismometer is indicative of the rise in flow volume, turbulence, and the bed-frictional motions associated with the onset of erosion.

The arrival of Phase 2 heralded the advent of the lahar proper. It was characterised by a rise in sediment concentration to peak, small drops in both stage height and velocity, and the dramatic increase in water chemistry concentrations of conductivity and dissolved chloride and magnesium, along with a decrease in pH, indicating the arrival of water originating from the Crater Lake. The seismic response to this phase is in sharp contrast to that of Phase 1, with the [relatively] abrupt rise in ground vibrational amplitude corresponding to the increased sediment content. This amplitude remained high until the sediment concentration reached c. 40 wt.%, at which there was a reduction in the energy of the ground motions. It was at this point that the concentration of sediment within the flow had reached its optimal level for interparticle spacing to allow terminal velocity for each particle and hence maximum measured particle pressure. After this, sediment concentration continued to rise, coinciding with a decrease in the stage and velocity profiles, producing a more laminar-like type flow. As the concentration rose to peak, the interparticle spacing decreased, restricting the motion of individual particles, and reducing the resulting pressure from collisional impacts. The relatively large proportion of fines within this phase is indicative of its high erosion capabilities. As such, it would be expected that the motions of particles along the channel boundaries would be frictional and saltational in nature as material is excited into suspension and sheared along channel sides. Following the classifications by *Cole et al.* (2009) and those indicated in Chapter 4, the three-dimensional excitation of the frequency response seen for this phase is indicative of frictional and saltational motion, as expected (Figure 5.4d, page 121). Relatively little energy is seen in the collision-related frequency range, though this is likely due to the dampening and dissipation of the higher frequencies due to the sheared side margins.

Phase 3 immediately follows the peak in sediment concentration, and is associated with a change in lahar rheology as the sediment-water mixture flows in a more laminar-like fashion. This is supported by in situ observations and analysis of the video footage. The flow developed an increasingly oily surface appearance, while surface turbulence and splashing was dampened to produce an almost flat surface with a few ripples, as seen spreading from the true right of the channel across to the left in the photographs in Figure 5.6. The high sediment concentration, combined with the loss of flow volume, dampened the amplitude of the seismic record in both the horizontal and vertical

components (Figure 5.4e, page 121) because of the restricted interparticle spacing allowed by the geometric constraints of the more packed state. As the flow continued to decrease in discharge and velocity, sediment concentrations also lowered because of the reduction in horizontal force acting on particles, promoting settling. The relative concentration of sediment within the flow, however, remained high, promoting a more slurry-like Bingham-type flow. The increased viscosity of this phase, in combination with the lower particle collisional pressures, dampened the ground vibrational amplitudes from those of previous phases.

The tail phase (Phase 4) of the flow is primarily distinguished as following the peak in Crater Lake-associated water concentration and is characterised by the return to normal streamflow values. This boundary to the start of phase 4 has been assigned based on the 4-phase model of *Cronin et al.* (1999) because of the lack of any other comprehensive boundaries for other phases in the flow record. The tail phase of the flow extends over a long period. It is unclear as to when the channel returned to fully pre-lahar normal streamflow conditions. Despite a return to pre-lahar stage and velocity levels, the flow continued to have a higher than normal suspended sediment concentration. This phase is not easily distinguishable in the seismic record. Decreases in the sediment concentration, stage, and velocity profiles of the flow are indicated by the highly reduced ground vibrational amplitudes associated with this phase, while both frictional and collisional motions can be seen in the three-dimensional profile. This is likely a reflection of the increased settling of coarser particles that can no longer be held in suspension, and the related elutriation of fines due to displacement of zones of fluid.

5.7 Conclusions

The data and observations collected at Colliers bridge show that the flow was a fully-developed hyperconcentrated flow, as characterised by dynamic suspension of sand and gravel particles *Pierson* (2005). The lahar occurred as a series of four main phases, distinguished by distinctive changes in sediment and chemical concentrations, flow rheology, stage and velocity profiles, and ground vibrational energies. These are similar to those hypothesised by *Cronin et al.* (1999), but, with the more precise data here,

they can be defined as follows:

Phase 1: ***Rising limb of the flood wave.*** This encompasses a rapid rise to peak stage and discharge of the flow. Suspended sediment concentrations are low, while there is no change in water chemistry. Broken trees and other debris are seen floating along the surface of the flow. Corresponding ground vibrational amplitudes are low, and consist of predominantly bed-frictional motion represented in both channel-parallel and -perpendicular directions.

Phase 2: ***Rising sediment concentration to peak.*** This phase corresponds to the period of peak ground vibrational energy and the advent of the lahar proper. It is accompanied by an increase in suspended sediment to peak concentrations of c. 63 wt.%, consisting of both coarse (>63 μm) and finer-grained (<63 μm) particles. Stage and velocity levels are below peak, but remain high. Concurrently, water chemistry concentrations show dramatic increases in conductivity and dissolved chloride and magnesium, along with decrease in pH, indicating the arrival of water originating from the Crater Lake. Predominant motion of particles within this stage consisted of rolling and saltation of bedload material, and collisions between particles and with the substrate for suspended sediment load.

Phase 3: ***Lahar recessional limb.*** This phase comprises the transition from more laminar-like flow back towards more turbulent flow conditions as suspended sediment concentrations decreased to c. 32 wt.%. Stage and velocity levels also decreased, while water chemistry showed continued increase to least-diluted fractions of Crater Lake-originating water. This indicates a dilution effect by stream water of such in the front of the lahar proper. Ground vibrational amplitudes were dampened from those of previous phases, due to increased viscosity of the flow and lower particle pressures resulting from a combination of the increases in sediment concentration and falling stage and velocity levels.

Phase 4: ***Lahar tail.*** This phase comprises the transition back towards normal streamflow conditions. Water chemistry initially remained at a uniform rate, then slowly dropped back towards normal streamflow chemistry. This is probably due to continued dilution of Crater Lake water by the incorporation of additional stream wa-

> ter. Ground vibrational amplitudes decreased to near-background signals. Both frictional and collisional particle motions occurred. As flow volume continued to decrease, particle settling occurred, causing displacement of zones of fluid and the elutriation of fines held in [transient] suspension.

The correlation of data between the phases seen within this lahar illustrate that the seismic record of a flow can be used to provide information, not only about its bulk composition and dynamics, but also its changing nature over time. These phases of a flow show changes in sediment concentration, indicating active erosion and deposition, and, in cases of Crater Lake-originating lahars, increases in dissolved chloride and magnesium levels. The assumption that peak vibrational amplitudes occur as a flow first passes a sensor is not definitive. These peak amplitudes may also not occur at a time of peak sediment concentration. Instead, they can be associated with peak stage and velocity profiles when the optimal sediment concentration for interparticle spacing and terminal velocities can be reached, allowing for maximum particle pressure. Peak sediment concentration is often higher and results in a more packed state that restricts particle movement and pressure. This may not always be clearly defined in a seismic trace, but shifts in the relative frequency distribution profiles can indicate the change between turbulent and laminar rheology.

The seismic data can also be used to locate periods of changing dynamics within the flow. That is, the frequency distribution profiles are likely to be indicative of the erosion capacity of the lahar over time. Research into the behavior of streamflow erosive capabilities has shown that movement of stable-bed material only occurs when destabilizing forces, such as drag and buoyancy, are greater than the stabilizing force of the weight of the particle eroded (e.g., *Knighton* (1998)). Erosion of material occurs once the boundary shear stress has exceeded a critical level. The limiting conditions for bedload entrainment relate to flow shear velocity, particle size and density, and the density and kinematic viscosity of the fluid (e.g., *Raudkivi* (1990)). Once a particle has begun to move, it will migrate into suspension via turbulent mixing with the flow above. Of the many different criteria defining thresholds for sediment entrainment, the degree of this turbulence is considered to be highly influential on the erosive capacity of a flow (e.g., *Nino et al.* (2003)). As has been demonstrated previously (Chapter 4), the distribution of frequencies within a spectral profile can indicate the relative

motions of particles within a flow. The low-frequency range (<20 Hz) is associated with bed-frictional motion, as defined from the records of snow-slurry lahars. These types of flow move as a single, continuous plug of material that slides along the base of a channel. As such, it is an indication of the drag and shear velocity along contacts with the channel substrate. Thus, in a water-rich, turbulent lahar, it is reasonable to infer that erosion and entrainment of material may occur during periods containing this low-frequency component.

The analyses presented above have proven that internal variations of a lahar over time occur and can have a significant impact on the localised motions and dynamics as it passes a site. Correlations between seismic records and other data show that they can be used, not only to estimate bulk compositions and dynamics, but to also indicate transformations within the flow itself. Additional information and analyses of the erosional and depositional behaviours of a flow, and corresponding seismic signals, would aid in the identification of key characteristics that could be defined for each of these flow conditions. Comparisons of these temporal variations between different sites along a channel may herald further information as to the development and evolution of these potentially destructive phenomena.

Chapter 6

Downstream transition of a moving lahar

Chapter 6 describes visual and instrumental observations of the 18th March 2007 Mt. Ruapehu Crater Lake-breakout lahar as recorded at multiple sites along its channel path. From these, interpretations are made of the temporally- and spatially-varying internal dynamics and evolution of the flow as it moved downstream from source.

6.1 Introduction

The analyses made in Chapter 5 have shown that lahars are highly dynamic and vary greatly with time at a single site. Understanding the changing properties of a flow as it passes a single point is necessary for the effective mitigation of the hazard such a flow poses at that location. Observations of real-world lahars, however, have witnessed an evolution of flow that also occurs with increasing distance from source (e.g., *Pierson and Scott* (1985); *Cronin et al.* (2000a)). This continually evolving behaviour, with constant phases of incorporation and deposition of material as it travels downstream, makes the development of an easily-applicable whole-flow inundation model highly complex. Previous chapters have illustrated the adaptability of seismic sensors to the monitoring of lahars at a point along a channel. An array of sensors along the path of a lahar from source to termination would provide a method of monitoring this evolving downstream behaviour. Sensors deployed at a number of sites along the Whangaehu River at Mt Ruapehu, New Zealand, were ideally placed to allow for such monitoring of the downstream variations in the March 2007 Crater Lake-breakout lahar. This

chapter details the results of these records, and provides a comprehensive analysis of the temporally- and spatially-varying properties of the lahar as it traveled from source.

6.2 Site-specific temporal variations in signals

The threat from a breakout lahar at Mt Ruapehu was first recognised 11 years and 4 months before the actual event took place (*Keys and Green* (2008)). This lapse in time between the realisation of the likely outcome of dam-failure and the resultant lahar provided the opportunity to install mitigation measures to minimise the risk to the more vulnerable sections of the likely inundation pathway, such as bridges and the possible overflow into the Waikato River (*Pierson* (2002)). In addition, this delay in time also allowed for the installation of a series of sensors along the length of the Whangaehu Channel that could monitor the flow without the necessity of the constant presence of any human witnesses. This study has focused on only those sites that either exclusively, or in combination with other instruments, utilised seismic sensors (Figure 1.2). Table 1.1 details the different monitoring methods available at each of the sites discussed herein.

6.2.1 Eastern Ruapehu Lahar Warning System (ERLAWS)

The Eastern Ruapehu Lahar Warning System (ERLAWS) consists of three sites along the uppermost reaches of the Whangaehu catchment, at distances of 0 km, 2.2 km, and 4.6 km from source (Figure 1.2b; Table 1.1). The system was installed primarily as a response to the threat of dam collapse which followed the 1995-96 eruption episode that deposited c. 7.6 m of tephra on top of the previous lake outlet (*Keys and Green* (2008)). At each of the three monitoring sites, acoustic flow monitors (AFM) were installed to detect the passage of the flow and then linked to an alert system for emergency response personnel. As no alert would be issued unless a minimum of two sites detected increased ground motion, the multiple site system had the advantage of minimising, and allowing for the recognition of, false alarms that could be triggered by unrelated noise effects, such as movement near the sensor(s) or bad weather conditions (e.g., *Pierson* (2002); *Keys* (2009)).

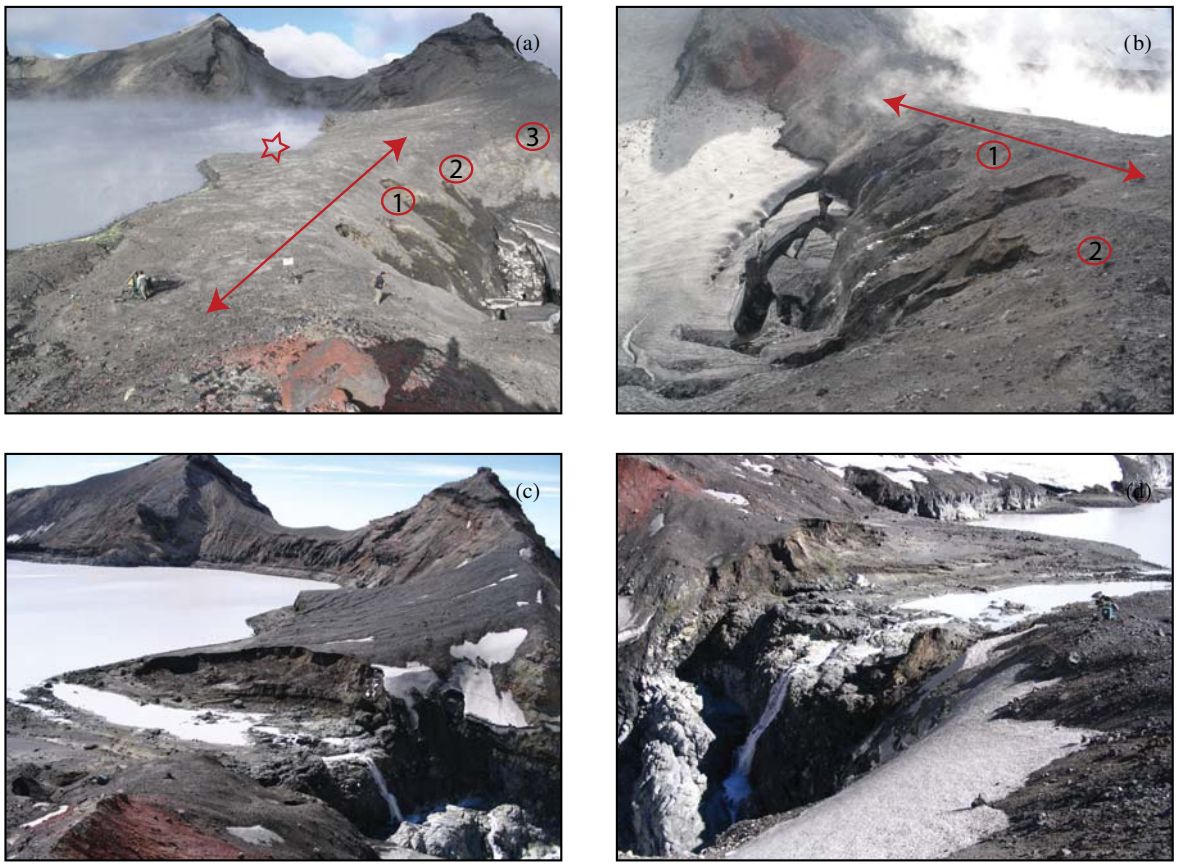

Figure 6.1: *Photographs showing the area of the tephra dam at the Crater Lake and the installation sites of the buried instrumentation. (a-b) Before dam collapse, taken 19th January 2007. (Photographs courtesy of S.J. Cronin). (c-d) After dam collapse and outflow of water, taken 19th March 2007. (Photographs courtesy of H.J.R. Keys). Arrows indicate the location of the tripwire; circles indicate the geophones 1-3; star indicates the pressure transducer.*

6.2.1.1 Site 1 - the Crater Lake

At the Crater Lake itself, the Department of Conservation and GNS Science installed a gas bubbler (Figure 6.1a) to measure the increasing lake level to ± 3 mm precision at 10-second intervals (e.g., *Massey et al.* (2009)). By constantly measuring this increase, predictions could be made as to the likely volume of water released in the event of a breakout, which in turn could be used to model areas at risk of inundation. These measurements were also used as the basis of the alert level warning system that predicted likely response of the dam at that level, the anticipated time for the lake to rise to the next level, and the action time recommended for the emergency response personnel (for more information on the different alert levels, see *Massey et al.* (2009)). In addition, a series of vertical-component 10 Hz geophones and a tripwire (Figure 6.1a and b) were installed across the dam to monitor any movement or erosion that would indicate a

weakening in the structure and alert to any imminent collapse. An automated digital still camera was also installed to the east of the dam looking down on the downward slope of the tephra barrier, and captured images at 1-minute intervals during daylight hours.

Each of the sensors installed at the Crater Lake recorded the collapse of the tephra dam on 18th March 2007 (Figure 6.2). This collapse was preceded by a prolonged period of wet weather over several days that caused an increase in the lake level of c. 0.3 m between 13th and 15th March (e.g., *Massey et al.* (2009)). This level again increased by a further 0.1 m on the morning of 18th March, providing the trigger for the dam collapse to begin in earnest. Before this, a few collapse scarps had begun to become visible in the months prior to failure (e.g., Figure 6.1a and b), while lake seepage had been identified as early as December 2006 (e.g., *Massey et al.* (2009)). The seismic signals related to the breach collapse clearly show a minimum of five phases in the record. Correlations with the lake level, tripwire, and still camera images allow for a quantification of the steps within the breach sequence that produced these signals (Figure 6.2).

Prior to the initiation of the main breach sequence, there was a relatively minor increase from c. 21:55 (UT, 17th March) in the vibrational record of geophone 1, located within the dam itself. This increase was not, however, of either sufficient strength or duration to exceed the preset threshold of 500 mV to trigger an alert. A subsequent double spike in signal at c. 22:45 (UT) that did exceed this threshold also did not trigger a faster sampling rate or an alert as no corresponding signal was recorded on the sensors of sites 2 or 3. Correlation with the still camera images, however, suggest that these spikes could be related to the retrogression of one of the eastern-most erosion scarps.

The main bulk of signal that is associated with the collapse of the tephra dam occurred between c. 23:07 (UT, 17th March) and c. 01:00 (UT, 18th March). After this, the signal returned to below-threshold levels and the faster sampling rate was abandoned. This bulk signal is comprised of five pulses or phases. Correlations with the other data records indicate that these phases are clearly related to a sequential collapse and failure of the tephra dam, summarised in Table 6.1.

The first of these phases (I), hereafter called stages to distinguish from the time-

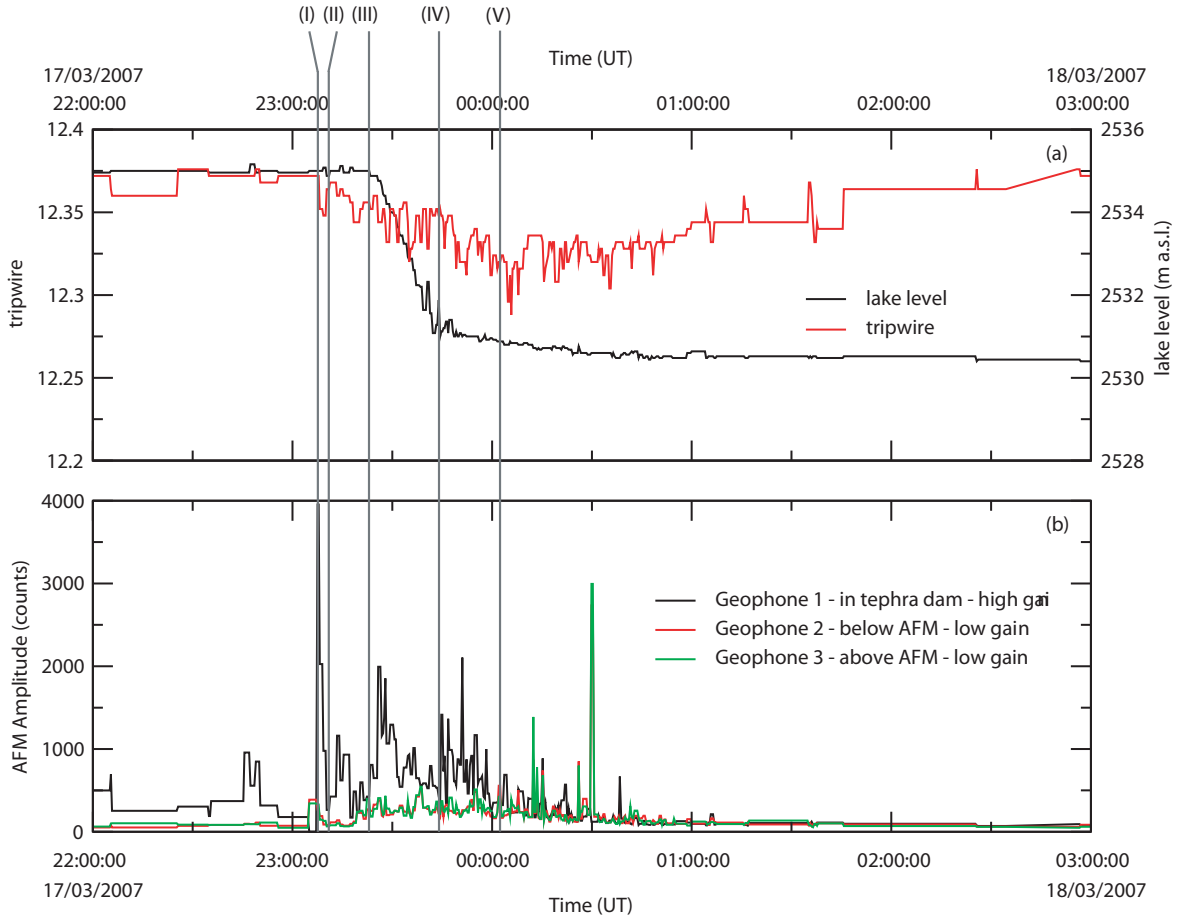

Figure 6.2: *Comparison of data at the Crater Lake/ERLAWS site 1, showing the geophysical record of the breach sequence and outflow through the dam. Data courtesy of the Department of Conservation (DOC). Locations of instruments can be seen in Figure 6.1. (a) Removal of the tripwire and subsequent draw-down of the lake level after breach. Black line is lake level, measured in m above sea level (a.s.l.); Red line is tripwire record. (b) Seismic response of the geophone record of the collapse and outflow. Black line is high gain signal from geophone 1, positioned in the dam; Red line is low gain signal from geophone 2; Green line is low gain signal from geophone 3. Roman numerals (I-V) correspond to variations in breach sequence as listed in Table 6.1.*

varying phases of Chapter 5, is comprised of a short, sharp spike in the geophone record at c. 23:07 (UT), and is the maximum recorded peak on geophone 1 (Figure 6.2b). Still camera images from the same time indicate that this is related to rapid headward erosion of [near] the central part of the dam (Figure 6.3a). The second stage (II) began at c. 23:09 (UT) and is characterised by a smaller, more drawn-out peak in the geophone record. Still camera images indicate that there was a continued collapse of the erosion scarp enlargened in stage I. The signal from the tripwire also indicates movement within the dam near the sensor, though it was not pulled at this time (Figure

Date (dd/mm/yyyy)	Time (UT)	Stage	Details
17/03/2007	23:07-23:08	(I)	Geophone 1 records largest spike; rapid headward erosion towards lake at approx. central part of dam
	23:09-23:10	(II)	Rapid enlarging of the erosion scarp, forming single channel towards the lake. Initial breach of dam occurs at 23:10 with draw-down of c. 3 cm in 8 mins.
	23:21-23:22	(III)	Rapid failure of large section of the downstream dam face connecting all erosion scarps. Remaining dam fails, tripwire pulled at 23:22, followed by rapid draw-down of lake.
	23:45-23:57	(IV)	Series of peaks recorded on geophone 1, possibly relating to lateral erosion and failure of dam flanks as breach widened.
18/03/2007	00:02	(V)	Breach widened to full width of 45 m

Table 6.1: *Summary table detailing the main failures in the Crater Lake-breakout breach sequence of the tephra dam.*

6.2a). While lake level measurements remain relatively high, draw-down did occur (c. 3 cm over 8 minutes), suggesting a [small] channel had been eroded through the dam.

The rapid failure of a large part of the downstream face of the dam marks the start of stage III at c. 23:21 (UT). The geophone record increased in signal strength for all three sensors. The tripwire signal also [briefly] showed increased signal before it was pulled at 23:22 (UT), indicating the official start of the dam collapse proper (Figure 6.2). Lake drawdown increased dramatically at this point as a large section of the tephra dam was removed from the central channel. Still camera images corroborate the rapid failure of the dam (Figure 6.3b vs c).

The geophone and lake level records continued at a relatively steady rate until c. 23:45 (UT). At this point, the seismic signals increased to another localised peak while the rate of drawdown decreased (Figure 6.2b). This is designated as the start of stage IV. Correlation with still camera images indicate that this may be associated with the lateral erosion and collapse of the flanks of the remaining tephra dam. A fifth stage (V) is designated as the time at which this flank material is fully eroded and the breach had widened to its maximum width of 45 m. The amplitudes of the seismic record continued to decrease, along with the rate of lake drawdown, during this period as the flood of water out of the lake lessened in intensity (Figure 6.2). It is likely that the anomalously large spike visible on Geophone 3 at c. 00:30 (UT) can be attributed to

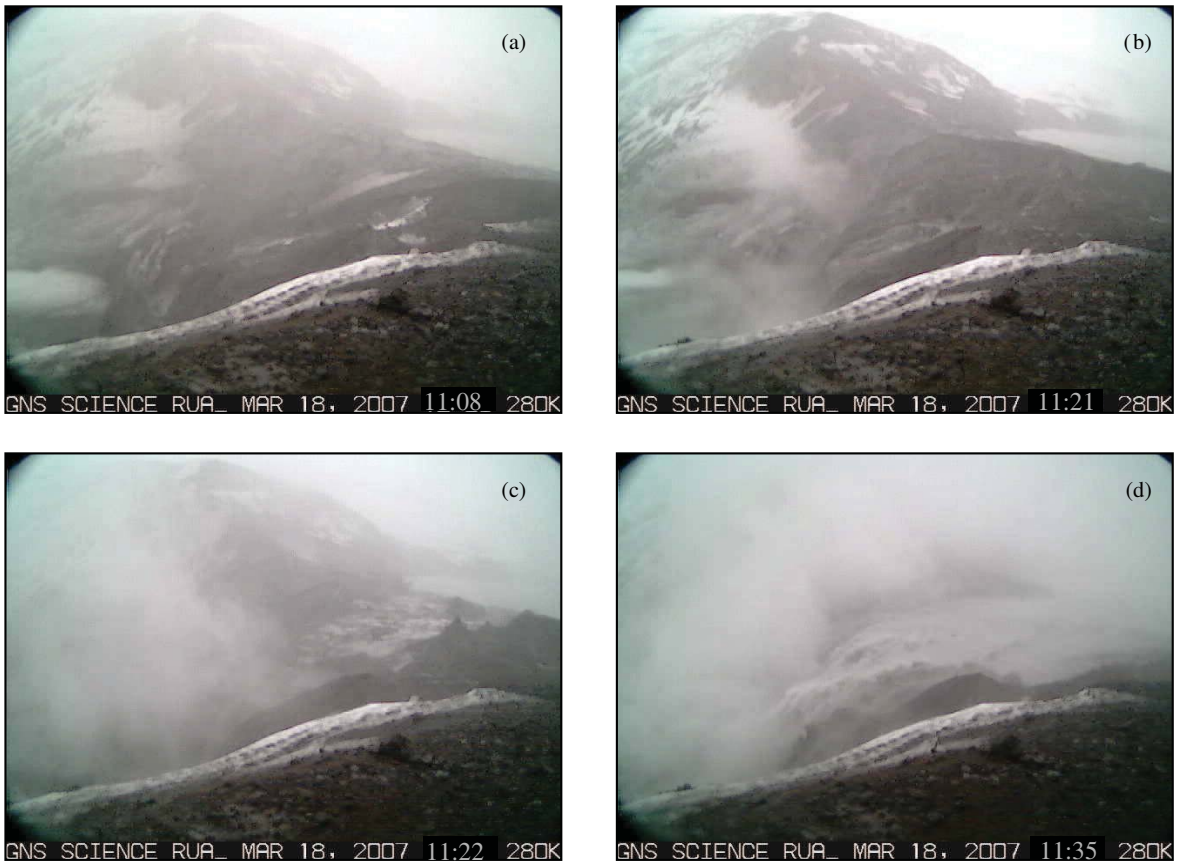

Figure 6.3: *Still camera images illustrating the breach and collapse sequence of the Crater Lake tephra dam. Roman numerals (I-V) correspond to variations in breach sequence as listed in Table 6.1. (a) taken at 23:08 (UT, 17th March), corresponding to (I). Initial rapid erosion of central part of dam back towards lake; (b) taken at 23:21 (UT). Erosion scarp widened, forming a single channel with initial breach at 11:10 (UT); (c) taken at 23:22 (UT), corresponding to (III). Large failure of dam face, tripwire pulls at 23:22 (UT), rapid draw-down of lake; (d) taken at 23:35 (UT). Rapid draw-down of lake, breach widened to most of channel. All images courtesy of V. Manville/GNS Science.*

a small collapse within the few remnants of the dam rather than to the outflow itself. Correlation, and hence confirmation, of this possible collapse with still camera images, however, are hindered by the inclement weather that obscured many of the images from the period.

6.2.1.2 Site 2 - near the Alpine Club hut

The second ERLAWS site consists of two geophones located c. 2.2 km downstream from the Crater Lake. The sensors at this site clearly recorded the lahar as it passed. The three main pulses within the signal can be associated with stages III-V as seen in the record from the Crater Lake (Figure 6.4b). The earlier stages I and II are not clear.

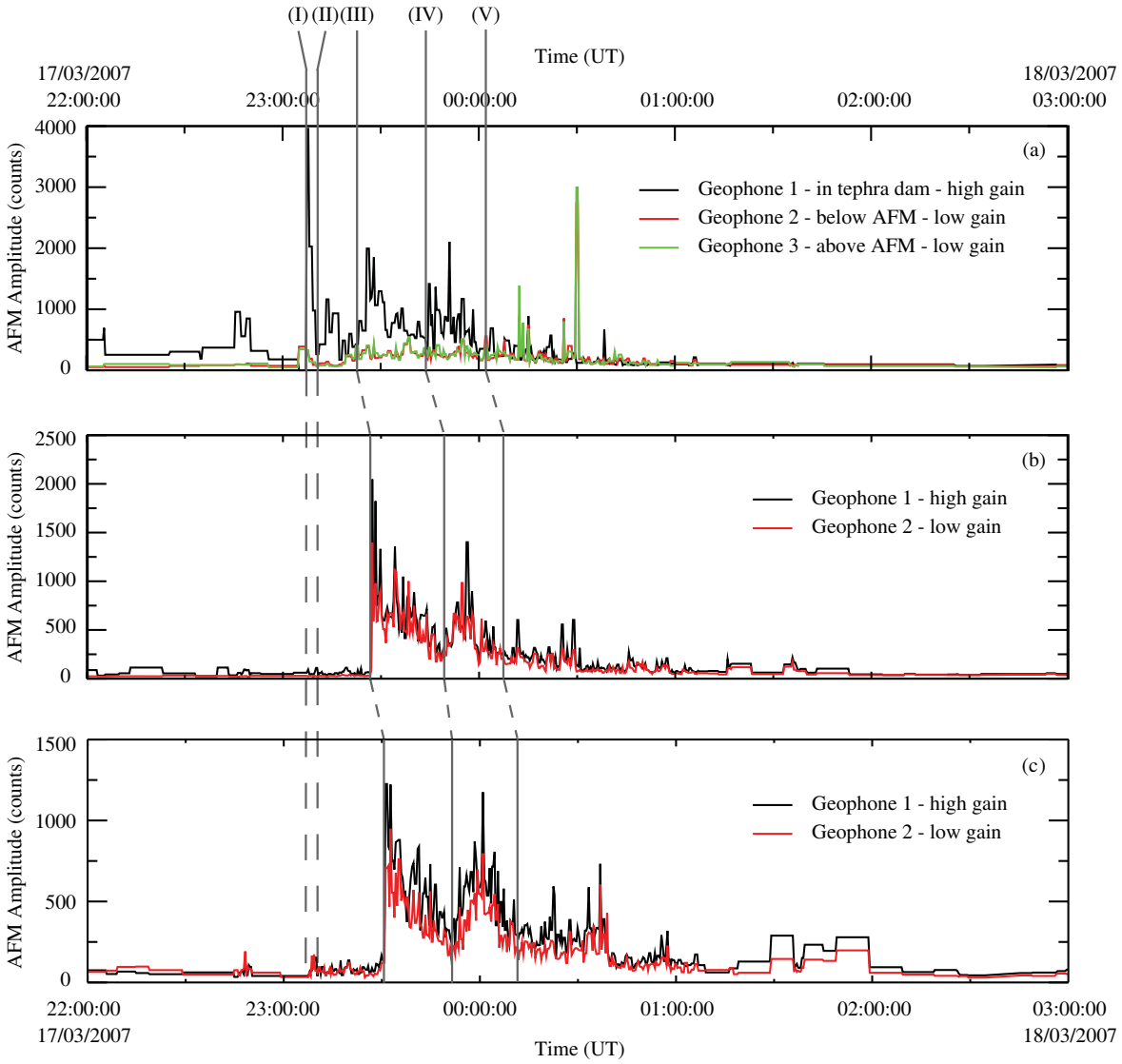

Figure 6.4: *Comparison of the geophone records of the Eastern Ruapehu Lahar Warning System sites: (a) Site 1 (Crater Lake); (b) Site 2 (c. 2.2 km from source); (c) Site 3 (near Tukino skifield village; c. 4.6 km from source). For all sites, Black line is high gain signal from geophone 1; Red line is low gain signal from geophone 2; Green line is low gain signal from geophone 3. Roman numerals (I-V) correspond to variations in breach sequence as listed in Table 6.1 and tracked between sites.*

There is some increase of signal in the record during these periods that is likely the result of the initial drainage from the singular small channel eroded into the dam during stage II. The predominant excitation comes from the larger volume of water release by the main collapse of the dam. There is an abrupt decrease in signal intensity at c. 00:30 (UT, 18th March). A similar decrease in intensity can be seen in the geophone record of site 1, but it is far less pronounced. Correlations with the still camera images from the Crater Lake indicate that this is likely related to a decrease in the outflow of

water from the lake as it was restricted to the central part of the breach. This implies that a sixth stage in the breach sequence might be appropriate.

Post-lahar surveys and LiDAR studies used to differentiate areas of deposition and erosion suggest that the flow eroded a relatively large volume of material by the time it had arrived at the second ERLAWS site (*Procter et al.* (2010)). Prior to the breakout lahar, a landslide had occurred in the upper Whangaehu Channel approximately 500 m downstream of the Crater Lake outlet[1]. The lahar eroded c. 1×10^6 m^3 of material from the toes of the landslide (now known as the Whangaehu landslide). In addition to this, the loss of toe support reactivated the landslide, initially blocking [part] of the channel before being eroded away by the flow (*Massey et al.* (2007)).

6.2.1.3 Site 3 - near the Tukino Skifield Village

ERLAWS site 3 consists of two geophones located c. 70 m above the river bed in a loosely compacted alluvium c. 4.6 km downstream of the lake outlet. The seismic record of the lahar at this point in the channel is very similar to that of site 2, indicating little had occurred to markedly change the bulk characteristics and behaviour of the flow (Figure 6.4c). Observers at c. 4 km downstream from source (c. 0.6 km upstream of site 3) reported that the flow was watery and muddy in appearance. Video footage and still camera images confirm this, and show the flow to be consistent with a turbulent hyperconcentrated streamflow (e.g., *Pierson* (2005)). Analysis of LiDAR data indicate that erosion had occurred between sites 2 and 3, suggesting the lahar had eroded a combined total of c. 3×10^6 m^3 of boulder-rich, gravelly sand over the first 5 km of its path (*Procter et al.* (2010)).

6.2.2 Dome Shelter (DS)

The Dome Shelter site consists of a single seismometer installed by GNS Science (GeoNet) as part of its general volcano-monitoring array. The sensor is housed in contact with a concrete base slab inside the Dome Shelter hut, and is a short-period

[1]Some ambiguity appears in the literature about the exact location of the landslide. *Massey et al.* (2007) locate the landslide 500 m downstream of the lake outlet, while *Procter et al.* (2010) position it c. 2 km from the outlet. For the purposes of this study, however, its exact position between sites 1 and 2 is not necessary; the volume of material available for remobilisation is much more important. In this respect, the estimated amount of material eroded is consistent between the studies, and is therefore considered reliable.

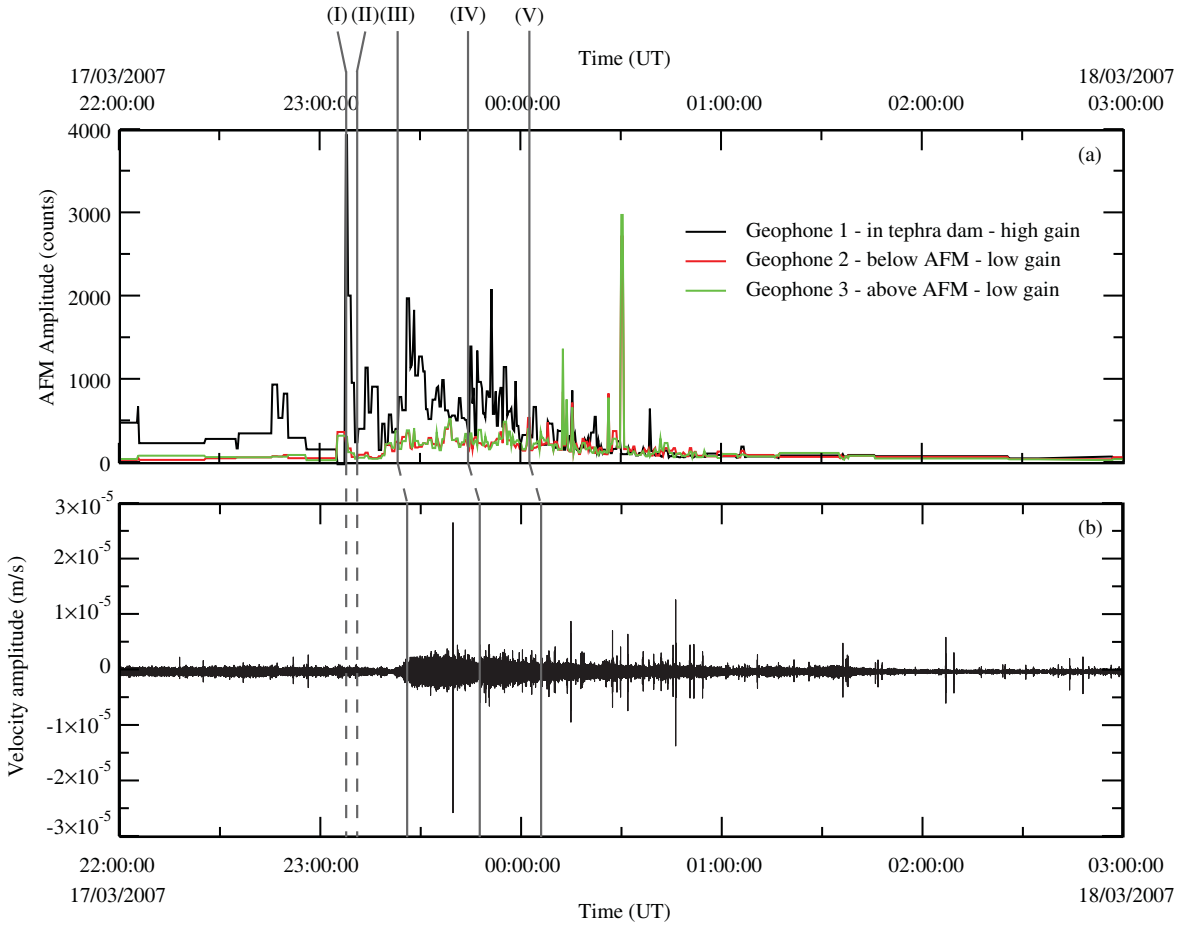

Figure 6.5: *Comparison of the seismic records of the breach sequence as recorded at sensors at the dam and on the opposite side of the lake. Roman numerals (I-V) correspond to variations in breach sequence as listed in Table 6.1. (a) the Eastern Ruapehu Lahar Warning System (ERLAWS) Site 1. Seismic response of the geophone record of the collapse and outflow. Black line is high gain signal from geophone 1, positioned in the dam; Red line is low gain signal from geophone 2; Green line is low gain signal from geophone 3. (b) the GeoNet volcano monitoring station at Dome Shelter. Vertical component time-series trace (100 sps) of lahar.*

seismograph.

The sensor was able to record the outflow of water from the lake, though the initial collapses of erosion scarps and minor outflow of stages I and II were attenuated too quickly to be recorded (Figure 6.5). The time-series trace is [somewhat] overshadowed by the sharp spike of a localised tremor at c. 23:40 (UT). The different pulses of stages III and IV, however, are clearly visible. Barely distinguishable is the change in behaviour associated with the start of stage V. The possible stage VI seen at both sites 2 and 3 of the ERLAWS array is not distinguishable at the Dome Shelter location.

6.2.3 Round-the-Mountain-Track (RTMT)

The Round-the-Mountain-Track (RTMT) monitoring site was successful in recording a wide range of data as the lahar passed. The instrumentation at the site included a broadband seismometer, two geophones, a radar stage gauge, a pore pressure temperature transducer, and a load cell. Many of the instruments were installed on a lava bluff to the true right of the channel, with the stage gauge positioned directly above the river bed. The seismometer and one of the geophones were buried c. 0.5-1 m down on the lava bedrock, while the second geophone was installed c. 100 m upstream. The pore pressure transducer and the load cell were installed into the bedrock of the channel base, to minimise the risk of erosion. All the instrumentation recorded the lahar, with the exception of the load cell that failed to record properly. Their results are displayed in Figure 6.6.

Figure 6.6a illustrates that the arrival of the lahar was associated with a sharp rise in stage level and pore pressure. The stage gauge was unable to record the exact height of the frontal flood wave as the fast rate of change between pre- and post-lahar arrival water level was too fast for it to register (see Chapter 2.3.1 for more details). An approximation of the likely stage profile was reconstructed from pore pressure measurements to indicate the relative height of the frontal wave (Figure 6.6a, blue dotted line). This reconstructed maximum stage height is in good agreement with the maximum water level suggested by post-lahar tideline measurements (*Procter* (2009)). The pore pressure and stage measurements remain predominantly in good agreement with each other for the remainder of the flow. The increase in pore pressure that occurs slightly before that of stage height at c. 01:50 (UT) is likely to be related to the start of a braided channel within the deposit during the tail of the flow where sediment is deposited and eroded locally to the pore pressure transducer. It is unclear when whole-flow deposition began, but latter flow stage levels remain higher than pre-event levels, indicating a bulk deposition of c. 4 m. The pore pressure record also remains high, though it does begin to decrease slowly after c. 02:00 (UT, 18th March). As the height of the deposit remains [relatively] level, this decrease in the pore pressure is likely related to the beginning of water drainage from the deposit. The temperature recorded by the pore pressure sensors correlates well with a decrease in overall bulk temperature

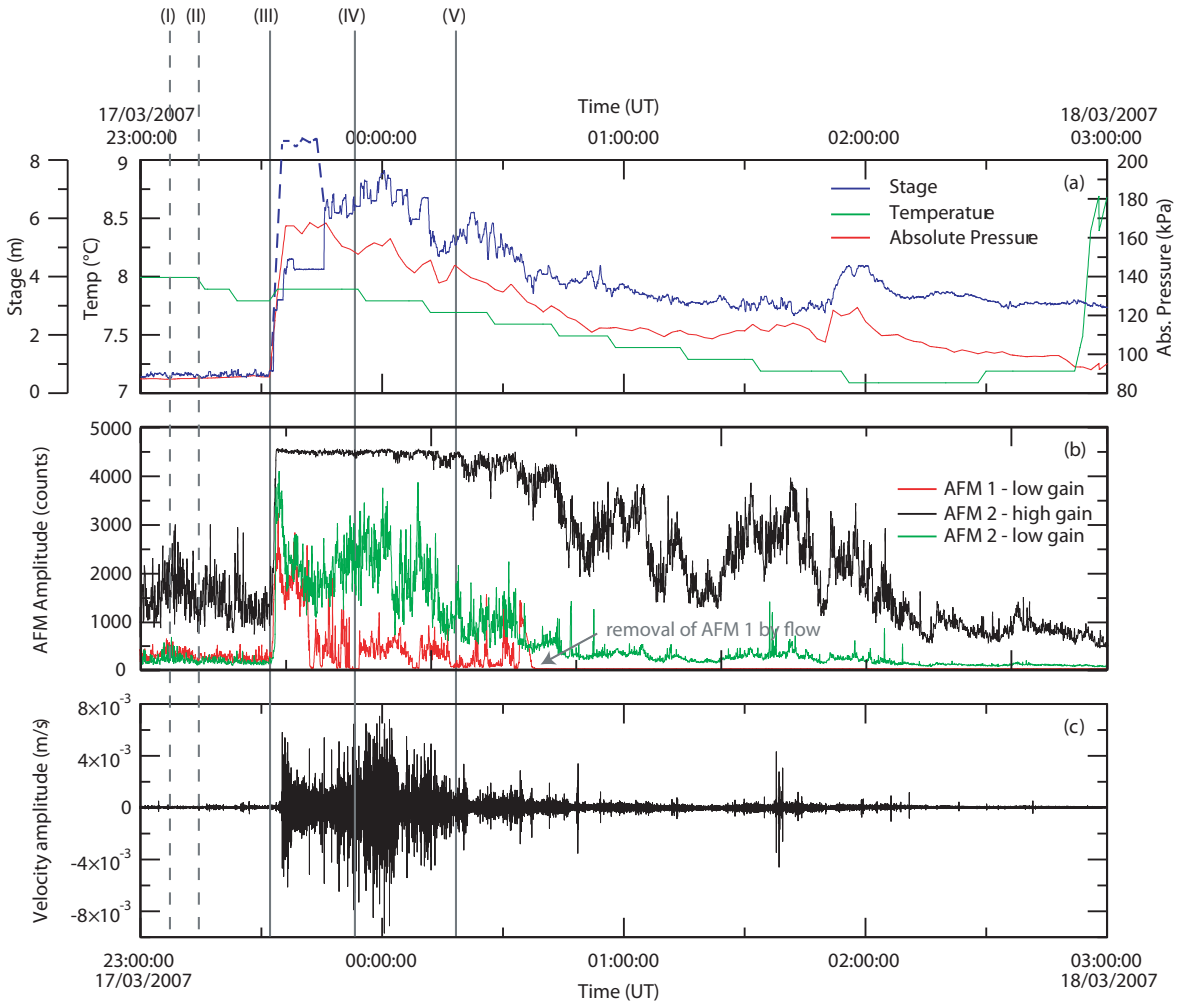

Figure 6.6: *Comparison of bulk flow characteristics at the Round-the-Mountain-Track. (a) Stage, temperature, and absolute pressure profiles. Blue line is stage (dotted blue line is reconstructed approximation based on pore pressure measurements); Green line is temperature; Red line is absolute pressure. (b) Seismic response recorded on geophones. Red line is low gain signal from geophone 1; Black line is high gain signal from geophone 2; Green line is low gain signal from geophone 2. (c) Vertical component time-series trace (100 sps) of lahar. Roman numerals (I-V) correspond to variations in breach sequence as listed in Table 6.1.*

as the lahar passed over it. Prior to the lahar flow, the water level in the streambed over the sensor had been minimal. As the flow passed over, and later deposited material, the thick flow above would have caused a lowering of near-bed region temperatures, possibly exacerbated by colder glacier-originating material eroded in the upper reaches of the channel.

The seismic response to the lahar showed a similar, but less distinct, pattern as that observed at monitoring sites closer to source. No correlation can be made to signals associated with stages I and II. From this, it is inferred that the RTMT site, at c.

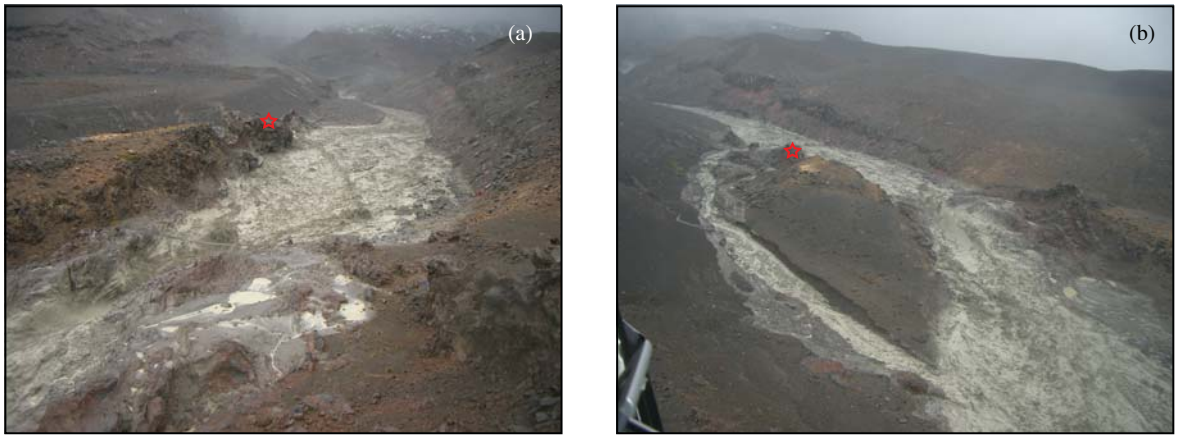

Figure 6.7: *Photographs illustrating the behaviour of the tail phase of the lahar at the RTMT site (7.4 km from source), taken from a survey helicopter. Main instrumentation site marked with star. (a) upstream view of lahar over walking bridge from true left side of channel. Note change in flow behaviour across width of channel due to deposits at different points along the far side of river; (b) upstream view of lahar from true right side of channel, showing the bifurcation of flow on either side of the lava bluff. (Photographs courtesy of H.J.R. Keys).*

7.4 km, was too far from source to pick up the signals from the initial erosion scarp collapses. The two geophones, because of their relative locations and heights above the channel, both to each other and to the seismometer, recorded different seismic profiles (Figure 6.6b). Both sensors recorded both high and low gain signals. Although not plotted herein, the high gain signal of sensor 1, just as with that of geophone 2, was swamped by ground-vibration amplitudes for much of its duration. This sensor (geophone 1) was located in the upper-channel position, closer to the channel bed, and was eroded by the flow at c. 00:40 (UT, 18th March). Aerial survey of the area during the tail phase of the lahar observed a bifurcation of flow had occurred at some point during its passage at the approximate location of geophone 1 (Figure 6.7). It is inferred, therefore, that this bifurcation occurred at c. 00:40 (UT), and was responsible for the removal of geophone 1. Geophone 2, however, continued to record the tail of the lahar as it passed the monitoring site.

Figure 6.8 illustrates the changing spectral density that occurred in the seismographic record as the lahar passed the RTMT site. The pre-event distribution of frequencies show a predominantly higher frequency fraction (Figure 6.8b). The sharp cut-off of the high frequency peaks in all components indicate that they are likely to range to even higher frequencies. The sampling rate of the instrument (100 sps), however, has limited the highest recordable frequency to 50 Hz because of the Nyquist

frequency. Small peaks at c. 5 Hz and c. 12 Hz also occur in the channel-parallel direction, while the channel-perpendicular and vertical components remained generally consistent from c. 0-45 Hz. During the passage of the lahar, the relative distribution of frequencies altered, with a higher fraction of energy associated with lower frequencies (c. 5-15 Hz). The initial front of the flow increases the energy observed on all frequencies and components, though there is a preferential increase in the lower frequency fraction, especially in the channel-parallel direction (Figure 6.8c). During the low ground-vibrational amplitude period following the arrival of flow (Figure 6.8d), there was a general dampening of all frequencies, with the exception of c. 4-6 Hz which increased in the horizontal components, especially the channel-parallel direction. Stage IV is characterised by the increase of energy in the higher frequency fraction, while the lower frequencies remain relatively consistent with the previous period of flow (Figure 6.8e). The tail phase of the flow (Figure 6.8f and g) indicates a generally consistent decrease in energy across all frequencies with decreasing ground-vibrational amplitude, though the energy in all frequencies remains much higher than normal streamflow values.

6.2.4 OnTrack Flood Gauge (OT)

The OnTrack Flood Gauge (OT), installed as a warning system for floods and lahars following the 1953 Tangiwai Disaster, is located c. 28 km from source (Figure 1.2; Table 1.1). The site now consists of the gauge itself positioned at the lower of two bends in the channel, and was augmented by the installation in 2006 of a broadband seismometer located at the approximate mid-point between the two channel bends (see Figure 4.5, page 100). In addition, a webcam was installed near the gauge by Horizons Regional Council, and recorded images every 30 seconds. Due to the bow wave produced by the lahar on the flood gauge, the flow height profile recorded by its stage sensor is unreliable. Using the pre- and post-event LiDAR surveys (data captured by Fugro Spatial Solutions Pty Ltd (Australia) and New Zealand Aerial Mapping) of the site, however, wetted perimeter profiles were produced, providing alternatives to a direct stage height measurement. These profiles were created using the LiDAR data as a base line or zero level above which relative flow height could be measured in conjunction with estimates made from the bow wave against the flood gauge itself from the webcam

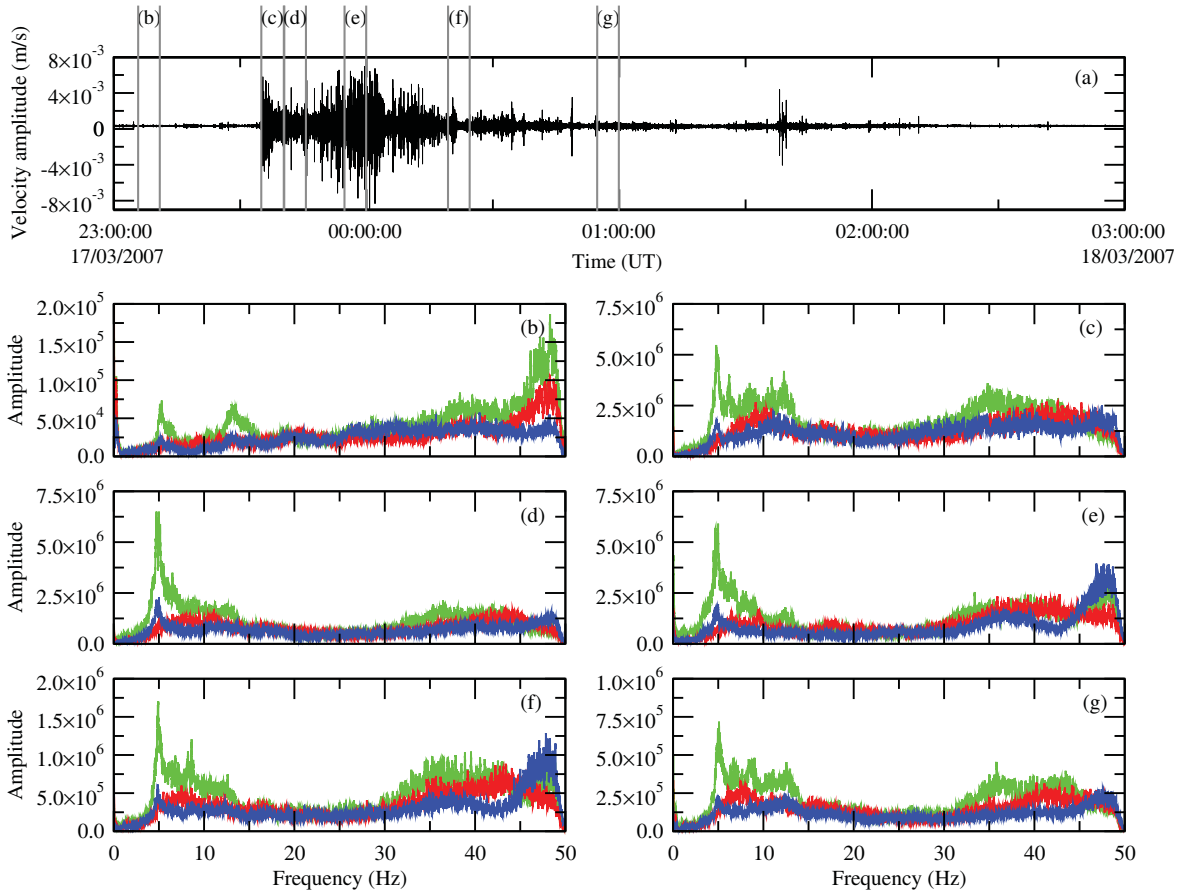

Figure 6.8: *Changing spectra associated with different phases in bulk flow characteristics: (a) Vertical component time-series trace (100 sps) of lahar. (b)-(g) 20-point running average total spectra calculated over 5-minute segments. Note different y-axis scales. Blue lines are vertical motion; Red lines are channel-perpendicular motion; Green lines are channel-parallel motion.*

images available throughout the flow (data provided by J.N. Procter and E.E. Doyle, respectively). Calculations were also possible using this bow wave height to generate a reasonably dependable velocity profile.

The wetted perimeter profiles calculated from LiDAR data at the OT site show a generally consistent behaviour over the length of the flow, with an exception at c. 00:50-01:00 (UT, 18th March) where a large peak in the profile calculated using the pre-event data can be seen while only a minimal peak is visible in the profile using the post-event data. The two profiles do, however, concur a sharp rise in flow height at the initial onset of the lahar. This is accompanied by a sharp increase in the velocity profile from normal streamflow. The velocity at peak wetted perimeter (and hence stage) levels decreased slightly from its initial peak value, but rose again as the wetted perimeter decreased

rapidly (Figure 6.9a). Correlations with the seismic profile recorded by the broadband sensor indicate that this frontal part of the flow contains the greatest ground-vibrational energy of any point in the flow, before a rapid decrease in energy occurs coinciding with the sharp decrease in wetted perimeter (Figure 6.9b). The observations made by *Cronin et al.* (1999) and in Chapter 5 suggest a segregation of this frontal part of the lahar into two phases. The first of these is comprised of an almost-pure streamwater wave that travels ahead of the lahar proper and is characterised by the rise to peak stage level. The second phase designates the period of rising sediment concentration to peak. It seems reasonable to apply this phase segregation to the flow at the OT. The low-but-increasing energy observed in the seismic profile can be correlated with onset and rise-to-peak in the wetted perimeter profile, and is hence regarded as Phase 1. This assumption of a near-pure streamwater wave at the front of the flow is corroborated by the still camera images recorded by the council's webcam (Figure 6.10a). Correlation of these images with the suggested period of rising sediment concentration imply that the distinct decrease in seismic energy and wetted perimeter is an appropriate boundary for the limit of Phase 2 (Figure 6.10b and c).

Observations of the third and fourth phases in a flow made by *Cronin et al.* (1999) and in Chapter 5 indicate that stage, velocity, and sediment concentration profiles all decrease during these phases. This is reflected in the still camera images recorded by the council's webcam (Figure 6.10d-f). The boundary between the two was designated as the point of peak Crater Lake-originating water concentration. The OT monitoring site, however, was not equipped with water sampling instruments and no data regarding variations in water chemistry exist. As such, the boundary between the two phases must be defined using another method. The anomalously high peak in wetted perimeter calculated from the pre-event LiDAR data at c. 00:51-00:58 (UT; Figure 6.9a) is likely related to a difference in channel morphology between the pre- and post-event profiles due to a temporally-localised erosion, but overall bulk-flow deposition, of material. This, therefore, is an unlikely candidate for the boundary between phases 3 and 4. A subsequent relative variation in the wetted perimeter profiles at c. 01:15 (UT), however, correlates well with the general decrease in the velocity profile, inferring a change in flow behaviour. The greater decrease in wetted perimeter calculated from the pre-event LiDAR data compared to the post-event data suggests an overall deposition of sediment

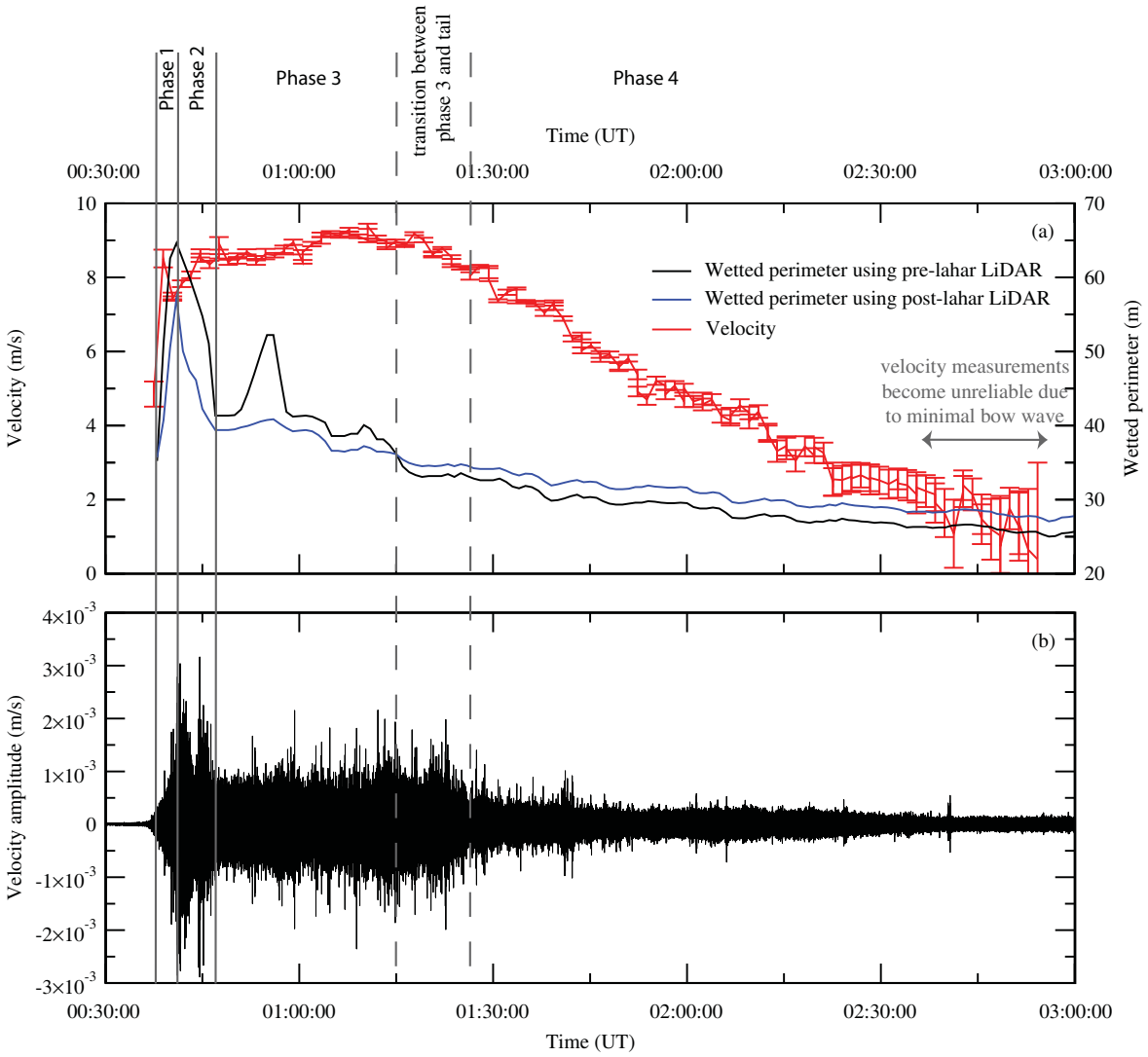

Figure 6.9: *Comparison of bulk flow characteristics at the OnTrack Flood Gauge. (a) Wetted perimeter and velocity profiles. Black line is wetted perimeter as calculated using LiDAR data collected before the lahar; Blue line is wetted perimeter as calculated using LiDAR data collected after the lahar; Red line is velocity. (b) Vertical component time-series trace (100 sps) of lahar. Phases marked correspond to variations in flow behaviour, similar to those witnessed in Cronin et al. (1999) and Chapter 5.*

began to occur. Seismic energy, however, still remained relatively high for a further c. 10 minutes (Figure 6.9b), indicating a still-high level of particle collisions, and hence likely sediment concentration, remained. As such, a single boundary point between phases 3 and 4 is not easily distinguishable. Instead, the period between initial bulk deposition, decreased velocity, and decreased ground-vibrational amplitude is defined as the transitional period between the two phases.

As with the analysis of the seismic signals at the RTMT site, the seismograph record

Figure 6.10: *Photographs illustrating the evolving nature of the lahar at the OnTrack Flood Gauge, corresponding to mid-times of spectra slices typical of different phases displayed in Figure 6.11b-g. (a) pre-lahar normal streamflow; (b) onset of flow (phase 1); (c) peak sediment concentration reducing turbulence and forming a smooth and oily surface; (d) high stage with decreasing sediment concentration and increasing turbulence (phase 3); (e) continued decreasing sediment concentration, increasing turbulence, and largely decreased stage height of late phase 3/early phase 4; (f) latter phase 4 with approximate pre-lahar stage levels but retaining higher-than-normal sediment concentration. All images courtesy of Horizons Regional Council.*

at the OT monitoring site was analysed to determine variations in the spectral density of the signal in three-dimensions (Figure 6.11). The relative amplitude and distribution profiles for the three components remain fairly consistent with one another. The horizontal components show similar profiles across most frequencies with preferential excitation above c. 5 Hz. The vertical distribution also exhibits a similar profile above c. 10 Hz, while frequencies below this are noticeably reduced in comparison. Phase 1 is characterised by increased energy in these distribution profiles (Figure 6.11c). The spectral profile of Phase 2 continued to have high energy in the lower end of the frequency spectrum, while the profile was relatively reduced for the higher end of the scale (Figure 6.11d). By the third phase, the spectral profile had returned to a profile more like that of Phase 1 (Figure 6.11e). The relative amplitudes were comparable for each frequency between the two phases. The tail phase of the flow again showed a return to a similar profile of a previous phase (Figure 6.11f and g). The distribution of the tail phase spectral density amplitudes was similar to that of Phase 2. It remained such for the length of the tail of flow with decreasing amplitude as the flow continued.

6.2.5 Tangiwai rail bridge (TRB)

The monitoring site at the Tangiwai rail bridge (TRB) is located c. 42 km from source. It consists of a radar stage gauge bolted to the upstream side of the lower part of the bridge at a mid-point between its central pylon and the true right side of the channel. In addition, there is an AFM installed on the banks of the true right side of the channel. This monitoring station is located at the approximate site of the 1953 Tangiwai Disaster in which a similar flow destroyed the then rail bridge just prior to the passage of the Auckland-Wellington Express train (e.g., *O'Shea* (1954)). The activation and alerts sent out by the ERLAWS and OnTrack Flood Gauge sensors on 18th March 2007 (see above) ensured that all trains due to cross the bridge were halted long before the arrival of the lahar at Tangiwai. The cessation of trains prevented not only another disaster befalling the rail bridge but also any corruption of signal by noise relating to crossing locomotives.

Figure 6.12 shows the response of the monitoring equipment to the lahar at the TRB. The lahar arrived with a rapid increase in the stage profile of c. 4 m, which continued for c. 5 minutes, rising to a peak of c. 5.3 m above the channel base.

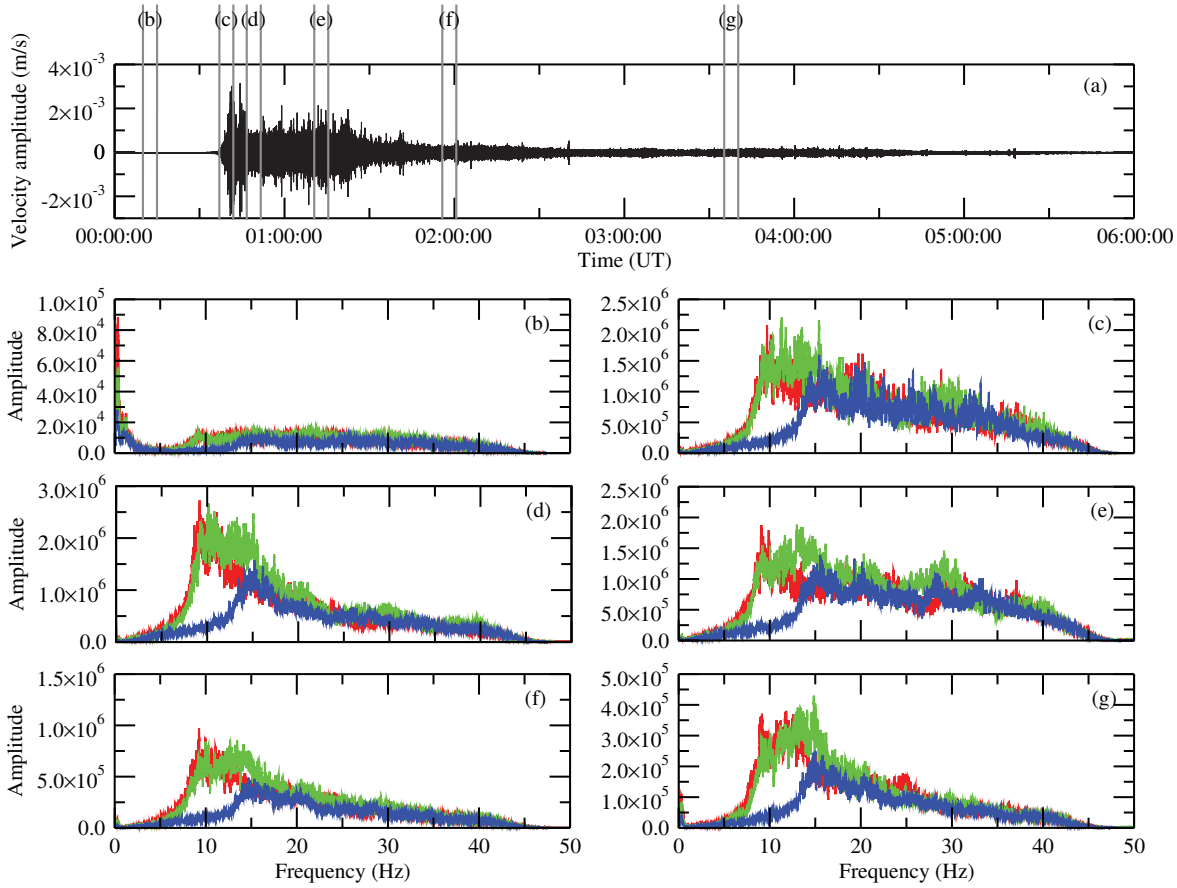

Figure 6.11: *Changing spectra associated with different phases in bulk flow characteristics at the OnTrack Flood Gauge: (a) Vertical component time-series trace (100 sps) of lahar. (b)-(g) 20-point running average total spectra calculated over 5-minute segments. Note different y-axis scales. Blue lines are vertical motion; Red lines are channel-perpendicular motion; Green lines are channel-parallel motion.*

This rising stage level is concurrent with an initial rise in ground vibration amplitude followed by a small drop to a lower amplitude as the stage rose to peak. The following slight drop in stage and subsequent return to a higher level coincided with a rise in ground velocity motion. Video footage of the arrival of the lahar indicates an almost pure water wave in the frontal part (Figure 6.13a), followed by a visibly rising sediment concentration. The observed changes in flow characteristics can be correlated to the approximate time of the changes seen in the geophysical records. As such, this point is ascribed as the boundary between phases 1 and 2.

While limited images were taken during the tail of the flow (Figure 6.13b), photographs and video footage do not exist for the main bulk of its passage past the TRB. In addition, there were no witnesses present at the rail bridge and records are unavailable from those [non-scientific] few at the nearby road bridge. As such, there is no

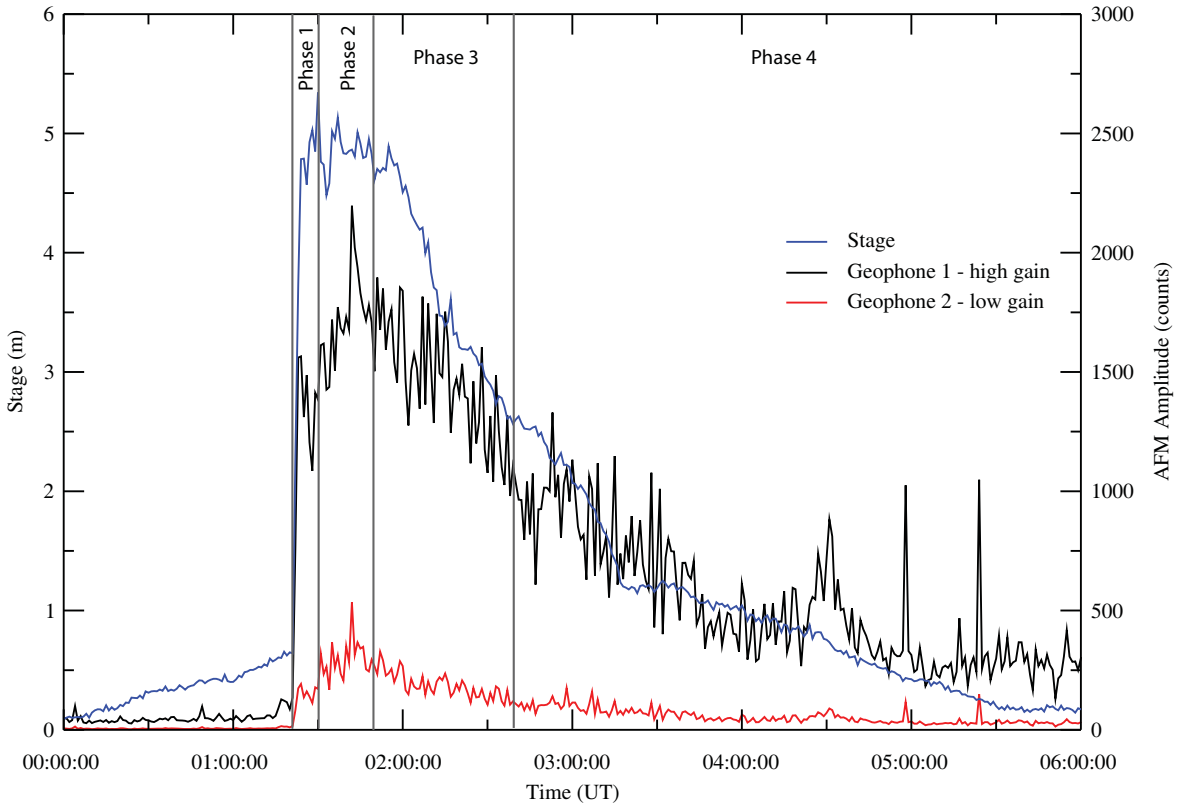

Figure 6.12: *Comparison of bulk flow characteristics at the Tangiwai rail bridge. Blue line is stage; Black line is high gain signal from geophone 1; Red line is low gain signal from geophone 2. Phases marked correspond to variations in flow behaviour, similar to those witnessed in Cronin et al. (1999) and Chapter 5.*

observational record of any changes in the behaviour of the flow during the transitions between the expected phases 2, 3, and 4. The geophysical record, therefore, is the only evidence of any changes in flow characteristics and behaviour. The seismic signature of the main bulk of the flow shows changes in the sensor response to the lahar passage, most notably in the high gain profile. After the initial rise in ground vibrational amplitude associated with phase 1, the amplitude continued to rise to its peak. The response then began to decline after c. 01:49, coinciding with a small initial drop in stage height. This was then followed by an overall decreasing ground vibrational response that correlates well with the more dramatic drop in stage height between c. 02:00 and c. 03:20 of c. 3.5 m. A shift in the geophone response occurs at c. 02:45 with a change in the rate of decrease of the energy associated with ground vibrations. This shift aligns well with a slight change in the stage level decrease rate during this main part of the lahar. Another shift in the geophone response occurred in the latter part of the flow at c. 03:50, while a distinct change in the water level occurred with a

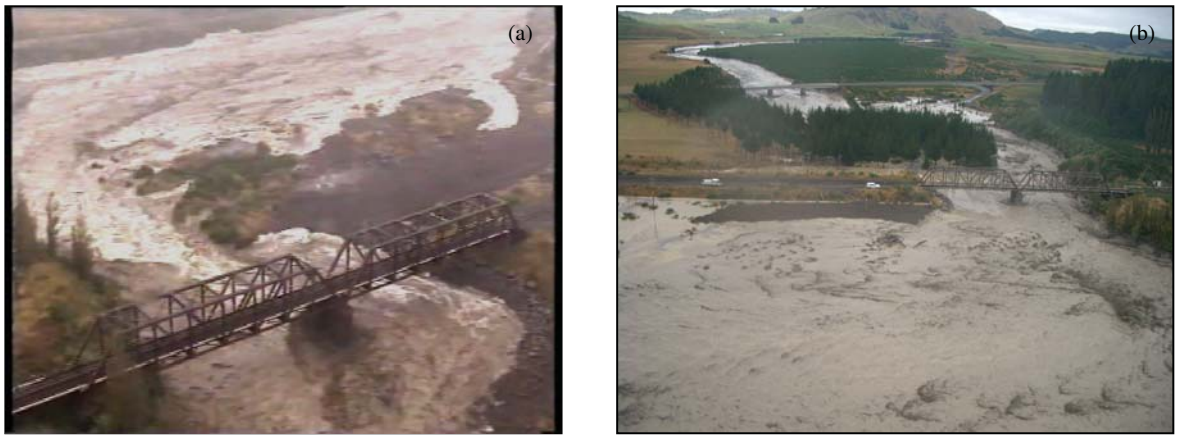

Figure 6.13: *Photographs illustrating the evolving nature of the lahar at the Tangiwai rail bridge. (a) onset of flow (phase 1), looking upstream of rail bridge. (Image courtesy of camera footage provided by G. Mackley).; (b) tail of flow, looking downstream over rail (foreground) and road (background) bridges. (Photograph courtesy of H.J.R. Keys).*

more gradual rate of decrease from c. 03:20 to its return to normal streamflow heights.

Following the 4-phase segregation of a lahar as defined by *Cronin et al.* (1999) and further explored in Chapter 5, phase 2 consists of rising sediment concentration to peak that is immediately preceeded by the near-pure water wave of phase 1. The observations of Chapter 5 suggest that this phase is characterised by high ground vibrational amplitudes to peak with a high stage level that drops as the water level decreases slightly. This is attributed to the restrictions on the collisional energy produced by particle-particle and particle-substrate interactions because of reduced freedom of movement. As such, the period of decreased stage height and ground motion at c 01:49 is ascribed to the boundary between phases 2 and 3. Phase 3 is considered to be the period during which the fraction of Crater Lake-originated water rises to peak, before the tail of phase 4. As no bucket samples of the flow were taken at this site, there is no record of the fraction of this water present at any point along its passage. Correlations with the temporal variations in flow observed at Colliers bridge (Chapter 5.5) suggest that the rate of stage height decrease associated with this phase boundary does not vary greatly. In addition, the change in this rate that occurs at the TRB at C. 03:20 happens after the phase boundary does at the downstream site. As such, the phase boundary is assigned to the shift in flow characteristics implied by the change in ground vibrations at c. 02:45. Further phases are possible, such as is suggested at 03:20 and 03:50. As no definitive additional phase changes were observed in the comprehensive

dataset collected at Colliers bridge, however, it is assumed that the 4-phase segregation model of *Cronin et al.* (1999) is the most appropriate to use here also.

6.2.6 Colliers bridge (CB)

As has been previously described in Chapter 5, the dataset collected at the Colliers bridge monitoring site was one of the most comprehensive obtained for this lahar. The site is situated c. 83 km from the source of flow, and was equipped with a broadband seismometer. Video and camera images were collected for large parts of the flow, and bucket samples were taken every 10-15 minutes (see Chapter 5.2 for further details). These were later analysed for water chemistry and sediment content.

The observations and analysis of the data collected at Colliers bridge has been detailed in Chapter 5. The results of these analyses (shown in Figures 5.3-5.6) have supported the segregation of the lahar into four phases, as suggested by *Cronin et al.* (1999). These phases consist of an initial near-pure water wave that encompasses a rapid rise in stage and discharge of flow, with little suspended sediment, and dominated by bed-frictional motion. Phase 2 comprises the period of rising sediment concentration to peak and heralds the advent of the lahar proper. Stage and velocity levels remain high, while water chemistry indicates the influx of Crater Lake-originated material. Collisional and saltating motion of particles dominate this phase. The third phase is associated with the rise-to-peak of the fraction of Crater Lake-originated water. Suspended sediment concentrations decrease, along with stage and velocity levels. Ground vibrational amplitudes decrease because of the dampening effect of the increased viscosity of flow and restricted freedom of particles preventing maximum collisional energy production. Phase 4 comprises the transition of the lahar back towards normal streamflow conditions. While localised peaks, or small pulses, can be seen in the seismic record, there is no correlation possible with the other datasets as to whether these represent further phases in the transition of the lahar or not. As flow volume decreased, particles settled out of suspension, causing displacement of zones of fluid and localised elutriation of fines held in [transient] suspension. As no confirmation of additional phases can be made, it is assumed that the 4-phase model is correct.

6.3 Discussion

6.3.1 Proximal sites

In the generation area of the 18th March 2007 lahar, seismic signals aid in the interpretation of the Crater Lake dam-failure mechanisms and timing. Subtle changes in the signal intensity recorded on vertical-component, 10 Hz geophones, on and near the dam, show a sudden and rapid period of headward erosion of rills/small gullies during the rainstorm-initiated dam collapse. Over only one minute, the geophones picked up a strong signal pulse (Stage I, Figure 6.2), which probably resulted from sudden slips and rockfalls developing in the existing erosion gullies, causing them to rapidly propagate inward to the dam crest. This led to a short respite period (Stage II) where gradual draw-down of the lake occurred through a small and stable channel that was not visible on photographic records (*Massey et al.* (2009)), but could be seen as an eight-minute long medium-amplitude peak in the geophone signal. Sudden, rapid slumping and failure of the dam face occurred again to generate a strong energy peak on the geophone, heralding the catastrophic release of Crater Lake water (Stage III). This initial, violent release tailed off after c. 20 minutes, and was followed by a further peak in seismic energy (Stage IV), associated with additional tephra slumping, bank erosion and collapse that led to widening of the breakout breach.

It appears that throughout the dam-failure event, the geophone signals reacted most strongly to rockfall, slumping and debris collapsing events, with apparent low signal response relating to differing outflow rates from the Crater Lake. As seen at the Round-the-Mountain-Track, OnTrack Flood Gauge, and Colliers Bridge sites (Figures 6.8, 6.11, and 5.4, respectively), vertical-component seismic signals in the 1-10 Hz range from broadband seismographs are the least responsive to lahar flow, with dominant energy magnification in cross- and parallel-channel signals. Vertical component signals appear to reflect the saltation or collision of large particles in the flow with the channel base. As described in Chapter 3, the dominant momentum of flows and vectors of particle motion are often parallel with flow; therefore, flow-parallel signals are exacerbated. Due to the U-shaped geometry of the channel, cross-channel energy is also often amplified, with collisions against any channel wall augmenting this. At the breach area, the initial flow would have been primarily water, relatively shallow

and with low sediment concentration. This water-dominated flow likely generated little vertical-component signal, except when bank-erosion, or other tephra-bank collapses, occurred.

From the initiation point to the next recording sites, 2.2 and 4.6 km downstream, evidence of the initiation events and initial spill-over flow (Stages I and II) had largely disappeared. Instead, these sites show that two major peaks in flow had formed, with a third peak developing at the more distal site (Figure 6.4). The two major peaks show a strong correlation to Stage III and IV peaks in the dam-geophone records. The relatively subtle transition to Stage IV implied by the dam-geophone record appears to have marked a major bank-erosion and widening episode, leading to a strong surge-like increase in discharge from the lake. The third apparent peak in flow, recorded weakly at 2.2 km and more strongly at 4.6 km from source, seems also to relate to a spike in a geophone signal (Geophone 3 on Figure 6.4) recorded at the source. This may reflect a landslide of up to 1 x 10^6 m^3 of debris, with its toe entering the Whangaehu channel at c. 2 km from source (immediately upstream of the 2.2 km geophone site). Entry of this debris appears to be caused by erosion of the toe of a pre-existing landslide by the initial part of the lahar.

Downstream, on the multi-component record at the Round-the-Mountain-Track (RTMT) site 7.4 km from source (Figure 6.6), there appears to be no record of the initial breach sequence, but a strong representation of three pulses of flow in the river-level record. The first two pulses in the river appear to reflect the geophone-signal defined Stages III and IV described above, with the third pulse representing an expansion of the seismic peak observed at the 4.6 km geophone site (possibly landslide related). This evidence confirms that the geophone signal's Stages III and IV were related to peaks in flow discharge from the Crater Lake, which propagated through to at least 7.4 km from source.

The analysis of frequency response in relation to the passage of the lahar at the RTMT shows that after the arrival of the first flow peak (Figure 6.8d) and during the second peak flow (Figure 6.8e), the strongest amplification of signal was in the channel-parallel component. As discussed in Chapters 3 and 4, strong channel-parallel signals in the low-frequency range indicate friction between particles and the river bed, associated with sliding or rolling motion downstream, or also saltation signals with

a dominant down-channel vector, rather than random and cross-channel motion. In Chapter 4, the difference between the relatively turbulent 18th March 2007 lahar and the plug-flow like 25th September 2007 snow-slurry lahar were emphasised. Here, by analysing the relative signal strengths inside the 18th March lahar, it appears that the periods indicated by Figure 6.8d and e show the strongest evidence for sliding, rolling or down-flow saltation of large particles, consistent with periods when particle concentrations were highest. This implies that the initial peak of flow may have been more dilute than these later portions, in accordance with the observations of watery peak-flow and clear-water peak tide-line erosion as reported by *Procter et al.* (2010).

6.3.2 Distal sites

The proximal records show that the flow was complex, developing two peaks that resulted directly from a two-step erosion and spillout of Crater Lake, as well as a third peak, possibly related to reactivation of a landslide in the upper Whangaehu valley. In the distal sites, this initial character of the flow is influenced by other transformational processes, including repeated sedimentation and erosion (as described by *Procter et al.* (2010)) and entrainment of stream-water in the flow path, as hypothesised by earlier studies of lahars in this catchment (*Cronin et al.* (1997); *Cronin et al.* (1999)), eye-witness observations of the lahar (*Manville and Cronin* (2007)), and the highly detailed multi-component record of Colliers Bridge (82 km from source), as presented in Chapter 5.

From the 7.4 km RTMT site, the next instrumental observations were made some 21 km further downstream at the OnTrack Gauge. Here was the first opportunity to calculate the surface velocity throughout the lahar passage and, via still-images, evaluate the properties of the flow. At this site (Figure 6.9) the seismic record preserves what could be a relict of the initial two-peaks generated by the step-wise dam collapse and these are reflected in the surface velocity, but not in the flow-wetted perimeter or height. However, flow images reveal that the initial part of the flow may have been considerably more dilute than the flow front. This implies that this segregation into two peaks may rather be a bow-wave of stream water pushed ahead of the lahar proper, as postulated for earlier flows by *Cronin et al.* (1999) and as seen more clearly in downstream sites (Chapter 5). The equivalent seismic energy between cross and down-

channel components (Figure 6.11) indicates that the flow was at all times turbulent, with little plug-like behaviour. Cross and down-channel seismic energy was higher in the second seismic peak (Figure 6.11d), suggesting that its sediment concentration was possibly higher than during the initial watery peak flow. At this site, either or both mechanisms could be operating to lead to the two initial seismic energy peaks, although it appears that the formation of a frontal watery wave, by pushing stream water ahead of the flow, had already started.

By the time the flow had reached Tangiwai, 42 km from source, video evidence of the frontal wave shows it was almost pure water, and likely pushed ahead of the lahar proper. This led to two peaks in the stage and geophone records (Figure 6.12), with the second, higher-energy, seismic peak indicating when sediment concentrations in the turbulent flow were highest. This pattern in the flow passage was exacerbated downstream at Colliers Bridge, 83 km from source, where a full evolution of the flow had occurred into a leading bow wave of stream water, followed by a mixing zone and the trailing sediment-rich part of the lahar proper, rich in the original Crater Lake (as described in Chapter 5).

6.4 Conclusions

Analysis of the seismic records of the 18th March 2007 lahar from source to over 80 km distant show that this lahar had a complex, time-variable structure at any one site, and was highly spatially variable in structure over distance. Over the upper c. 7 km of travel, source-variations were the strongest influences on the flow character, with two apparent pulses in Crater Lake outflow interpreted to reflect step-wise, sudden failures of the impounding tephra dam and a third representing a subsequent landslide in the upper catchment. A step-wise failure of the dam was recognised in the analysis of *Massey et al.* (2009), although they concentrated on the initial weak outflow, which is here shown not to feature in geophone signals downstream of the dam. Here, the combined instrumental data along the upper Whangaehu catchment are used to show that a major peak in geophone signals, at least 23 min after the 23:22 (UT) landslide-induced breakout from the lake, was generated by side-wall collapse and/or deepening of the failure of the dam, leading to a significant pulse of increased outflow from Crater

Lake. A stepwise failure, either vertically or laterally, is consistent with the layered structure of the dam, with alternating, flat-lying coherent and weak tephra/breccia beds.

Seismic and other instrumental/photographic records show that while the source variations and upper-catchment landsliding processes were important over the first 7 km of flow, beyond this, other processes of lahar transformation became dominant. By 28 km from source, the formation of a watery bow wave ahead of the lahar (c.f., *Cronin et al.* (1999)) had started to overprint the earlier observed flow structure. In addition, continual sediment deposition and erosion along the channel (evidenced by topographic analysis of *Procter et al.* (2010)) had probably served to homogenise the initial surges in flow produced by stepwise lake-water release. Beyond 28 km from source, the observational data and seismic signals are consistent with progressively stronger development of a bow wave composed of ambient stream water leading the lahar proper. Sediment concentrations were highest in the lahar proper, along with concentrations of the acidic and salt-rich Crater Lake water.

Seismic signals, especially the relative excitement of frequency and the three different components, were useful to show differences in parts of a lahar moving past individual sites. In all cases, it appears that the 18th March 2007 lahar did not reach the stage of becoming a fully-fledged debris flow, with plug-flow or Bingham-flow characteristics. At times, there were signals associated with stronger laminar components of flow; these were usually recorded as a relative increase in the channel-parallel energy signals in the 5-15 Hz range over those of the equivalent cross-channel recordings. These differences were absent by 28 km from source, implying that the repetitive deposition and erosion observed along the channel to this point (c.f., *Procter et al.* (2010)) had homogenised the flow to become dominantly a hyperconcentrated flow, with turbulence dampened only during periods of peak sediment concentration.

Chapter 7

Conclusions and avenues for future research

Chapter 7 provides a summary of the results of this study and suggests areas in which future research might be concentrated.

7.1 Conclusions

Lahars and other mass flows are potentially highly devastating and put at risk large areas on the slopes of volcanoes around the world. These flows can vary greatly in size, from the very small (e.g., common, rain-triggered lahars) to the very large (e.g., Crater Lake dam outbreaks or eruption-triggered flows). In order to accurately model and predict likely inundation zones and resultant damage, it is fundamental to better understand the dynamics and flow mechanisms that control the behaviour of a lahar. To this end, a comprehensive dataset collection from monitoring sites along a lahar-prone channel is invaluable. The unpredictable nature and onsets of these types of flow, however, mean that detailed scientific monitoring of real-world examples are limited (e.g., *Lavigne et al.* (2000b)). In addition, many areas at risk from these flows are either too dangerous or remote to easily access. The expected Crater Lake outbreak lahar from Mt. Ruapehu, New Zealand, combined with repeated seasonal rain-triggered lahars at Mts. Merapi and Semeru, Indonesia, allowed for scientific monitoring of different flow types. By outfitting the affected channels with a variety of instrumentation, detailed datasets were able to be collected that have yielded invaluable resources to the understanding of lahar flow behaviour, the further development of seismic sensors as hazard warning instruments, and their use as additional sources of data collection and moni-

toring tools. The understanding of the variable behaviour possible during a lahar, as well as the identification of the specific flow type recorded, is fundamental to modelling approximations of flow volumes, sediment concentrations, likely inundation areas, and probable damage by the flow. It is essential for the development of future warning systems that the variations that can occur within a single lahar are better understood, as lahars represent a serious threat to the slopes of many volcanoes worldwide.

7.2 Avenues for future research

The outcomes of this study have provided new insight into the analysis of the internal dynamics of lahars, most notably advances in the interpretation of particle motions and interactions as recorded by seismic sensors. It is, however, recognised that this work is only a step along the way towards fully understanding the highly complex nature of lahars, correlating the ground vibrational response to their passage, and the ultimate provision of a remote monitoring system that can identify and assess the threat posed by any mass flow. Upon completion of this study, a number of aspects remain in need of further, focused investigation. The following avenues of research would contribute greatly to the better understanding of the dynamic processes inherent in, and hence possible mitigations of, lahars and other mass flows:

1. **Collection of more lahar data, with increased sampling rates, to better understand flow dynamics and leading to proxies of characteristics.** In order to better understand, and ultimately comprehensively predict the motions of, lahars and other mass flows, it is necessary to obtain as much data as possible to model as many of the different aspects of a flow as can be achieved. To this end, the continued experimentation and real-world observation and monitoring of such phenomena, with a wide range of different triggering mechanisms, sediment concentrations, volumes, and behaviours is essential. A key part to the scientific monitoring of these lahars must be a better sampling record of the sediment concentrations throughout a flow and, with development of vertical profile detectors and analysers, greater constraints to the distinct changes in such, both temporally and spatially. This in turn will allow for greater understanding of the geophysical records of lahars, and the effects differing characteristics have on the

record. With this knowledge, a more robust proxy of sediment concentration and flow volume may be developed from the geophysical record.

2. **Development of additional remote monitoring systems.** Current monitoring instrumentation are bounded by the limitations imposed on them due to problems with functionality and reliability that can arise from either contact with a highly destructive lahar or with the elements on a volcano. In addition, constant maintenance and replacement of equipment is both expensive and often not practical or safe because of the location of the monitoring site. As a result, the development of additional remote systems that need little maintenance would be highly beneficial for areas that would otherwise remain unmonitored.

3. **Comparative analyses between different mass flow types.** The analyses of the seismic profiles of snow-slurry lahars made during this study revealed significant differences in the spectral profiles as compared with the signals of both hyperconcentrated and debris flows. The inclusion, fraction, and/or domination of water within a lahar has significant effect on the ground vibrational response to its passage. A similarly distinct shift in the distribution of frequencies excited by avalanche movements (e.g., *Surinach et al.* (2001)) and rockfalls (e.g., *Vilajosana et al.* (2008)) have also been noted. A detailed and extensive comparative analysis is needed across a wide range of mass flows, including floods, block-and-ash flows, and pyroclastic flows, in addition to those already being studied, in order to quantify those frequency ranges affected by each type of flow. From this, a classification method for the different phenomena may be possible.

4. **Development of general volcano-monitoring sensors to detect and monitor lahars.** Due to the unpredictable natures and onsets of lahars, many volcanoes have lahar warning systems that detect the passage of a flow. These systems not only provide and alert of the oncoming flow to populated areas downstream, but also often record and trigger other monitoring sensors. In many other cases, however, no such systems are in place; detection of mass flows is restricted to those large enough to be recorded by the sensors used in the general monitoring of the volcano itself. This study has primarily concentrated on the analysis of recorded data from near-channel sources. Similar analyses of the flows at distances further

from the channels, however, could provide a detection and identification system for those edifices that are not equipped with detailed monitoring systems. It may also be possible using such sensors to track the passage of the flow, similarly to the method of *Jolly et al.* (2002) for locating pyroclastic flows at Montserrat, West Indies.

5. **Development of a program to detect, identify, and analyse a mass flow.** Many detection systems, such as those for lahars and avalanches, rely simply on the triggering of an alert once a sensor records a signal above a predetermined threshold for a set length of time. The snow-slurry lahars that were produced by the eruption of Mt. Ruapehu in September 2007, however, highlighted a flaw in this method. The relatively seismically quiet snow-slurry flows were unable to trigger the lahar warning system as the trigger thresholds were set to higher amplitudes than the flows reached. This is of great concern, as snow-slurry lahars have the potential to entrain large volumes of material and pose serious threat to areas downstream, such as occurred at Nevado del Ruiz, Columbia, in 1985 (e.g., *Pierson et al.* (1990)). To remove or lower these alert thresholds, used to prevent alert triggering by normal volcanic tremor or inclement weather, would result in the near-constant triggering of alerts when no lahar occurs. The development of a program that can analyse any possible 'lahar', either automatically or with minimal human interaction, and identify what type of flow, if any, caused the signal would prevent potentially deadly lahars from being missed by a warning system in the future.

Pursuing these avenues of research will lead to both more flow-specific monitoring equipment for those channels where required, development of more remote identification of mass flow movement using general volcano-monitoring sensors, and a classification and identification model for the mass flows themselves. Ultimately, this will allow for the development of better warning systems that will in turn help minimise the hazard posed by such phenomena.

Appendix A

Electronic files (on disc)

The attached CD contains all of the raw and final processed data files used during the course of this study, as well as the code files containing programs written in order to analyse the data as detailed below. Please note that this information also appears on the attached disc within the file "Electronic_files_details.txt".

A.1 Data files

The data files have been sorted according to the area at which the lahars took place (i.e., Ruapehu, Semeru, or Merapi), and have then been divided into raw and processed data file. Please see the file "Electronic_files_details.txt" for details as to the contents of each data file.

A.2 Code files

This following Matlab scripts on the attached disc were written and used to plot and analyse the seismic records of lahars:

trace_yaxis.m This function is to convert the seismic amplitude axis of a trace into ground motion velocity (m/s).

seis_true_time.m This function is to set up the correct start time for a seismic file read into Matlab.

spectra_analysis_suzy_0903.m This function is to calculate a spectra for various windows within a given long input signal. NB calls function spectra_analysis_suzy_0902.m

spectra_analysis_suzy_0902.m This function is to calculate amplitude and energy spectra of short signals, given an input signal "signal" with a length which is a power of 2. NB called by function spectra_analysis_suzy_0903.m

energy_data_extract.m This function is to extract seismic energy data from spectral analysis function answer file, for both a single lahar and any packets contained within.

Other programs used to analyse the seismic data were either contained within the 'sac' program available from Lawrence Livermore Laboratory or within MATLAB signal processing tools, or were provided by my supervisor, Dr. Steve Sherburn, and are therefore the intellectual property of GNS Science.

References

Aki, K. (1980), Attenuation of shear-waves in the lithosphere for frequencies from 0.05 to 25 Hz, *Physics of the Earth and Planetary Interiors*, *21*, 50–60.

Aki, K., and V. Ferrazzini (2000), Seismic monitoring and modeling of an active volcano for prediction, *Journal of Geophysical Research-Solid Earth*, *105*(B7), 16,617–16,640.

Alzwar, M. (1985), G. Kelut, *Tech. Rep. No. 108*.

Ancey, C. (2007), Plasticity and geophysical flows: A review, *Journal of Non-Newtonian Fluid Mechanics*, *142*(1-3), 4–35.

Arattano, M. (1999), On the use of seismic detectors as monitoring and warning systems for debris flows, *Natural Hazards*, *20*, 197–2013.

Arattano, M., and L. Marchi (2005), Measurements of debris flow velocity through cross-correlation of instrumentation data, *Natural Hazards and Earth System Sciences*, *5*(1), 137–142.

Arattano, M., and L. Marchi (2008), Systems and sensors for debris-flow monitoring and warning, *Sensors*, *8*(4), 2436–2452.

Arattano, M., and F. Moia (1999), Monitoring the propagation of a debris flow along a torrent, *Hydrological Sciences Journal-Journal Des Sciences Hydrologiques*, *44*(5), 811–823.

Bahavar, M., and R. North (2002), Estimation of background noise for international monitoring system seismic stations, *Pure and Applied Geophysics*, *159*, 911–944.

Baher, H. (2004), *Analog and Digital Signal Processing*, John Wiley and Sons, New York, USA.

Beauduin, R., P. Lognonn, J. P. Montagner, S. Cacho, J. F. Karczewski, and M. Morand (1996), The effects of the atmospheric pressure changes on seismic signals, *Bulletin of the Seismological Society of America*, *86*(6), 1760–1769.

Berger, C., B. W. McArdell, B. Fritschi, and F. Schlunegger (2010), A novel method for measuring the timing of bed erosion during debris flows and floods, *Water Resources Research*, *46*, doi:10.1029/2009WR007,993.

Bessason, B., G. Baldvinsson, and O. Thorarinsson (1999), Skynjun og greining snjofloa me bylgjumlingum, *Tech. Rep. Technical Report No. 99002*, University of Iceland, Engineering Research Institute.

Bessason, B., G. Baldvinsson, O. Thorarinsson, and G. Eirksson (2000), Detecting and analysis of avalanches using wave measurements, in *Snow engineering: recent advances and developments*, edited by E. Hjorth-Hansen, I. Holand, S. Lset, and H. Norem, pp. 33–40, Balkema, Rotterdam.

Bessason, B., G. Eiriksson, O. Thorarinsson, A. Thorarinsson, and S. Einarsson (2007), Automatic detection of avalanches and debris flows by seismic methods, *Journal of Glaciology*, *53*(182), 461–472.

Beverage, J., and J. Culbertson (1964), Hyperconcentrations of suspended sediment, *Journal of Hydraulic Division, American Society of Civil Engineers*, *90*, 117–126.

Blong, R. (1984), *Volcanic Hazards*, North Ryde.

Bottacin-Busolin, A., S. Tait, A. Marion, A. Chegini, and M. Tregnaghi (2008), Probabilistic description of grain resistance from simultaneous flow field and grain motion measurements, *Water Resources Research*, *44*(W09419).

Bridge, J. (2003), Sediment transport by unidirectional water flows, in *Encyclopedia of sediments and sedimentary rocks*, edited by G. Middleton, M. Church, M. Coniglio, L. Hardie, and F. Longstaffe, pp. 609–619, Kluwer Academic Publishers, Dordrecht, The Netherlands.

Brodscholl, A., S. B. Kirbani, and B. Voight (2000), Sequential dome-collapse nues ardentes analyzed from broadband seismic data, Merapi Volcano, Indone-

sia, *Journal of Volcanology and Geothermal Research*, *100*(1-4), doi:10.1016/S0377–0273(00)00,145–1.

Bulthuis, H., A. Prosperetti, and A. Sangani (1995), 'Particle stress' in disperse two-phase potential flow, *Journal of Fluid Mechanics*, *294*, 1–16.

Burtin, A., L. Bollinger, J. Vergne, R. Cattin, and J. L. Nabelek (2008), Spectral analysis of seismic noise induced by rivers: A new tool to monitor spatiotemporal changes in stream hydrodynamics, *Journal of Geophysical Research-Solid Earth*, *113*(B5), doi:10.1029/2007JB005,034.

Calder, E., R. Luckett, R. Sparks, and B. Voight (2002), Mechanisms of lava dome instability and generation of rockfalls and pyroclastic flows at Soufriere Hills volcano, Montserrat, in *The eruption of Soufriere Hills volcano, Montserrat, from 1995 to 1999*, vol. 21, edited by T. Druitt and B. Kokelaar, pp. 173–190, Geological Society of London, London, U.K.

Calvache, M. L. (1990), Pyroclastic deposits of the November 13, 1985 eruption of Nevado-del-Ruiz Volcano, Colombia, *Journal of Volcanology and Geothermal Research*, *41*(1-4), 67–78.

Caplan-Auerbach, J., S. G. Prejean, and J. A. Power (2004), Seismic recordings of ice and debris avalanches of Iliamna Volcano (Alaska), *Acta Vulcanologica*, *16*(1-2), 9–20.

Carrivick, J., V. Manville, and S. J. Cronin (2008), A fluid dynamics approach to modelling the 18th March 2007 lahar at Mt Ruapehu, New Zealand, *Bulletin of Volcanology*, pp. doi:10.1007/s00,445–008–0213–2.

Caruso, P., and M. Pareschi (1993), Estimation of lahar and lahar-runout flow hydrograph on natural beds, *Environmental Geology*, *22*(2), 141–152.

Chen, C. (1988), General solutions for viscoplastic debris flow, *Journal of the Hydraulics Division - ASCE*, *114*, 259–282.

Chen, J., S. Chang, and M. Yeng (1991), Characteristics of underground sound generated by debris flows and the fabrication of NJ-2 type debris-flow alarm (in Chinese),

in *2nd National Debris Flow Conference*, Chinese Academy of Science, Chengdu, China.

Chow, V. (1959), *Open Channel Hydraulics*, McGraw-Hill, New York.

Chow, V. (1988), *Applied Hydrology*, McGraw-Hill, New York.

Christenson, B., and C. Wood (1993), Evolution of a vent-hosted hydrothermal system beneath Ruapehu Crater Lake, New Zealand, *Bulletin of Volcanology*, *55*, 547–565.

Christenson, B., M. Crump, and R. Glover (1992), Ruapehu Crater Lake bathymetry, temperature profile and water column chemistry, in *International Symposium on Hazardous Crater Lakes*, pp. 25–29, Misasa and Tateyama, Japan.

Cole, S. E., S. J. Cronin, S. Sherburn, and V. Manville (2009), Seismic signals of snow-slurry lahars in motion: 25 September 2007, Mt Ruapehu, New Zealand, *Geophysical Research Letters*, *36*, 10.1029/2009gl038,030.

Cooley, J., and J. Tukey (1965), An algorithm for the machine calculation of complex Fourier series, *Mathematics of Computation*, *19*(90), 297–301.

Coussot, P., and M. Meunier (1996), Recognition, classification and mechanical description of debris flows, *Earth-Science Reviews*, *40*(3-4), 209–227.

Cronin, S. J., V. E. Neall, J. A. Lecointre, and A. S. Palmer (1996), Unusual "snow slurry" lahars from Ruapehu volcano, New Zealand, September 1995, *Geology*, *24*(12), 1107–1110.

Cronin, S. J., V. E. Neall, J. A. Lecointre, and A. S. Palmer (1997), Changes in Whangaehu river lahar characteristics during the 1995 eruption sequence, Ruapehu volcano, New Zealand, *Journal of Volcanology and Geothermal Research*, *76*(1-2), 47–61.

Cronin, S. J., V. E. Neall, J. A. Lecointre, and A. S. Palmer (1999), Dynamic interactions between lahars and stream flow: A case study from Ruapehu volcano, New Zealand, *Geological Society of America Bulletin*, *111*(1), 28–38.

Cronin, S. J., J. A. Lecointre, A. S. Palmer, and V. E. Neall (2000a), Transformation, internal stratification, and depositional processes within a channelised, multi-peaked lahar flow, *New Zealand Journal of Geology and Geophysics*, *43*(1), 117–128.

Cronin, S. J., V. E. Neall, J. A. Lecointre, and A. S. Palmer (2000b), Dynamic interactions between lahars and stream flow: A case study from Ruapehu volcano, New Zealand: Reply, *Geological Society of America Bulletin*, *112*(7), 1151–1152.

Dalziel, S. (2005), Digiflow user guide, p. http://www.dampt.cam.ac.uk/lab/digiflow.

Denlinger, R. P., and R. M. Iverson (2001), Flow of variably fluidized granular masses across three-dimensional terrain 2. Numerical predictions and experimental tests, *Journal of Geophysical Research-Solid Earth*, *106*(B1), 553–566.

Donoghue, S. (1991), Late Quaternary volcanic stratigraphy of the south-eastern sector of Mount Ruapehu ring plain, New Zealand, Phd, Massey University, Palmerston North.

Donoghue, S., V. Neall, A. S. Palmer, and R. Stewart (1997), The volcanic history of Ruapehu during the past 2 millennia based on the record of the Tufa Trig tephras, *Bulletin of Volcanology*, *59*, 136–146.

Doyle, E., S. Cronin, S. E. Cole, and J. C. Thouret (2009), The challenges of incorporating temporal and spatial changes into numerical models of lahars, in *18th World IMACS Congress and MODSIM09 International Congress on Modelling and Simulation*, edited by R. Anderssen, R. Braddock, and L. Newham, pp. 2665–2671, Modelling and Simulation Society of Australia and New Zealand and International Association for Mathematics and Computers in Simulation, Cairns, Australia.

Doyle, E., S. Cronin, S. E. Cole, and J. C. Thouret (2010), The coalescence and organisation of lahars at Semeru volcano, Indonesia, *Bulletin of Volcanology*, pp. doi:10.1007/s00,445–010–0381–8.

Endo, E. T., and T. Murray (1991), Real-Time Seismic Amplitude Measurement (RSAM) - a Volcano Monitoring and Prediction Tool, *Bulletin of Volcanology*, *53*(7), 533–545.

Fagents, S. A., and S. M. Baloga (2005), Calculation of lahar transit times using digital elevation data, *Journal of Volcanology and Geothermal Research Modeling and Simulation of Geophysical Mass Flows*, *139*(1-2), 135–146.

Fagents, S. A., and S. M. Baloga (2006), Toward a model for the bulking and debulking of lahars, *Journal of Geophysical Research-Solid Earth*, *111*(B10).

Flix, G., and N. Thomas (2004), Relation between dry granular flow regimes and morphology of deposits: formation of leves in pyroclastic deposits, *Earth and Planetary Science Letters*, *221*(1-4), doi:10.1016/S0012–821X(04)00,111–6.

Galgaro, A., P. R. Tecca, R. Genevois, and A. M. Deganutti (2005), Acoustic module of the Acquabona (Italy) debris flow monitoring system, *Natural Hazards and Earth System Sciences*, *5*(2), 211–215.

Genevois, R., P. R. Tecca, M. Berti, and A. Simoni (2000), Debris-flow in the Dolomites: Experimental data from a monitoring system, in *Debris-Flow Hazards Mitigation: Mechanics, Prediction and Assessment*, edited by Wieczorek and Naeser, pp. 283–291, Rotterdam.

Glicken, H., and Y. Nakamura (1988), Restudy of the 1888 eruption of Bandai Volcano, Japan, in *Kagoshima International Conference on Volcanoes*, pp. 392–395.

Graettinger, A., V. Manville, and R. Briggs (2010), Depositional record of historic lahars in the upper Whangaehu Valley, Mt. Ruapehu, New Zealand: implications for trigger mechanisms, flow dynamics and lahar hazards, *Bulletin of Volcanology*, *72*, doi:10.1007/s00,445–009–0318–2.

Gray, J., and J. Gartner (2009), Technological advances in suspended-sediment surrogate monitoring, *Water Resources Research*, *45*, doi:10.1029/2008WR007,063.

Hackett, W., and B. F. Houghton (1989), A facies model for a Quaternary andesitic composite volcano: Ruapehu, New Zealand, *Bulletin of Volcanology*, *51*, 51–68.

Hadley, K. C., and R. LaHusen (1995), Technical manual for an experimental acoustic flow monitor, *Tech. Rep. Open-File Report 95-114*, US Geological Survey.

Hancox, G., I. A. Nairn, P. Otway, G. Webby, N. Perrin, and J. Keys (1997), Stability assessment of Mt. Ruapehu Crater Rim following the 1995-1996 eruptions, *Tech. Rep. 43605B*, Institute of Geological and Nuclear Sciences.

Hatton, L., M. Worthington, and J. Makin (1986), *Seismic Data Processing: Theory and Practice*, Blackwell Scientific Publications, Oxford, UK.

Healy, J. (1954), Origin of flood and ruapehu lahars., in *Tangiwai Railway Disaster: Report of Board of Inquiry*, Government Printer, Wellington, N.Z.

Hodgson, K. (1993), Late quaternary lahars from mount ruapehu in the whangaehu river valley, unpublished phd, Massey University, Palmerston North.

Hodgson, K. A., and V. R. Manville (1999), Sedimentology and flow behavior of a rain-triggered lahar, mangatoetoenui stream, ruapehu volcano, new zealand, *Geological Society of America Bulletin*, *111*(5), 743–754.

Huang, C. J., H. Y. Yin, and C. L. Shieh (2003), Experimental study of the underground sound generated by debris flows, in *Debris-flow hazards mitigation: mechanics, prediction and assessment*, edited by D. Rickenmann and C.-l. Chen, pp. 743–753, Millpress, Rotterdam.

Huang, C. J., C. L. Shieh, and H. Y. Yin (2004), Laboratory study of the underground sound generated by debris flows, *Journal of Geophysical Research-Earth Surface*, *109*(F1).

Huang, C. J., H. Y. Yin, C. Y. Chen, C. H. Yeh, and C. L. Wang (2007), Ground vibrations produced by rock motions and debris flows, *Journal of Geophysical Research-Earth Surface*, *112*(F2).

Hurlimann, M., D. Rickenmann, and C. Graf (2003), Field and monitoring data of debris-flow events in the Swiss Alps, *Canadian Geotechnical Journal*, *40*(1), 161–175.

Hurst, A., and S. Sherburn (1993), Volcanic tremor at Ruapehu: characteristics and implications for the resonant source, *New Zealand Journal of Geology and Geophysics*, *36*, 475–485.

Itakura, Y., H. Inaba, and T. Sawada (2005), A debris-flow monitoring devices and methods bibliography, *Natural Hazards and Earth System Sciences*, *5*(6), 971–977.

Iverson, R. M. (1997), The physics of debris flows, *Reviews of Geophysics*, *35*(3), 245–296.

Iverson, R. M., and R. P. Denlinger (2001), Flow of variably fluidized granular masses across three-dimensional terrain 1. Coulomb mixture theory, *Journal of Geophysical Research-Solid Earth*, *106*(B1), 537–552.

Iverson, R. M., S. P. Schilling, and J. W. Vallance (1998), Objective delineation of lahar-inundation hazard zones, *Geological Society of America Bulletin*, *110*(8), 972–984.

Janda, R. J., N. G. Banks, T. C. Pierson, M. L. Calvache, and J. C. Thouret (1986), Interaction between ice and pyroclastic sediments erupted during the 13 November 1985 eruption of Nevado del Ruiz, Columbia, *EOS Transactions AGU*, *67*(16), 406.

Johnston, D. M., B. F. Houghton, V. E. Neall, K. R. Ronan, and D. Paton (2000), Impacts of the 1945 and 1995-1996 Ruapehu eruptions, New Zealand: An example of increasing societal vulnerability, *Geological Society of America Bulletin*, *112*(5), 720–726.

Jolly, A. D., G. Thompson, and G. E. Norton (2002), Locating pyroclastic flows on Soufriere Hills Volcano, Montserrat, West Indies, using amplitude signals from high dynamic range instruments, *Journal of Volcanology and Geothermal Research*, *118*(3-4), 299–317.

Keys, H. (2003), Minor change confirmed in the elevation of the lava surface controlling the overflow of Crater Lake, Mount Ruapehu., *Tech. rep.*, Department of Conservation.

Keys, H. (2007), Lahars of Ruapehu Volcano, New Zealand: risk mitigation, *Annals of Glaciology*, *45*, 155–162.

Keys, H. (2009), Lessons from the warning system and management for Ruapehus Crater Lake breakout event of 18 March 2007, in *Symposium of NZ Society on*

Large Dams, vol. 35, pp. 49–56, Institution of Professional Engineers New Zealand, Proceedings of Technical Groups, Wellington, New Zealand.

Keys, H., and P. Green (2008), Ruapehu lahar New Zealand 18 March 2007: Lessons for hazard assessment and risk mitigation 1995-2007, *Journal of Disaster Research*, *3*(4), 284–296.

Kim, Y., M. Muste, A. Hauet, W. Krajewski, A. Kruger, and A. Bradley (2008), Stream discharge using mobile large-scale particle image velocimetry : A proof concept, *Water Resources Research*, *44*(W09502), doi:10.1029/2006WR005,441.

Knighton, D. (1998), *Fluvial forms and processes. A new perspective.*, A Hodder Arnold Publication, London.

Lahr, J. C. (1989), HYPOELLIPSE/Version 2.0: A computer program for determining local earthquake hypocentral parameters, magnitude, and first motion pattern, *Tech. Rep. Open-File Report 89-23*, U.S. Geological Survey.

LaHusen, R. (2005), Acoustic flow monitor system - user manual, *Tech. Rep. Open-File Report 02-429*, U.S. Geological Survey.

Lavigne, F. (2004), Rate of sediment yield following small-scale volcanic eruptions: a quantitative assessment at the Merapi and Semeru stratovolcanoes, Java, Indonesia, *Earth Surface Processes and Landforms*, *29*(8), 1045–1058.

Lavigne, F., and H. Suwa (2004), Contrasts between debris flows, hyperconcentrated flows and stream flows at a channel of Mount Semeru, East Java, Indonesia, *Geomorphology Hazards of Mass Movements*, *61*(1-2), 41–58.

Lavigne, F., and J. C. Thouret (2000), Lahars: deposits, origins, and behaviour, *Bulletin De La Societe Geologique De France*, *171*(5), 545–557.

Lavigne, F., and J.-C. Thouret (2002), Sediment transportation and deposition by rain-triggered lahars at Merapi Volcano, Central Java, Indonesia, *Geomorphology*, *49*(1-2), 45–69.

Lavigne, F., J. C. Thouret, B. Voight, H. Suwa, and A. Sumaryono (2000a), Lahars at Merapi volcano, Central Java: an overview, *Journal of Volcanology and Geothermal Research*, *100*(1-4), doi:10.1016/S0377–0273(00)00,150–5.

Lavigne, F., J. C. Thouret, B. Voight, K. Young, R. LaHusen, J. Marso, H. Suwa, A. Sumaryono, D. S. Sayudi, and M. Dejean (2000b), Instrumental lahar monitoring at Merapi Volcano, Central Java, Indonesia, *Journal of Volcanology and Geothermal Research*, *100*(1-4), doi:10.1016/S0377–0273(00)00,151–7.

Lavigne, F., A. Tirel, D. Le Froch, and S. Veyrat-Charvillon (2003), A real-time assessment of lahar dynamics and sediment load based on video-camera recording at Semeru Volcano, Indonesia, in *Debris-Flow Hazards Mitigation: Mechanics, Prediction, and Assessment*, vol. 2, edited by D. Rickenmann and C. Y. Chen, pp. 871–882, Millpress, Rotterdam.

Leonard, G. S., D. M. Johnston, D. Paton, A. Christianson, J. Becker, and H. Keys (2008), Developing effective warning systems: Ongoing research at Ruapehu volcano, New Zealand, *Journal of Volcanology and Geothermal Research*, *172*(3-4), 199–215.

Leprettre, B. J. P., J. P. Navarre, and A. Taillefer (1996), First results from a preoperational system for automatic detection and recognition of seismic signals associated with avalanches, *Journal of Glaciology*, *42*(141), 352–363.

Liu, C.-H., R. Nagel, D. Schecter, S. Coppersmith, S. Mujumdar, O. Narayan, and T. Witten (1995), Force fluctuations in bead packs, *Science*, *269*, 513–515.

Lowe, D. R., S. N. Williams, H. Leigh, C. B. Connor, J. B. Gemmell, and R. E. Stoiber (1986), Lahars initiated by the 13 November 1985 eruption of Nevado-del-Ruiz, Colombia, *Nature*, *324*(6092), 51–53.

Lube, G., and S. J. Cronin (2008), The June 2006 eruption of Merapi Volcano, Java, Indonesia - a study tour to gain a first-hand understanding of the dynamics, hazards and engineering mitigation of pyroclastic density currents, *Tech. rep.*, Massey University.

Lube, G., S. J. Cronin, and J. N. Procter (2009), Explaining the extreme mobility of volcanic ice-slurry flows, Ruapehu volcano, New Zealand, *Geology*, *37*(1), 15–18.

Macedonio, G., and M. Pareschi (1992), Numerical simulation of some lahars from Mount St Helens, *Journal of Volcanology and Geothermal Research*, *54*, 65–80.

Major, J. J. (1997), Depositional processes in large-scale debris-flow experiments, *Journal of Geology*, *105*(3), 345–366.

Major, J. J. (2003), Hindered settling, in *Encyclopedia of sediments and sedimentary rocks*, edited by G. Middleton, M. Church, M. Coniglio, L. Hardie, and F. Longstaffe, pp. 358–360, Kluwer Academic Publishers, Dordrecht, The Netherlands.

Major, J. J., and R. M. Iverson (1999), Debris-flow deposition: Effects of pore-fluid pressure and friction concentrated at flow margins, *Geological Society of America Bulletin*, *111*(10), 1424–1434.

Major, J. J., and T. C. Pierson (1992), Debris flow rheology: Experimental analysis of fine-grained slurries, *Water Resources Research*, *28*(3), 841–857.

Major, J. J., T. C. Pierson, and K. M. Scott (2005), Debris flows at Mount St Helens, Washington, USA, in *Debris-flow Hazards and Related Phenomena*, edited by M. Jakob and O. Hunger, pp. 685–731, Praxis. Springer, Berlin, Heidelberg.

Manville, V. (2004), Palaeohydraulic analysis of the 1953 Tangiwai lahar: New Zealand's worst volcanic disaster, *Acta Vulcanologica*, *XVI*(1/2), 137–152.

Manville, V. (2006), EQC Project No. 06/518. The predicted Ruapehu Crater Lake lahar: maximising the scientific gain, *progress report EQC Project No. 06/518*.

Manville, V., and S. Cronin (2007), Break-out lahar from New Zealand's Crater Lake, *EOS Transactions AGU*, *88*, 441–442.

Manville, V., K. A. Hodgson, B. F. Houghton, J. R. H. Keys, and J. D. L. White (2000), Tephra, snow and water: complex sedimentary responses at an active snow-capped stratovolcano, Ruapehu, New Zealand, *Bulletin of Volcanology*, *62*(4-5), 278–293.

Marchi, L., M. Arattano, and A. M. Deganutti (2002), Ten years of debris-flow monitoring in the Moscardo Torrent (Italian Alps), *Geomorphology*, *46*(1-2), 1–17.

Marcial, S., A. A. Melosantos, K. C. Hadley, R. G. LaHusen, and J. N. Marso (1996), Instrumental lahar monitoring at Mount Pinatubo, in *Fire and Mud: Eruptions and Lahars of Mount Pinatubo, Philippines*, edited by C. G. Newhall and R. S. Punongbayan, pp. 1015–1022, University of Washington Press, Seattle and London.

Mascarenhas, F., K. Toda, M. Miguez, and K. In oue (2005), *Flood Risk Simulation*, International Series on Progress in Water Resources, WIT Press, Southampton, U.K.

Massey, C., S. Nelis, and H. Keys (2007), Whangaehu Landslide - Preliminary findings from the inspection carried out on 25 April 2007, *Tech. Rep. GeoNet landslide response report*, GeoNet / GNS Science.

Massey, C., V. Manville, G. Hancox, H. Keys, C. Lawrence, and M. McSaveney (2009), Out-burst flood (lahar) triggered by retrogressive landsliding, 18 March 2007 at Mt Ruapehu, New Zealand - a successful early warning, *Landslides*, pp. doi:10.1007/s10,346–009–0180–5.

McCutcheon, S., and J. Bradley (1984), Effects of high sediment concentrations on velocity and sediment distributions, in *Water for resource development*, pp. 43–47, American Society of Civil Engineers, Coeur d'Alene, Idaho.

McNamara, D., and R. Buland (2004), Ambient noise levels in the continental United States, *Bulletin of the Seismological Society of America*, *94*(4), 1517–1527.

Mukhopadhyay, B., J. Cornelius, and W. Zehner (2003), Application of kinematic wave theory for predicting flash flood hazards on coupled alluvial fan-piedmont plain landforms, *Hydrological Processes*, *17*(4), 839–868.

Nairn, I. A., C. Wood, and C. Hewson (1979), Phreatic eruptions of Ruapehu: April 1975, *New Zealand Journal of Geology and Geophysics*, *22*, 115–173.

Neall, V. (1996), Hydrological disasters associated with volcanoes, in *Hydrology of Disasters*, *Water Science and Technology Library*, vol. 24, edited by V. Singh, pp. 395–425, Kluwer Academic Publishers, Dordrecht.

Neumann van Padang, M. (1951), *Catalogue of the active volcanoes of the world including solfatara fields*, vol. Part 1 - Indonesia.

Nino, Y., F. Lopez, and M. Garcia (2003), Threshold for particle entrainment into suspension, *Sedimentology*, *50*(2), 247–263.

Norris, R. (1994), Seismicity of rockfalls and avalanches at three Cascade Range volcanoes: implications for seismic detection of hazardous mass movements, *Bulletin of the Seismological Society of America*, *84*, 1925–1939.

Nott, P., and J. Brady (1994), Pressure-driven flow of suspensions: simulations and theory, *Journal of Fluid Mechanics*, *275*, 157–199.

O'Brien, J. (1999), FLO-2D Users Manual, (Version 99.2), 157.

Okuda, S., H. Suwa, K. Okunishi, K. Yokoyama, K. Ogawa, and S. Hamana (1979), Synthetic observation of debris flows (part 5), *in japanese with english abstract*, Kyoto University.

Onset Computer Corporation (2006), HOBO U20 Water Level Logger Manual (Part MAN-U20-001-04), *Tech. Rep. Doc: 11172-A*, Onset Computer Corporation.

O'Shea, B. (1954), Ruapehu and the Tangiwai Disaster, *New Zealand Journal of Science and Technology*, (B-36), 174–189.

Österlund, J. M., A. V. Johansson, and H. M. Nagib (2000), Comment on a note on the intermediate region in turbulent boundary layers [phys. fluids 12, 2159 (2000), doi:10.1063/1.1287613], *Physics of Fluids*, (12), doi:10.1063/1.1287,660.

Palmer, B., A. Purves, and S. Donoghue (1993), Controls on accumulation of a volcaniclastic fan, Ruapehu composite volcano, New Zealand, *Bulletin of Volcanology*, *55*, 176–189.

Parsons, J. D., K. X. Whipple, and A. Simoni (2001), Experimental study of the grain-flow, fluid-mud transition in debris flows, *Journal of Geology*, *109*(4), 427–447.

Patra, A. K., A. C. Bauer, C. C. Nichita, E. B. Pitman, M. F. Sheridan, M. Bursik, B. Rupp, A. Webber, A. J. Stinton, L. M. Namikawa, and C. S. Renschler (2005), Parallel adaptive numerical simulation of dry avalanches over natural terrain, *Journal of Volcanology and Geothermal Research*, *139*(1-2), 1–21.

Peterson, J. (1993), Observations and modeling of seismic background noise, *Tech. Rep. Open-File Report 93-322*, US Geological Survey.

Pierson, T. C. (1995), Flow characteristics of large eruption-triggered debris flows at snow-clad volcanoes: constraints for debris-flow models, *Journal of Volcanology and Geothermal Research Models of Magmatic Processes and Volcanic Eruptions*, *66*(1-4), 283–294.

Pierson, T. C. (1998), An empirical method for estimating travel times for wet volcanic mass flows, *Bulletin of Volcanology*, *60*(2), 98–109.

Pierson, T. C. (2002), Evaluation of lahar mitigation proposals at Mt Ruapehu, *Tech. Rep. Internal Series 63*, New Zealand Department of Conservation.

Pierson, T. C. (2005), Hyperconcentrated flow - transitional process between water flow and debris flow, in *Debris-flow Hazards and Related Phenomena*, edited by M. Jakob and O. Hunger, pp. 159–202, Praxis. Springer, Berlin Heidelberg.

Pierson, T. C., and J. E. Costa (1987), A rheological classification of subaerial sediment-water flows, in *Debris flows / avalanches: Process, recognition and mitigation*, vol. 7, edited by J. E. Costa and G. Wieczorek, pp. 1–12, Geological Society of America Review of Engineering Geology.

Pierson, T. C., and K. M. Scott (1985), Downstream dilution of a lahar - transition from debris flow to hyperconcentrated streamflow, *Water Resources Research*, *21*(10), 1511–1524.

Pierson, T. C., R. J. Janda, J.-C. Thouret, and C. A. Borrero (1990), Perturbation and melting of snow and ice by the 13 November 1985 eruption of Nevado del Ruiz, Colombia, and consequent mobilization, flow and deposition of lahars, *Journal of Volcanology and Geothermal Research*, *41*(1-4), 17–66.

Pitman, E. B., C. C. Nichita, A. Patra, A. Bauer, M. Sheridan, and M. Bursik (2003), Computing granular avalanches and landslides, *Physics of Fluids*, *15*(12), 3638–3646.

Procter, J. (2009), Towards improving volcanic mass flow hazard assessment at New

Zealand stratovolcanoes, unpublished Ph.D. Thesis, Massey University, Palmerston North, New Zealand.

Procter, J. N., S. Cronin, I. Fuller, M. Sheridan, V. Neall, and H. Keys (2009), Lahar hazard assessment using Titan2D for an alluvial fan with rapidly changing geomorphology: Whangaehu River, Mt. Ruapehu, *Geomorphology*, p. doi:10.1016/j.geomorph.2009.10.016.

Procter, J. N., S. J. Cronin, I. Fuller, G. Lube, and V. Manville (2010), Quantifying the geomorphic impacts of a lake-breakout lahar, Mt. Ruapehu, New Zealand, *Geology*, *38*(1), doi:10.1130/G30,129.1.

Raffel, M., C. Willert, and J. Kompenhans (1998), *Particle Image Velocimetry: A Practical Guide*, Springer, New York.

Raffel, M., C. Willert, S. Wereley, and J. Kompenhans (2007), *Particle Image Velocimetry: A Practical Guide*, 2nd edition ed., Springer-Verlag, Berlin, Heidelberg, New York.

Rangaraju, K. G. (1993), *Flow through Open Channels*, Tata-McGraw Hill.

Raudkivi, A. J. (1990), *Loose boundary hydraulics*, Pergamon, New York.

Rickenmann, D. (1991), Hyperconcentrated flow and sediment transport at steep slopes, *Journal of Hydraulic Engineering*, *113*(11), 1419–1439.

Rodolfo, K. S. (2000), The hazard from lahars and jokulhlaups, in *Encyclopedia of Volcanoes*, edited by H. Sigurdsson, B. F. Houghton, S. R. McNutt, H. Rymer, and J. Stix, pp. 973–995, Academic Press, San Diego, CA, USA; London, UK.

Savage, S. B., and K. Hutter (1989), The motion of a finite mass of granular material down a rough incline, *Journal of Fluid Mechanics*, *199*, 177–215.

Schmeeckle, M. W., and J. M. Nelson (2003), Direct numerical simulation of bedload transport using a local, dynamic boundary condition, *Sedimentology*, *50*(2), 279–301.

Schmeeckle, M. W., J. M. Nelson, and R. L. Shreve (2007), Forces on stationary particles in near-bed turbulent flows, *Journal of Geophysical Research-Earth Surface*, *112*(F2).

Scott, K. M., J. Vallance, and P. Pringle (1995), Sedimentology, behaviour, and hazards of debris flows at Mount Rainier, Washington, *Professonal Paper 1547*, USGS.

Sear, D. A., W. Damon, D. J. Booker, and D. G. Anderson (2000), A load cell based continuous recording bedload trap, *Earth Surface Processes and Landforms*, *25*(6), 659–672.

Siswowidjojo, S., N. Widaningsih, A. Rubiati, B. Mulyati, and G. De Neve (1994), Laporan pelaksanaan bimbingan gunungapi G. Semeru di Kabupaten Lumajang, Propinsi Jawa Timur, September 1994 [Report on works carried out at Semeru volcano in the Lumajang district, East-Java province, September 1994.], *Tech. rep.*, Volcanological Survey of Indonesia.

Smith, G. (1986), Coarse-grained nonmarine volcaniclastic sediment: terminology and depositional process, *Geological Society of America Bulletin*, *97*, 1–10.

Smith, G., and W. Fritz (1989), Volcanic influences on terrestrial sedimentation, *Geology*, *17*, 375–376.

Smithsonian Institute, G. (2008), *Bulletin of the Global Volcanism Network*, *33*(07), 12.

Sohn, Y. K. (1997), On traction-carpet sedimentation, *Journal of Sedimentary Research*, *67*(3), 502–509.

Solinst Canada Ltd (2006), Levelogger Gold Model 3001 Data Sheet, *Tech. rep.*, Solinst Canada Ltd.

Stevens, N. F., V. Manville, and D. W. Heron (2003), The sensitivity of a volcanic flow model to digital elevation model accuracy: experiments with digitised map contours and interferometric SAR at Ruapehu and Taranaki volcanoes, New Zealand, *Journal of Volcanology and Geothermal Research*, *119*(1-4), 89–105.

Stilwell, W., H. Hopkins, and W. Appleton (1954), Derailment of Wellington-Auckland Express at Whangaehu River Bridge between Tangiwai and Karioi Railways Stations on 24 December 1953., *Inquiry report*, this is a Board of Inquiry report re the Tangiwai Disaster sent to the Hon. Minister of Railways in April 1954.

Stutzmann, E., G. Roult, and L. Astiz (2000), GEOSCOPE station noise levels, *Bulletin of the Seismological Society of America*, *90*(3), 690–701.

Surinach, E., G. Furdada, F. Sabot, B. Biescas, and J. M. Vilaplana (2001), On the characterization of seismic signals generated by snow avalanches for monitoring purposes, *Annals of Glaciology*, *32*, 268–274.

Surinach, E., I. Vilajosana, G. Khazaradze, B. Biescas, G. Furdada, and J. M. Vilaplana (2005), Seismic detection and characterization of landslides and other mass movements, *Natural Hazards and Earth System Sciences*, *5*(6), 791–798.

Suwa, H., T. Yamakoshi, and K. Sato (2000), Relationship between debris-flow discharge and ground vibration, in *Debris-Flow Hazards Mitigation: Mechanics, Prediction, and Assessment*, edited by G. Wieczorek and N. Naeser, pp. 311–318, Rotterdam.

Takahashi, T. (1991), *Debris Flow*, IAHR Monograph Series, Rotterdam.

Tanguy, J. (1994), The 1902-1905 eruptions of Montagne Pelee, Martinque: anatomy and retrospection, *Journal of Volcanology and Geothermal Research*, *60*, 87–107.

Thompson, C. (1984), The weather and climate of the Tongariro Region, *Tech. Rep. Misc. Pub. 115*, New Zealand Meterological Survey.

Thouret, J. C., F. Lavigne, K. Kelfoun, and S. Bronto (2000), Toward a revised hazard assessment at Merapi volcano, Central Java, *Journal of Volcanology and Geothermal Research*, *100*(1-4), doi:10.1016/S0377–0273(00)00,152–9.

Thouret, J. C., F. Lavigne, H. Suwa, B. Sukatja, and Surono (2007), Volcanic hazards at Mount Semeru, East Java (Indonesia), with emphasis on lahars, *Bulletin of Volcanology*, *70*(2), 221–244.

Toro, E. (1997), *Riemann solvers and numerical models for fluid dynamics*, Springer-Verlag.

Tungol, N. M., and M. T. M. Regalado (1996), Rainfall, Acoustic Flow Monitor records, and observed lahars of the Sacobia River in 1992, in *Fire and Mud: Eruptions*

and Lahars of Mount Pinatubo, Philippines, edited by C. G. Newhall and R. S. Punongbayan, pp. 1023–1032, University of Washington Press, Seattle and London.

Uhira, K., H. Yamasato, and M. Takeo (1994), Source mechanism of seismic-waves excited by pyroclastic flows observed at Unzen Volcano, Japan, *Journal of Geophysical Research-Solid Earth*, *99*(B9), 17,757–17,773.

US Department of Commerce (1992), The June 1991 eruption of Mount Pinatubo, Phillippines, *Tech. Rep. Product Number 739-A11-007*, National Geophysical Data Centre.

VEGA Grieshaber KG (2009), VEGAPULS 62 Operating Instructions, *Tech. Rep. 28435-EN-090305*, VEGA Grieshaber KG.

Verstoppen, H. (1992), Volcanic hazards in Columbia and Indonesia: lahars and related phenomena., in *Geohazards Natural and Man-made*, edited by G. McCall, D. Laming, and S. Scott, pp. 33–42, Chapman and Hall, London, UK.

Vignaux, M., and G. Weir (1990), A general model for Mt Ruapehu lahars, *Bulletin of Volcanology*, *52*(5), doi:10.1007/BF00302,050.

Vilajosana, I., E. Surinach, A. Abellan, G. Khazaradze, D. Garcia, and J. Llosa (2008), Rockfall induced seismic signals: case study in Montserrat, Catalonia, *Natural Hazards and Earth System Sciences*, *8*, 805–812.

Waldron, H. (1967), Debris flow and erosion control problems caused by the ash eruptions of Irazu Volcano, Costa Rica, *Tech. rep.*

Williams, H., and A. McBirney (1979), *Volcanology*, San Francisco, CA.

Williams, R., A. J. Stinton, and M. F. Sheridan (2008), Evaluation of the Titan2D two-phase flow model using an actual event: Case study of the 2005 Vazcun Valley lahar, *Journal of Volcanology and Geothermal Research*, *177*, 760–766.

Wilson, K. (1985), Comparison of hyperconcentrated flows in pipes and open channels, in *Proceeding of International Workshop on Flow at Hyperconcentrations of Sediment*, pp. 115–138, International Research and Training Center on Erosion and Sedimentation, Beijing.

Witham, C. (2005), Volcanic disasters and incidents: a new database, *Journal of Volcanology and Geothermal Research*, *148*, doi:10.1016/j.jvolgeores.2005.04.017.

Xu, J. X. (1999), Erosion caused by hyperconcentrated flow on the Loess Plateau of China, *Catena*, *36*(1-2), 1–19.

Yamasoto, H. (1997), Quantitative analysis of pyroclastic flows using infrasound and seismic data at Unzen, Japan, *Journal of Physics of the Earth*, *45*, 297–416.

Zanuttigh, B., and A. Lamberti (2007), Instability and surge development in debris flows, *Reviews of Geophysics*, *45*, RG3006.

Zargola, M. V., and A. J. Smits (1998), Mean flow scaling of turbulent pipe flow, *Journal of Fluid Mechanics*, *373*, 33.

Zen, M., and D. Hadikusumo (1965), The future danger of Mt. Kelut (Eastern Java - Indonesia), *Bulletin Volcanologique*, *28*, 275–282.

Zenit, R., M. L. Hunt, and C. E. Brennen (1997), Collisional particle pressure measurements in solid-liquid flows, *Journal of Fluid Mechanics*, *353*, 261–283.

Zobin, V. M., J. Orozco-Rojas, G. A. Reyes-Davila, and C. Navarro (2005), Seismicity of an andesitic volcano during block-lava effusion: Volcan de Colima, Mexico, November 1998-January 1999, *Bulletin of Volcanology*, *67*(7), 679–688.

Zobin, V. M., I. Plascencia, G. Reyes, and C. Navarro (2009), The characteristics of seismic signals produced by lahars and pyroclastic flows: Volcan de Colima, Mexico, *Journal of Volcanology and Geothermal Research*, *179*(1-2), 157–167.